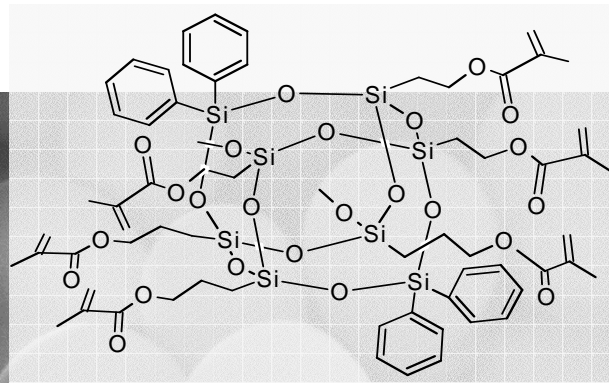




UNIVERSITY
OF TRENTO - Italy

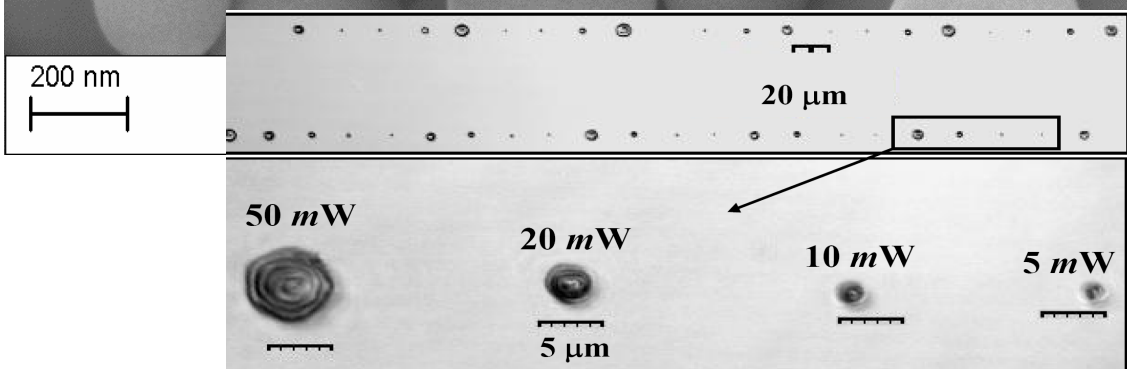
Department of Materials Engineering
and Industrial Technologies

Doctoral School in Materials Engineering – XXII cycle



Nanostructured hybrid organic/inorganic materials by the nanobuilding blocks (NBB) approach

Valeria Tagliazucca



28th January 2010

Secondo eminenti scienziati il calabrone non può volare perché il peso del suo corpo è sproporzionato alla portata delle ali; ma il calabrone non lo sa e continua a volare!

Ai miei cari

TABLE OF CONTENTS

PREFACE AND OBJECTIVES.....	7
1 SOL-GEL DERIVED HYBRID MATERIALS.....	15
1.1 Sol-Gel Background	15
1.2 Hydrolytic process	16
1.2.1 Chemical background.....	16
1.2.2 Silicates hydrolysis-condensation.....	17
1.3 Non-Hydrolytic approach	27
1.3.1 Hydroxylation reaction	27
1.3.2 Aprotic condensation.....	28
1.3.3 Condensation with in-situ water formation.....	31
1.4 Hybrid materials and Nanocomposites.....	32
1.4.1 Hybrid materials: classification and structural units.....	32
1.4.2 Nanocomposites	34
1.5 Design strategies of hybrids	36
2 APPLICATIONS OF SILICON-BASED O/I HYBRIDS.....	38
2.1 Coatings.....	39
2.2 Optical Materials	44
2.3 Membranes and Sensors	46
2.4 Drug Release	52
3 NANO BUILDING BLOCKS (NBBs)	55
3.1 Silicon-Based Nano Building Blocks	57
3.2 Polyoxometalates (POMs).....	59
3.3 Metal-oxo clusters (MOCs)	61
3.4 Tin-based NBB.....	63
3.5 Nanoparticles (NP)	64
4 SYNTHESIS OF Si-BASED NANO BUILDING BLOCKS (Si-NNB) ..	65
4.1 General considerations.....	66

4.2	Precursors	67
4.2.1	Difunctional precursors (D)	67
4.2.2	Trifunctional precursors (T)	67
4.3	Reaction conditions	68
5	EXPERIMENTAL.....	71
5.1	Low functionality derived hybrids (D/T _L).....	71
5.1.1	Syntheses of D/T _L samples	73
5.1.2	Syntheses procedure for base-catalysed D/T _L NBB.....	73
5.1.3	Syntheses procedure for acid catalysed D/T _L NBB.....	74
5.2	D/T - Characterisation	75
5.2.1	FT-IR characterisation of the samples.....	80
5.2.2	ATR-FTIR characterisation.....	84
5.2.3	Raman spectroscopy characterisation	86
5.2.4	NMR characterisation	90
5.2.4.1	¹³ C NMR.....	92
5.2.5	Gel Permeation Chromatography (GPC).....	95
5.2.5.1	Samples characterization.....	96
5.2.6	DSC measurements	99
5.3	High functionality derived hybrids.....	105
5.3.1	Syntheses of D/T _H samples.....	106
5.3.2	D/T _H syntheses.....	108
5.4	D/T _H characterisation	109
5.4.1	Raman spectroscopy	117
5.4.2	NMR spectroscopy characterisation	118
5.4.2.1	²⁹ Si NMR	118
5.4.2.2	¹³ C NMR.....	119
5.4.2.3	¹ H NMR.....	121
5.4.3	Gel Permeation Chromatography (GPC).....	122
5.4.3.1	Samples characterisation	122
5.4.4	DSC measurements	128

5.5	Self-condensation derived NBB	130
5.5.1	Performed syntheses.....	130
5.5.2	Synthesis and procedure	130
5.5.3	FT-IR characterisation of the precursors.....	131
5.5.4	NMR characterisation.....	134
5.5.4.1	²⁹ Si NMR.....	134
5.5.4.2	¹³ C NMR	136
5.5.5	¹ H NMR	138
5.5.6	GPC measurements.....	139
6	APPLICATIONS.....	143
6.1	Lithography.....	144
6.1.1	Optical lithography.....	146
6.1.2	Resolution.....	149
6.1.3	Light sources	150
6.2	Two Photon Polymerization.....	151
6.2.1	Two-photon absorption (TPA).....	151
6.2.2	General applications in photonics	152
6.3	Characterisation.....	153
6.3.1	UV photolithography	153
6.3.2	Matrices preparation.....	154
6.3.3	G _S -1 characterisation.....	154
6.3.4	FT-IR characterisation.....	155
6.3.5	Film patterning	155
6.3.6	G _S -2 characterisation.....	157
6.3.7	Two Photon Polymerisation (TPP)	157
6.3.8	Matrices characterisation	159
6.3.9	TPIP- D/T _H -1 matrices	161
6.4	Conclusions	165
7	NANO PARTICLES (NP).....	171
7.1.1	Syntheses approaches.....	175

7.2	The Sol-Gel method for silicon-based NP.....	177
7.3	Stöber method	178
7.3.1.1	Mechanism.....	180
7.3.2	Modifications to the original SFB method	180
7.3.3	Nanoparticles dye doping.....	181
7.3.3.1	Rhodamine dyes	183
8	SYNTHESIS OF MODIFIED Si-NP	184
8.1	Precursors	184
8.2	Experimental	185
8.2.1	<i>Characterization Techniques</i>	186
8.3	Synthesis and procedure standardization	188
8.3.1	MTES-NP	188
8.3.2	FT-IR characterisation of MTES-1 NP sample	190
8.3.3	SEM characterisation of the sample	191
8.3.4	N ₂ physisorption characterisation.....	192
8.4	NP prepared from a single precursor.....	194
8.4.1	Syntheses and procedure.....	194
8.4.1.1	Single precursor RTES-NP	195
8.4.2	FT-IR characterisation of the precursors	196
8.4.3	FT-IR characterisation of the samples.....	198
8.4.4	NMR characterization.....	200
8.4.4.1	²⁹ Si CP-MAS NMR.....	200
8.4.4.2	¹³ C MAS NMR	202
8.4.5	SEM characterisation.....	204
8.4.6	N ₂ Physisorption characterisation.....	206
8.4.7	Thermal analyses (TG-DTA).....	207
8.5	NP prepared from two precursors - Binary systems (RR'-NP)..	209
8.5.1	Syntheses and procedure.....	209
8.5.1.1	RR'NP- synthesis	209
8.5.2	FT-IR characterisation of the precursor.....	210

8.5.3	FT-IR characterisation of the samples	211
8.5.4	Multinuclear NMR chracterization.....	214
8.5.4.1	²⁹ Si MAS NMR	214
8.5.4.2	¹³ C MAS NMR	216
8.5.5	SEM characterisation	218
8.5.6	N ₂ Physisorption characterisation	220
8.5.7	Thermal analyses (TG-DTA).....	222
8.5.8	Contact angle measurements.....	224
8.6	Dye doping.....	228
8.7	High temperature behaviour of organic-modified NP.....	231
8.7.1	Evolution of NP sizes.....	237
9	EXPERIMENTAL	239
9.1	Methacrylate-based NP (MMp-NP)	239
9.1.1	MMp-NP syntheses.....	239
9.2	MMp-NP characterization	240
9.2.1	FT-IR characterization of the samples.....	240
9.2.2	SEM characterization of MMp-NP	241
9.2.3	Multinuclear NMR characterisation.....	242
9.2.3.1	²⁹ Si NMR characterisation.....	242
9.2.3.2	¹³ C NMR characterisation	243
9.2.4	DSC analyses.....	245
9.2.5	Thermal analyses (TG).....	246
9.2.6	N ₂ physisorption	248
10	APPLICATIONS.....	249
10.1.1	Methods and measurements	249
10.1.2	Coatings characterisation.....	251
	FINAL REMARKS.....	255
	REFERENCES	257

PREFACE AND OBJECTIVES

The challenge to combine organic with inorganic components to obtain new desirable properties is not just a recent industrial and academic target; as a matter of fact, successfully organic-inorganic (O/I) hybrid polymers were commercialized by the painting industries since the 1950s. If we take a deeper look into mankind history, we can easily observe that hybrid materials coexist with man since ages (Egyptian inks, green bodies of China ceramics, Mayan frescos, etc.)^[1], even if the “O/I hybrid” concept was coined in the 80s when the new approach of mild chemistry process of inorganic synthesis of glasses and ceramic began.

The motivation to create new materials, in the form of academic research and looking for industrial application, comes from the careful observation of nature, which has a great ability to combine the inorganic with the organic or biologic components ranging from tenth up to few tens of nanometres, allowing the construction of smart natural materials where different properties or functions (mechanics, density, permeability, colour, hydrophobicity, etc...) find a harmonious compromise.

Several aspects have to be associated with such a high level of integration: miniaturization to accommodate the maximum of the elementary functions in a small volume, optimization of complementary possibilities between organic and inorganic components and finally a fine regulation and hierarchy to obtain the final structure. In current life it is possible to find some examples of this fine regulation in natural O/I hybrids, such as bone and teeth tissue of vertebrates, in the silica skeleton of the diatoms or in the crustacean carapaces (Fig.1).

¹ C. Sanchez, B. Julián, P. Belleville, M. Poppal, *Applications of hybrid organic-inorganic nanocomposites*, J. Mater. Chem, 2005, 15, 3559- 2592

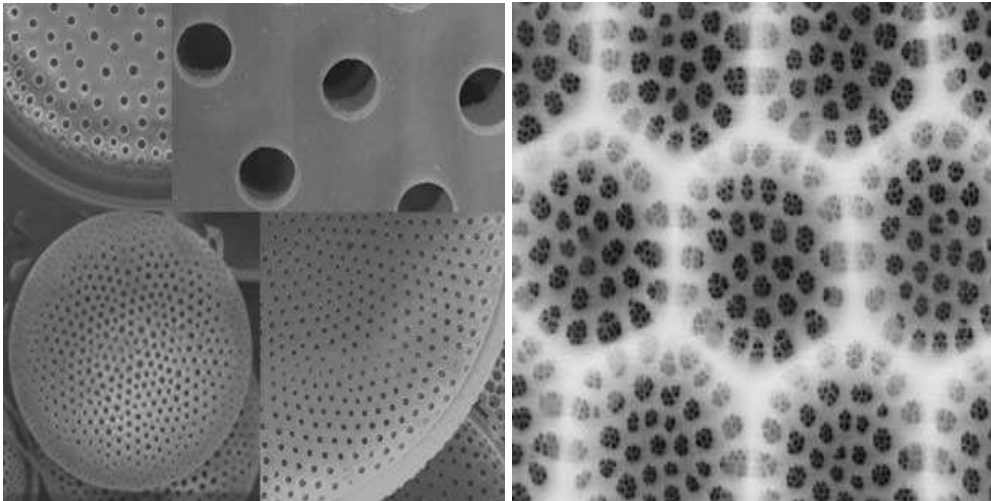


Fig. I: scanning electron microscopy images of natural hierarchically well organized O/I hybrids: diatoms [2]

Sol-Gel processing yields both inorganic and hybrid organic-inorganic materials; at the beginning it was exploited as a simple chemical synthesis method for forming inorganic glasses at low temperature (i.e. room temperature), but it became an easy technology to create new materials with the growing interest in polymer chemistry, processing and structure-properties relationships. A plethora of new materials with a bewildering variety of properties was synthesised and commercialised in the last three decades.

Hybrid O/I materials are not just physical mixtures of two different moieties on a molecular level, but are homo- and heterogeneous systems derived from inorganic and organic components that exhibit a synergetic combination of the typical properties of each constituent.

As a matter of fact, by preparing hybrid materials via sol-gel, it is possible to overcome some typical drawbacks of the inorganic sol-gel processing, as crack formation in coatings due to the high shrinkage^[3].

² Sumper, <http://www.biologie.uni-regensburg.de/Biochemie/Sumper/index.html>

³ C.J. Brinker, and G.W. Scherer, *Sol-Gel Science* (Academic Press, Dan Diego 1990)

The introduction of an organic phase is generally used to better control the shaping and processing of the material, to improve chemical stability, biocompatibility, electronic and/or optical properties and to balance hydrophobicity/hydrophilicity ratio affecting parameters such as wettability and solvation. On the other hand the inorganic counterpart provides thermal stability, electronic, magnetic, redox properties, refractive index or density.

Hybrid materials can be seen as multifunctional advanced materials with applications ranging from (micro)-electronics, optics, membranes, nanoparticles, protective coatings, catalysis, paints, pharmaceuticals, fuel cells, photovoltaic, sensors, bio-immunoassays and therapeutic vectors; within this frame the aim of the thesis is to find appropriate syntheses of O/I nanobuilding blocks (NBB) and nanoparticles (NP).

NBB should be used for the preparation of hybrid films by further polymerisation of their reactive functions, particularly for methacrylate and epoxy-based matrices for patternable films, which find application in opto-microelectronics.

NP should be employed as active-fillers for nanocomposites. They should have tuneable size, narrow size distribution and allow a good particles dispersion; therefore, different trialkoxysilanes bearing various functionalities were exploited in the syntheses. P should also be dopable in order to obtain an analytical tool for direct monitoring the filler dispersion in the polymeric matrices.

The basic information concerning the sol-gel method, the non-hydrolytic and the in situ water production routes are summarised in the background (Chapter 1). The sol-gel method is presented as synthetic approach for the production of hybrid O/I materials and the two strategies used in the thesis work (non-hydrolytic and in situ water production) are described. The keyword “nanobuilding block” (NBB) is introduced and the advantages of the NBBs assembly for the preparation

of O/I hybrid materials are highlighted. The general introduction is concluded with the NBBs' applications (Chapter 2).

The experimental section of this work is divided into two parts.

The first part reports the synthesis of NBB derived from the condensation of alkoxysilanes. A deep description of different classes of NBBs (Chapter 3) and the general requirements for the preparation of Si-based NBB (Chapter 4) are presented. The two synthetic strategies used in this work are confronted. Reaction evolution is monitored by Fourier transformed infrared spectroscopy (FT-IR). The final properties of the samples are characterised by different analytical methods (NMR, ATR/FT-IR, Raman GPC and DSC). In the end a brief conclusion concerning the syntheses, syntheses parameters and products structure will be given.

In Chapter 5 some applications of the NBB prepared as patterned films are briefly described. This part of the work has been done in collaboration with research groups of the University of Padua.

The second part of the work is addressed to the preparation of organic-modified nanoparticles (NP) (Part 2- chapter 6). A brief introduction of NP prepared by the Stöber method is presented (Chapter 7). The critical development of new experimental conditions is described (Chapter 8) and the use of the best obtained synthetic parameters to synthesise NP from single and binary mixtures of organosilanes bearing different functional groups is exposed (Chapters 8 and 9).

The obtained NP are characterised by different analytical techniques (FT-IR, multinuclear NMR, SEM, FE-SEM, TG, DSC and N₂ physisorption).

The influence of functional groups on particles' size and condensation degree was studied.

The results of the preliminary study on the optical properties of the doped NP are presented, as well as the first results, on the thermal behaviour (Chapter 8).

Finally the synthesis of methacrylate-derived NP, to be used as active fillers and the study of their polymerisation ability were accomplished. An introductory study of their use to prepare protective coatings was done in collaboration with the University of Trento - Dep. of Materials Engineering and Industrial Technologies) and the Polytechnic of Turin.

GENERAL INTRODUCTION:

Sol-Gel Background and Applications

1 SOL-GEL DERIVED HYBRID MATERIALS

1.1 Sol-Gel Background

The sol-gel process is used as a general method for preparing oxides by chemical synthesis in solution, the so-called “wet route”, and in mild conditions. It involves the inorganic network evolution through the formation of a colloidal suspension (sol) and its following gelation to form a solid network where the continuous liquid phase is retained (gel). The general scheme of the process is reported in Fig. 2 .

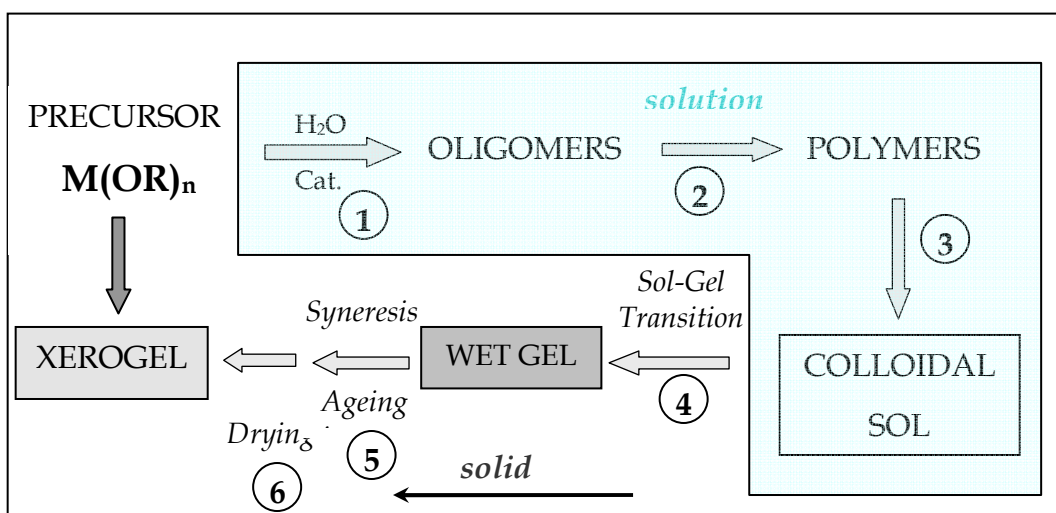


Fig. 2: General scheme of the main transformations occurring during the sol gel synthesis [1]

At a macroscopic scale, the process is very simple because it involves the transformation of a molecule (precursor) into a solid material. On the contrary, at the nano- and microscopic scales, the process is very complex, since it consists of several transformations involving three different state of matter: solution, colloid and solid.

At first, the molecular precursor gives rise by hydrolysis-condensation to nanometric linear and cyclic oligomers, which by polycondensation gradually become intermingled to yield cross-linked polymers (10-

100 nm). The polymers then aggregate into colloids (Fig. 2, 1-3). The colloidal solution is a viscous sol.

The second step is the transformation of the sol into a gel i.e. the sol-gel transition (Fig. 2, 4); the condensation reaction takes place at the colloids' surface and new few bonds create a solid wide meshed network capable to retain the solvent. By choosing the appropriate conditions it is possible to obtain uniform particles by precipitation from the sol (Fig. 2, 4).

After the gel formation (Fig. 2, 5), the number of bonds between the colloids increases, speeding up the solid densification. The process involves the expulsion of the solvent from the pores (syneresis) and leads to an amorphous solid with particle size and porosity depending on the experimental conditions.

The ageing process (Ostwald ageing process) [1] controls the macroscopic characteristics such as texture (specific area, density, porosity, hydrophilicity, etc...). Drying (Fig. 2, 6) by evaporation under room temperature and pressure causes the shrinkage of the gel network leading to a solid material called *xerogel*. The xerogel is converted in a dense ceramic by heat treatment.

1.2 Hydrolytic process

1.2.1 Chemical background

Sols are generally prepared starting from metal alkoxides $M(OR)_n$ ($M = Si, Ti, Zr, Al, \text{ etc.}$ and $OR = OC_nH_{2n+1}$) as precursors. The inorganic polymerization proceeds by hydrolysis of the alkoxy group of the molecular precursors in organic solvents, to introduce a reactive hydroxyl group on the metal, leading to a hydrolyzed molecule (reaction 1). This hydrolyzed precursor can react with hydrolyzed and not-hydrolyzed molecules in the condensation step.

The condensation step proceeds via formation of oxo-bridges and elimination of water or alcohol (reaction 2), or via metal-hydroxo-bridges formation (reaction 3), depending on the reaction (oxolation or olation).

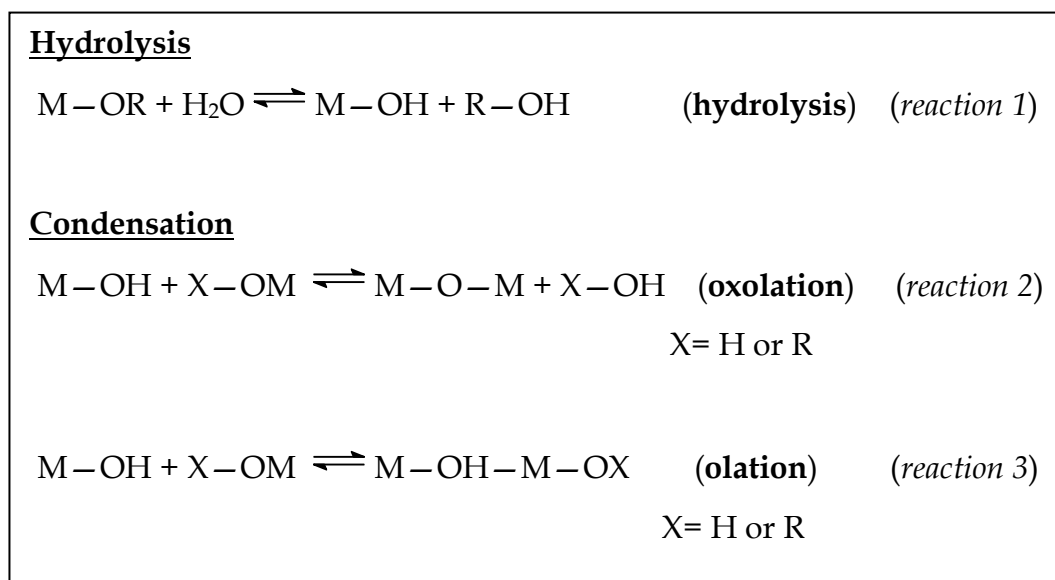


Fig. 3: hydrolysis and polycondensation reactions

The morphology and structure of the final inorganic framework strongly depend on the contribution of all the described reactions. Thus, it is possible to tailor the morphology and structure through the growth's control of the oxo-polymers. The main parameters controlling the reaction are: nature of precursors, temperature, solvent, hydrolysis ratio and use of catalyst.

1.2.2 Silicates hydrolysis-condensation

Silicon alkoxides are the most commonly used precursors in sol-gel processing [2], but this nucleus is less prone respect to the other metals to hydrolysis, condensation and other nucleophilic reactions.

Generally metal alkoxides are very reactive. The electronegative alkoxide groups make the metal atoms highly prone to nucleophilic attack,

and their hydrolysis rate is much higher than the one observed for silicon alkoxides [2, 3]. This is due to the high electrophilic character of the metal and to the metal ability of expanding the coordination sphere.

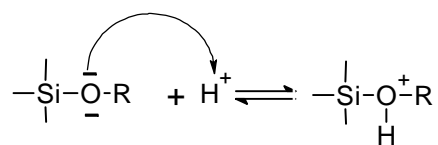
Silicon is more electronegative than transition metals and possesses lower partial positive charge on the nucleus; this makes the silicon less susceptible to nucleophilic attack and the kinetics of hydrolysis and condensation is considerably slow.

In order to speed up the reactions it is possible to use both acid and base catalysts.

✓ ACID-CATALYZED HYDROLYSIS AND CONDENSATION

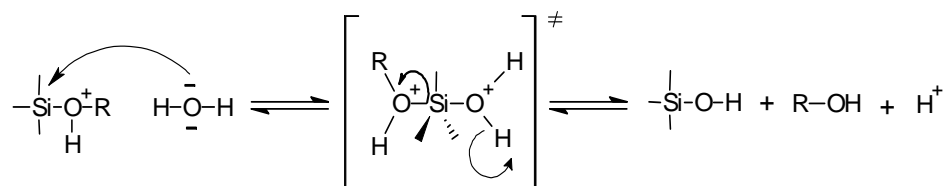
Hydrolysis

Under acid conditions, the alkoxide group undergoes a first fast protonation step



Scheme 1: hydrolysis first step in acidic catalysis - fast protonation

The electron density is withdrawn from the silicon atom, which becomes more electrophilic and therefore more susceptible to water attack.

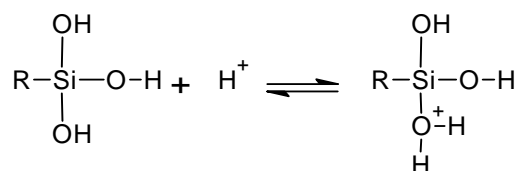


Scheme 2: hydrolysis second step in acidic catalysis - formation of 5-coordinated intermediate

The second step is a S_N2 type reaction, with the formation of a 5 fold-coordinated intermediate, which leads to a new Si-OH bond with inversion of the silicon tetrahedron and loss of an alcohol molecule [4].

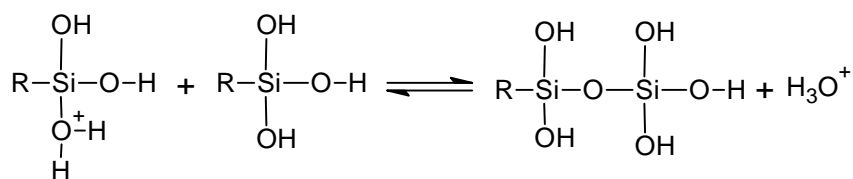
Condensation

It is generally accepted that the acid-catalyzed condensation mechanism involves a protonated silanol species.



Scheme 3: acid-catalyzed condensation : silanol protonation

Protonation of the silanol makes the silicon nucleus more electrophilic and thus more susceptible to nucleophilic attack. Silanols contained in monomers of weakly branched oligomers are the most likely to be protonated, since they are the most basic species.



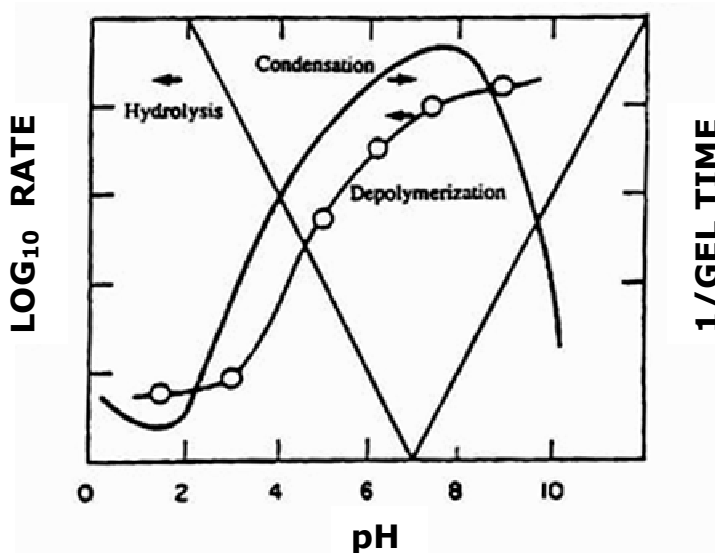
Scheme 4: acid-catalyzed condensation : formation of siloxane bonds

Therefore, condensation reactions may occur preferentially between neutral species, and monomers with protonated silanols, chain end groups, etc.

✓ **BASE-CATALYZED HYDROLYSIS AND CONDENSATION**

Hydrolysis

Compared to the acid-catalyzed hydrolysis run with the same amount of catalyst, the base-catalyzed process is much slower (Fig. 4).

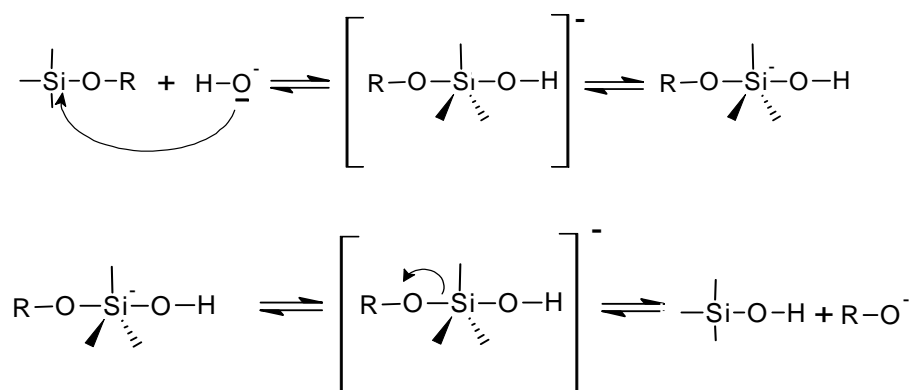


In a first rapid step, water dissociates to produce hydroxyl anions which are nucleophilic.



Scheme 5: hydrolysis first step in basic catalysis - water dissociation

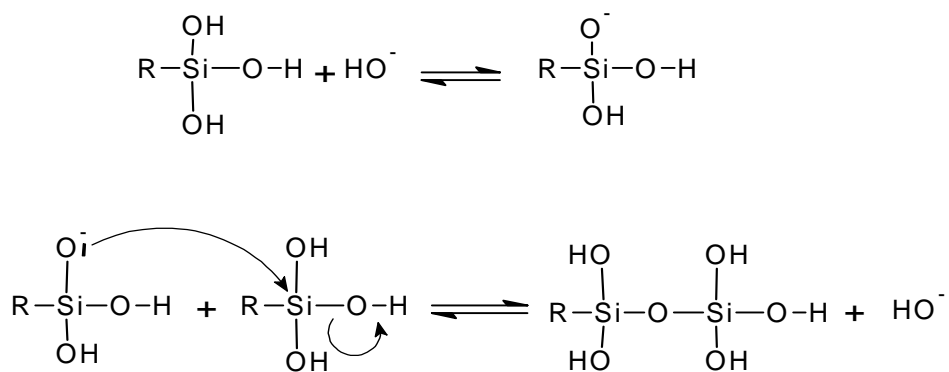
The hydroxyl anion attacks the silicon atom to form a stable penta-coordinated intermediate (S_N2 mechanism), that decays through a second transition state in which any of the surrounding ligands can acquire a partial negative charge.



Scheme 6: Hydrolysis second step in basic catalysis - formation of transition state (SN2 type reaction)

Condensation

The most widely accepted mechanism involves the attack of a nucleophilic deprotonated silanol on a neutral species.



Scheme 7: base catalyzed condensation

The reaction mechanism is S_N2 type, and the formed intermediate can be 5-fold or 6-fold coordinated.

The nature of the catalyst does not only influence the reaction kinetic, but also the obtained final structure.

Under acid catalysis, sol-gel derived silicon oxide networks yield mainly linear or randomly branched polymers, which entangle and form additional branches during gelation (Fig. 5). Since the degree of crosslinking is quite low in these conditions, the obtained siloxane structure is a mobile, elastic, and interwoven network. In this case the gel can easily shrink, rearranging as the solvent is removed during the syneresis step. The drying process leads to a highly microporous structured material.

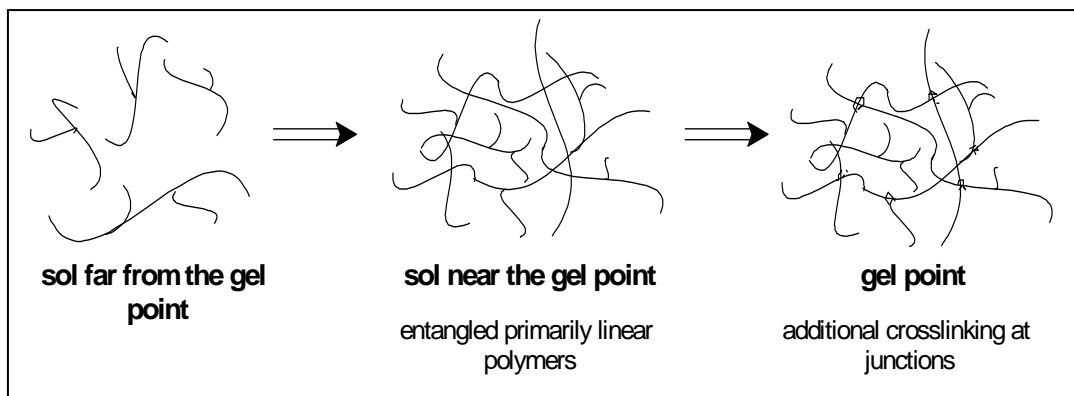


Fig. 5: Sol-gel structures obtained via acid catalysis

On the other hand under basic conditions, highly branched clusters are obtained, which do not interpenetrate prior to gelation and thus behave as discrete clusters (Fig. 6). As the solvent is removed, clusters undergo further condensation by rearrangement of the clusters themselves. The shrinkage stops at an early stage of drying, due to the clusters stiffness, and this results in larger pores and in meso- or macroporous materials after drying.

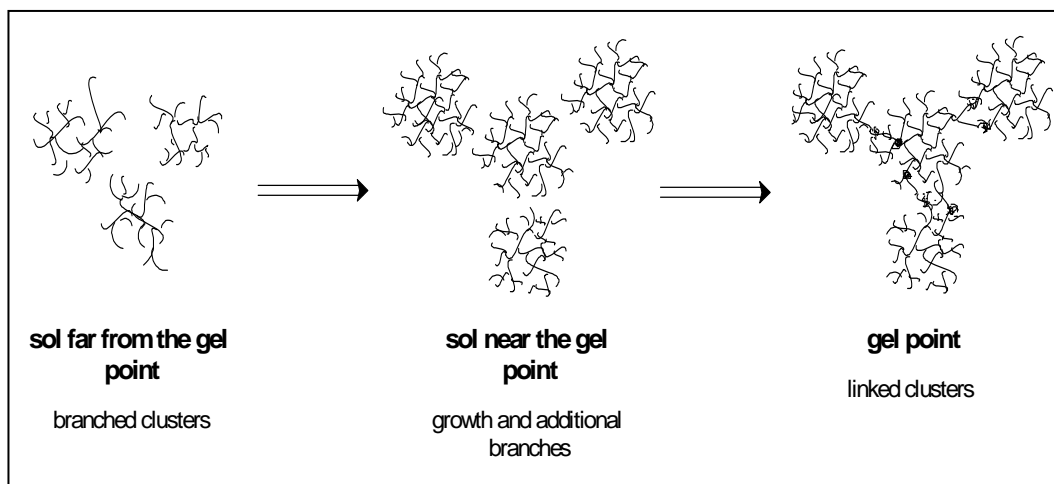


Fig. 6: Sol-gel structures obtained via basic catalysis

OTHER FACTORS

Hydrolysis and condensation's kinetics are not only affected by the uses of a catalyst. Other highly influencing parameters are: precursor, H_2O/Si , hydrolysis ratio, solvent.

✓ PRECURSORS

The hydrolysis rate of alkoxysilanes decreases with the increase in length or branching (steric hindrance) of the alkoxide groups.

The inductive effects are also of great importance. The substitution in the metal coordination sphere of alkoxy-groups with alkyl groups increases the electron density on silicon. On the contrary, replacement of alkoxides with hydroxyl (in hydrolysis) or bridging oxygen (in condensation) decreases the electron density on silicon, increasing the stability of positively and negatively charged transition states respectively.

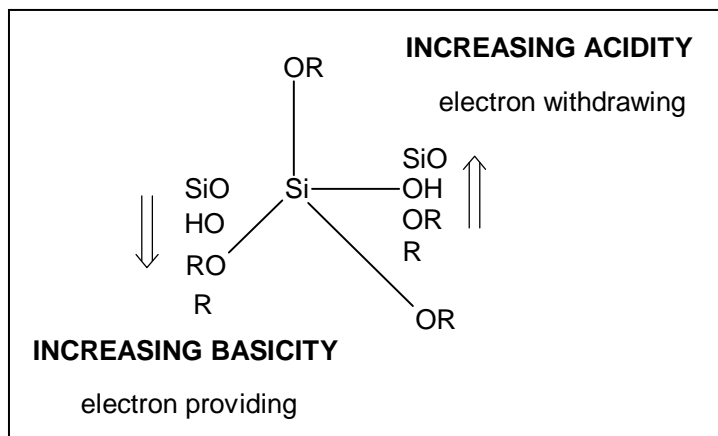


Fig. 7: inductive effects of substituent on silicon

✓ H₂O/Si RATIO

The water/alkoxide ratio r is defined as $r = [\text{H}_2\text{O}]/[\text{Si}(\text{OR})_n]$. Increasing the molar ratio r is expected to promote the hydrolysis reaction speeding up the process. High r values cause a more complete hydrolysis of monomers before condensation between the species occurs. Alcohol and water-producing condensation reaction rates are affected by the different extent of monomer hydrolysis. Generally, with under-stoichiometric additions of water, the alcohol forming condensation reaction is favoured ($r < 2$), whereas the water producing condensation reaction is preferred for higher values of r ($r \geq 2$).

✓ SOLVENT

Solvents are generally used to prevent phase segregation during the initial stages of the hydrolysis reaction, since silicon alkoxides are not miscible with water. The solvent improves the system homogenization, and influences the gelation kinetics by controlling the concentrations of silicates and water [4].

Solvents may be classified in polar and nonpolar, and protic or aprotic. The polarity largely determines the ability of solvating polar

or nonpolar species. On the contrary, the ability of protic solvents determines the strength of solvation of ions through hydrogen bonding. Since hydrolysis is catalyzed by H^+ ($pH < 7$) or OH^- ($pH > 7$), solvent molecules bonded to these ions via hydrogen bond reduce the catalytic activity under acid and basic condition respectively.

Aprotic solvents do not bond to hydroxyl via hydrogen bonds, leading to more nucleophilic ions, whereas H^+ becomes more electrophilic using protic solvents [5].

All the reactions involved in the sol-gel process are equilibria (Fig. 3, chapter 1.2.1) reactions, therefore it is possible to have reverse reactions as reesterification (Fig. 8-1) or alcoholysis or hydrolysis of the siloxane bond (Fig. 8-2a-b).

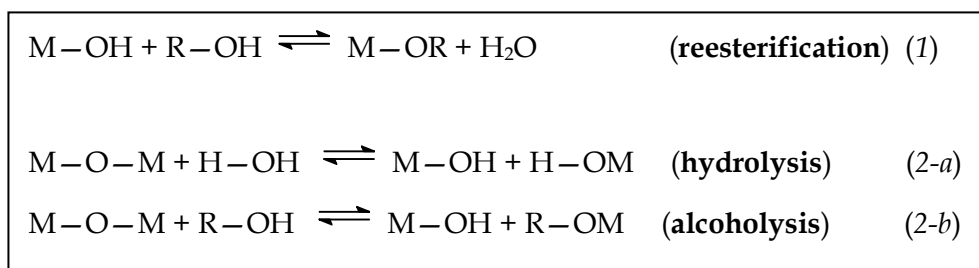


Fig. 8: reverse reactions

Aprotic solvents do not participate in reverse reactions as hydrolysis (Fig.7-2-a) or reesterification (Fig.7-1), because they do not possess sufficiently electrophilic protons and are unable to be deprotonated to form sufficient strong nucleophiles (OH^- and OR^-).

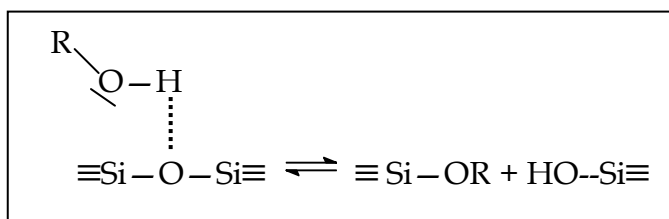
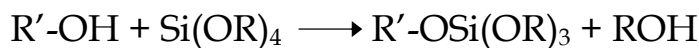


Fig. 9: reverse reaction via protic solvent

Therefore they do not formally take part to the sol-gel processing reactions (they are considered “inert”), although they may influence reaction kinetics by increasing nucleophiles’ and decreasing electrophiles’ strength.

Another competitive reaction is transesterification, in which an alcohol displaces an alkoxide group to produce another alcohol molecule (Scheme 8).



Scheme 8: transesterification reaction

This reaction is commonly employed in exchange reactions with metal alkoxide precursors as schematized hereafter:



This chemical modification is employed to slow down or speed up the hydrolysis and condensation rates in order to control the condensation pathways of the evolving gel and its final texture. For example, hydrolysis rates decrease with bulky alkoxy ligands. If transesterification is an undesired process, it is possible to overcome the problem by using the parent alcohol (i.e. ethoxides in ethanol).

1.3 Non-Hydrolytic approach

In the conventional sol-gel method, based on hydrolysis-condensation of molecular precursors such as metal alkoxides, it has been extensively reported [4 and references therein] that the structures and properties of gel depend on the initial stages of polymerization. A major problem with metal alkoxides is the ability to control the reaction rate, which is in general too fast, resulting in a poor control of the microstructure of the final oxide material.

An alternative strategy is provided by the non-hydrolytic sol-gel route, in which precursors, experimental conditions, catalysts and reaction mechanisms are changed [6, 7].

This approach has several advantages including the possibility to avoid the use of a solvent and the reduction of residual silanol groups in the final product.

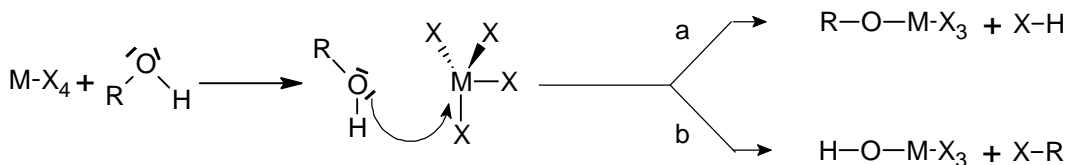
The non-hydrolytic process involves the reaction between a metal halide and an oxygen donor such as an alkoxide, an alcohol or an ether under non-aqueous conditions, with the release of a small molecule (R-X) as an alkyl halide, an ester or an ether as by-product.

Two different reactions are exploited: hydroxylation reactions and aprotic condensation. In the case of condensation, rigorous aprotic conditions have to be maintained by use of heterofunctional condensation reactions excluding hydroxyl groups.

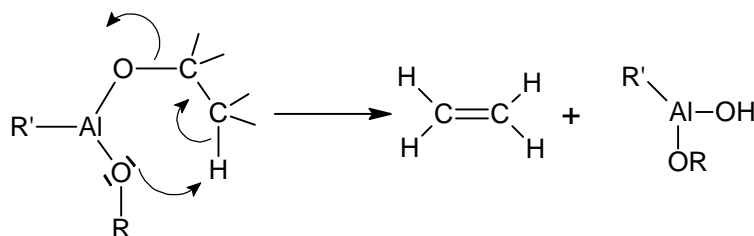
1.3.1 Hydroxylation reaction

One non-hydrolytic hydroxylation method is provided by the reaction between alcohols and metal halides (scheme 9). The reaction pathway involves the coordination of the alcohol oxygen lone pair to the metal centre, followed by the cleavage of either an alkoxy (scheme 9-a) or a

hydroxyl (scheme 9-b) group. Pathway (b) is preferred if the R substituent group is an electron-donor one, leading to a R-X by-product molecule. Another method is the thermal decomposition of a metal alkoxide precursor in a temperature range of 200-300°C, where hydroxyl groups are formed via cyclic elimination (scheme 10), with the simultaneous release of an olefinic compound [8]. This reaction type is involved during the calcination of non-hydrolytic gels into oxides where residual alkoxy groups are thermally degraded [9].



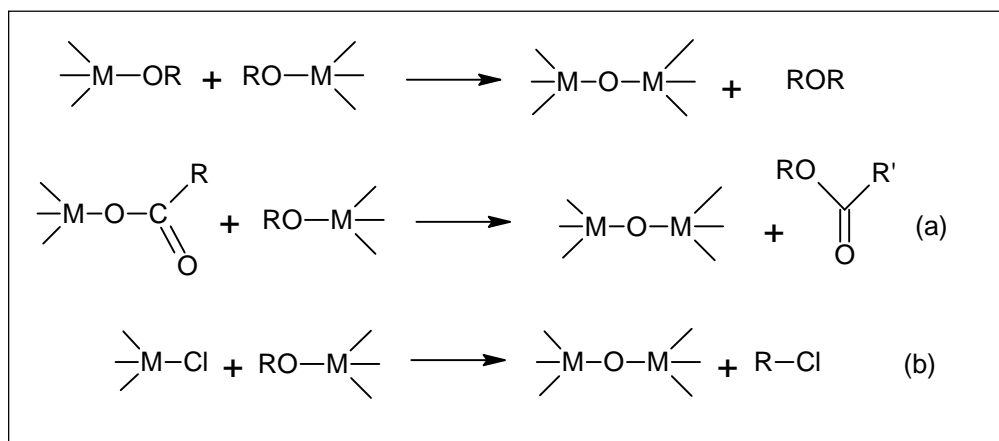
Scheme 9: two potential mechanism of non-hydrolytic hydroxylation bonding OH or OR groups



Scheme 10: thermal decomposition of a metal alkoxides precursor

1.3.2 Aprotic condensation

The formation of an oxo bridge is given by the condensation reaction between functional groups bonded to two different metal centres by elimination of small organic molecules (alkyl halide, ether or ester) as illustrated in scheme 11.



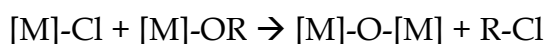
Scheme 11: aprotic condensation reactions involved in non-hydrolytic method

✓ ESTER ELIMINATION

The condensation reaction between a metal carboxylate and metal an alkoxide is proposed in scheme 11-a, and involves the coordination of the carbonyl oxygen of the carboxylic group to the metal alkoxide centre. This reaction decreases the electron density at the carbonyl carbon, allowing the nucleophilic attack of oxygen. Avoiding the use of solvent with coordination ability (i.e. pyridine) allows to avoid competitive coordinating pathways, thus enhancing the condensation reaction.

✓ ALKYL HALIDE ELIMINATION

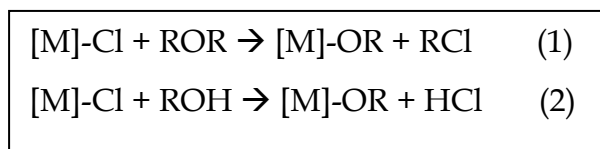
This reaction is based on the non-hydrolytic condensation between a metal alkoxide and a metal chloride, with the elimination of alkyl chloride. It involves the nucleophilic cleavage of OR bonds and therefore it is influenced by the electronic effects on the carbon centre (scheme 12).



Scheme 12: alkyl halide elimination

Generally this reaction occurs in a temperature range between room temperature and 100°C for transition metals. In the case of the less reactive silicon, Lewis acid catalysts (FeCl₃, AlCl₃) [10] are required to promote the condensation reaction.

One advantage of this method stays in the possibility to produce in situ the desired alkoxy group by etherolysis (scheme 13-1) or alcoholysis (scheme 13-2) of the metal chlorides. This opportunity is particularly interesting if the alkoxide precursor is expensive or not commercially available.



Scheme 13: etherolysis (1) and alcoholysis (2) of metal chlorides

Vioux et al. studied the etherolysis-condensation of titanium tetrachloride and titanium tetraisopropoxide [11], and highlighted the redistribution reaction between chloride and isopropoxide ligands. The first step of the ligands exchange mechanism (Fig. 10) is similar to the first step of condensation mechanism shown in scheme 12-b, with the exception that a M-O bond is cleaved in the intermediate Lewis adduct instead of a C-O bond.

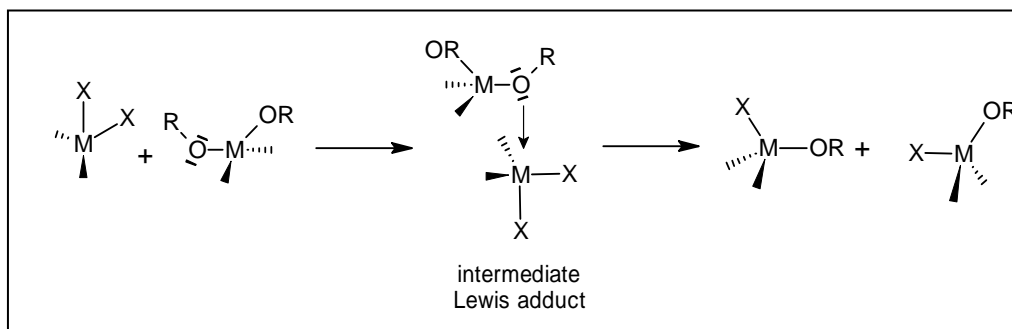
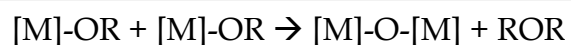


Fig. 10 : ligands exchange mechanism

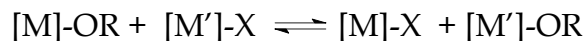
✓ **ETHER ELIMINATION**

So far, ether elimination (scheme 14) has been reported only as a secondary reaction in the condensation of dimethyldimethoxysilane with tetrachlorosilane in the production of liquid methoxylated polysiloxane resins, at 130°C in the presence of a Lewis acid catalyst [7]. The main expected reaction was the elimination of methylchloride, but also dimethylether was produced.



Scheme 14: ether elimination

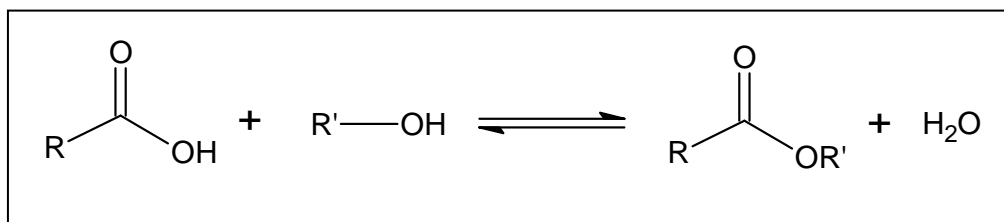
The reactive chloroalkoxide species are produced by ligand exchange between metal chloride and the oxygen donor; mechanisms and kinetics depend on the nature of these precursors.



Scheme 15: interchange of ligands

1.3.3 Condensation with in-situ water formation

This method is a compromise between the hydrolytic and the strictly defined non-hydrolytic process; it takes advantage of the peculiar positive aspects of the hydrolytic method, but avoiding the uncontrolled reaction rate and the heterogeneity in the final products by controlling the water production, which is generated directly into the reaction medium [12] under not rigorous controlled atmosphere. The in-situ water production (ISWP) exploits an esterification reaction, (Scheme 16), where both the amount and the kinetics of water produced are controlled by the features of the carboxylic acid and the alcohol.



Scheme 16: general esterification reaction between a carboxylic acid and an alcohol

1.4 Hybrid materials and Nanocomposites

1.4.1 Hybrid materials: classification and structural units

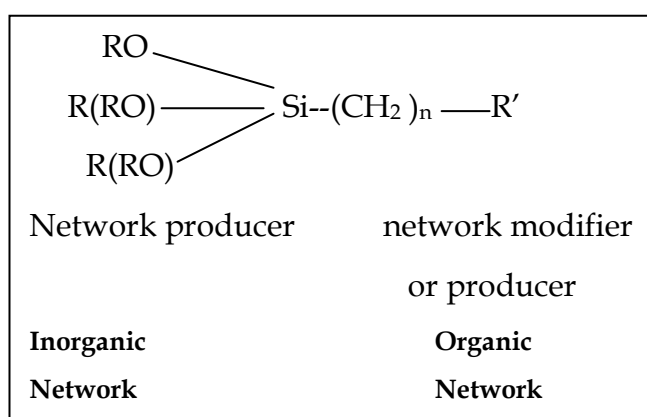
Nature, accessibility and extent of interface interactions are the key point to tune hybrids final properties. In the early 90s, Sanchez et Ribot [13] proposed a classification of hybrids based on the nature of the interactions between inorganic and organic moieties. This classification is still valid in the case of silicon-based hybrids, which are the materials studied in this thesis work.

Class I: the two phases interact only by weak interaction as van der Waals forces, electrostatic forces or hydrogen bonding. Among these hybrids we can find materials embedding organic dyes or optically active molecules [14-16], or composites where the fillers are produced in situ in a polymeric matrix [17-20].

Class II: the components of the two phases are linked by strong chemical bonds as ionic or covalent bonds. In this case the precursor has the general formula R'-M(OR)_n. The OR group undergoes hydrolysis to yield the inorganic backbone, while the R' group which is

the organic function bounded to the metal M insensitive towards hydrolysis. Typical class II hybrid material with wide applications are ORMOCER®s.

The structural units, which compose hybrid materials, cover the range from pure inorganic precursors (type I) to organic polymers (type IV) as shown in Fig. 11. All these precursors can be further classified taking in account their ability to modify the network [21].



Type I: Inorganic network producers - alkoxides of: Al (Aluminium tri-*sec*-butylate), Si (Tetraethoxysilane - TEOS, tetramethoxysilane - TMOS), Ti (Titanium isopropoxide), Zr (Zirconium butylate), etc.

Type II: Inorganic network producers with organic non reactive functions (end groups, as methyl), which act as network modifiers.

Type III: Inorganic backbone with organic reactive functions, which can further polymerize or react (methacryl or epoxy groups). These precursors can co-condense via Si-O-Si bonds.

Type IV: Organic monomers, which can react with the metal alkoxides via crosslinking or polymerization reactions.

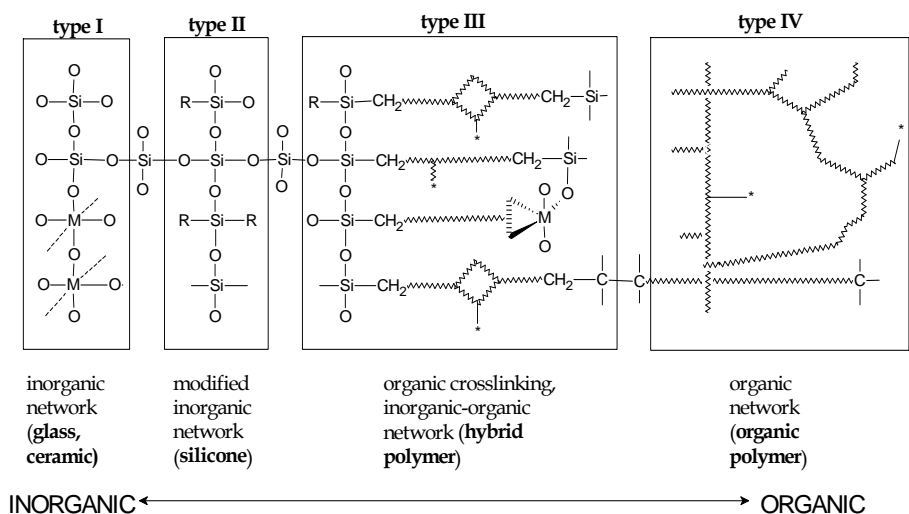


Fig. 11: Structural units of organic-inorganic hybrids and of its precursors type (* additional functional group) [21]

1.4.2 Nanocomposites

The term nanocomposite is used when the organic or the inorganic structural units are in the size range 1÷100 nm. In this definition it is possible to include porous media, colloids, gels and copolymers, but it is commonly referred to the combination of a bulk matrix and nano-dimensional phases [22].

Examples of discrete inorganic units for nanocomposites are nanoparticles, nanorods, carbon nanotubes, polyhedral oligomeric silsesquioxanes (POSS). Nanocomposites are usually obtained adding these building blocks in organic polymers.

Nanocomposites are found in nature, for example in the structure of the bone tissue and the abalone shell. In industry, nanoscale organo-clays have been used to control the rheological properties of polymer solutions (i.e. as paint viscosifiers) or as thickening agents in cosmetics since the mid 1950s. Although the term "nanocomposites" was not already used, the

polymer/clay composites were topic of textbooks [23] already in the 1970s.

The reinforcing material can be made up of particles, sheets (i.e. exfoliated clay stacks) or fibres (i.e. carbon nanotubes or electrospun fibres). The interface between the matrix and the reinforcement phase is typically an order of magnitude greater than for conventional composite materials. Ajany et al. observed that, with polymer nanocomposites the properties related to local chemistry, polymer chain mobility and configuration, degree of polymer chain ordering, degree of thermoset cure or crystallinity are directly affected by the extent of the interface between filler and matrix [22].

In terms of mechanical properties, nanocomposites differ from conventional composite materials due to the high surface to volume ratio of the reinforcing phase and/or its high aspect ratio. This means that a relatively small amount of nanofillers has an observable effect on the macroscale properties of the composite. For example, adding carbon nanotubes improves the electrical and thermal conductivity. Other kinds of nanoparticles may result in enhanced optical properties (i.e. CdS nanoparticles), dielectric properties, heat resistance or mechanical properties such as stiffness, strength and resistance to wear (clay mineral) and damage. In general, the nano-reinforcement is dispersed into the matrix during processing in a low (from 0.5% to 5%) “mass fraction” (or the percentage by weight); this is due to the low filler percolation threshold, especially for the nanometre-thin platelets, such as clays, or for carbon nanotubes.

1.5 Design strategies of hybrids

The main chemical pathways exploited for the preparation of hybrid materials are schematized in Fig. 12.

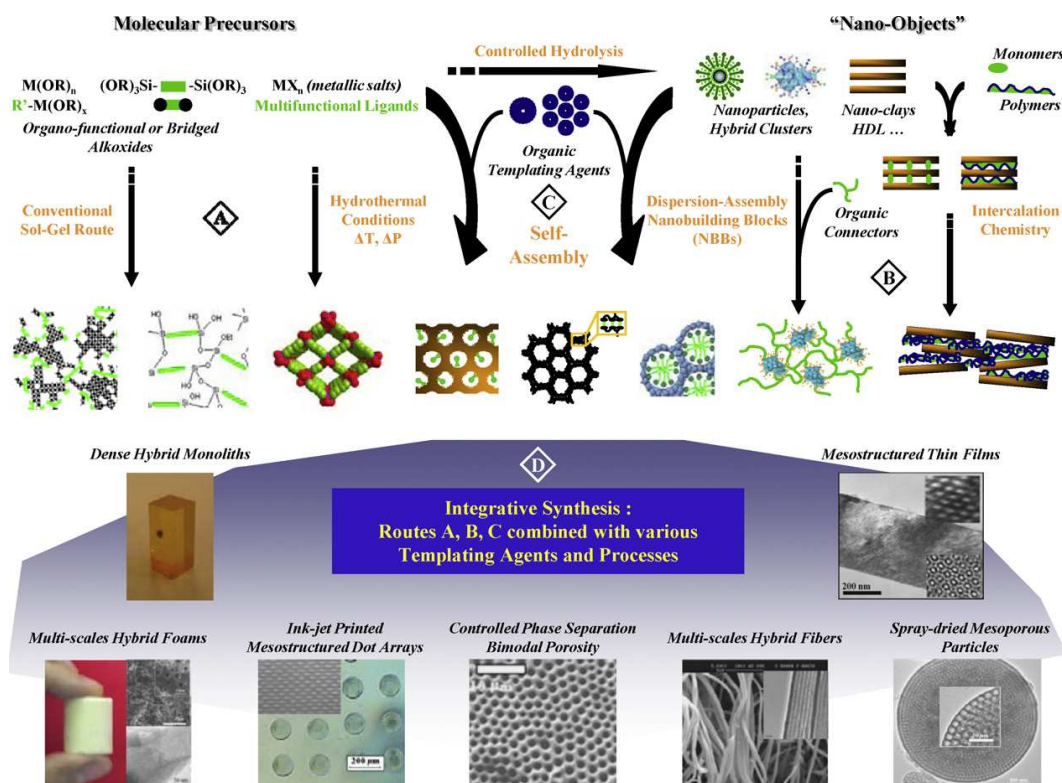


Fig. 12 Design strategies to obtain new hybrid materials via Sol-Gel [Errore. L'origine riferimento non è stata trovata.]

Path A corresponds to the soft chemistry route including the conventional sol-gel chemistry (A1-A2), where *route A1* shows the possibility to obtain the amorphous hybrid network via the conventional sol-gel process, through the hydrolysis of a mixture of organically modified metal alkoxides and metal alkoxides or metal halides. In *route A2*, homogeneous hybrid materials with a higher degree of (self)-organisation are achieved, thanks to the use of bridged precursors as silsesquioxanes $X_3Si-R'-SiX_3$ where R' is an organic spacer and X is Cl, Br or OR [24]. *Route A3* is mainly exploited for the preparation of absorbents [25-27] and catalysts, for which

the hybrid materials are synthesised using organic templates in polar solvents.

Path B introduces Nano Building Blocks (NBBs), which are preformed objects of defined size that keep their integrity into the final material. They can be clusters, organically pre- or post-modified nanoparticles, and layered compounds that can assembly (*route B1*) or can be dispersed into a reactive matrix (*route B2*). Moreover, they are usually functionalized with organic reactive functions which act as spacers and allow their connection at the mesoscale.

Path C is called “self-assembling procedure” and exploits the use of organic surfactants, which act as structure directing agents (*route C1*). By the recent approach C2 highly ordered structures are obtained, as the periodically mesoporous hybrid silicas, presenting organic reactive functions within the inner inorganic walls [29]. *Route C3* is a combination of self-assembly and NBB approaches.

Path D, through the control of phase separation phenomena, leads to hierarchically organized final material also at the micron scale [28].

2 APPLICATIONS OF SILICON-BASED O/I HYBRIDS

At the beginning of the research on organic modified materials, hybrids were studied and synthesised for achieving enhanced mechanical properties [30-31]

It has been demonstrated that PDMS (polydimethylsiloxane)-SiO₂ hybrid systems containing less than 15 molar% PDMS show high hardness values [32]. The measured hardness can be ten times higher than that of plastics such as polycarbonates and the Brittle index - defined as the ratio of hardness to elastic modulus - can be much lower than that of pure oxides [33].

The first successful applications of O/I hybrids in the coatings field were scratch or abrasion resistant coatings for transparent polymer substrates (CR39 based lenses) [34]. Other coating lacquers, based on thermal or UV cured ormosils (organic modified silicates), have been developed for various substrates (ceramics, metals, polymers). Taber abrasion tests (cycles of abrasion) according to the ASTM-D1044 method indicated that the optical transparency (measured by the Haze-value, which increases when optical transparency decreases) decreased in uncoated samples. In the case of O/I hybrid coated plastics, the Haze values were approximately around 1.5% whereas for uncoated samples, they were in the range 20-50% [35]. Hardness and elastic modulus were also measured and confirmed the effectiveness of the abrasion resistance of these coatings [36].

During the last decades many new applications have been found [37a-d]. O/I hybrids provide excellent matrices to be doped with a variety of inorganic, organic and biological compounds, which show an enhanced

activity in monitoring gases, solvents, pH and bioactive molecules. Hybrids can be used as protective coatings and for the preparation of catalytic materials; moreover, they have been widely exploited for photonic applications, for instance in the fabrication of waveguides and in the field of information transmission.

2.1 Coatings

Coatings are probably the main field where most commercial sol-gel products are found. In particular, protective coatings do not only protect but also give longevity, avoiding the degradation of the material on which they are deposited. The sol-gel process provides an excellent route for the synthesis of many non-toxic, crack-free and transparent coatings.

✓ PROTECTIVE COATINGS

The interest in the sol-gel method for protective coatings increased in the last decades, especially since the technique appears to be competitive also under the economical point of view. The first patent related to SiO₂ and TiO₂ coatings is dated back to 1939 [38].

Through this route it is possible to synthesise and deposit coatings of various compositions and properties. The coating can be deposited with a wide range of techniques as: dipping, spinning, rolling and electrophoretic deposition (EPD). The use of a protective coating on metals permits the deposition of a barrier coat that insulates the metal from the aggressive environment. One case of particular importance is constituted by metal structures used in the aerospace industry and made of aluminium and its alloys, which durability should be ensured for long time (decades). Hybrid coatings have been extensively studied, varying the metal substrate and the precursors in the coating solution [39], and the resistance against

corrosion was evaluated vs. change in gloss by a humidity cabinet test. The colour change in uncoated aluminized steel indicated oxidation, whereas the coated part maintained the same colour, showing good resistance to corrosion. Menning [40] compared inorganic with hybrid coatings through tests of static oxidation, XRD analysis, electrochemical measurements and salt spray corrosion test. The result was that inorganic thick silica coatings provided the highest protection factor against oxidation at 800°C but hybrid coatings reduced O₂ penetration to a greater extent and presented better electrochemical behaviour. Similar results were obtained by Galliano [41] and Gallardo [42] on AISI 316L steel and TEOS/MTES hybrid coating produced in acidic medium. A comparison study between two different steels (304 and 316 both stainless) was done by Chou et al. [43] using a methacryloxypropyltrimethoxysilane (MPTMS) based hybrid coating. The coatings were uniform and crack free, and in the case of AISI 316L, there was a neat enhancement in corrosion protection, whereas for the 304L steel the results were unsatisfactory, probably because of different interactions between coating and substrate surface. Gallardo [44] demonstrated that the improved properties of O/I hybrid coatings in resistance of the metal corrosion, are due to the final amount of organic material present in the coating, thus high sintering temperature leads to a worsening in the protective properties. Recently EPD has been used to produce hybrid SiO₂ coatings from colloidal sols in basic condition. This permits to include in situ produced particles in the sol [45]. Further on, EPD makes possible to produce thicker coatings improving the barrier against electrolyte corrosion properties.

Hybrid materials are also used as additives in composite materials, exploiting the UV curing technique to cure the final coating. This

method is efficient, environmental friendly and needs just a suitable UV photoinitiator to crosslink the coating in a very short time [46]. Methacryl-functionalised silica nanocomposites were produced by both bottom-up and top-down approach leading to 80 μ m film thickness [47]. Physical and electrochemical performances of the coatings were tested, resulting in stiffness improvement and in better barrier properties for both approaches.

Hybrid sol-gel coatings for the protection of transparent plastics have been one of the first commercial products resulting from this technology. As mentioned in the introduction of this chapter, organic resins are used as optical lens material since PGG Industries commercialised them in the 1940's (CR39®).

The incorporation of titanium alkoxide resulted in a higher refractive index ($n_D = 1.533$) of the hybrid material in comparison to the simple poly(methyl)siloxanes used as scratch resistant coatings on top of poly(methyl) methacrylate (PMMA) or polycarbonate (PC) sheets. Substitution of titanium-based particles with boehmite particles increased by about the 30% the microhardness values of the hybrid material [48].

Other important parameters influencing the abrasion resistance of hybrid coatings are the curing conditions. Optimal curing conditions lead to a linear correlation between abrasion resistance and microhardness results of the coatings [49].

In the automotive field the scratch resistant clear coats are based both on the incorporation of hard nanoparticles into flexible polymer matrix [50] and on achieving a higher cross-linked system. The "dual-cure" method exploits isocyanate (-NCO) polyol crosslinking in addition to the radical UV initiated polymerization [51].

✓ ART CONSERVATION

The sol-gel process has been used in the last years as elective technique to preserve and conserve artistic handwork, from wood to stone consolidation or glass and metal surfaces protection [52].

A very delicate point in art conservation is that each conservation situation requires a peculiar analysis and a deep knowledge of degradation process and interactions between material and coating [53, 54].

Since 1998, sol-gel derived materials were proposed by Sym [55] as suitable materials for artists, even if we find the first patent in stone preservation in 1926 [56]. Since then, O/I hybrids were successfully applied to different artefacts: stone [57, 58], wood [59], glass [60]. Methyltrialkoxisilanes are probably the most used reagents in conservation as they render stones water repellent and are able to consolidate marbles [61, 62].

Last Judgment mosaic in Prague [63] was treated using O/I hybrid, for preventing the corrosion process to which the outdoor mosaic was subject. Another recent study was carried out on the conservation of the *Grande Vetrata* (Great Stained-Glass Window) of SS. Giovanni e Paolo Church in Venice [64].

Another interesting application of coatings is for functional purposes. Various functional coatings were studied in the last decades [65-67], such as O/I hybrid and nanocomposites coatings.

In the last year, the demand for high-performance, design and safety of automobile windows considerably increased.

✓ FUNCTIONAL COATINGS

In the field of automotive functional coating, the main products are sun-reflective windows, antireflective glasses and optical filters and

blue-reflecting car rear view mirrors. Usually reflective applications exploit a layered system in which the layers are stacked and have alternating refractive index; moreover the layer thickness is in the range of light wavelength. The reflected light is reduced by destructive interference and does not exceed 0,2%. When nanoparticles (NP) were used in the coatings, it was also possible to decrease the reflective loss at 550 nm to 1% [68]. Compared to traditional vapour deposition technologies, the sol-gel process has several advantages especially for the treatment of plastics and glass large area parts [69]. These advantages are mainly due to the ability to coat both sides of the substrate at the same time and the low cost for coating area.

An example of O/I hybrid material that leads to low refractive index layer was studied by Takahashi and co-workers in 1997 and has found an application in the automotive field as antireflective coating for windows [70].

Another application of sol-gel in the automotive field is the HUD system, originally developed for aircraft use, and commercialized in 1988 by Nissan Motor after a joint study with Central Glass. A HUD (head up device), is a transparent display presenting data without requiring the user to look away from the usual point of view. It consists of an ultra bright vacuum fluorescent tube (VFT) used as display light source, optical lenses for focusing the images, a reflective mirror, a transparent curved aperture cover and a combiner. The coating is prepared from a mixed silicon e titanium alkoxides solution and deposited by dip-coating. This technique permits to fulfil all the standard requirements demanded by ANSI and the Japan Industrial Standards.

Another application is the design of water repellent automotive glasses for securing sight of the drivers. Various coatings have been

prepared starting from solutions containing polyfluorinated alkylsilanes [71]. The superhydrophobic properties that allow the water sliding are very attractive. Furukawa studied the relationship between sliding angle and contact angle hysteresis of a series of fluorinated polysiloxanes with perfluorooctyl groups and trichlorosylethyl groups, plus three different fluorinated silane coupling agents. The sliding angle decreases as the mobility of the polymer surface increases and the easiness of alkyl chain reorientation in polysiloxanes is an important factor that affects slipperiness of water droplets. The produced coating exhibited a high durability [72].

2.2 Optical Materials

Upcoming industrial applications are found in the field of micro-optics and electronics. In the electronic field, the components are classed into either passive or active devices. A passive device does not supply any power gain (amplification) to a circuit or system. It has no control action and does not require any input other than a signal to perform its function, such as resistors, capacitors and inductors. Active devices are capable of controlling voltages or currents and can create a switching action in the circuit, as diodes, transistors and integrated circuits.

Many properties of hybrid materials in combination with low temperature processing are the peculiar characteristics exploited to prepare optical materials. In order to obtain films not only for passive I/O components (I/O = input-output, meaning to describe a device that transfers data from a system to or from a peripheral device), but also for useful active I/O devices, O/I hybrids can act as hosts to lanthanide ions at high concentration, (U(600) [73]).

Excellent optical transparency, good thermal and mechanical stability of hybrid materials are the peculiar characteristics exploited to prepare optical waveguides [74].

Waveguides can be created by a single large photomask approach or by continuous approach, in which the patterns are produced from smaller masks and are then carefully aligned. Misalignments of less than 5 μm were observed between waveguide endings on a sample prepared from two step-out of 101.6 mm masks on silicon wafer [75].

Not only pure silicon derived hybrids are used to prepare waveguides; Porque and co-workers studied a photopolymerizable layer structure from organosilicate and organozirconate precursors with low optical losses (<0.5 dB/cm) [76], in which the zirconium precursor enabled the control over the refractive index. In the last ten years the opto-electronic market has grown exponentially, especially the customer area of organic light emitting diodes (OLEDs) displays. This is because hybrid materials, especially polymer-based nanocomposites, can be deposited as thin film even on flexible and foldable supports. Interesting properties are also exhibited from matrices, which incorporate polyhedral oligomeric silsesquioxanes (POSS). These materials are used as active layers in OLED with improved performances (higher thermo-mechanical stability and controlled optical emission) compared to those obtained from polymer only [77]. Flat screen colour display can also be based on dye-doped microspheres acting as pixels [78].

Hybrid nanocomposites are also an interesting platform for non-linear optical (NLO) material. A new NLO sol-gel material was prepared from a modified sol-gel process, in which the free radical polymerization process is exploited, in order to obtain an interpenetrating inorganic-organic matrix (IHM). MPTMS was used as precursor and as growing free radical for the polymerisation [79]. A short review of nanocomposites as NLO materials was given by Sanchez et al. in [80] and more recently Innocenzi

et al. [81] exhaustively reported on the use of organic-inorganic hybrid materials in the field of optics.

2.3 Membranes and Sensors

Since asymmetric cellulose membranes were developed in the 1960s for water desalting, various breakthroughs in membrane applications have been achieved with the use of synthetic polymers and advanced ceramics. At the present time the design of new materials for membrane application is still in progress and has to match severe selectivity criteria. Industrial membrane processes under development as gas separation, nanofiltration or sensing deal with small gas, vapour or liquid concentrations. Examples of satisfactory separation that are possible only thanks to the membranes produced in recent years are nitrogen/oxygen gas separation, or the selective extraction of biological molecules of interest from their natural environment media, as the separation of one specific amino acid from a mixture of several amino acids [82-83].

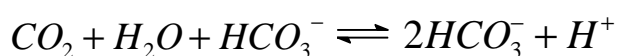
✓ GAS SENSORS

Since their earlier synthesis by the sol-gel process [84], inorganic membranes have been based mainly on silica-derived materials. Silica membranes are still widely used and usually they are synthesised by the acid catalyzed hydrolysis and condensation of tetraalkoxysilanes. The structure of the networks resulting from the sol-gel process of tetraalkoxysilanes, $\text{Si}(\text{OR})_4$ (R is an alkyl group), depends on the nature of catalyst used in the reaction (acid or basic), temperature and sol concentration [85] The above mentioned method generally suffers from a time dependent change in the response of the polysiloxane network that is related to ageing effects. An improvement in this field was made when hybrid materials were used, as in the case of networks prepared from

phenyltrimethoxysilane (Ph-SiOMe₃), its copolymers and other trialkoxysilanes. The resulting hybrid displays distinctly improved properties in terms of long-term stability, and gas permeability.

Two examples of membranes used as gas sensor are given below.

Carbon dioxide and other acid gases are usually tested via acid-base reactions occurring inside sensor membrane. For weak acids, as CO₂, a bicarbonate buffer (pH 8-9) is contained in a gas-permeable polymer. The following acid-base reaction occurs in the buffer:



The change in pH is detected by a pH indicator dye contained in the sensor layer. The reaction is fully reversible.

Generally the pH indicator is suspended in an aqueous buffer solution in form of small droplets, into a hydrophobic polymer. This device presents several drawbacks, like the difficulty in controlling the osmolarity and ionic strength of the water-buffer system and the droplets size, which are not stable.

To overcome these problems, a new approach was used based on a common dye, pyranine (Fig. 13), which is immobilized in a hydrophobic sol-gel derived glass. The glass matrix offers a highly stable microporous environment that can easily be deposited on a suitable substrate by the dip-coating technique [86].

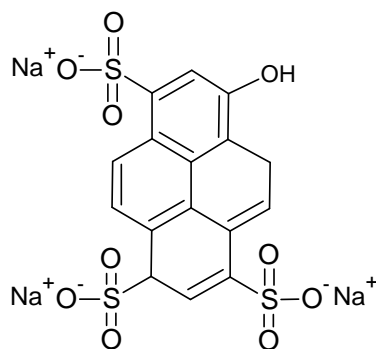


Fig. 13: pyranine dye

This material offers high sensitivity and rapid response of the polymer films. With the same dye, Von Bülzingslöwen et al. [87] developed a CO₂-sensor for modified atmosphere packaging applications. The internal buffer system was a solution of cetyltrimethylammonium hydroxide. The obtained system (Ruthenium complex/pyranine) is compatible with life-time based fluorimetric sensors and with established optical oxygen sensor technology. The sensor is stable for over seven months.

Biochemical oxygen demand (BOD), is usually defined as the amount of oxygen required by bacteria for stabilizing decomposable organic matter under aerobic conditions [88]. This test is one of the most important in stream-pollution-control activities.

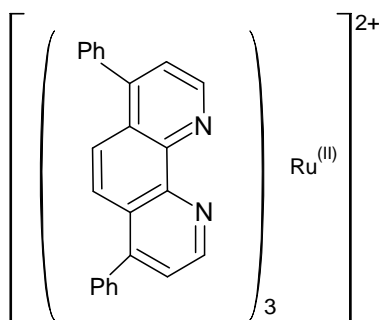


Fig. 14 : ruthenium dye

With a perchlorate salt of the ruthenium complex in Fig. 14, embedded in an organically modified silicate film, a sensing film was produced for BOD measurements. The sensor is based on a combination between an optical fibre for dissolved oxygen (DO) monitoring and an immobilized culture of seawater microorganisms (*Bacillus licheniformis*, *Dietzia maris* and *Marinobacter marinus*) in a modified sol-gel matrix [89, 90].

The results of the biosensor are in good agreement with measurements determined by conventional BOD₅ method for seawater samples.

✓ SOLVENT SENSORS

Matrices synthesised from methyltrimethoxysilane (MTMOS) and tetramethoxysilane (TMOS), in various ratio were used to entrap a Reichardt's betain dye (2,6-diphenyl-4-(2,4,6-triphenyl-N-pyridino)phenolate, (Fig. 15), with retention of its sensitivity to environment polarity. The entrapped dye was used to probe the effective polarity within the pores of the siloxane network; the hybrid material is therefore potentially suitable for the development of alcohol sensors. Avnir et al. prepared different matrices starting from various trifunctional precursors (methyl-, vinyl-, propyl-, isobutyl- and phenyltrimethoxysilane) co-polymerized with tetramethoxysilane. From solvatochromic studies it was found that the polarities of the hybrids depend on the precursor, precursor proportion and the solvent at the interface [92].

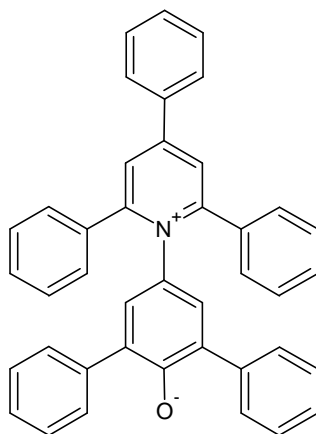


Fig. 15 Reichardt's dye (2,6-diphenyl-4-(2,4,6-triphenyl-N-pyridino)phenolate)

The ratio between trimethoxy substituted silane (R-TMS) and TMOS has a great influence on polarity, which decreases when the R-TMS :

TMOS increases. These results allowed to prepare sensing materials for polar and apolar solvents by changing TMOS/ R-TMS ratio.

✓ CATALYSIS

Heterogeneous catalysis provide the opportunity for recovering and recycling catalysts from the reaction medium with the possibility to improve processing steps, and to achieve better process economics and environmentally friendly industrial manufacturing. The sol-gel technology has the ability to increase the catalytic activity of dopant molecules thanks to the superior thermal stability, inertness, porosity and high surface area of the supports towards the entrapped molecules.

Depending on the application, sol-gel materials can be micro- (pores $< 20 \text{ \AA}$), meso- (pores $20 \text{ \AA} - 50 \text{ \AA}$) or macroporous (pores $>50 \text{ \AA}$), and offer several advantages over the classical immobilization procedure employed in the preparation of heterogeneous catalysts [93]. If the reagents in solution have smaller size respect to the average pore diameter, these materials afford superior catalytic performances respect to similar heterogeneous catalysts prepared by impregnation methods.

The grafting procedure on amorphous silica is one efficient method for obtaining efficient catalysts. For example, aminopropyl-functionalized silicas have been the most widely studied organic-inorganic hybrid solids. Angeletti and co-workers showed that these hybrid organic/inorganic solids could be effective base catalysts for the Knoevenagel condensation reaction at room temperature in continuous flow reactors [94]. Macquarrie and co-workers examined guanidines tethered to silica as base catalysts for epoxidation reactions [95]. Harmer et al. [96] reported the use of perfluorosulfonic acid-silane in the co-condensation of silica, using traditional sol-gel

techniques. In this case the activities of both grafted and co-condensed silica hybrids were reported as similar. The grafted acid catalyst was tested in several acid-catalyzed reactions, such as aromatic alkylation, alkenes isomerization, and Friedel-Crafts acylation and the respective conversions were 99, 95 and 89%.

Other catalyst is obtained from the family of mesoporous materials (M41S, SBA-15, MCM-41...). These materials have relatively uniform pore sizes and void volumes [97]. The pore sizes can be tailored on the basis of the synthesis method and can range from about 15 to 100 Å. Rather than amorphous solids, ordered mesoporous materials can serve as well defined supports, and can be modified by grafting organic groups, in order to obtain a catalyst. Sartori and co-workers used aminopropyl-functionalized MCM-41 as a catalyst for the nitroaldol condensation of aldehydes and nitroalkanes [98].

Further on, mesoporous silicas own pore systems, which have sizes large enough to accommodate small biological entities as proteins or enzymes. The immobilization can involve both physisorption and chemical bonding, although with the latter there is the risk of denaturation of the biological entity and the loss of the activity. Various enzymes (trypsin, lysozyme, lipase, etc...) [99-101] were immobilised in either MCM-41/48 or SBA-15 phases with good results. General reviews on this subject were made by Fröba et al. [102] and Davis et al. [103].

2.4 Drug Release

Compared with conventional dosage forms, controlled drug release systems (DRS) offer numerous advantages, such as reduced toxicity, enhanced drug efficiency and improved patient compliance.

To be effective drug carriers need therefore low toxicity, biodegradability, encapsulation and release ability and finally specific surface functionalities. Generally, biocompatible polymers were employed as carriers; however in these matrices the major problem is the drug distribution homogeneity into the polymer, which can affect the drug release rates affecting reproducibility. So far silica nanoparticles (NP) have been proven to be non-toxic and to have an easily modified surface that improves the drug delivery capability and efficiency [104]. The surface of silica NP is generally modified with specific functional groups of biomacromolecules by chemical binding or physical adsorption [105,106]. In addition to solid-core silica NP, also hollow NP have been used as carriers [107-110]. Compared to the solid-core the hollow NP have a higher load capacity, but weaker interactions between the particle and the drug, which makes the controlled release of the drug more difficult. These weak interactions are due to low efficiency of organic modification, since generally the hollow spheres are produced with sacrificial templates and post-treatment steps in order to obtain the hollow-core. This major problem was avoided by Shi et al. [107] synthesising the NP by a one-pot route from ureidopropyltriethoxysilane (UPTES), which acts as both organosilica precursor and co-template. Another interesting material with loading and releasing properties is mesoporous MCM-41, which was studied as DRS from Vallet-Regí and co-workers since 2001 [111]. Since then, many researchers focused on this new application in mesoporous materials, studying the different surface properties and pore textures, which influence the drug release rate [112]

PART 1:

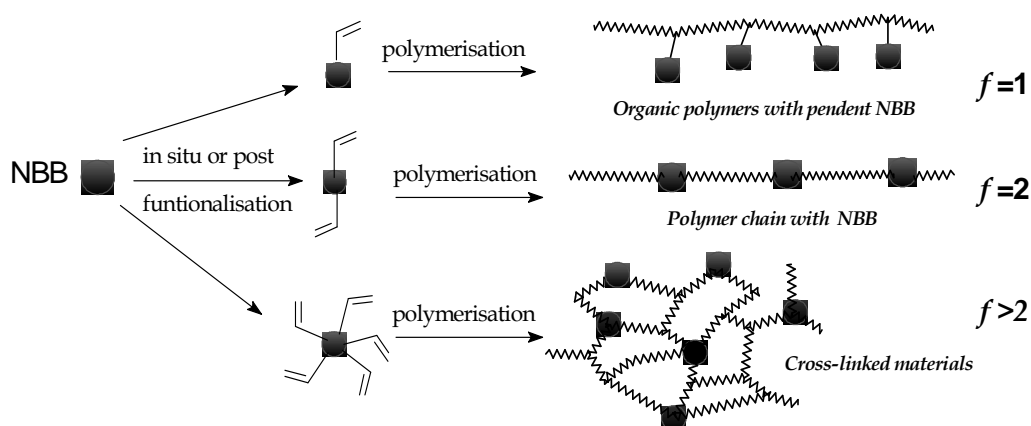
O/I Hybrids: NBBs

Introduction

The first part of the thesis work is devoted to the synthesis of Si-based NBBs. A short introduction on NBBs will be presented, concerning the general considerations on the synthesis procedures.

3 NANO BUILDING BLOCKS (NBBs)

Nano Building Blocks are pre-condensed nanometre sized species, containing reactive polymerizable ligands and non-reactive functionalities. They can assemble through their reactive organic groups to obtain O/I hybrid materials with controlled extent of phase interaction, thus allowing the possibility to tune the structure properties relationship. The nature of the interface between organic and inorganic moieties, the connectivity and the functionality (f) of the NBB are of paramount importance in determining the final structure of the final hybrid material, as the functionality or number of reactive functions or anchoring sites per monomeric unit [113]. If only one reactive function is present organic polymers with inorganic pendants are obtained, whereas if the functionality is equal to two, linear chains are obtained. In the case of f higher than two, polymerization leads to cross-linked systems as depicted in the following scheme.



The use of NBBs as starting unit (molecular “brick”) for obtaining hybrid O/I structure is an approach developed with various systems such as oligosilsesquioxanes and derivatives [114, 115, 116], organically modified polyoxometalates (POM) [113, 117], transition metal-oxo clusters (MOCs) [118], organotin-oxo clusters and functionalised nano-sized particles (metal oxides, metals and chalcogenides)[119].

Some typical structures of organically modified functionalised NBB units are presented in Fig. 16.

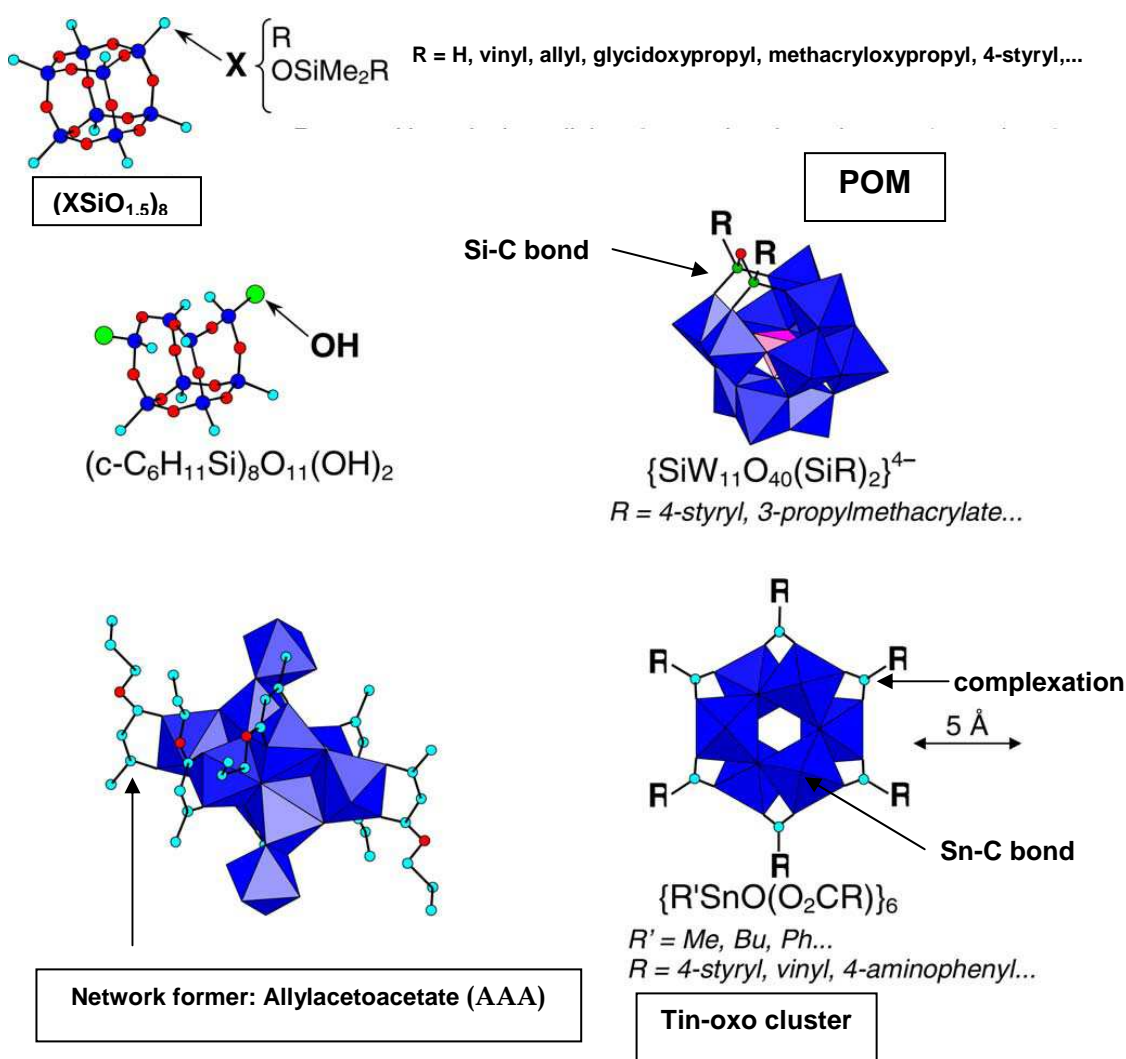


Fig. 16: examples of oxo clusters exploitable as NBBs [113]

3.1 Silicon-Based Nano Building Blocks

Silicon-based NBBs are probably the most studied building blocks for the preparation of hybrid materials and they offer a large possibility for organic functionalisation thanks to the stability of the Si-C bond.

Generally, they correspond to cage structures of general formula $(\text{RSiO}_{1.5})_n$, with n ranging from 6 to 18 [120, 121 a-b], known as polyhedral oligomeric silsesquioxanes (POSS) (Fig. 17)[121 c].

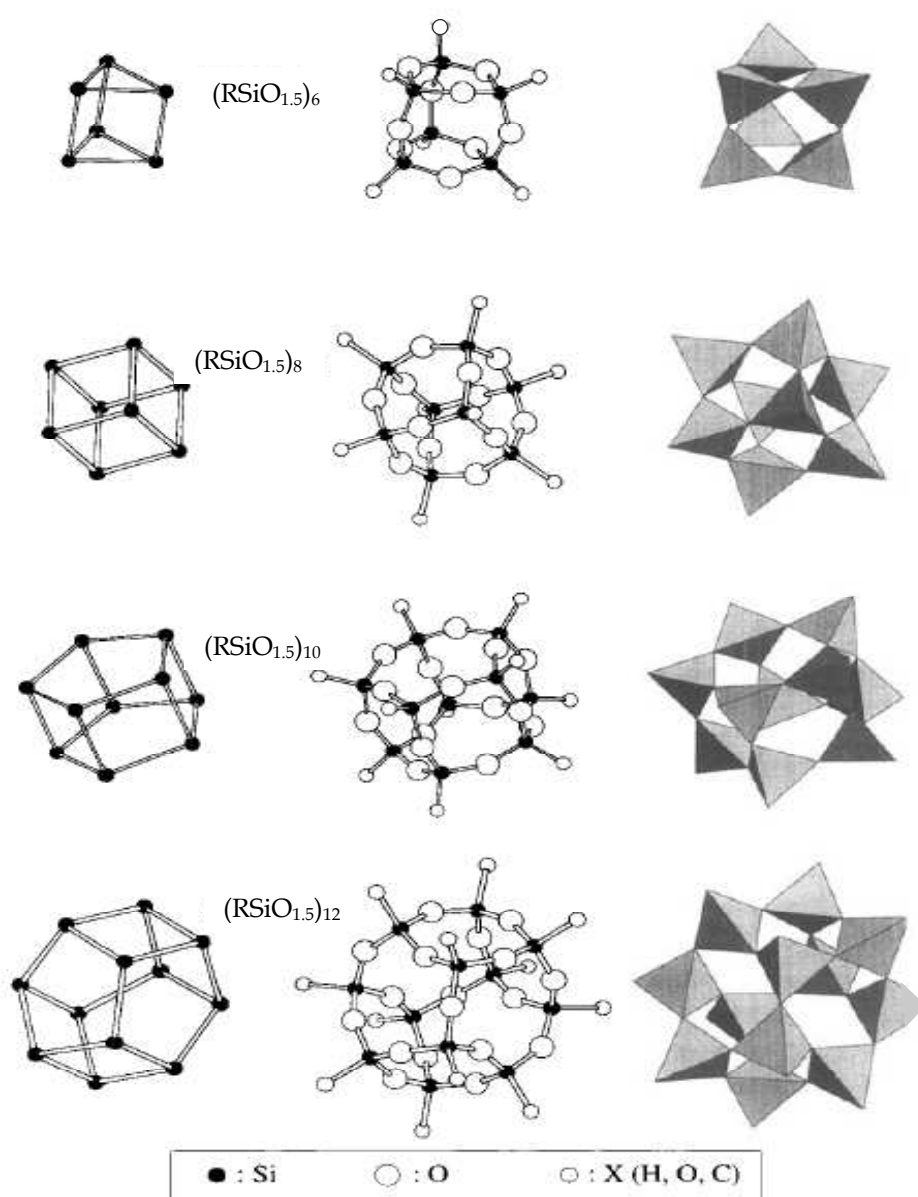


Fig. 17: molecular structure of some $(\text{RSiO}_{1.5})_n$ cages [117]

The term silsesquioxane denotes that each silicon atom is connected to three oxygen atoms $\{\text{SiO}_3\}$. The prefix *oligo* is often used to indicate a small number of silsesquioxane links and the prefixes “octa-, penta-, deca-, etc” are used to indicate a specific number of these links. POSS are also commonly abbreviated as T_n (T is the designation for a silicon bearing the three oxygens and n is the number of silicon present in the cage) and the most studied structure is the T_8 -cage ($\text{R}_8\text{Si}_8\text{O}_{12}$) (Fig. 17).

After the first reports about the preparation of non-functional silicon-oxo clusters in the 1960s, these compounds became of great interest with the synthesis of polyhedral oligohydridosilsesquioxanes (POHSS), where the functional group R is a hydrogen ($\text{HSiO}_{1.5}$)_n [122, 123]. Hydridospherosiloxanes (POHSS), aroused big interest also because of the possibility of functionalisation through hydrosilylation [124, 125] or substitution reactions with silanols or alcohols [126] that leads to a large variety of POSS.

Other slightly different nano-bricks have been used as precursor for functionalised NBBs. These compounds exhibit not fully condensed frameworks as for example $(\text{c-C}_6\text{H}_{11}\text{Si})_8\text{O}_{11}(\text{OH})_2$ and $(\text{RSi})_7\text{O}_9(\text{OH})_3$ (Fig. 18).

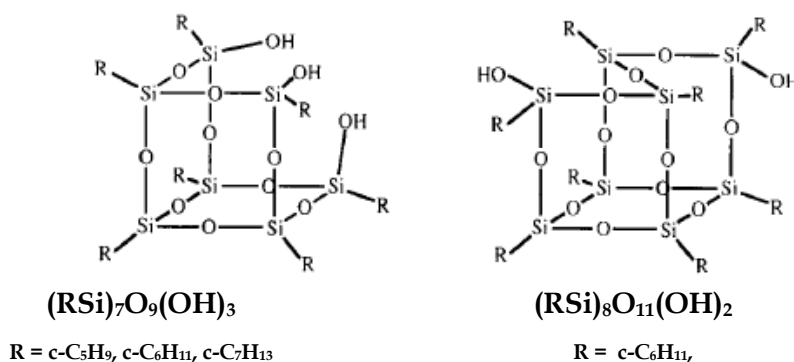


Fig. 18: schematic molecular structures of incomplete POSS

All these compounds exhibit a stable siloxane framework, which is recovered in the final material.

Furthermore, NNB that contain at least one reactive function can be used as platform for O/I hybrid materials after the assembling process by exploiting their reactive groups [127a].

Recently, POSS gained a place in the commercial market. Due to their excellent compatibility with common monomers, functionalised POSS molecules can be easily incorporated into various types of formulations for the preparation of polymeric matrix-based composites. Typical improvements in properties include higher T_g , process temperature, resistance to water and solvent, scratch/wear resistance, mechanical properties, and resistance to environmental damage such as oxidation, UV degradation and erosion.

3.2 Polyoxometalates (POMs)

POMs are small compact oxide networks based on the sharing of MO_6 structural units ($M = Mo, W, \text{ or } V$) and form a peculiar class of clusters with very interesting structure, electronic properties and final use in different fields from medicine to catalysis and magnetic materials [Errore. L'origine riferimento non è stata trovata.b-c].

The large number of synthesised POMs can be split in three classes: *i) heteropolyanions*, including hetero anions such as SO_4^{2-} , PO_4^{3-} . These represent by far the most explored subset of POM clusters. The most studied are Keggin $\{XM_{12}O_{40}\}$ and Wells-Dawson $\{X_2M_{18}O_{62}\}$ anions (where $M = W \text{ or } Mo$ and $X = \text{tetrahedral template}$), which are the archetypal systems. In particular W-based POMs are robust and this has been exploited to develop Keggin's derived ions with vacancies that can be systematically linked to larger aggregates using electrophiles [128]. *ii) isopolyanions*, composed of a metal oxide framework, but without the internal heteroatom/heteroanion. These clusters are very unstable with respect to the ones with the "heteropolyanion core".

They can be easily functionalised with organic functions through M–O–Si–C bonds by grafting on lacunar polyoxometalates [129]. Typical examples are reported in

Fig. 20. Both compounds can be isolated and crystallized; iii) *Mo-blue* and *Mo-brown*, related to the molybdenum blue type species reported by Scheele in 1783. Their composition was unknown until Müller et al. in 1995 reported their synthesis and structural characterisation. A long work on the crystallization conditions allowed to obtain the molecule {Mo132}, which has the shape of a giant wheel and is responsible of the intense blue colour obtained by the reduction of acidified solutions of molybdate (Mo^{VI}) [130]. This molecule is composed of 132 molybdenum atoms with an inner cluster shell of 60 Mo^{V} atoms with icosahedral symmetry arranged like the C_{60} bucky ball [131] and has 20 nanoscale pores and 20 channels providing access to the inside of the capsule.

The resulting spherical systems can be described by the following general formulation: $(\text{Pentagon})_{12} (\text{Mo})\text{Mo}_5\text{Mo}'_5\text{)}_n$ ($n= 12$: spherical systems; $n= 14, 16$: wheel type systems; pentagon refers to $\{(\text{Mo})\text{Mo}_5\}$ units, i.e. one pentagonal MoO_7 unit sharing edges with five MoO_6 octahedra).

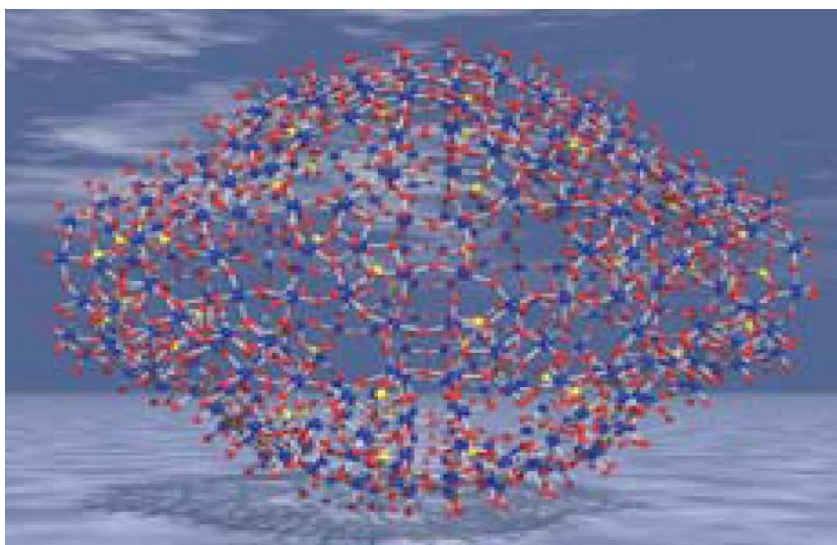


Fig. 19: the structure of the {Mo368} "lemon" shaped cluster.

Judenstein et al. [Errone. L'origine riferimento non è stata trovata.] reported the synthesis of POM of type $[\text{SiW}_{11}\text{O}_{40}(\text{SiR})_2]^{4-}$ with different R groups (i.e. H, vinyl, allyl, methacryloxypropyl, styryl).

Co-polymerization of polyoxotungstates with formula $[\gamma\text{-SiW}_{10}\text{O}_{36}(\text{SiR})_4]^{4-}$ (R= methacryloxypropyl) with water soluble polymers (polyacrylamide) leads to hybrid gels, in which the modified POM acts as cross-linker. In this case, it is possible to have application in photo- and electrochromism fields, electrochemistry, catalysis and as super-absorbent materials.

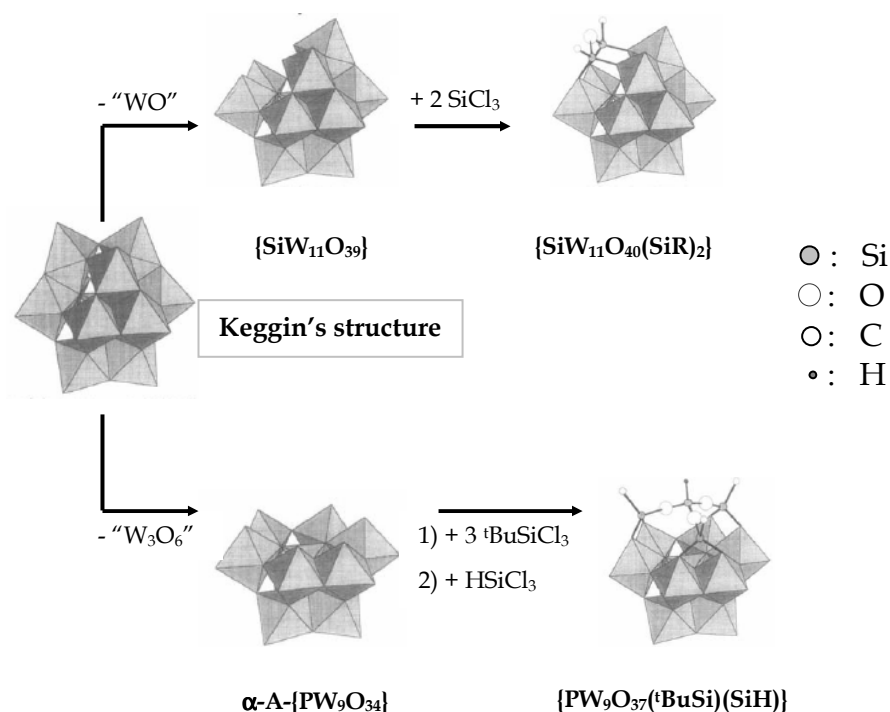


Fig. 20: molecular structures of POM using polyhedra

3.3 Metal-oxo clusters (MOCs)

Many researchers have prepared and described the structures of different transition metal (Ce^{IV} ; Nb^{IV} , Ti^{IV} , Zr^{IV}) oxo clusters bearing strong ligands (β -diketone, β -ketoester, carboxylic acid, etc...). Such species are mainly

prepared through the controlled hydrolysis of the corresponding metal alkoxides $M(OR)_n$ or their corresponding complexed alkoxides $M(OR)_n \cdot x(LZ)_x$ (where LZ is the complexing ligand) [113, 117].

A large number of oxo-alkoxo clusters, $M_xO_y(OR)_z$, have also been prepared, exploiting the use of ligand containing an assembling/polymerizable function (i.e. acetoacetate (AAA), methacrylate (OMc) or acrylate (OAc)). Because of the presence of several alkoxy groups on the surface, the NBBs exhibit a poor stability in presence of water or nucleophiles (except for titanium ones). Therefore their polymerization must be performed in nonprotic solvents such as THF, benzene or toluene.

The structure of titanium and zirconium oxo clusters are the most reported in literature and can be used as model systems to understand the construction of hybrid materials, particularly at the organic-inorganic interface.

The stability of Ti-oxo clusters towards water depends on their oxo/M and alkoxo/M ratios, and larger cluster such as $Ti_{16}O_{16}(OEt)_{32}$ or $Ti_{12}O_{16}(OPr)_{16}$, are generally more stable respect to small species such as $Ti_7O_4(OEt)_{20}$, where alkoxo/M ratio is higher. The differences between these clusters are mainly assigned to three parameters: *i*) presence of titanium atoms with unsatisfied coordination that decreases the stability of the compound towards nucleophilic substitution, *ii*) stability of the oxo-core depending on the number of "bulk" oxo-bridges present (i.e. those with high coordination to Ti(IV)), *iii*) the clusters bearing highly coordinated O bridges are more stable towards hydrolysis. Furthermore, the presence of strong chelating ligands might hinder nucleophilic attacks.

Metal-oxo-alkoxo clusters can be used as O/I nanofillers in hybrid materials of class I or can be post-functionalised in order to obtain a reactive NBB, which strongly interacts with the matrix (class II hybrid material).

3.4 Tin-based NBB

Tin as silicon is characterised by the high stability of M-C (sp^3) bond, particularly towards nucleophilic attacks. This characteristic offers a strong covalent link between tin-oxo polymers and functionalised organic moieties and, on the other hand, reduces the inorganic functionality of tin favouring the formation of oxo clusters that can be used as NBBs [113, 117].

Tin oxo-carboxylate clusters such as $\{R\text{SnO}(\text{O}_2\text{CR}')\}_6$ ($R = \text{alkyl}$ and $R' = \text{organic function}$) are known as “Tin-6” and are a family of NBBs in which the carboxylate groups can be used as assembling functions. In Tin-6 structure, the metal atoms are six-coordinate and exhibit a hexagonal prismatic or “drum” shape with the bridging carboxylate groups on the six faces of the drum (Fig. 21).

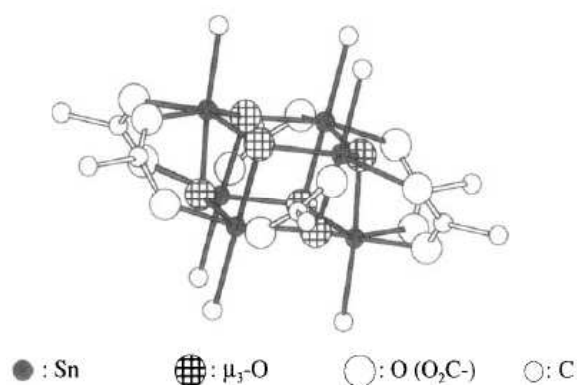


Fig. 21: molecular structure of $\{R\text{SnO}(\text{O}_2\text{CR}')\}_6$ [117]

Another interesting family of tin-based NBBs derives from $\{R\text{SnO}(\text{O}_2\text{CR}')\}_6$ oxo cluster or “Tin-12” (Fig. 22). This cluster can be prepared following different synthetic pathways [132], in which the charge of Sn is balanced by different anions (i.e. OH^- , Cl^- , $\text{R}'\text{CO}_2^-$, $\text{R}'\text{SO}_3^-$) located at both cage poles. Functionalised Tin-12 is able to assemble especially when R is a butenyl or a 3-butenyl, thus it can be used as NBB for the synthesis of tin-based hybrid materials [133]

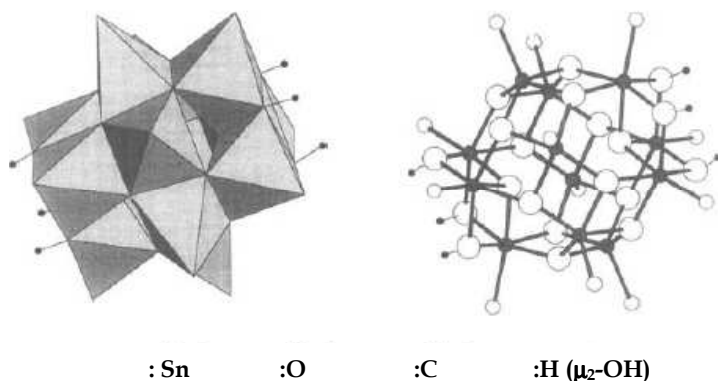


Fig. 22: molecular structure of "tin-12" (only C atoms directly bound to tin have been drawn) [117]

Classically covalent and ionocovalent bonds are used to functionalise or assemble tin-based nanobuilding blocks.

3.5 Nanoparticles (NP)

The transition between clusters and particles is still subject of debate and has generated much research. The stability problems, observed for small clusters, can be avoided with the use of larger species such as nanocolloids or nanoparticles, which size is largely under $1\mu\text{m}$ (nanometre scale).

In the last decades, many novel and versatile methodologies have been developed in order to allow multiscale processing of NP. Several physical methods such as MBE (molecular beam epitaxy), OMVPE (organometallic vapour phase epitaxy), mechano-synthesis, fast quenching of inorganic vapours, nanolithography and laser or electrical ablation are currently employed to produce nanomaterials. On the other hand wet chemical routes (employed in the thesis) offer low cost, high versatile and efficient methodologies to nanoparticles and nanostructured materials. Moreover soft chemistry allows kinetics tuning through nucleation and growth [134], as well the control on particles size and morphology.

Growth kinetics are controlled by various parameters as: competitive mechanism of growth/inhibition of the solid phase in presence of complexing surface capping agents [135], confinement of the reaction volume through the use of micelles, microemulsions or vesicles, pH and ionic strength range for which the interfacial tension is low.

Gold nanoparticles, semiconductor nanocrystals, nanospheres are some of the systems studied in this field. This kind of NBB can be adequately functionalised with organic groups, thus allows designing plenty of new hybrid materials and devices. It is possible to create hybrid materials introducing the already functionalised NP into polymer or organic hosts, synthesising the nanoparticles directly inside the matrix, polymerising functionalised metal-oxo NP or connecting particles with adequate organic spacers.

Nanoparticles will be presented and studied in depth in Part 2 of this thesis.

4 SYNTHESIS OF Si-BASED NANO BUILDING BLOCKS (Si-NNB)

In this chapter, the synthesis of Si-based NBB belonging to class II hybrids will be presented. A brief introduction with the general consideration about synthesis requirements for specific application will be followed by the discussion on the results obtained on synthesised NBBs.

The NBB are prepared by co-condensation of a difunctional and a trifunctional Si-alkoxide or by the self-condensation of a trifunctional Si-alkoxide, varying condensation promoter, solvent, and reaction temperature. Two different approaches were used: non-hydrolytic condensation and *in situ* water production for hydrolysis-condensation.

4.1 General considerations

Siloxane based hybrid O/I materials present several advantages, especially in the photonic field [136] since many precursors are commercially available or can be easily synthesised and modified, the control of precursor reactivity can be achieved through catalysis (acidic, basic or nucleophilic) and finally transparent monoliths or films without cracks or defects can be easily processed.

Photonic devices, especially storage and telecommunication applications, need particular requirements to be satisfied since the transmission losses in the NIR range at the most important wavelengths (830, 1310 and 1550 nm) should be as low as possible [137]. Thus, for successful applications in photonic devices, the hybrid materials have to be developed reducing the presence of strong absorbing chemical groups like -OH (also derive from water) and -CH (alkyl) groups [138].

Typical low optical losses reported in literature [139] for silicon-based hybrid materials are 0.3 dB/cm at 1320 nm and 0.6 dB/cm at 1550 nm.

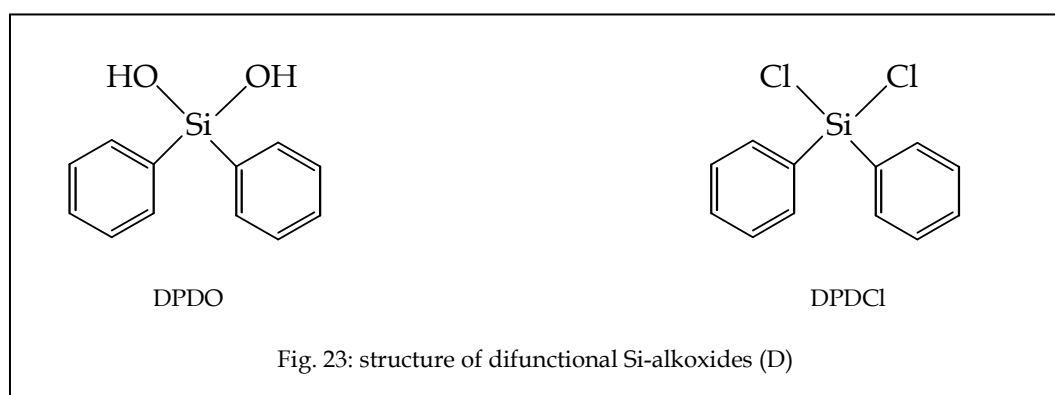
Another required parameter is a tuneable refractive index, which can be obtained changing the organic group R directly bonded to the silicon atom. A higher refractive index is achievable by introducing for example phenyl groups [138].

In order to avoid or minimize residual OH functions and improve condensation, the NBB were first synthesised through the non-hydrolytic route. Anhydrous solvents and standard Schlenck techniques were employed. The *in situ* water production route was exploited in order to increase the hydrolysis and condensation rate in particular reactions, in which a high amount of reactive functions was required and the non-hydrolytic pathway demonstrated to be unsuccessful.

4.2 Precursors

4.2.1 Difunctional precursors (D)

Diphenylsilanediol (DPDO) and diphenyldichlorosilane (DPDCI) are commercially available reagents with two phenyl rings, suitable for increasing the refractive index of the final hybrid material (Fig. 23). The hydroxyl and chlorine groups respectively can react with the methoxide groups of the trifunctional Si-alkoxides.



4.2.2 Trifunctional precursors (T)

Methacryloxypropyltrimethoxysilane (MPTMS) and glycidoxypropyltrimethoxysilane (Glymo) are commercially available trifunctional Si-alkoxides bearing organic reactive functions (Fig. 24), which allow the further assembly of the obtained NBBs. The condensation between MPTMS or Glymo and a difunctional precursor leads to products with the presence of reactive methacryl or epoxy functional groups respectively. Syntheses were performed either with low and high amount of trifunctional precursors, labelled as "D/T_L" and "D/T_H" samples respectively. Self-condensation of Glymo, for the preparation of NBBs bearing reactive epoxy functions, was also performed and the obtained product was labelled "G".

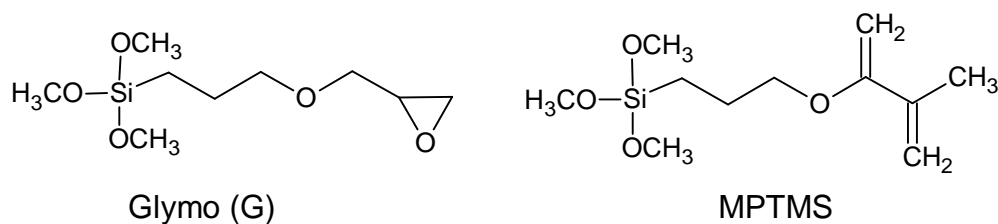


Fig. 24: structure of trifunctional Si-alkoxides

4.3 Reaction conditions

Hybrids properties are affected by nature and extent of interface interactions, and the control of molecular and supramolecular structures is fundamental to tailor the materials properties. One possibility to achieve these objectives is offered by the preparation of hybrid nanocomposites from pre-synthesized Si-based NBB, exploiting the molecular precursors' condensation by the non-hydrolytic sol-gel process.

The use of silicon alkoxides as NBB precursors leads, as explained in the introduction, to slow rates for the condensation reaction. In order to improve the reaction rate, a catalyst, or better a condensation promoter is required.

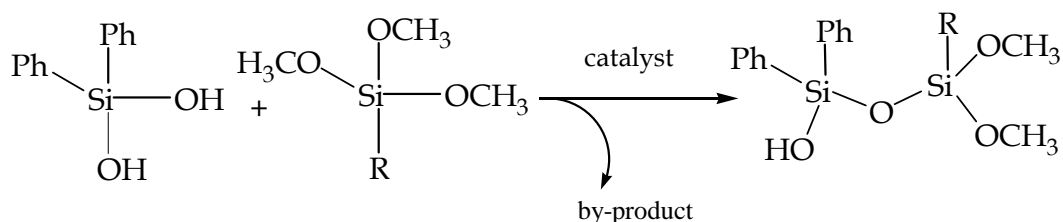
At the Department of Materials Engineering and Industrial Technologies of the University of Trento, previous experiments on the condensation behaviour of DPDO with trifunctional alkoxy silanes (triethoxysilane, TREOS or vinyltriethoxysilane, VTES) were conducted, using a base catalyst (pyridine, TEA, BuLi) in order to reduce the self-condensation of DPDO [140]. The best results for DPDO/TREOS and DPDO/VTES hydrolysis-condensation process were found with pyridine as condensation promoter. DPDO linear self-condensation was minimized by the presence of bulky phenyl group and the production of cyclic species was favoured by a high dilution of the reactive mixture [141].

The interest for MPTMS based-NBB (HYBRIMER® or ORMOCERS®) obtained via non-hydrolytic condensation for electronic and optical applications aroused since the early years 2000.

With the goal of obtaining stable and reliable methacrylate-based hybrid materials, the condensation reaction has been optimized exploiting the previous results obtained by the research group in Trento. They demonstrated that, in base catalysed condensation, the first step is the deprotonation of the two Si-OH groups of DPDO and the formation of silanolates, Si-O⁻. Thus, in this work, base with different pKa value (NEt₃ pKa 11.01; pyridine pKa 5.21) were used as condensation promoters, and their ability to run deprotonation and siloxane condensation was studied.

Different acids (Ti(OPr^t)₄, TiCl₄, dibutyl dilauryl Tin (DBDLT), trifluoroacetic acid (TFA), acetic acid (AcA) were also used in order to compare the catalytic activity as condensation promoters.

The co-condensation reaction between difunctional (Ph₂-Si-X₂) and trifunctional (R-Si-(OCH₃)₃) alkoxy-silanes is depicted schematically in Scheme 17. The X groups of the difunctional precursor (OH, Cl₁) are condensed with Si-OMe groups with the presence of a suitable catalyst, and Si-O-Si bonds are formed with the elimination of a by-product. Different molar ratios between D: T have been used. DPDCI was used in order to exploit the higher reactivity of the Si-Cl groups compared to Si-OH groups of DPDO.



Scheme 17: co-condensation between difunctional and trifunctional Si-alkoxides

The reaction progress can be easily followed by FT-IR spectroscopy, monitoring the disappearance of Si-OMe groups and the formation of Si-O-Si groups in the condensation product. The reactive (methacrylate, epoxy) and non reactive (phenyl) organic functions are also detected by FT-IR.

The reactions were run in dry tetrahydrofuran (THF). Unfortunately the Si-O-Si stretching vibrations in the FT-IR spectra: ν_{as} (Si-O-Si) \sim 1200-1000 cm^{-1} and ν_{s} (Si-O-Si) 900-800 cm^{-1} , overlap with signals due to THF (ν_{as} C-O) at 1065 cm^{-1} and ν_{s} (C-O) at 908 cm^{-1} . Thus, other solvents were also exploited in the syntheses (Appendix C). For low trifunctional content samples D/T_L, D : T ratios were 1:1, 1:1.5 and 1.5:1. For high trifunctional content (D/T_H) the D:T ratio was fixed to 1:5, in order to guarantee a higher availability of reactive functions for polymerization.

In order to ensure a good condensation process, the *in situ* water production (ISWP) route was also studied. Since ISWP exploits an esterification reaction between an alcohol and a carboxylic acid, a deep study on the influence of the nature of these two reactants was conducted. Finally, self-condensation reactions were performed using Glymo (G) as precursor and ISWP as synthetic route for the preparation of epoxy-based NBBs (G_s).

All the syntheses performed for the preparation of [D/T_L], [D/T_H] and [G_s] are reported in detail in Appendix C. In the following paragraphs only the most representative syntheses will be discussed, on the basis of the characterization results.

5 EXPERIMENTAL

5.1 Low functionality derived hybrids (D/T_L)

All reagents were used without further purification unless otherwise stated. Drying and distillation procedures for the used solvents are described in detail in [142]. The list of employed reagents and solvents is reported below.

Reagents

- Diphenylsilanediol (DPDO) 95%,
- Methacryloxypropyltrimethoxysilane (MPTMS) 98%,
- Glycidoxypropyltrimethoxysilane (Glymo) 98%,
- Tetrahydrofuran (THF) 99.8%,
- Ethanol (EtOH) >99.8%,
- Triethylamine (NEt₃ - TEA) 99%,
- Titanium isopropoxide (TIPO) 97%,
- Dibutyl dilauryl Tin (DBDLT) 95%

CHARACTERIZATION TECHNIQUES

➤ *Fourier transformed infrared spectroscopy (FT-IR)*

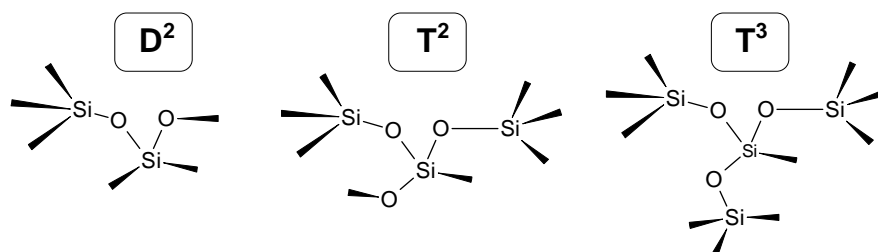
FT-IR was used to control the reaction evolution. FT-IR spectra of the solutions were recorded with a Thermo Optics Avatar 550 instrument in transmission mode, using KRS5 platelets, in the 4000–400 cm⁻¹ range (64 scans, 4 cm⁻¹ resolution).

Attenuated total reflection infrared (ATR/FT-IR) spectra were collected in the 4,000–550 cm⁻¹ range on a Nicolet 870 E.S.P. with a Golden GateMK2 Diamond Specac cell (50 scans, 2 cm⁻¹ resolution).

➤ *Multinuclear magnetic resonance spectroscopy (NMR)*

^{29}Si NMR is a useful technique to provide information about the local environment of silicon atoms. All the interactions between nuclei are spatially dependent and the different local structural units can be distinguished looking at the chemical shift.

Si units are labelled according to classical D_m^n and T_m^n notation, with D and T representing two and three functional silicon respectively (related to the number of oxygen atoms linked to silicon) n is the number of oxo bridges and m the number of silicon atoms in the cyclic species.



^{29}Si and ^{13}C NMR spectra were recorded with a Bruker Advance 400 spectrometer operating at 79.49 and 100 MHz respectively, using D_2O as external lock and Ernst angle to minimize acquisition time. Chemical shifts (ppm) are referenced to tetramethylsilane (TMS).

➤ *FT-Raman*

FT-Raman spectra were recorded on a JASCO, RFT-600 in the 4,000–150 cm^{-1} range.

➤ *GPC (gel permeation chromatography)*

GPC was performed on a Viscotek instrument with UV/RI detectors and ULTRASTYRAGEL HR2+HR1+HR0.5 columns (4.6x300mm) from Waters were used. The mobile phase used was THF. As standards, polystyrene beads of different Mw were used (Mw: 575; 1,090; 2,170; 3,070; 10210; 19,640; 19,510; 49,170).

➤ *Differential scanning calorimetry (DSC)*

DSC curves were recorded on a DSC 2010 TA instrument, with a heating rate of 10°C/min in the range 30–200°C in N₂ flow (100 cc/min).

5.1.1 Syntheses of D/T_L samples

The list of samples is reported in Table 1. The reaction parameters used (condensation promoter, precursors ratio and reaction temperature) are the consequence of the results obtained on several syntheses, by changing the reaction conditions (Table Appendix C).

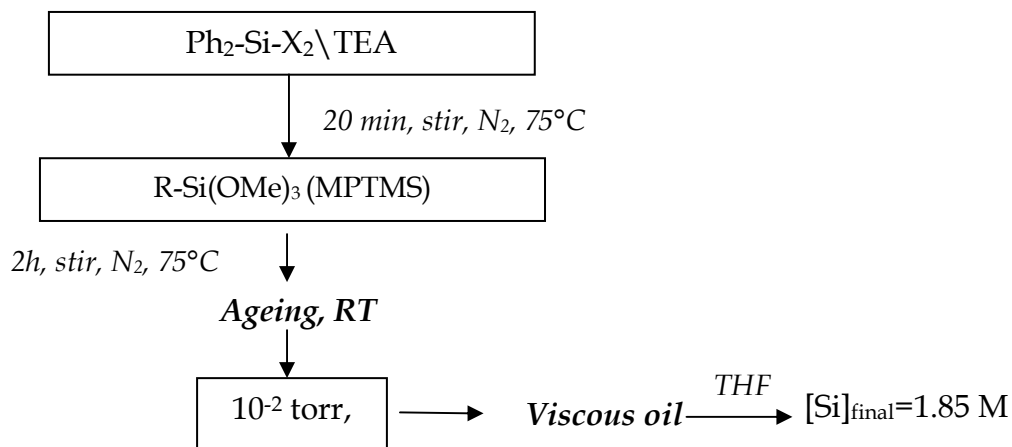
Sample	Ph ₂ -Si-X ₂ (D)	R-Si(OCH ₃) ₃ (T)	D:T	Solvent (S)	S:D	Cat.	Temp
D/T _L -1	DPDO	MPTMS	1.5:1	THF	20:1	TEA (2)	RT
D/T _L -2	DPDO	MPTMS	1:1.5	THF	20:1	TIPO(1%[Si])	75°C
D/T _L -3	DPDO	Glymo	1:1	THF	5:1	DBDLT (1%[Si])	RT

Table 1: D/T_L NBBs

5.1.2 Syntheses procedure for base-catalysed D/T_L

NBB

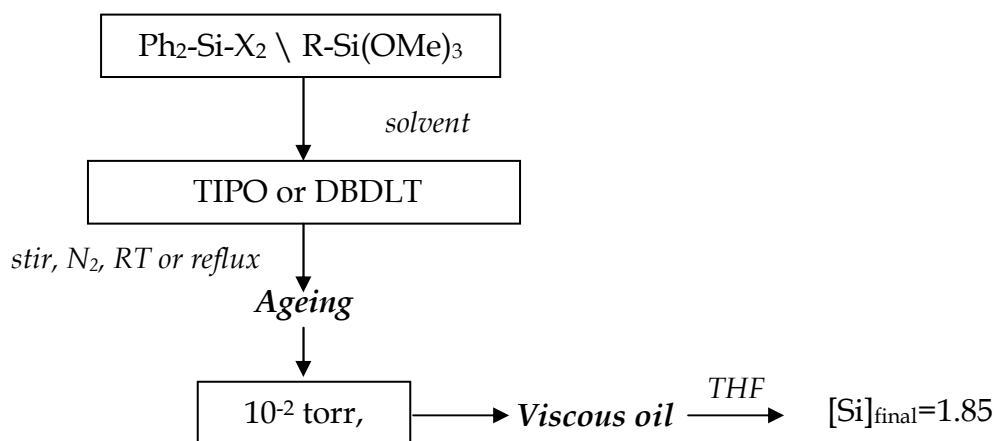
The synthesis of D/T_L NBBs with TEA is schematically presented in Fig 25 and described in Appendix A (Synthesis 1). Dry THF and toluene were distilled under N₂ and over Na-benzophenone. Reactions were carried under nitrogen atmosphere using standard Schlenk techniques.

Fig. 25: general reaction scheme for base catalysed D/ T_L -NBB

5.1.3 Syntheses procedure for acid catalysed D/ T_L NBB

The synthesis of D/ T_L NBBs with acid catalyst is schematically presented in

Fig. 26 and described in Appendix A (Syntheses 2 and 3). Solvents were dried and distilled, and reactions were carried under nitrogen atmosphere using standard Schlenk techniques.

Fig. 26: general reaction scheme for acid catalysed D/ T_L -NBB

5.2 D/T - Characterisation

FT-IR Characterisation of the precursors

The syntheses are based on the non-hydrolytic sol-gel route exposed in Chapter 1.2 (Introduction).

The exploited process is the co-condensation reaction between DPDO ($\text{Ph}_2\text{-SiOH}_2$) and trifunctional alkoxy silanes ($\text{R-Si-(OCH}_3)_3$) bearing either a methacryloxypropyl or a glycidoxipropyl group (Fig. 24), in order to obtain siloxane bonds.

The condensation between DPDO and MPTMS or Glymo in THF with TEA, TIPO or DBDLT is monitored by FT-IR as function of reaction time. The reaction evolution can be mainly followed observing the disappearance of the signals due to the DPDO silanols ($\nu\text{Si-OH}$, Table 2) and of the of MPTMS and Glymo $-\text{OCH}_3$ groups (Tables 3 and 4), and the simultaneous appearance of the broad band between $1200\text{-}1000\text{ cm}^{-1}$ due to the formation of the Si-O-Si bond (Scheme 17). We also should pay attention to the persistency of the signal of the organic reactive group ($\nu\text{C=O}$ and $\nu\text{C=C}$ of the methacrylate group in MPTMS, Table 3, and epoxy ring vibrations of Glymo, Table 4) and to the typical vibrations (νCH , $\delta\text{C=C}$, $\delta\text{C-H}$, δ_{oop}) due to the phenyl groups for DPDO (Table 2). For the sake of clarity, the spectra of silicon precursors and solvent are presented below (Figures 3-6), and the assignments of the main peaks are reported in Tables 2-5.

DPDO

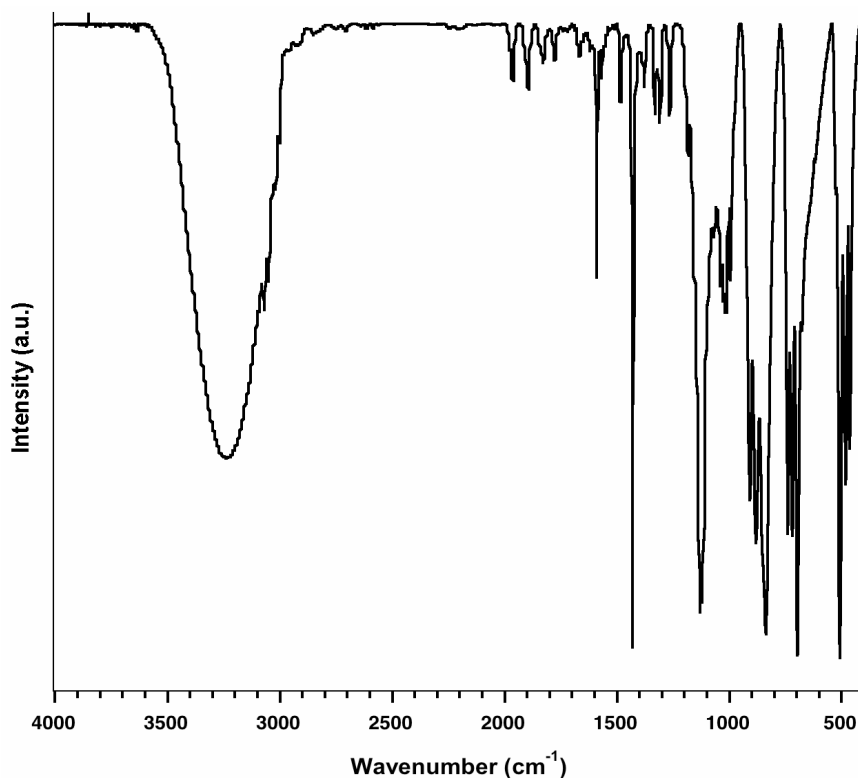


Fig. 27: FT-IR spectrum for DPDO (Transmittance)

Assignment	Wavenumber (cm ⁻¹)	ACRONYMS AND SYMBOLS
vOH	3284 (br)	st: strong
vCH [Ph]	3065 (w), 3050 (w)	m: medium
overtones [Ph]	2000-1650 (w)	w: weak
v -C=C- [Ph]	1592 (m), 1431 (st)	br: broad
vSi-C _(Ph)	1129 (st)	v: stretching vibration
δSi-OH	1040 (w), 1020	δ: deformation vibration
vSi-OH	879 (st), 841 (st)	ρ: rocking vibration
δ _{oop} C-H [Ph]	739 (st), 717 (st)	ω: wagging vibration
δ C-CH [Ph]	695 (st)	ip: in plane
v _s Si-O	481 (m)	oop: out of plane
		as: antisymmetrical
		s: symmetric

Table 2: DPDO typical FT-IR vibrations

MPTMS

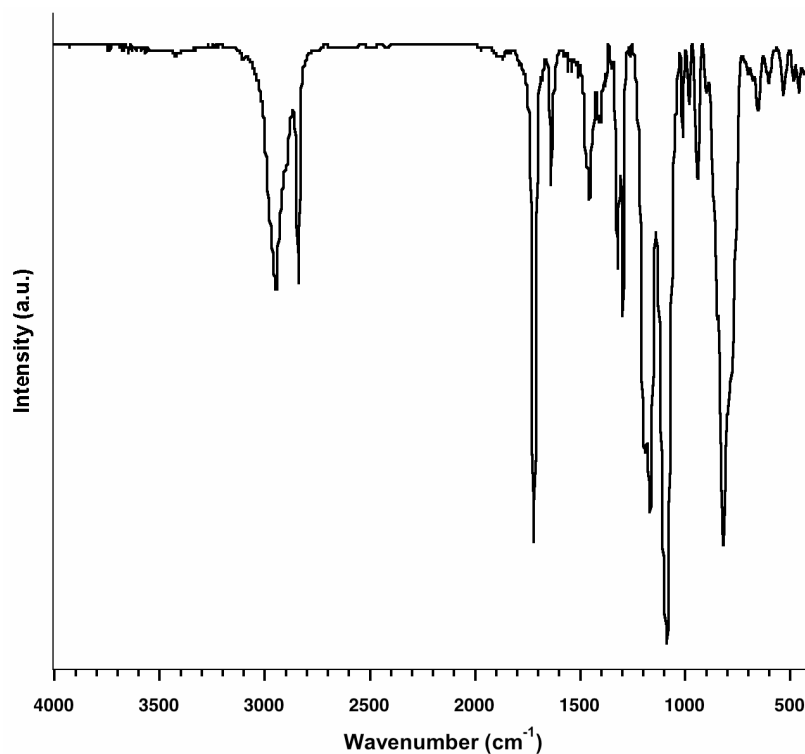


Fig. 28: FT-IR spectrum for MPTMS (Transmittance)

Assignment	Wavenumber (cm ⁻¹)
ν_{as} CH [CH ₃]	2943 (st)
ν_{s} CH [CH ₃]	2841 (w)
ν -OCH ₃	2838 (st)
ν C=O	1719 (st)
ν C=C	1636 (m)
δ_{ip} CH ₂	1457 (m), 1420 (w)
ν C-O-C [α,β insat ester]	1323 (m), 1302 (m)
Si-OMe	1190 (m), 1086 (st)
ν C=O [α,β insat ester]	1169 (st)
w CH ₂	944 (m)
δ_{oop} CH (-C=C-)	820 (st)

Table 3: MPTMS typical FT-IR vibrations

GLYMO

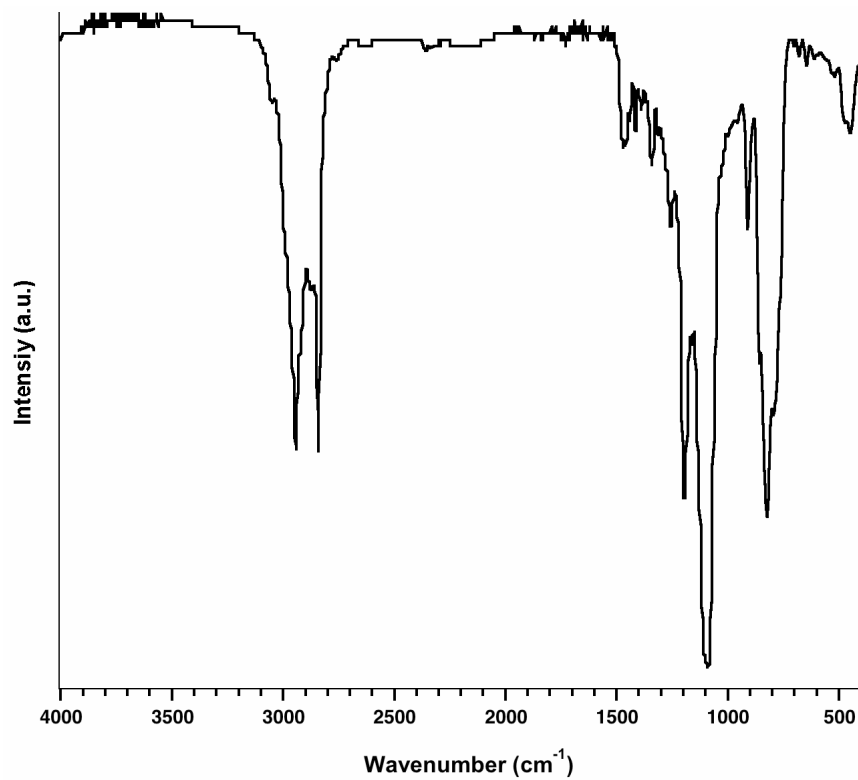


Fig. 29: FT-IR spectrum for Glymo (Transmittance)

Assignment	Wavenumber (cm ⁻¹)
ν CH (epoxy ring)	3047 (w)
ν_{as} CH [CH ₃]	2943 (st)
ν_s CH [CH ₃]	2841 (w)
ν -OCH ₃	2838 (st)
δ_{ip} CH ₂	1467 (w)
ν_s epoxy ring	1256 (w)
ν_{as} epoxy ring	912 (m)
δ epoxy ring	855 (w)
Si-OMe	1193 (m), 1085 (st)

Table 4: Glymo typical FT-IR vibrations

THF

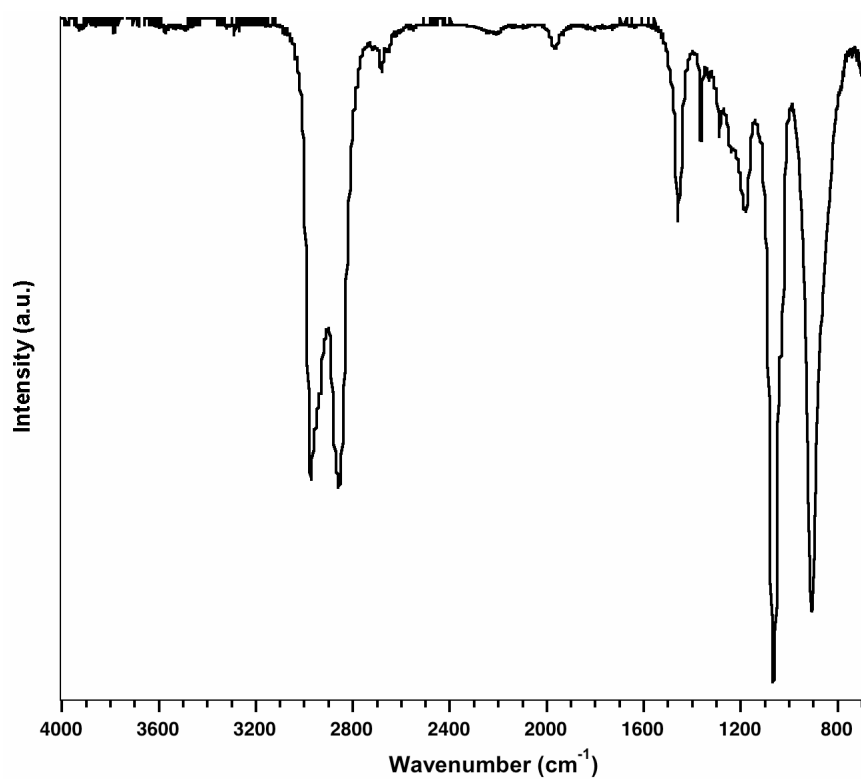


Fig. 30: FT-IR spectrum for THF (Transmittance)

Assignment	Wavenumber (cm ⁻¹)
$\nu_{\text{as}} \text{CH} [\text{CH}_2]$	2972 (st)
$\nu_{\text{s}} \text{CH} [\text{CH}_2]$	2858 (st)
δCH_2	1462 (m)
$\omega\text{CH}_2 [\alpha\text{-CH}_2]$	1367 (w)
$\nu_{\text{as}} \text{C-O-C}$	1181 (m)
ring stretching	1068 (st)
ring breathing	906 (st)

Table 5: THF typical IR vibrations

The FT-IR spectra recorded during the condensation reactions are characterized by strong overlapping with the THF signal due to epoxy ring breathing (1068 cm^{-1}). However, peaks at higher wavenumber, siloxane network) do not overlap with the solvent, as $\nu\text{Si-OH}$ of DPDO and νOCH_3 for the trifunctional silicon-alkoxide; and can be used to follow the reaction.

5.2.1 FT-IR characterisation of the samples

➤ BASE CATALISED NBB (D/ T_L -1)

As reported above, a useful band to characterize the chemical modification of DPDO is $\nu\text{Si-OH}$, which is found at 841 cm^{-1} for DPDO in THF solution (spectrum in Appendix A).

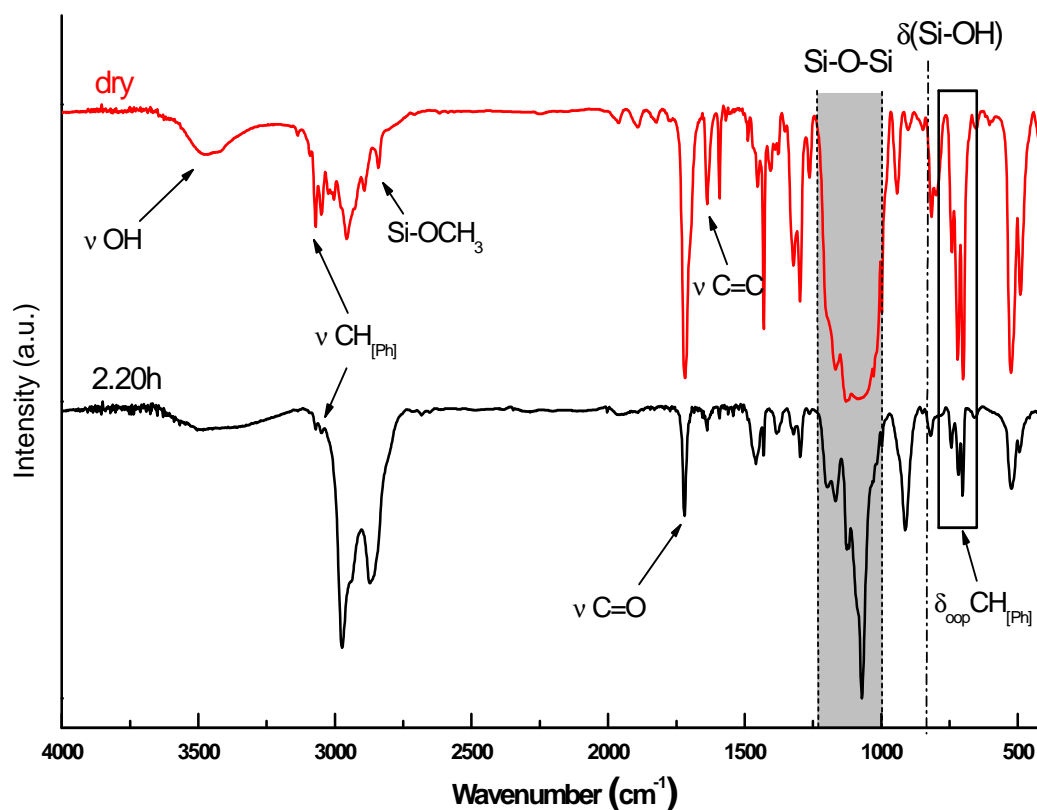


Fig. 31: FT-IR spectra for condensation reaction in sample- D/ T_L -1

This band moves to 849 cm^{-1} (TEA, D/T_L-1) in the condensation mixture, and progressively decreases in intensity during the reaction. The successful condensation is marked by the consumption of Si-OH and the according complete disappearance of $n\text{Si-OH}$ of DPDO.

Also the decreasing of the signal attributed to the Si-OMe groups of MPTMS (Table 3) and the new Si-O-Si bands signals can be used as parameter to control the hydrolysis and condensation reaction progress.

After 7 days the region including the characteristic vibrations for Si-O-Si bonds has completely changed in aspect. Two main peaks are visible at 1127 and 1085 cm^{-1} coupled with two small peaks recognisable at 1028 and 1017 cm^{-1} . These peaks are indicative for the presence of cyclic products. The band at 1127 cm^{-1} can be assigned to large strain-less cage T_n ($n > 8$) structures [143, 144], whereas the 1085 and 1017 cm^{-1} bands can be attributed to cyclic tetramers (or pentamers) and trimers respectively [146]. On the other hand the peak at 1028 cm^{-1} is due to the Si-O stretching mode of linear oligosiloxane chains. All typical vibrations of the aromatic phenyl ring system (Table 3) and of the methacryl function (Table 3) are preserved.

➤ ACID CATALISED NBB (D/T_L-2)

The ν Si-OH signal, that is found at 841 cm^{-1} in THF solution (spectrum 1 in Appendix A), moves to 844 cm^{-1} (TIPO, D/T_L-2) in the condensation mixture, and progressively disappears during the reaction, as the bands due to the CH_3O stretching and the deformation vibrations of Si-OCH₃ bonds (Fig. 32). Spectra between 24 h and 7 days are not shown since no significant changes are observable, except a decrease in the broad band at 3459 cm^{-1} (ν OH).

After 14 days the region including the characteristic vibrations for Si-O-Si bonds shows an evolution. A very strong and sharp peak at 1128 cm^{-1} is visible coupled with a band at 1092 cm^{-1} and two shoulders at 1036 and 1018 cm^{-1} . The presence of cyclic species as cyclotrisiloxane and cyclotetrasiloxane rings are accompanied by vibrations at 1018 and 1092 cm^{-1} respectively, whilst the band at 1036 cm^{-1} is mainly ascribed to linear or branched species. Cage like structures (T_n type) are also present (1128 cm^{-1}). Also in this sample the typical vibrations of the aromatic phenyl ring system (Table 2) and of the organic reactive function (Table 3) are preserved.

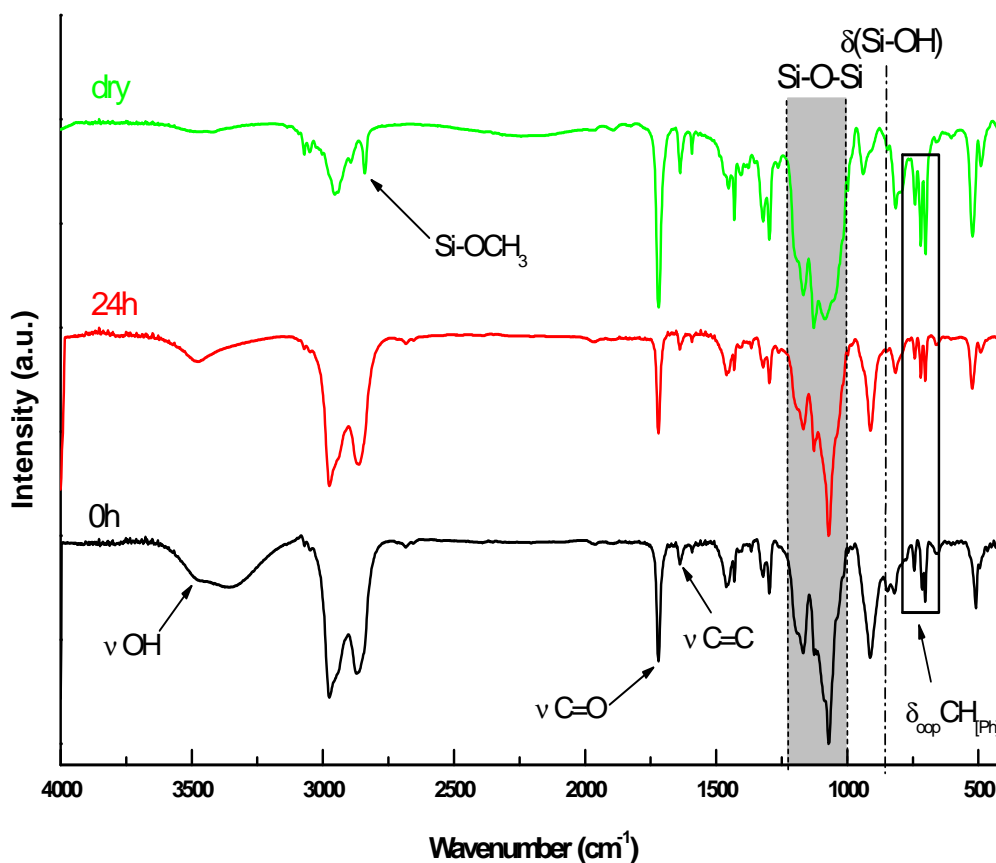


Fig. 32: FT-IR spectra for condensation reaction for sample- D/ T_L -2

➤ ACID CATALISED NBB (D/T_L-3)

The evolution of the ν Si-OH signal is difficult to follow, since there is a strong overlapping with the band signal due to the epoxy ring deformation at 910 cm^{-1} (Fig. 33). Thus, the condensation can just be studied by following the consumption of the methoxy groups of Glymo with the decrease in intensity of the signal attributed to the stretching vibrations (ν OCH₃) at 2838 cm^{-1} .

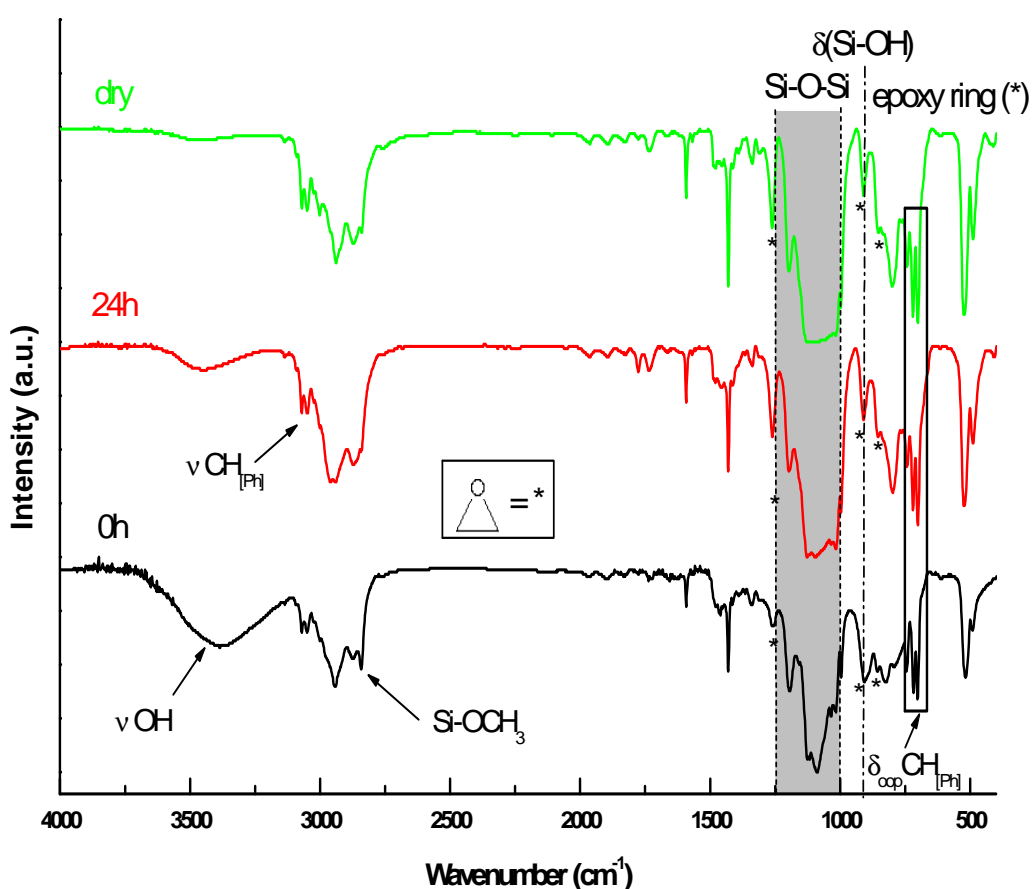


Fig. 33: FT-IR spectra for condensation reaction of sample- D/T_L-3

After 7 days the region including the characteristic vibrations for Si-O-Si bonds appears as a broad band and the single contributions are difficult to distinguish, sign of a large number of products.

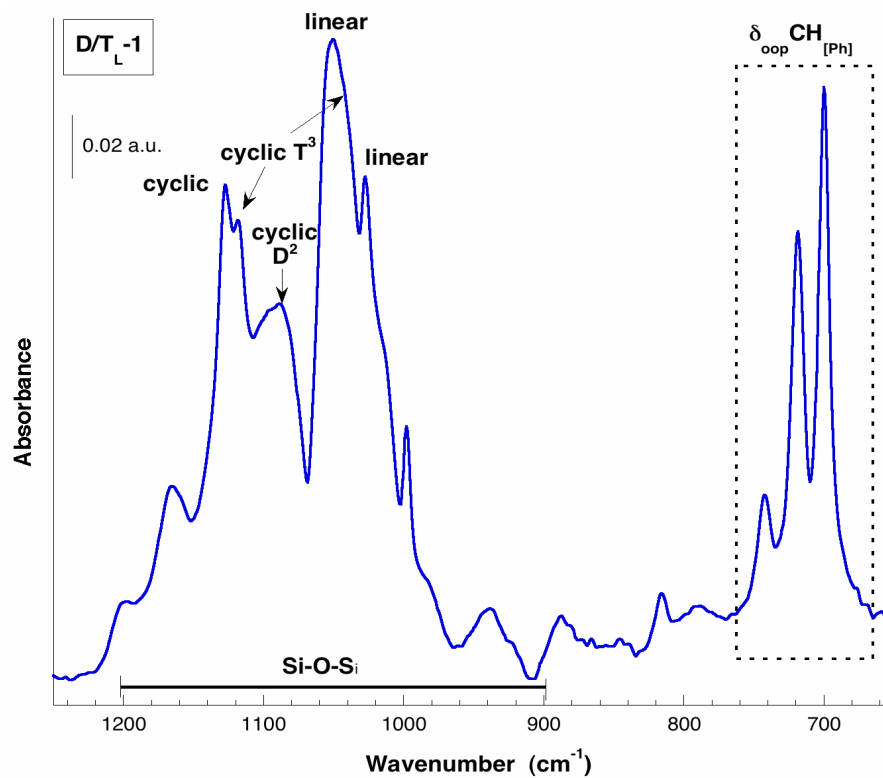
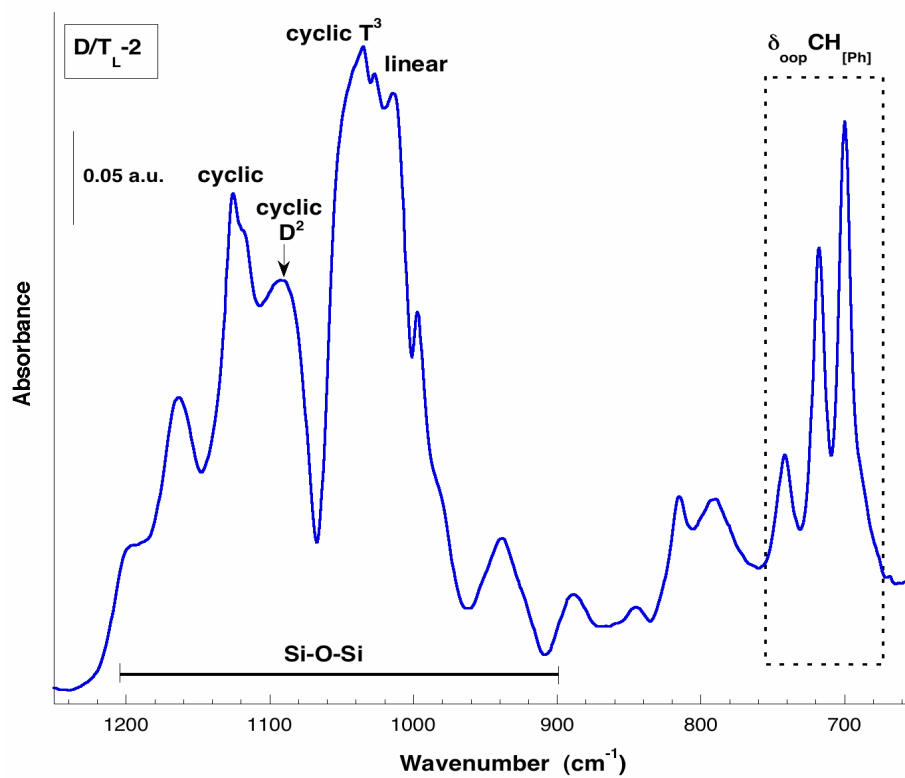
There is a strong overlapping also of THF bands with the ν_{as} vibration band of the epoxy ring, but after drying in vacuum and removing the solvent, all typical vibrations of the epoxide function (epoxy ring bands, see Table 4) and of the phenyl system ($\delta_{\text{oop}}\text{C-H}$ and $\delta\text{C-CH}$ vibrations, see Table 2) are clearly observable (Fig. 33).

5.2.2 ATR-FTIR characterisation

ATR-FTIR spectra of D/T_L-1 and D/T_L-2 final samples were obtained subtracting the THF spectrum to samples spectra.

In the 1200–900 cm^{-1} region, typical of ν_{as} Si-O-Si stretching bands of condensation products, the spectra of both samples are dominated by a quite broad band characterised by three main components, the relative intensities of which differentiate between the two products. In sample D/T_L-1 (Fig. 34) the main absorption at 1050 cm^{-1} with a component at 1027 cm^{-1} is due to linear condensation products. However, the presence of a relatively intense signal at 1127 cm^{-1} indicates the formation of cyclic structure. The absorption at 1118 with the shoulder at 1043 cm^{-1} corresponds to cyclic T^3 products. For sample D/T_L-2 (Fig. 35) the absorption at 1035 cm^{-1} corresponding to cyclic T^3 products, but there are also two intense peaks at 1026 and 1013 cm^{-1} respectively, attributable to linear products.

For both samples the presence of the aromatic ring is confirmed by the absorption signals in the region 745–695 cm^{-1} (dashed area in Fig. 34 and Fig. 35).

Fig. 34: ATR-FT spectrum of sample D/T_L-1Fig. 35: ATR-FT spectrum of sample D/T_L-2

5.2.3 Raman spectroscopy characterisation

Raman spectra have been collected in the 4000–150 cm^{-1} range. As for FT-IR spectroscopy, the typical Raman vibrations of reagents are presented in the following tables. Raman spectroscopy has been used in order to acquire more information on the presence of cyclic oligosiloxanes in our samples.

Raman characterisation of precursors

DPDO	Assignment	Wavenumber (cm^{-1})
	ν_{CH} [Ph]	3052
	ν -C=C- [Ph]	1589
	ν Si-Ph	1190, 1158, 1128
	ν Si-Ph	1030
	δ_{ip} [Ph]	1000, 623
	δ_{oop} [Ph]	690

Table 6: Raman characteristic vibration of DPDO with assignments [145]

MPTMS	Assignment	Wavenumber (cm^{-1})
	ν_{CH} [CH_3]	2930
	ν_{CH} [CH_2]	2892
	$\nu_{\text{C=O}}$	1713
	$\nu_{\text{C=C}}$	1637
	$\delta_{\text{as}}\text{CH}$	1453
	$\delta_{\text{s}}\text{CH}$	1404
	$w(\text{CH}_2)_{\text{n}^-}$ (MPTMS)	1294
	$\nu_{\text{C-C}}$ skeletal (MPTMS)	1195
	ν_{s} Si-O CH_3	641
	ν_{as} Si-O CH_3	607

Table 7: Raman characteristic vibration of MPTMS with assignments [145]

GLYMO	Assignment	Wavenumber (cm ⁻¹)
	ν_{as} CH ₂ ring	3049
	ν CH [CH ₃]	2930
	ν CH [CH ₂]	2892
	δ_{as} CH	1455
	δ_s CH	1413
	w (CH ₂) _n -	1338
	epoxy ring vibrations	1256
	ν C-C skeletal (MPTMS)	1195
	ν_s Si-OCH ₃	643
	ν_{as} Si-OCH ₃	611

Table 8: Raman characteristic vibration of Glymo with assignments [145]

Raman characterisation of samples

Fig. 36-Fig. 38 show the whole Raman spectra (4000–150 cm⁻¹) with inserts reporting the enlarged low frequency range (700–150 cm⁻¹), where it has been reported that the signals of polysiloxane rings can be observed [147, 148].

Since the doublet at 641 and 607 cm⁻¹ (ν_s Si-OCH₃, see Table 7), assigned to symmetric stretching vibrations of non hydrolysed methoxide groups, is completely disappeared, the absorption band at 602 cm⁻¹ for D/T_L-1 and at 601 cm⁻¹ for D/T_L-2 can be attributed to trisiloxane ring symmetric stretching [149].

Signals below 500 cm⁻¹, except the peak at 377 cm⁻¹ already present in MPTMS spectrum (Table 7) [150], could be attributed to network deformation modes of D and T units [151].

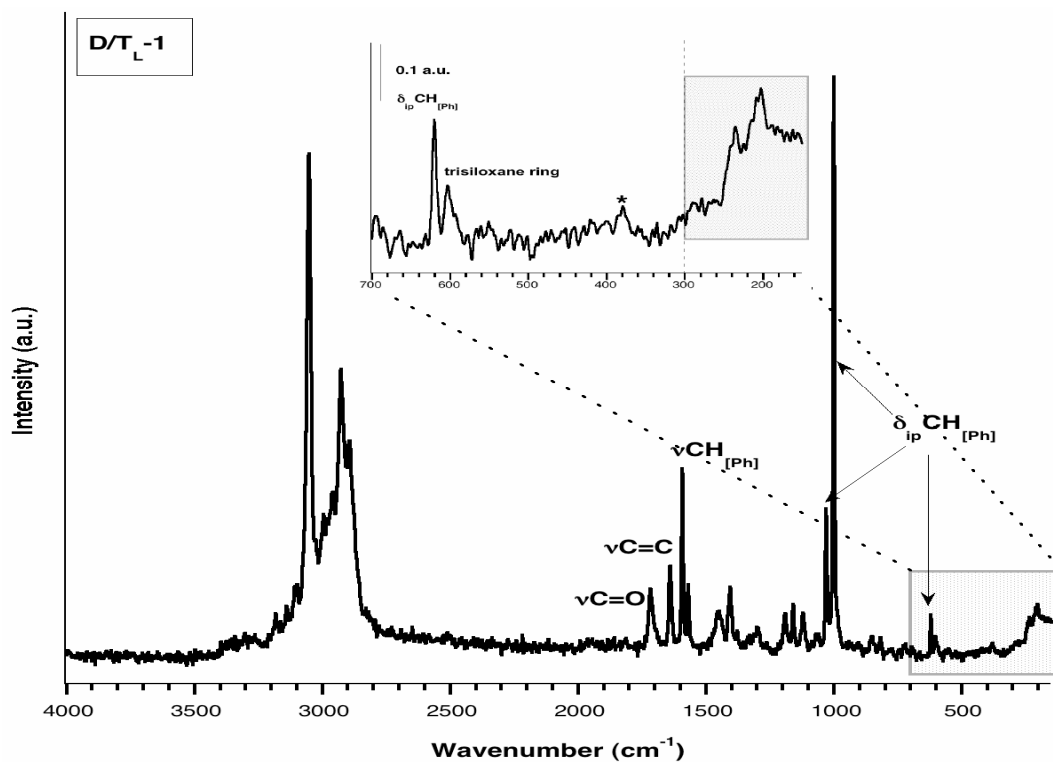


Fig. 36: Raman spectra od D/T_L-1 sample

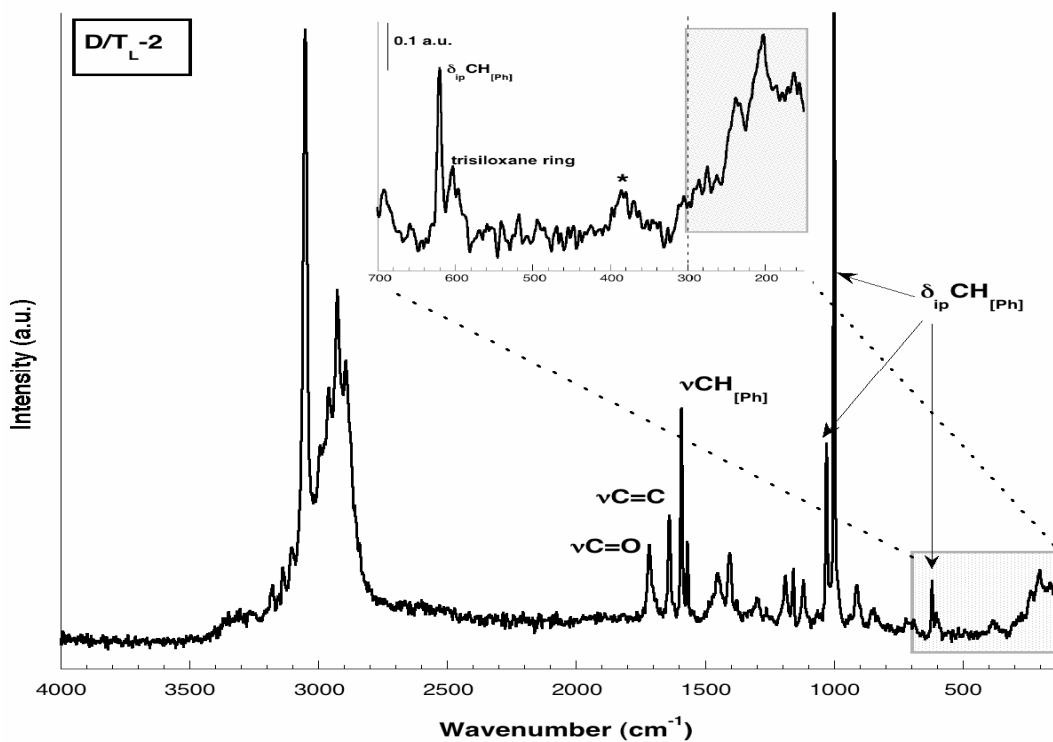


Fig. 37: Raman spectra od D/T_L-2 sample

In Fig. 36 and Fig. 37, the characteristic peaks of the reactive methacryl function are preserved ($\nu\text{C}=\text{O}$ at 1718 cm^{-1} and $\nu\text{C}=\text{C}$ at 1634 cm^{-1} , see Table 7). The presence of the phenyl ring is well observable from the characteristic absorption bands (Table 6).

The Spectrum collected for sample D/T_L-3 (Fig. 38) has a lower S/N ratio respect to the previous spectra, therefore peaks below 700 cm^{-1} are more difficult to detect and therefore a correct identification of cyclic species is not possible. Epoxy vibrational modes are observed at 3060 cm^{-1} ($\nu_{\text{as}}\text{CH}_2$ of the ring) 2999 cm^{-1} ($\nu_{\text{s}}\text{CH}_2$ of the ring) and 1256 cm^{-1} ($\nu_{\text{s}}\Delta$ Table 8). As for the sample with MPTMS as trifunctional precursor, the doublet at 643 and 611 cm^{-1} , due to the symmetric stretching vibrations of the non hydrolysed methoxy groups, can be used to follow the progress of the sol-gel reactions. The decrease in the doublet signal is proportional to the hydrolysis of the MeO-

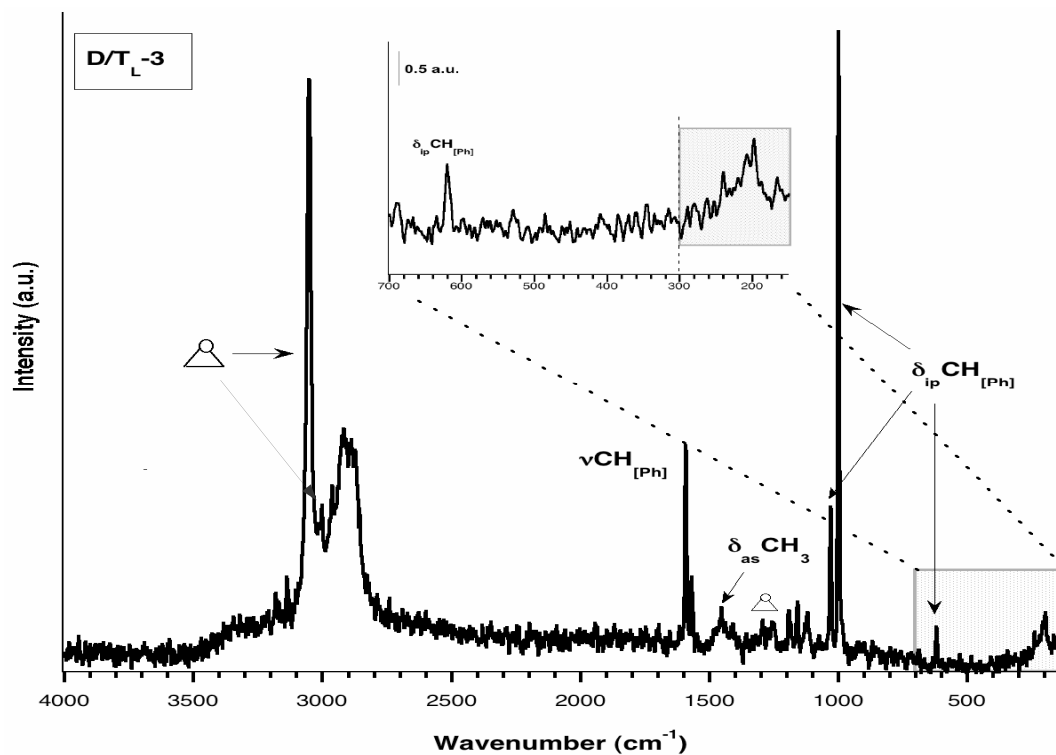


Fig. 38: Raman spectra od D/T_L-3 sample

5.2.4 NMR characterisation

Samples characterisation

The ^{29}Si NMR spectra have been recorded on samples at concentration 1.85M [Si] in THF, without further dilution, in order to avoid siloxane bonds rearrangements.

For sample D/T_L-1 (Fig. 39), in the spectral region characteristic of D-type signals, the resonance at -39.9 is due to terminal D¹ units, while the signals at -43.5 and -44.1 ppm are attributed to cyclic D² products (D₄ units). The signal at -47.6 ppm is associated with linear D² products. The ratio between D¹ and D² units was around 1:6; while the D² products ratio between in linear and cyclic units is 2:3 (see Fig. 39). In the T region, correlated resonances due to T² (-57.7 and -59.7 ppm) and T³ (-62.8, -64.9, and -66.5 ppm) units in a 1:2 ratio are evident.

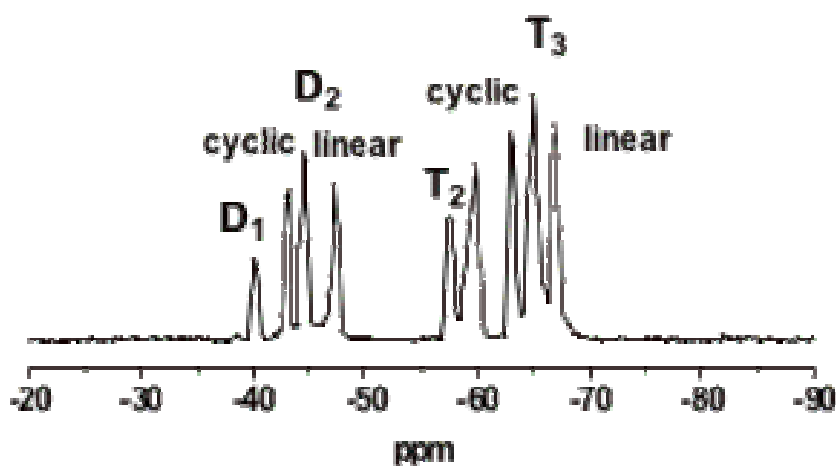


Fig. 39: ^{29}Si NMR of D/T_L-1

D/T_L-2 shows a similar spectrum. In the D signals region, the resonance at -39.9 is due to terminal D¹ units. Cyclic D² products present two signals at -42.0 and -44.1 ppm (D₄ units), while the signal at -47.1 ppm is associated with the linear products. The D² products can be separated in linear and cyclic units in a 1:2.5 ratio (Table 9). In the T region, resonances due to T²

(-58.2 and -59.4 ppm) and T³ (-63.9, -64.5, and -66.2 ppm) units in a 1:2 ratio are evident.

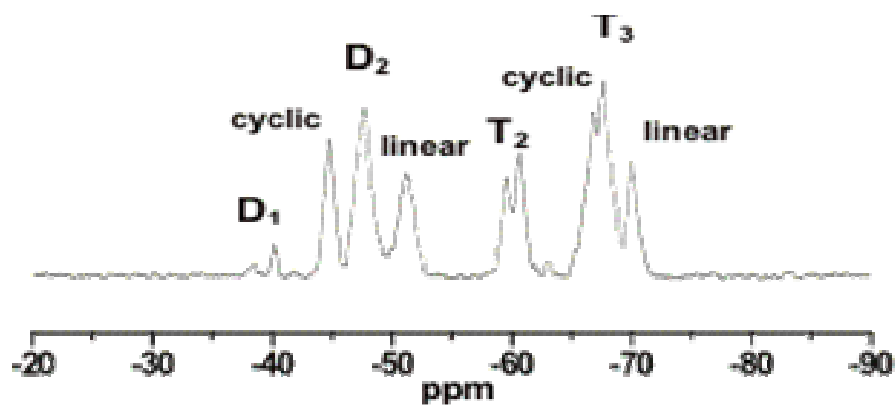


Fig. 40: ²⁹Si NMR of D/T_L-2

Sample	Assignment	δ(ppm)	Ratio
D/T _L -1	D ¹	-39.9	1
	D ² cyclic	-43.5, -44.1	4
	D ² linear	-47.6	2.5
	T ²	-57.7, -59.7	5
	T ³ cyclic	-62.8, -64.9	7
	T ³ linear	-66.5	3
D/T _L -2	D ¹	-39.9	1
	D ² cyclic	-42.0, -44.1	17
	D ² linear	-47.1	7
	T ²	-58.2, -59.4	2
	T ³ cyclic	-63.9, -64.5	3
	T ³ linear	-66.2	1

Table 9: estimated Dⁿ / Tⁿ ratio

Fig. 41 shows the spectrum obtained mixing DPDO and Glymo (1:1) in THF in the presence of DBDLT (D/T_L-3). In the spectral region characteristic of D-type signals, the resonance at -39.9 is due to terminal D¹ units.

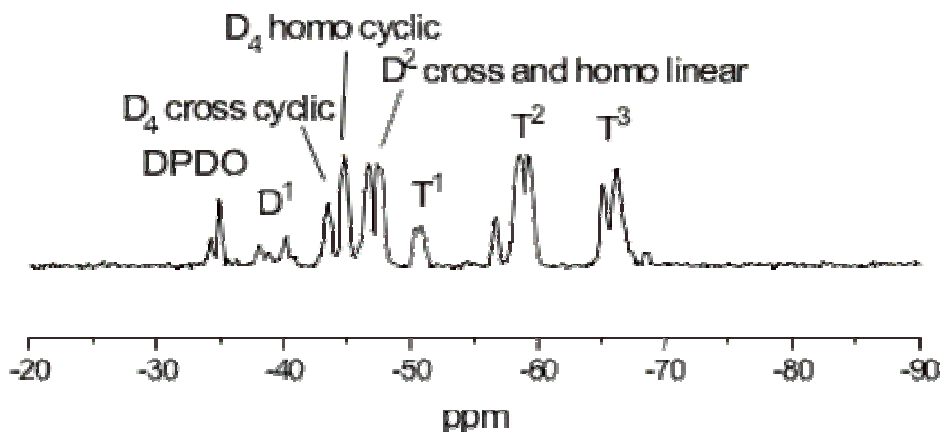


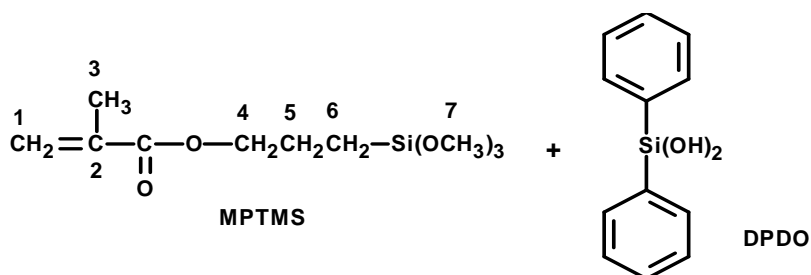
Fig. 41: ²⁹Si NMR of D/T_L-3

In the D² region the signals at -43.5 and -44.7 ppm are assigned to D₄ cross cyclic and D₄ homo cyclic units respectively; while the signals at -47.6 and -48.7 ppm are associated with D² cross and homo linear products respectively.

In the characteristic region of T-type signals, the resonance due to T² (-56 ÷ -60 ppm) and T³ (-63 ÷ -71 ppm) units are in the ratio 2:3. There are also signals between -50.0 and -51.5 ppm attributed to T¹ resonances. The unreacted DPDO is detected (-34.9 ppm).

5.2.4.1 ¹³C NMR

¹³C NMR spectra were collected in order to establish the stability of the polymerizable function in the obtained samples.



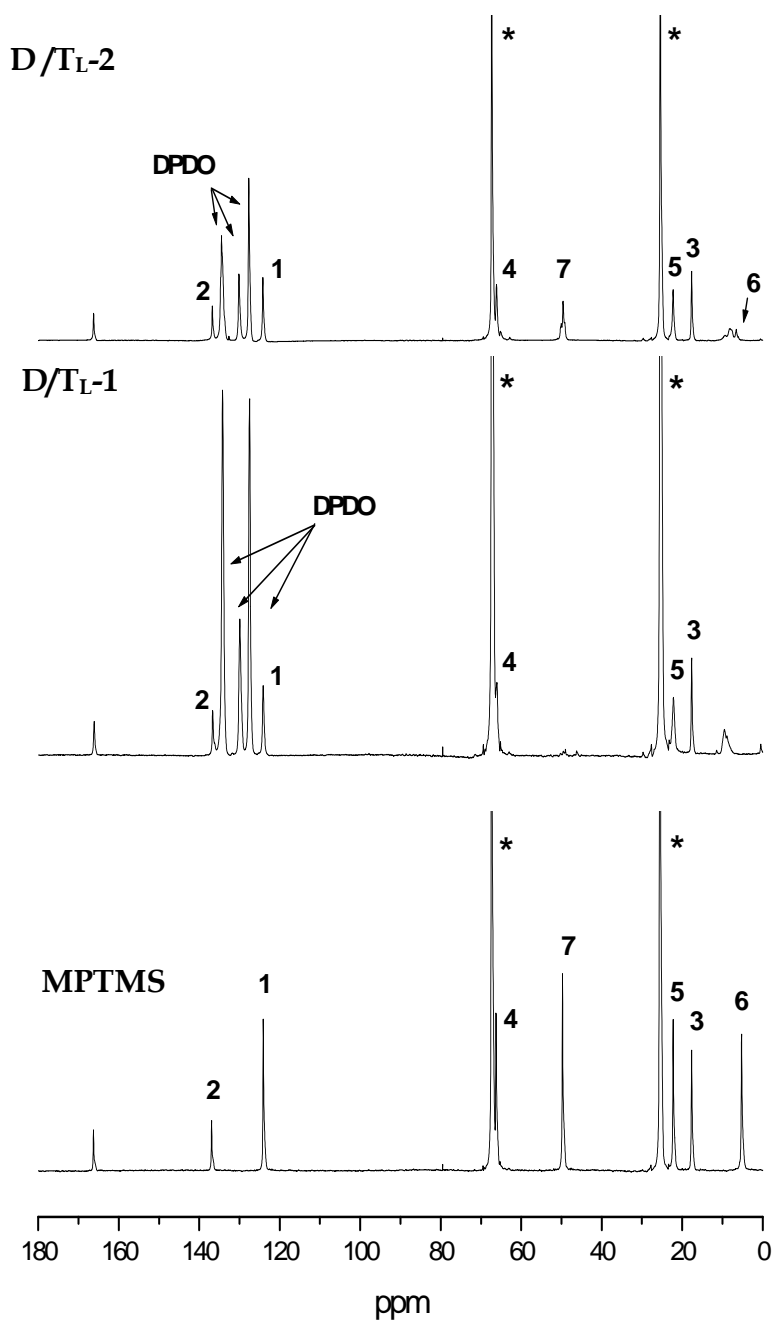


Fig. 42: ^{13}C NMR spectra of D/TL-1 and D/TL-2 and precursor (MPTMS). Solvent is marked with asterisk.

The spectra of D/TL-1 and D/TL-2 are very similar; the main difference is the complete disappearance of the Si-OCH₃ signal (quoted 7 in Fig. 42) in D/TL-1 respect to D/TL-2 and the stronger downfield shift to 9.4 ppm, of the methylene carbon of the propyl chain directly linked to silicon (quoted

6, -CH₂-Si) as a result of the progress of the condensation reaction. By comparison with MPTMS spectrum, the reactive methacrylate functions appear preserved in the two samples

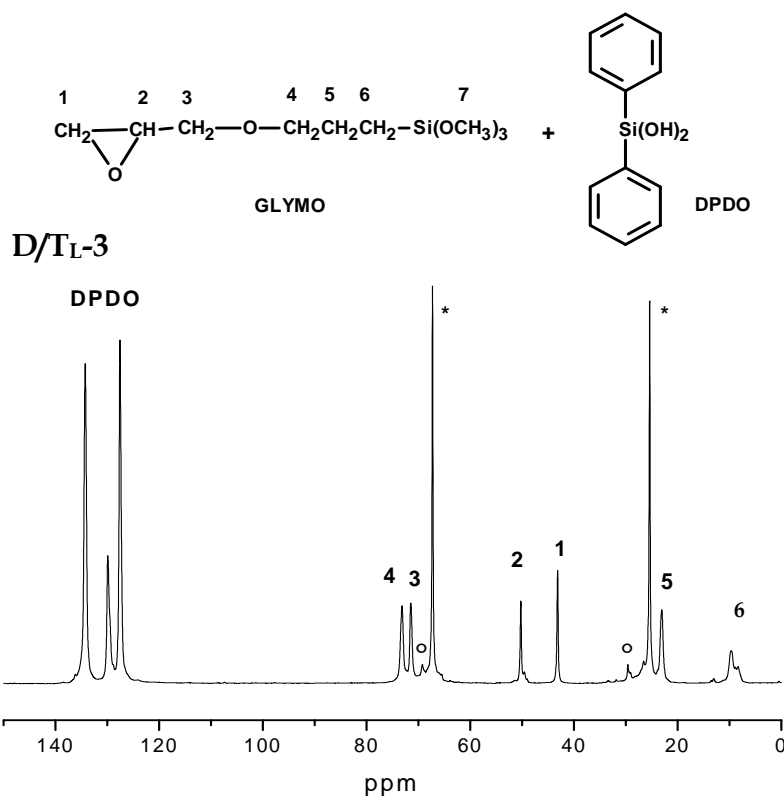


Fig. 43: ¹³C NMR spectra of D/TL-3 and precursors

The spectrum of D/TL-2 is shown in Fig. 42. It is possible to observe the consumption of MeO groups (quoted 7) and the conservation of the epoxy ring (1 and 2), except for a small amount of epoxy function that undergoes to ring opening (° peaks). The peak at 5.3 ppm in Glymo, quoted 6 in the structure, shifts to lower ppm owing to the condensation of the methoxy groups.

¹³C NMR assignments for Glymo precursor [154].

Carbon	1	2	3	4	5	6	7
Glymo, ppm	44.3	50.9	71.5	73.6	22.9	5.3	50.5

5.2.5 Gel Permeation Chromatography (GPC)

The principle of GPC operation is the separation of molecules on the basis of their hydrodynamic radius (R_h) or volume (V_h), and not on their molecular weight (M_w). Figure 20 illustrates the GPC operation. The separation process takes place in GPC columns, which are packed with porous materials such as polystyrene gels, glass beads, silica gel etc (A-D). Because of their size, the larger molecules cannot fit into the pores and elute faster through the porous packing materials than the smaller molecules (Fig. 44 B-C). As the molecules elute from the columns, they pass through a detector (C-D) the output is analyzed by a data processing system, which converts it into a chromatogram. Each molecular size will give rise to a peak in the chromatogram (C-D).

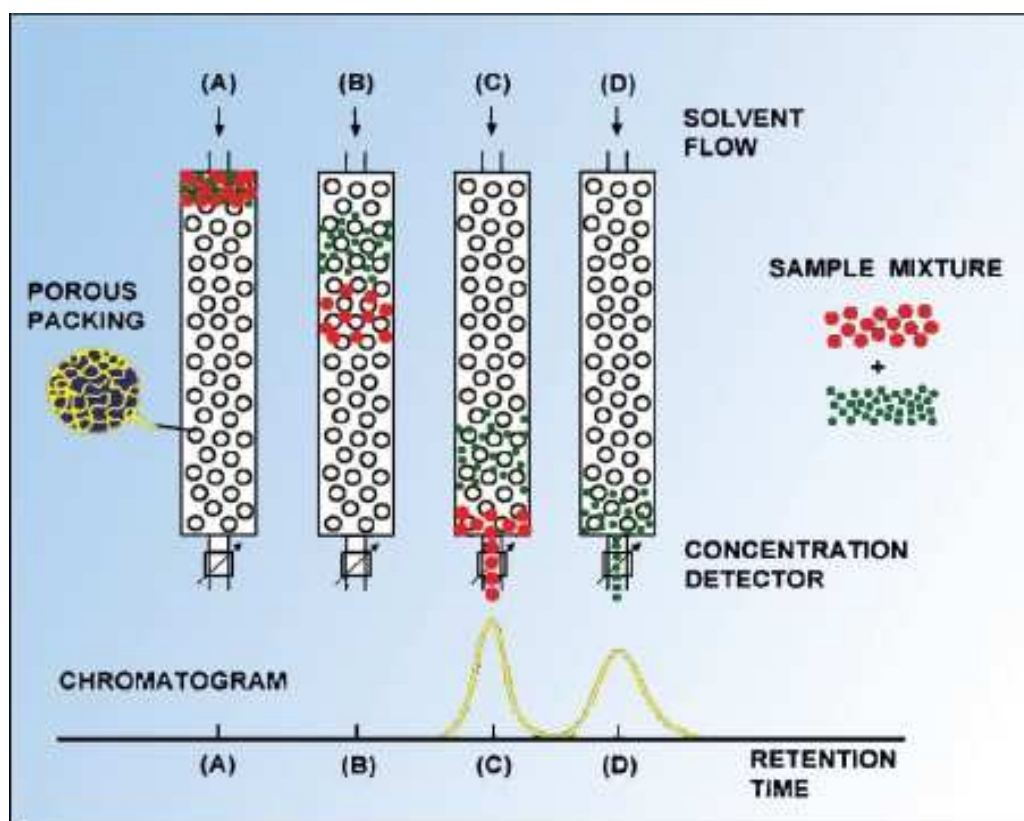


Fig. 44: principle of size exclusion in GPC analysis

The gel permeation chromatography process starts with continuous flow of the mobile phase through the system by means of a solvent delivery device, most commonly an isocratic pump. An in-line solvent degasser is employed to eliminate any vapour or gas in the line so that signal instability and noise are reduced. The sample is injected into the system either manually or by an autosampler.

5.2.5.1 Sample characterization

In order to define the size of the NBBs, gel permeation chromatography (GPC) has been performed. The samples have been dissolved in THF (final concentration sample between 1 and 5 mg/ml) and injected in the columns (100 μ l).

The calibration of the columns-system has been made with polystyrene standards of known molecular weight (Mw) in order to obtain a calibration curve. The measured molecular mass therefore refers to the mass of the polystyrene standard with the same size (or hydrodynamic volume). Thus, the obtained Mw is relative and not absolute. In order to check if the unreacted precursors were present also pure precursors were injected in the GPC instrument. The retention volumes are reported below.

Precursor Characterisation

Precursor	Retention Volume (mL)
DPDO	23.74
MPTMS	28.87
GLYMO	24.64

➤ BASE CATALYSED D/T_L

D/T_L-1 GPC diagram is characterized by three main peaks with signal at Mw 4576, 1461 and 499 (Fig. 45). The signal at Mw 499 is attributable to dimers, the main peak at 1,461 is probably due to a heptamer, which could be a cage type structure and the signal for Mw 4576 is probably due to a network type structure (possible structures are reported below in Fig. 46)

Mw	Retention Volume (mL) (Rv)
4,576	18.05
1,461	19.28
499	21.65
326	23.29

Table 10: GPC results for sample D/T_L-1

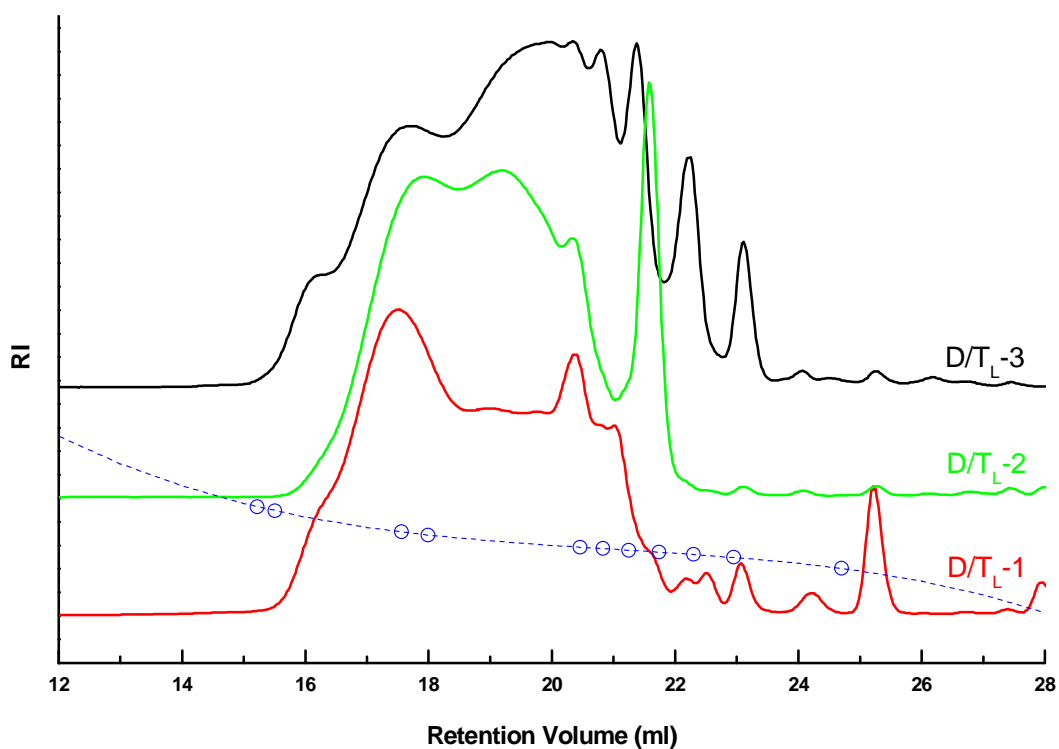


Fig. 45: GPC curves of D/T_L samples and calibration curve (dashed)

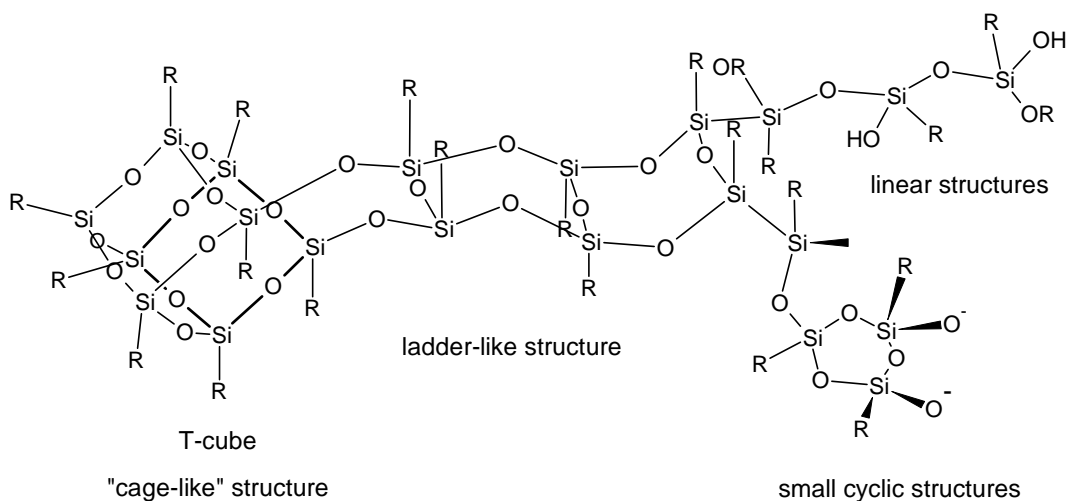


Fig. 46: structures: cage, ladder-like, linear

➤ ACID CATALYSED D/T_L

Mw	Retention Volume (mL) (R _v)
7431	17.62
3097	17.87
834	20.41
559	21.09
382	22.59
308	23.13

Table 11: GPC results for sample D/T_L-2

D/T_L-2 is characterized by a broad distribution of products with different molecular weights. Products range from dimeric species (high R_v, see Table 11) to two main products: a tetramer (Mw 834 - 25,3%) and probably a network type structure with Mw 7400 (34,6%). The peak at 3097 is probably due to a dimer formed by cage type structures.

Mw	Retention Volume (mL) (Rv)
17,243	15.25
5,235	17.73
2,921	19.85
1,323	19.87
655	20.82

Table 12: GPC results for sample D/T_L-3

Also D/T_L-3 sample is characterized by a broad distribution of products with different molecular weights (Fig. 45 and Table 12). The peak at 1,323 is probably due to a heptamer, which is probably a cage type structure. The main signal at Mw 2,921 (55.7% of RI area) is probably a dimer and the one with Mw 5,235 is probably due to a tetramer of cage structures. Again there is a network type structure with Mw 17,243.

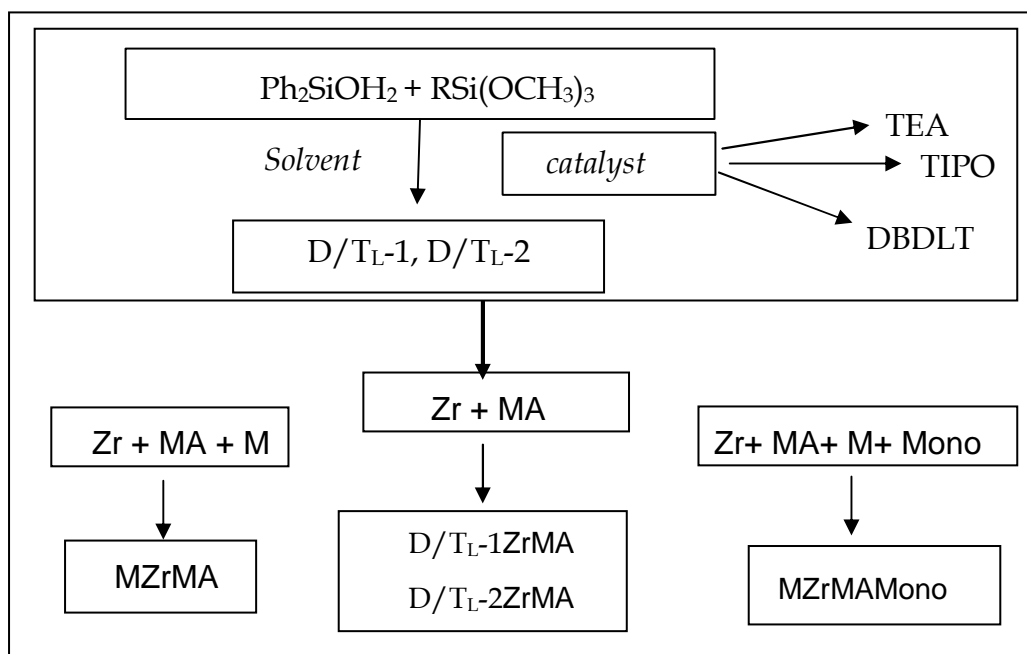
5.2.6 DSC measurements

DSC measurements have been performed in N₂ flow in order to study the thermal polymerization process of the samples and understand the availability of the reactive organic functions on the NBB.

NBBs have been added to properly defined sol-gel matrices (in collaboration with the Department of Mechanical Engineering of the Un. of Padua). Reagents used to prepare the matrices are: Zr(OBu^t)₄(Zr), methacrylic acid (MA), MPTMS (M) or NBB (D/T_L-1, D/T_L-2), triacrylate monomer (labelled Mono).

MATRICES

Matrices have been prepared in accordance with the following protocol (Scheme 18).



Scheme 18: protocol for matrix preparation

GENERAL PROCEDURE

MPTMS: Zr(OBu^t)₄: MA: Mono are in the ratio 1:3.5:2:5.

Water and HCl are added to MPTMS in ratio 1:3:0.01. The solution is stirred for 1h at RT in air in order to promote the hydrolysis of the methoxy groups (solution A). Zr(OBu^t)₄ was mixed with methacrylic acid for 5 min stirring (solution B), the methacrylate monomer is eventually added in this step. Methoxyethanol was used as solvent and added in order to obtain a final solution of 150g/L respect to the final (SiO₂+ZrO₂) moles. Solution A and B are mixed and neutralised with NaOH and left under stirring for 1h.

A thermal catalyst (BPO) was added in amount equivalent to the 2% molar of the acrylic groups. To allow the dispersion of BPO powders in the matrix the solution was treated in an ultrasound bath for 5-10 min. The viscous solution was left dry at air in dark conditions for 24 h.

Matrices containing NBBs are prepared in the same way, only substituting MPTMS with either D/T_L-1 or D/T_L-2.

The obtained matrices are analysed without further treatment.

The data of ΔH (J/g) and peak maximum temperature, calculated from DSC curves, are reported in Table 13

Matrix	Methacrylate precursor	ΔH (J/g)	Peak max (°C)
MZrMA	MPTMS	8	120
D/T _L -1ZrMA	D/T _L -1	92	103
D/T _L -2ZrMA	D/T _L -2	107	105
MZrMAMon	MPTMS+triacylate monomer	352	90

Table 13: DSC characteristic data of hybrid matrices

The matrices prepared with D/T_L-1 and D/T_L-2 NBB and with the triacylate monomer display, in the temperature range 90–160°C, a more intense polymerization effect with respect to the matrix obtained from pure MPTMS, featuring two main components: a main peak and a shoulder at high temperature. These two components account for two families of reactive double bonds. The first peak is assigned to the methacryloxypropyl group of MPTMS and the second peak derives probably from the methacryl group of MA. In most cases it is also possible to see a third peak between the first two, which is probably due to some methacryl functions of MPTMS that could be hindered inside the network and less available for polymerization. The position and intensity of the main peak depend on the composition of matrices.

A decrease in peak position and an increase in intensity are observed moving from the MZrMA matrix, the matrices prepared with D/T_L-1, to D/T_L-2 and finally to the matrix prepared with the branched triacrylate monomer, MZrMaMon. This trend indicates a more effective polymerization process that depends on the effective availability of the methacryl functions.

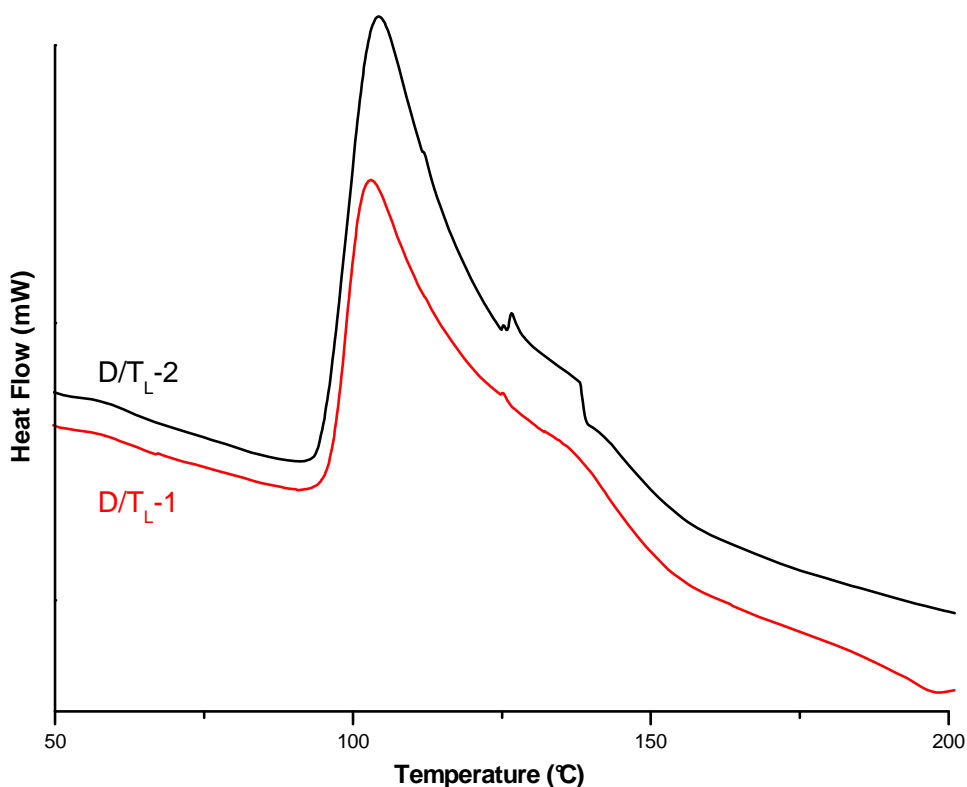


Fig. 47: DSC curve of D/T_L sample

STRUCTURAL CHARACTERIZATION of D/T_L NBB

Nanostructured units with different architectures and complexities have been obtained exploiting the non-hydrolytic condensation reaction, starting from DPDO and MPTMS or Glymo and exploiting different condensation promoters. Both TEA and TIPO resulted efficient in

promoting condensation for samples with MPTMS. DBDLT resulted the best promoter in the case of DPDO/Glymo gels, as it is a sufficiently strong acid to catalyse the condensation reactions, but mild enough to preserve the epoxy function in a major extent (see ^{13}C spectra at pag. 94). From the ^{29}Si NMR data, TEA promoter (D/T_L-1) leads to better cross-condensed D² and T³ units respect to the acid condensation promoters for MPTMS based samples (Fig. 40). This is attributable to the ability of TEA to deprotonate DPDO and promote the condensation reaction of the silanolate species (mechanism in Introduction pag. 7). The progress in the condensation reaction is confirmed by ^{13}C spectra (Fig. 42). On the other hand, the product obtained with the acid promoter TIPO (D/T_L-2) is less condensed, but the ratio cyclic/linear for both D and T units is higher respect to D/T_L-1. The presence of cyclic structures in all the samples is confirmed by the Raman results in the 600-150 cm^{-1} range [147]. DPDO/MPTMS samples show a higher amount of cyclic products with respect to the one prepared from DPDO/Glymo as precursors.

GPC analyses show that the base condensation promoter leads to a smaller quantity of final products with low Mw than the acid one.

In the case of MPTMS it is possible to propose the presence of cage-like structures formed by heptamer oligomers. The heptameric species is present as a single unit in D/T_L-1 and as a dimer of cages in the D/T_L-2. Dimers and trimers are present in both samples, but the acid condensation promoter seems to endorse the aggregation between oligomers and units of different sizes leading to more complex network-like structures.

Also in the case of Glymo precursor (D/T_L-3), the condensation gives rise to different species ranging from small oligomers (Mw 655) to more complex structures as the one at Mw 1,323 (main products, see Fig. 45), which is probably again a cage structure. In this case the other two peaks in the chromatogram are probably due to a dimer and a pentamer of cages

respectively, whereas the product with Mw 17,243 is due to a more complex network-like structure.

The complexity of the produced species is also confirmed by DSC data (Table 13). It is possible to observe a trend in thermal polymerisation. The polymerisation effect (decrease of peak position and increase in peak intensity) is due to the different availability (load and mobility of the network) of the reactive methacryl function in the obtained matrix.

In order to obtain more functionalised NBBs, samples with a higher MPTMS load were synthesised in the same condition. Unfortunately, the non-hydrolytic condensation process demonstrated to be not suitable for these samples.

5.3 High functionality derived hybrids

All reagents were used without further purification unless otherwise stated. The list of employed reagents and solvents is reported below.

Reagents

Diphenylsilanediol (DPDO)

Methacryloxypropyltrimethoxysilane (MPTMS)

Glycidoxypropyltrimethoxysilane (Glymo)

Alcohols

Ethanol (EtOH)

1-propanol (*n*PrOH)

2-Propanol (*i*PrOH)

n-Butanol (*n*BuOH)

sec- Butanol (*s*BuOH)

tert- Butanol (*t*BuOH)

Carboxylic acid

Acetic Acid (AcA),

Formic acid (FA),

Propionic acid (PA),

Acetylsalicylic acid (ASA),

Thioglycolic acid (TGA),

Salicylic acid (SA),

Chloroacetic acid (Cl-AcA),

Citric acid (CA),

Ascorbic acid (AA)

5.3.1 Syntheses of D/T_H samples

These NBBs are synthesized with the goal of producing patternable hybrid films for optical applications. MPTMS and Glymo are suitable precursors since they contain a reactive function ($-\text{C}(\text{CH}_3)=\text{CH}_2$ and \triangle respectively), exploitable in the photopolymerisation. In order to increase the network crosslinking degree, a high density of reactive groups is required. Therefore, the molar ratio of MPTMS or Glymo to DPDO was increased with respect to D/T_L samples to obtain new NBBs by the non-hydrolytic approach; However, the results obtained by means of the non-hydrolytic approach (presented in Appendix C) were not satisfactory. Thus, the “in situ water production” (*ISWP*) route was chosen to promote the hydrolysis and condensation reactions of samples with high trifunctional/difunctional silanes ratio.

The reference reaction was run with MPTMS precursor and acetic acid and ethanol (D/T_H-1) were used for producing the controlled amount of water through the esterification reaction.

Our goal was to relate the water availability for the sol-gel process to the kinetics of the esterification reaction run with different alcohol/acid mixtures in comparison with the standard reaction D/T_H-1. Thus, two different series of samples were synthesised, changing either the alcohol or the carboxylic acid respect to D/T_H-1.

Two protocols were followed:

1) changing carbon chain length of steric hindrance of the alcohol, passing from n-propanol to t-butanol (Table 14) → alcohol series (D/TH-2A-E);

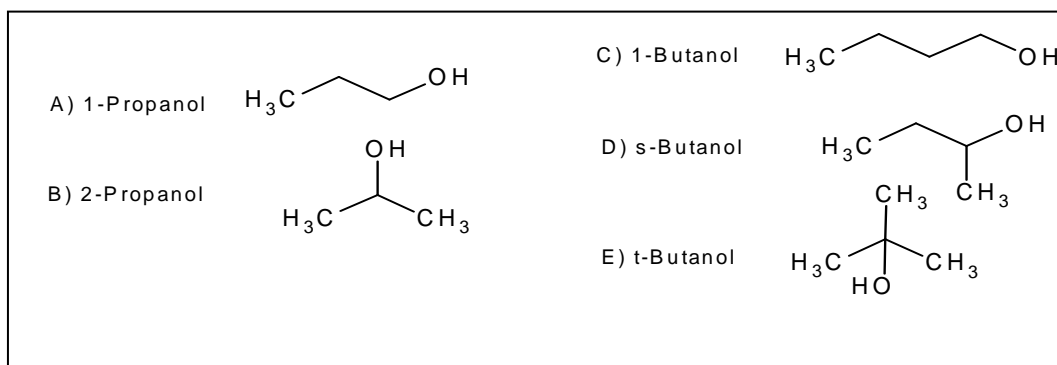


Table 14: alcohol series

2) varying the pK of the carboxylic acid (Table 15) → Acid series (D/TH-3A-H).

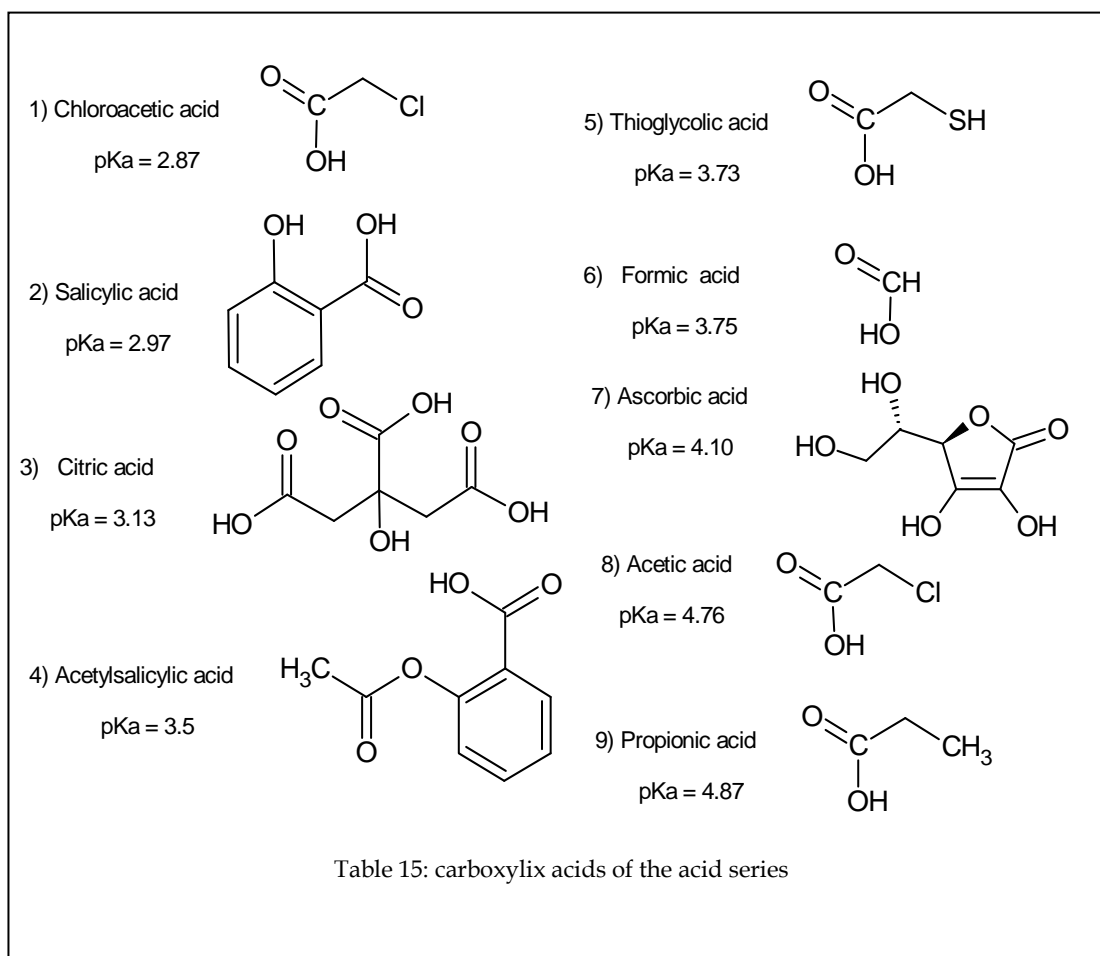


Table 15: carboxylic acids of the acid series

5.3.2 D/T_H syntheses

The samples were synthesized with the following molar ratios:

DPDO : MPTMS = 1 : 5; DPDO : alcohol : carboxylic acid = 1 : 4 : 2

Sample	Alcohol	Carboxylic acid	Temp
D/T _H -1	EtOH	AcA	75°C
D/T _H -2A	<i>n</i> PrOH	AcA	90°C
D/T _H -2B	<i>i</i> PrOH	AcA	75°C
D/T _H -2C	<i>n</i> BuOH	AcA	90°C
D/T _H -2D	<i>s</i> BuOH)	AcA	90°C
D/T _H -2E	<i>t</i> BuOH	AcA	75°C
D/T _H -3A	EtOH	PA	75°C
D/T _H -3B	EtOH	AA	75°C
D/T _H -3C	EtOH	FA	75°C
D/T _H -3D	EtOH	TGA	RT
D/T _H -3E	EtOH	ASA	75°C
D/T _H -3F	EtOH	CA	70°C
D/T _H -3G	EtOH	SA	70°C
D/T _H -3H	EtOH	Cl-AcA	70°C
D/T _H -4	EtOH	AcA	70°C

Table 16: Syntheses conditions of D/T_H samples

The synthesis scheme of D/T_H is presented in Fig. 48

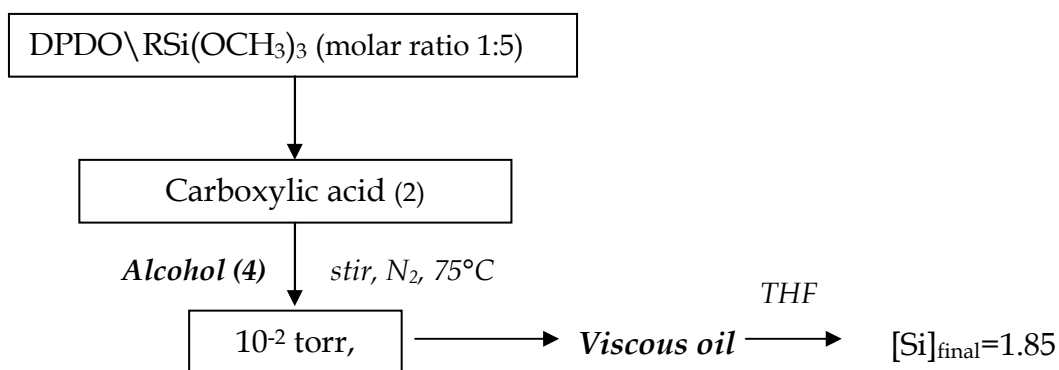


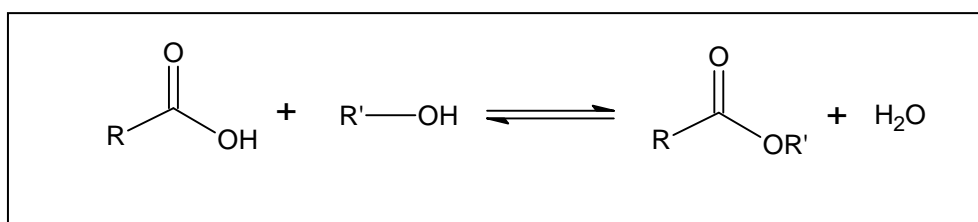
Fig. 48: general reaction scheme for D/T_H

The complete reaction procedures are exposed in Appendix A (synthesis 4 and 5).

5.4 D/T_H characterisation

FT-IR characterisation

The syntheses are based on the *ISWP* route that exploits an esterification reaction between a carboxylic acid (RCOOH) and an alcohol (R'-OH) with the controlled production of water (Chapter 1.2.3 in the Introduction



In D/T_H-1 the esterification reaction occurs between ethanol (EtOH) and acetic acid (AcA).

In the alcohol series, the carboxylic acid was fixed (AcA) and different alcohols were

In the case of the acid series, the alcohol was fixed (EtOH) and different carboxylic acids were used

The condensation between the two alkoxy silanes is monitored by FT-IR as function of reaction time in the range between 4000 and 400 cm⁻¹.

The alkoxy silanes precursor spectra are presented from page 65 to 67. The FTIR spectra and the main assignments for ethanol and acetic acid are shown below.

EtOH

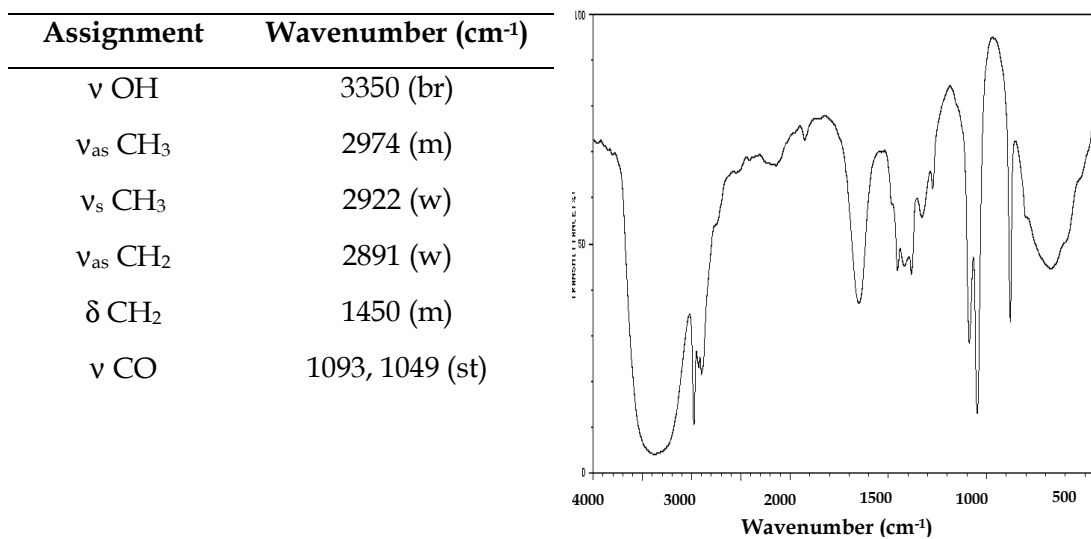
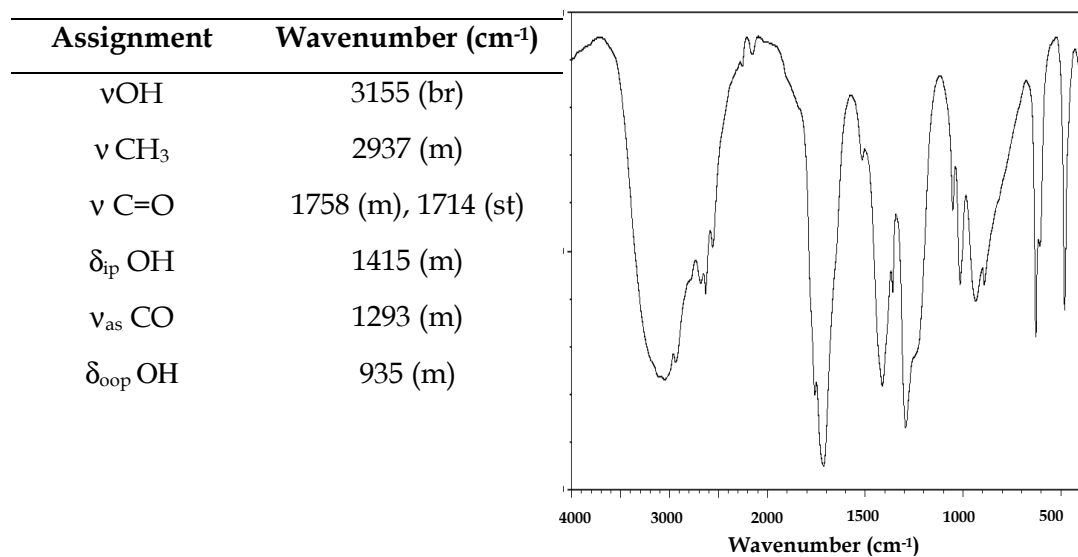


Fig. 49: FT-IR spectra and assignments for EtOH [152]

Acetic Acid (AcA)



➤ D/T_H-1 (EtOH/ AcA)

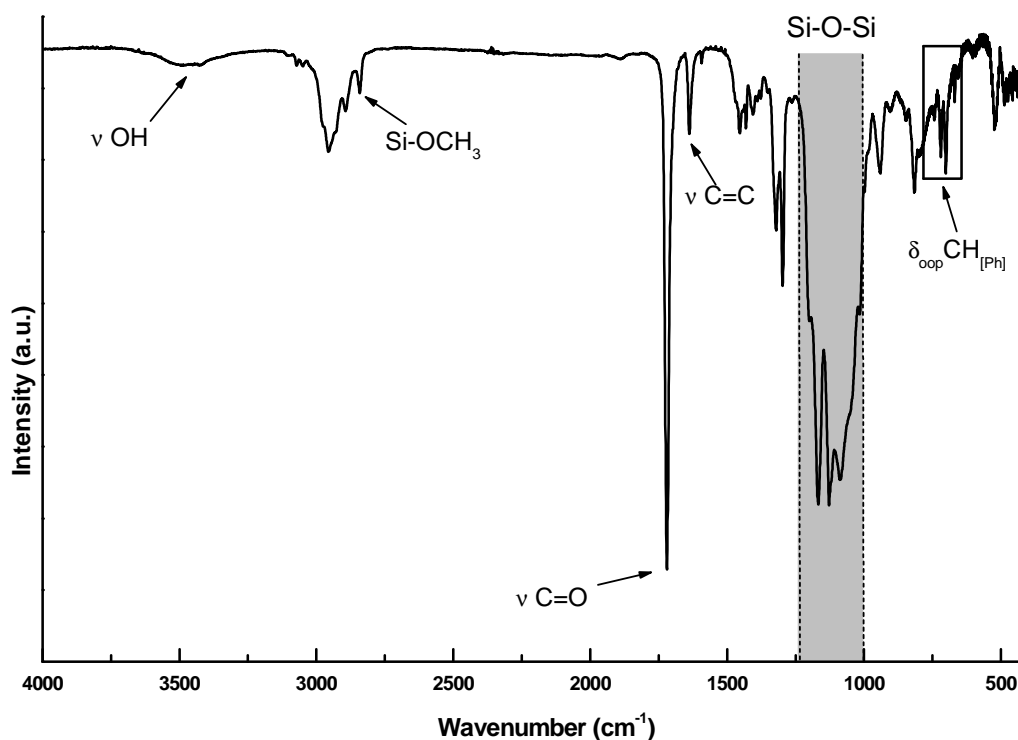


Fig. 51: FT-IR spectra after drying of D/T_H-1

The FT-IR spectra of the obtained samples are characterized by the strong overlapping of EtOH signal.

The deformation vibration of Si-OH of DPDO is found at 840 cm⁻¹ in EtOH solution (spectrum in Appendix C). This band moves to 846 cm⁻¹ in the condensation mixture, and progressively decreases in intensity during the reaction. The successful condensation is evidenced by the consumption of Si-OH and MeO- groups, with the disappearance of νSi-OH, and the decrease of Si-OMe signal of MPTMS (2940, 1167, 1078 cm⁻¹, see spectrum A). The progress of the condensation reaction can not be followed by considering only the signal due to the methoxy group, since the use of an excess of solvent can lead to a group exchange between alkoxide and alcohol.

The siloxane band, which is generated by the overlapping of Si-O-Si signals between 1200 and 1000 cm⁻¹, allows estimating the presence of

network type (cross-linked ladder) or cage type (polyhedral) structures. In D/T_H-1 (Fig. 51) both structure are present, with signals at 1127 and 1118 cm⁻¹ due to cyclic structures, whereas the signals at 1060 and 1015 cm⁻¹ are attributed to ladder like ones.

All typical vibrations of the aromatic ring system (phenyl) are clearly present (Fig. 51). The organic reactive function (methacryl) (ν C=O at 1715 cm⁻¹ and ν C=C at 1634 cm⁻¹) is preserved in the final product.

➤ ALCOHOL SERIES

In all cases (D/T_H2A-E), the typical vibrations of the aromatic phenyl ring system (δ_{oop} at 740, 720, 700 cm⁻¹) and of the methacryl group (ν C=O at 1719 cm⁻¹ and ν C=C at 1636 cm⁻¹) are present without changes in the FT-IR spectra (Fig. 52).

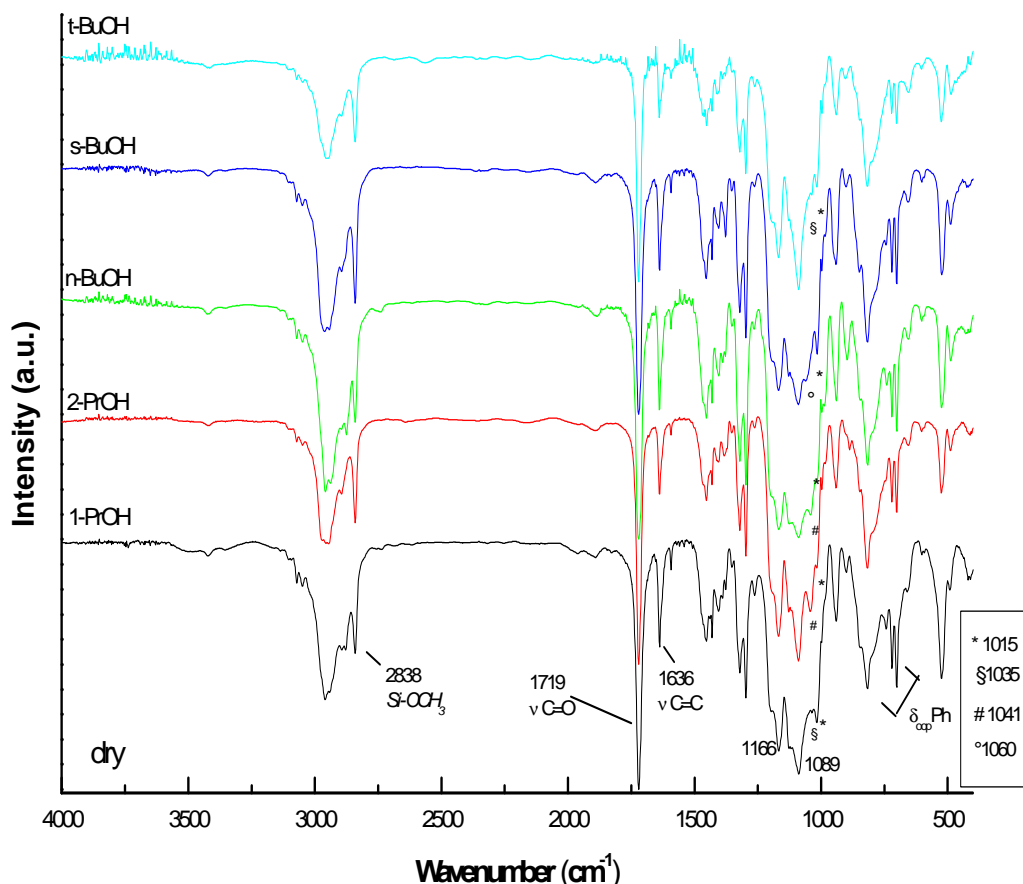


Fig. 52: FT-IR spectra for alcohol series- D/T_H 2(A-E)

In the spectra of all the samples are present the peaks located at 1089 cm^{-1} and 1127 cm^{-1} (polyhedral structures), and the signal at 1015 cm^{-1} , whose intensity changes with the increasing steric hindrance of the branched alcohols, due to the presence of linear structures.

A second peak at low wavenumber in the Si-O-Si bonds range is present in these samples. The intensity of this component increases with the length of the carbon chain. For 1-PrOH (D/T_H2A) as for *t*BuOH (D/T_H2E), the position changes from 1035 cm^{-1} to 1041 cm^{-1} for 2-PrOH (D/T_H2B) and *n*BuOH (D/T_H2C) and finally to 1060 cm^{-1} for *s*BuOH (D/T_H2D) (linear structures). The band due to residual Si-OMe groups is observable at 2938 cm^{-1} and increases in intensity with length and steric hindrance of the carbon chain of the alcohol.

➤ ACID SERIES

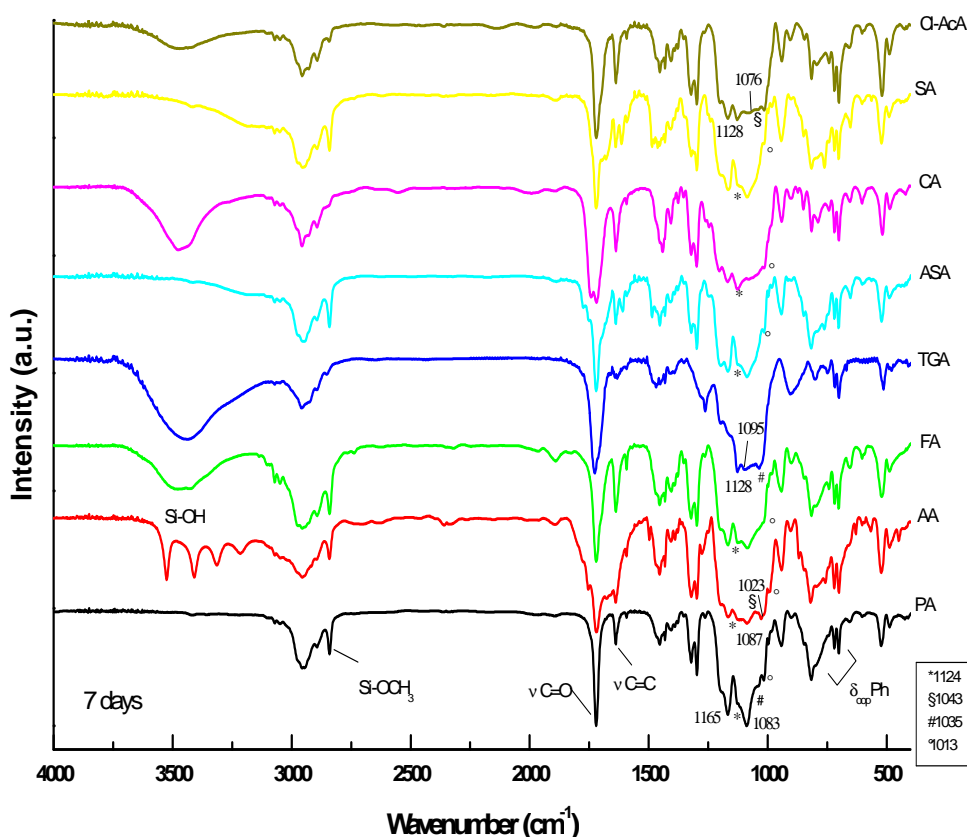


Fig. 53: FT-IR spectra for acid series-D/T_H 3(A-H)

Reactive functional groups are preserved in all cases as observable from Fig. 53. The Si-O-Si antisymmetrical stretching vibrations change according to the following table:

Label	Wavenumber (cm ⁻¹)				
	Cyclic tetramers	Cyclic trimers	cages	Ladder-like	Open chain
D/T _H 2A	1086	1017	1126, 1117		1033 (s)
D/T _H 2B	1086	1017, 1044	1127, 1119, 1111		1033 (s) 1023
D/T _H 2C	1087	1016 (s)	1128, 1117		1033 (s)
D/T _H 2D	1089	1042	1128, 1099, 1060	1155 (s)+ 1050	1032
D/T _H 2E	1083		1126		1049
D/T _H 2F		1011, 1015, 1042 (s)	1128, 1060(s)		1077, 1026 (s)
D/T _H 2G	1082	1013(s)	1128, 1117		1048 (s)
D/T _H 2H	1079	1016, 1043 (s)	1123		1035 (s)

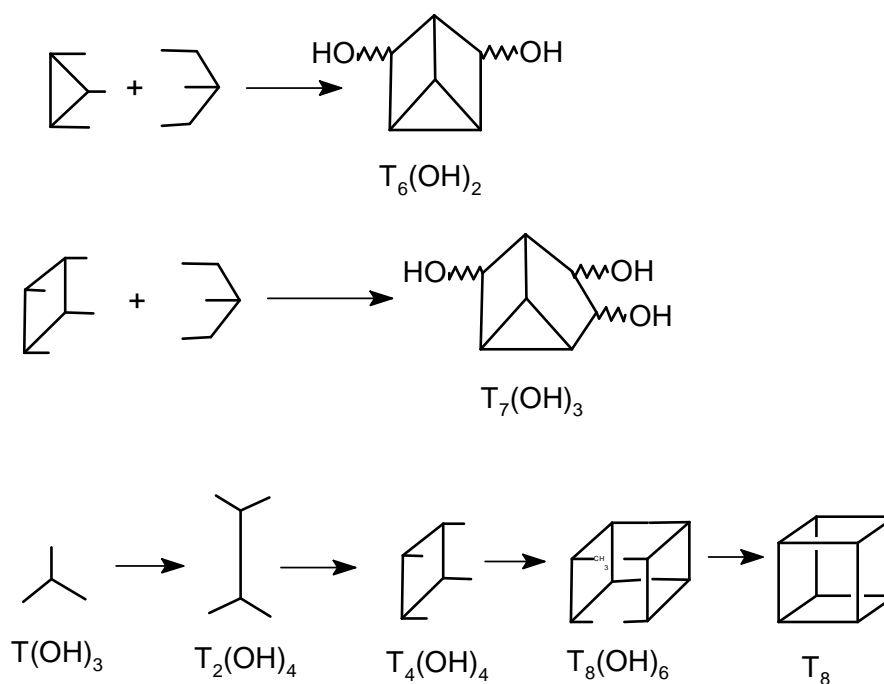
Table 17: vibrational band assignment and band frequencies (cm⁻¹) for different T-cube like silsesquioxanes (cages), cyclic and open chain polysiloxanes (s = shoulder)

In all samples the main peak is present at around 1125 cm⁻¹ and can be attributed to cage-like structures. A second peak at lower wavenumbers (in the range 1120-1100 cm⁻¹) suggests the presence of smaller structures as cyclic tetrasiloxanes (1020-1010 cm⁻¹) (Table 17), which can interact to give more complex structures (Scheme below). like cyclotrisiloxanes double rings found in T⁶ structures (about 1042 cm⁻¹) as suggested from Sassi et al. [152].

Acids with low pK lead to a more efficient condensation in terms of methoxy group consumption, but also to a larger range of products among which the most important are cage structures (1126 cm⁻¹). An exception to the trend in condensation ability is thioglycolic acid, which greatly increases the condensation rate. This is probably due to the presence of a

heteroatom in the acid chain, leading to a peculiar reactivity as for chloroacetic acid.

SCHEME for structure generation*



* adapted from [153]

D/T_H-4

D/T_H-4 sample was prepared mixing DPDO and Glymo in a 1:5 ratio and using EtOH/ AcA mixture.

The esterification reaction can be monitored, observing the splitting of the stretching vibrations of the carbonyl group around 1745 cm^{-1} ; one peak is due to the acid (1756 cm^{-1}) and the other to the ester (1722 cm^{-1}). The CO stretching of the acid disappears slowly and the band associated to the

stretching vibration of OH in $-\text{COOH}$ of the acid at 3405 cm^{-1} decreases significantly, as the reaction proceeds and water is created. The presence of water is confirmed by the small broad peak at 3467 cm^{-1} , due to νOH , which was overlapped to the stretching vibrations of the OH groups of the carboxylic acid at the beginning of the reaction, and by the appearance of a new peak at 1634 cm^{-1} typical of water. The almost complete disappearance of the peak due to the stretching vibrations of the methoxy group (Table 4) and the simultaneous formation of siloxane bridges ($1200\text{--}1000\text{ cm}^{-1}$) demonstrate the progress of the condensation reaction.

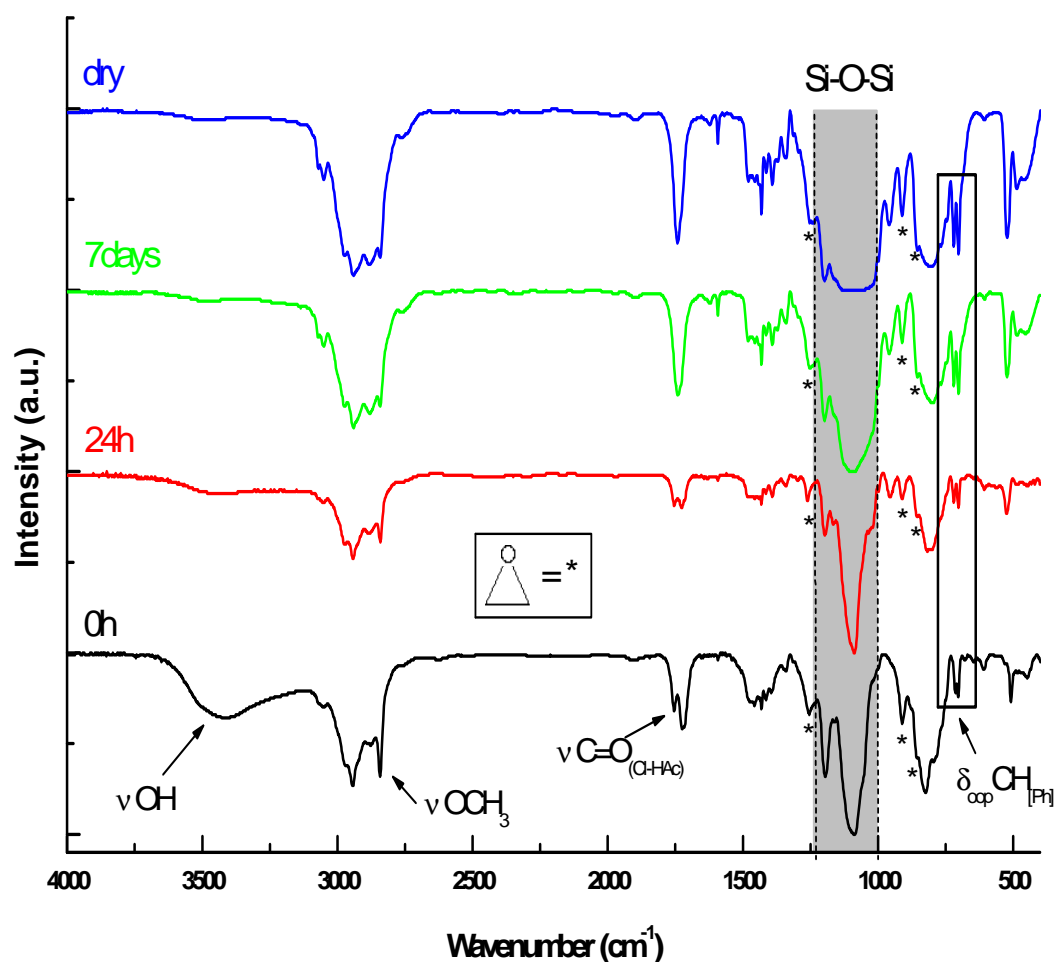


Fig. 54: Time evolution of FT-IR spectra of D/TH-4

The broad band formed by several overlapped peaks in the Si-O-Si range is due to a wide range of different products, from cyclic ones (1127, 1102, 1082 cm^{-1}) to linear or branched ones (1055, 1034, 1018 cm^{-1}).

The reactive epoxy group is still present as proved from the μ bands, characteristic of the epoxirane ring vibrations (Fig. 54). Also the aromatic rings are detectable in the spectra from the characteristic out of plane deformation vibrations of the phenyl (δ_{oop} at 745 and 714 cm^{-1} , and $\delta\text{C-CH}$ at 703 cm^{-1}).

5.4.1 Raman spectroscopy

Raman spectra have been collected in order to confirm the presence of siloxane cyclic oligomers.

Raman assignments of the precursors are reported at pages 86 and 73.

Raman characterisation of sample D/T_H-1

The whole spectrum of NBB D/T_H-1 (4000–150 cm^{-1} range) and the magnification of the low frequency range, where the signals of polysiloxane rings can be found [147] (700–150 cm^{-1}) are shown in Fig. 55. The disappearance of the doublet at 641 and 607 cm^{-1} (ν_s Si-OCH₃, see (Table 7) assigned to symmetric stretching vibrations of non hydrolysed methoxide groups, leads to assign the band at 603 cm^{-1} to trisiloxane rings breathing [149]. Signals below 500 cm^{-1} , except the peak at 377 cm^{-1} already present in MPTMS spectrum (Table 7) [150] could be attributed to network deformation modes of D and T units [101]. Respect to samples D/T_L-1 and D/T_L-2 presented in the previous chapter, this NBB shows more signals in the higher frequencies range of the 500-150 cm^{-1} range (Fig. 55). Especially the large signal around 407 cm^{-1} can be associated with T₈ cube-like species [124], whereas the broad peak around 555 cm^{-1} , can be

attributed to cyclic species arranged in ladder-like products such as four fold siloxane rings [144].

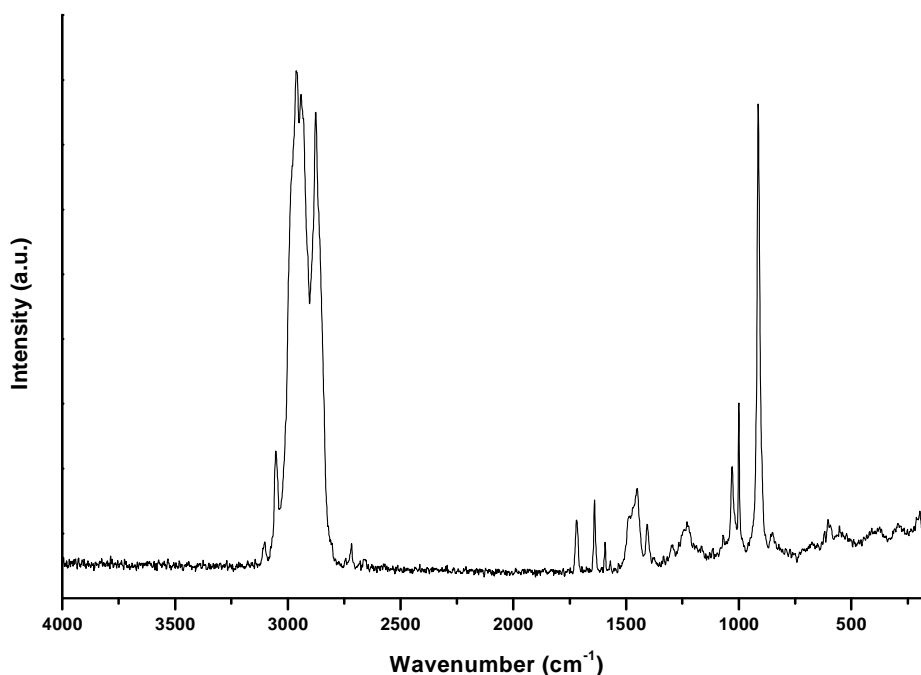
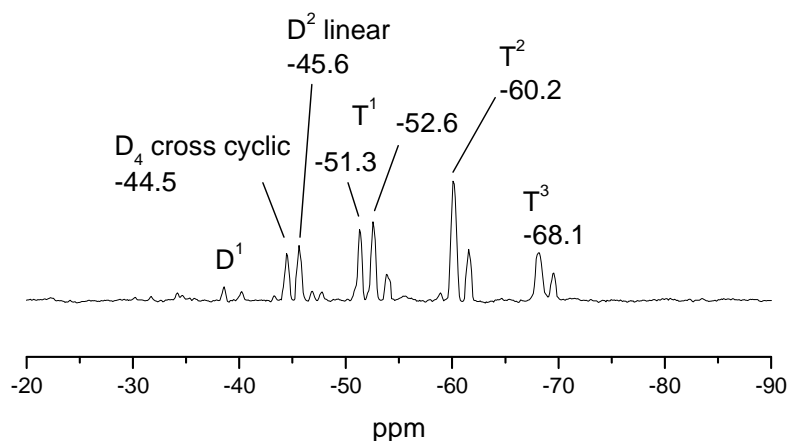


Fig. 55: Raman spectrum of D/T_H-1

5.4.2 NMR spectroscopy characterisation

5.4.2.1 ²⁹Si NMR

The ²⁹Si NMR spectrum of D/T_H-1 shows a small peak at -38 ppm (D¹), in the D-type region signals at -44.5 ppm attributed to D₄ cross cyclic products whereas at -45.6 ppm signals correspond to linear D² species. In the T-type region signals are found at -51.3 (T¹) and -52.6 ppm (T¹), at -60.2 T² and in the range -68.1÷-70 ppm due to T³ species. The ratio between T¹:T²:T³ species is 3:3:1. The homo-condensation of DPDO is not taken into account because of the steric hindrance of the phenyl ring [156 a,b], and the absence of the peak at -41.4 ppm due to D₄ homo-condensed species confirms this hypothesis. Finally no unreacted precursors are present in the final sample (no D⁰ or T⁰ signals).

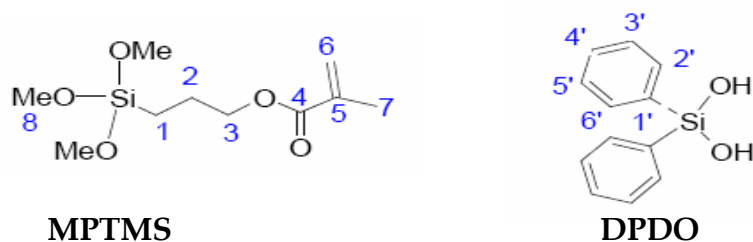
Fig. 56: ^{29}Si spectrum of D/ $\text{T}_{\text{H}}-1$

➤ D/ $\text{T}_{\text{H}}-4$

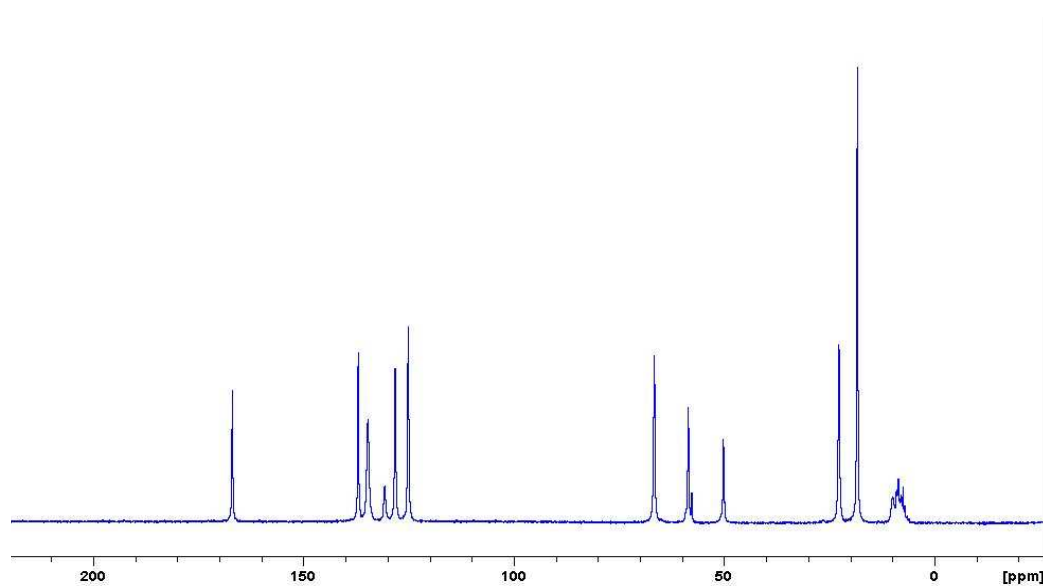
The ^{29}Si NMR spectrum shows a small peak at -39.9 ppm (D^1), whereas the main peak situated in the D-type region at -42.6 ppm can be attributed to D_4 homo cyclic. The resonance at -43.7 ppm corresponds to D^2 cross cyclic species correlated both with T^2 and T^3 species. In the T-type region the signals are low in intensity and are found at -50.7 ppm (T^2) and at -58.8 ppm (T^3). The quality of the spectrum is quite bad with a low S/N ratio, and it does not allow to correctly estimate the ratio between different Si units.

5.4.2.2 ^{13}C NMR

Carbon numbering is reported in Fig. 57 for MPTMS and DPDO precursors, and the chemical shift and the assignments are listed in Table 18.

Fig. 57: ^{13}C NMR quotation of carbons in MPTMS and DPDO

Carbon	1	2	3	4	5	6	7	8	1'	2'-6'	3'-5'	4'
MPTMS, ppm	10	25	67	167	137	125	18	51				
DPDO, ppm									131	134- 135	130- 128	124

Table 18: ^{13}C chemical shifts and signals assignments for MPTMS and DPDOFig. 58: ^{13}C spectrum of NBB D/ $T_{\text{H-1}}$

The ^{13}C NMR spectrum of D/ $T_{\text{H-1}}$ is shown in Fig. 58. The peaks at 58.78 and 18.62 ppm, attributed to ethoxy groups, and the residual peak at 50.43 ppm related to the unreacted methoxides indicates that an exchange reaction between MeO- groups of MPTMS and EtO- groups of the solvent (EtOH) occurred.

The presence of different OR groups linked to silicon is also confirmed by the splitting of the carbon quoted 1 (Fig. 57) in the 6-10 ppm range. Both homo and cross-condensation between the two precursors took place with the formation of Si-O-Si bonds, according to the resonances at 10 and 25 ppm (1 and 2 in MPTMS in Table 18) and to the signal for C quoted 2' and

6' (135 and 134 ppm respectively) in the above image of DPDO. The signals of the methacrylate function appear almost unaffected by the condensation reaction

Carbon	1	2	3	4	5	6	7	8	1'	2'-6'	3'-5'	4'
MPTMS, ppm	10	25	67	167	137	125	18	51				
DPDO, ppm									131	134- 135	130- 128	124

5.4.2.3 ^1H NMR

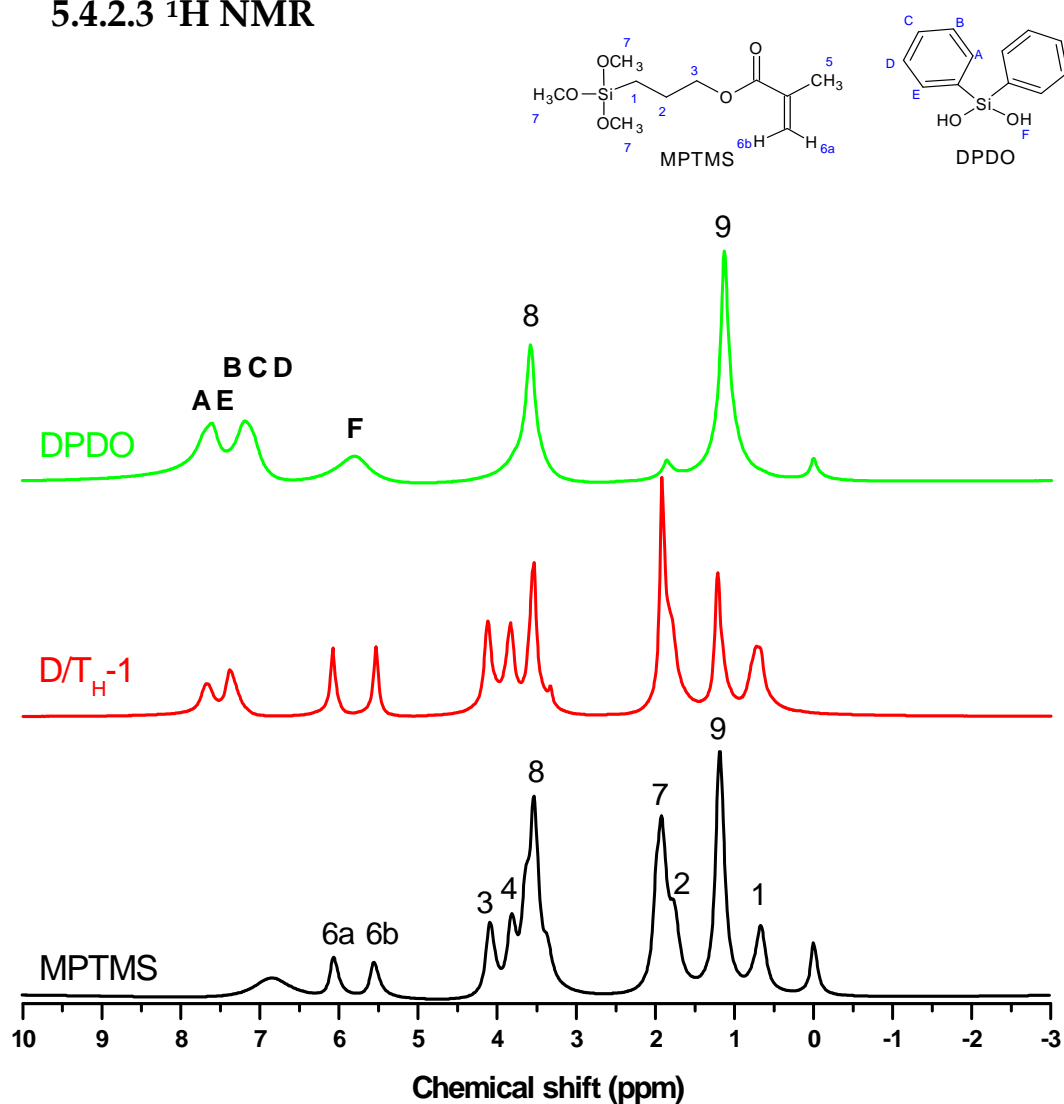


Fig. 59: ^1H spectra of precursors (DPDO and MPTMS) and D/T_H-1

The ^1H spectrum of the final product D/T_H-1 is compared in Fig. 59 with the precursors spectra, and shows all the resonances of the phenyl protons (A-E) of DPDO and of MPTMS skeleton ($-\text{CH}_2-$). The peaks at 3.64 and 1.32 ppm (8 and 9 respectively) are attributed to the presence of EtO- groups linked to silicon, whereas the peak at 2.01 is due to the residual methoxides, in agreement with ^{13}C results.

The broadening of peak quoted 1 is due to the group exchange reaction between precursor and solvent.

The peaks marked with an asterisk in the ^1H spectra of DPDO are due to the solvent used to dilute the pure precursor .

5.4.3 Gel Permeation Chromatography (GPC)

Precursors characterisation

Precursor	Retention Volume (mL)
DPDO	23.74
MPTMS	28.87
GLYMO	24.64
Cl-AcA	26,39

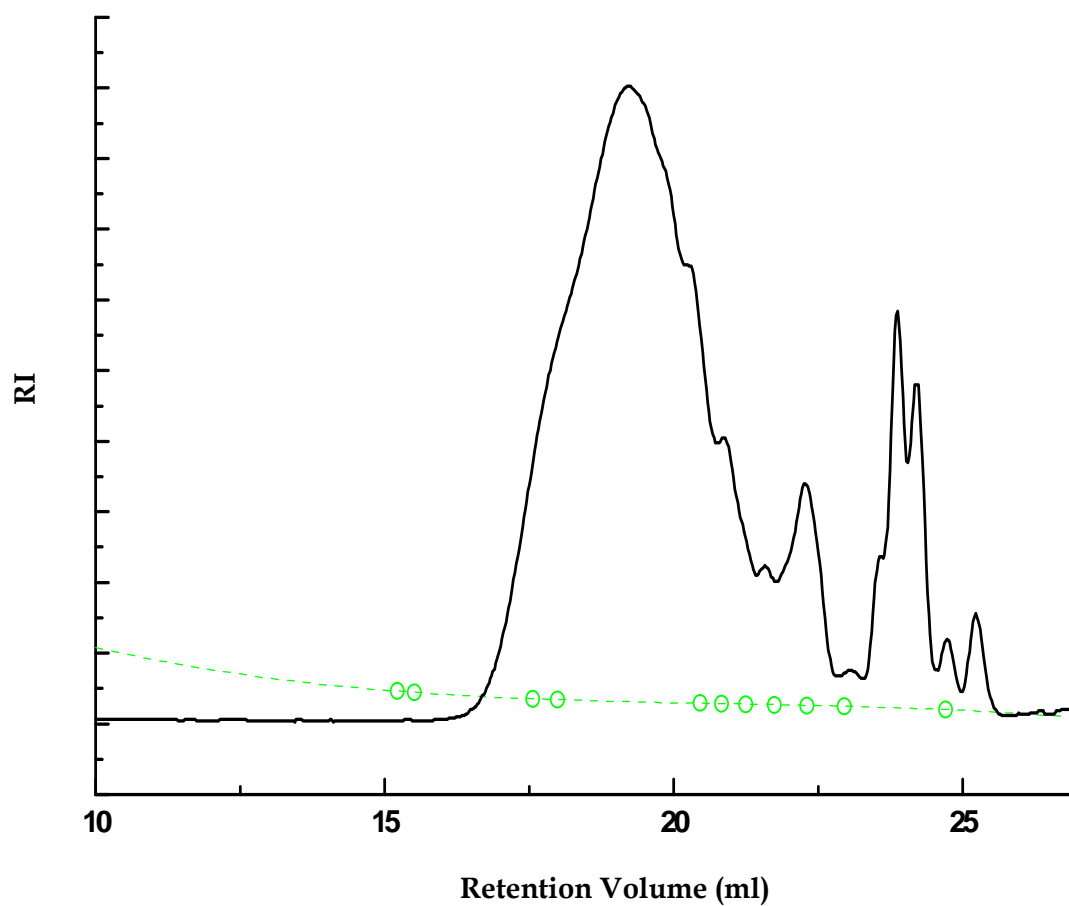
Table 19: Rv of precursors for D/T_H NBBs

5.4.3.1 Samples characterisation

The GPC diagram recorded on D/T_H-1 (Fig. 60) shows a main broad signal centred at Mw 1525, which can be attributed to a heptamer in a cage like structure and small contributions due to dimers (Mw 454, 386).

Data obtained are listed in Table 20.

Rv	Mw	%
19.51	1,523	74.6
21.87	454	3.0
22.34	386	3.2
23.65	280	6.5
23.99	246	12.7

Table 20: GPC results (Rt, Mw and percentage) for D/T_H-1Fig. 60: GPC curve of D/T_H-1 sample and calibration curve (dashed)

➤ ACID SERIES (D/T_H-3(A-H))

The GPC traces of reagents and D/T_H-3(A-H) are shown in Fig. 61. Due to solubility problems, samples D/T_H-3D and D/T_H-3E could not be analysed.

The negative peaks are markers called “reference peaks”, generally referred to the solvent. They are used to control the correct superimposition of all the chromatograms. Data collected from GPC curves are listed in the next tables.

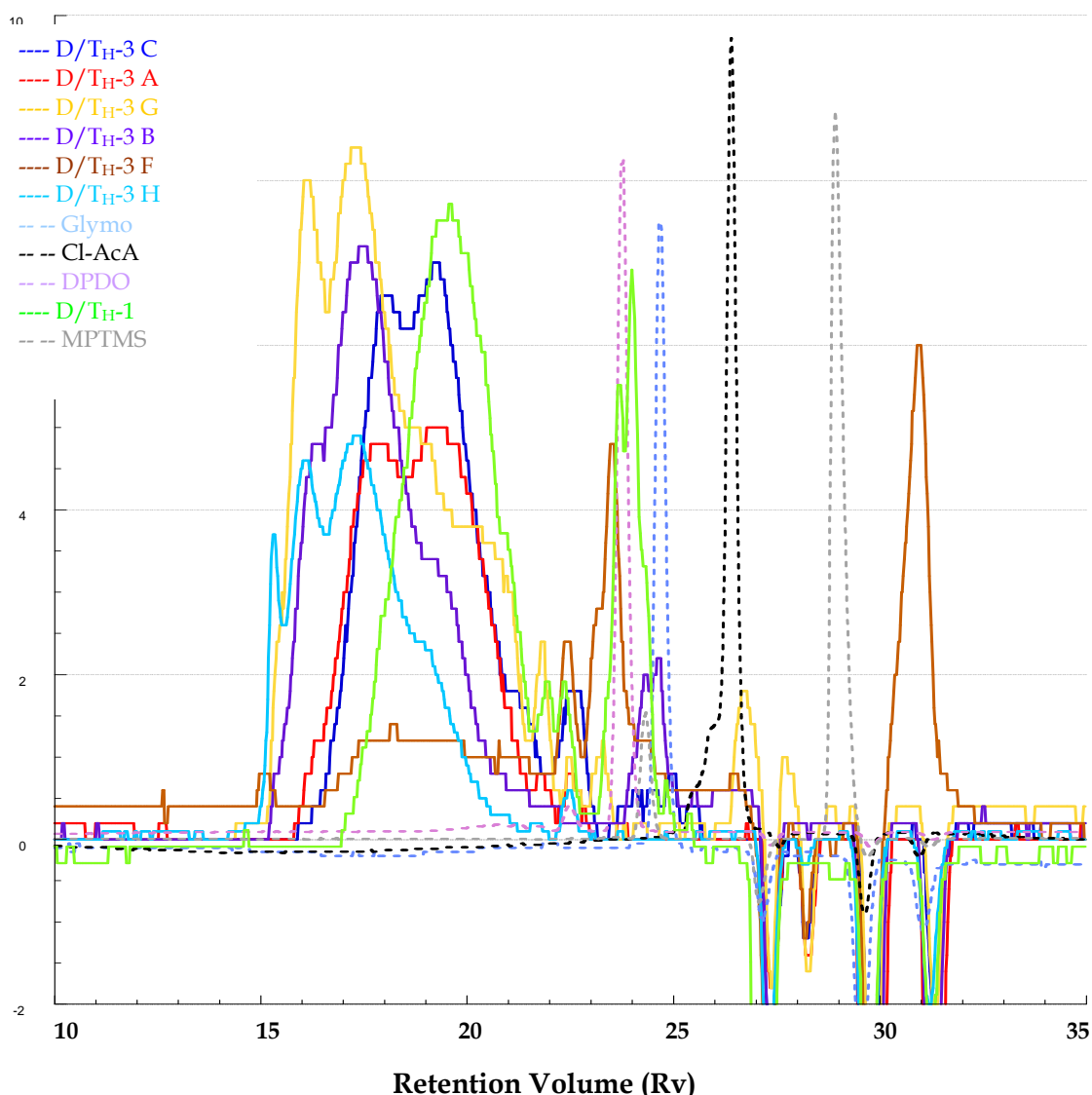


Fig. 61: GPC curves of precursors and (D/T_H-3(A-H)) samples

D/T_H-3A

Rv	Mw	%
17,856	2589	33,0
19,104	1251	61,6
21,808	506	3,0
22,500	382	2,4

D/T_H-3B

Rv	Mw	%
15,089	53103	2,0
18,251	2318	36,9
21,117	654	5,9
22,452	390	11,7
23,545	228	43,5

D/T_H-3C

Rv	Mw	%
18,103	2120	31,3
19,239	1238	56,5
21,117	650	7,8
22,549	374	4,4

D/T_H-3F

Rv	Mw	%
16,064	17120	24,7
17,312	4465	43,2
18,563	1567	16,9
20,326	876	10,7
21,828	531	3,2
23,247	292	1,3

D/T_H-3G

Rv	Mw	%
16,244	16706	18,05
17,460	3977	52,8
19,014	1214	18,15
24,328	168	3,1
24,688	135	7,8

D/T_H-3H

Rv	Mw	%
15,280	39418	8,3
16,087	17134	32,5
17,325	4268	49,4
19,041	1509	7,6
20,725	723	0,9
22,504	405	1,4

It is possible to distinguish five groups of peaks: around Rv (retention volume) 15, 16, 17, 18, 20, plus two small shoulders at Rv 19 and 20.

The reaction in D/T_H-3G is not completed, since unreacted DPDO is detected (Fig. 61 and Table 19).

Exception made for sample D/T_H-3F (citric acid), the peaks of which are broad and quite flat, all the other samples are characterised by two main sharp peaks. Formic (D/T_H-3C) and propionic acid (D/T_H-3A) present peaks at similar Rv (18.1/19.2 and 17.9/19.1) with similar proportions (see tables above). The other acids, which have a lower pK, lead to products with higher Mw.

Samples D/T_H-3F (citric acid), D/T_H-3G (salicylic acid) and D/T_H-3G (chloroacetic acid) can also be grouped: they have similar chromatograms,

consequence of the influence of the low pK. These acids increase the condensation rate but also favour the not negligible formation (8.3%) of species with high Mw that are probably complex network-like structures.

Respect to sample D/T_H-1 these products present more distinct and sharper peaks, indicative of a narrow distribution of oligomers, and there is not the residual presence of DPDO, which on the contrary is detected in GPC analysis of D/T_H-1, in accordance to ²⁹Si NMR data (Fig. 60).

GPC traces of D/T_H-3A-C show peaks similar to those found in D/T_H-1, indicating that acids with pK higher than 3.5 favours the production of low Mw species.

➤ D/T_H-4

Rv	Mw	%
15.19	45,340	35.7
15.77	16,857	13.3
17.15	5,383	14.3
19.56	1,736	11.6
20.03	934	12.2
22.26	383	9.4
24.06	245	2.7
24.71	186	0.8

Table 21: GPC results (Mw and percentage) for D/T_H-4

The GPC analysis (Fig. 62) leads to the same conclusions derived from the analysis of FT-IR spectra (previous paragraph); this synthesis leads to the production of structures that range from tetramers (Mw 934) to more complex cage-like structures (Mw 1,736), which probably corresponds to T₇ or T₈. Mw 5,383 corresponds probably to a trimer of cage

structures connected with linear species. The presence of DPDO together with high quantities of Glymo favours the aggregation between the single units into polymeric structures with high molecular weight (M_w 16,857 and 45,340) [115].

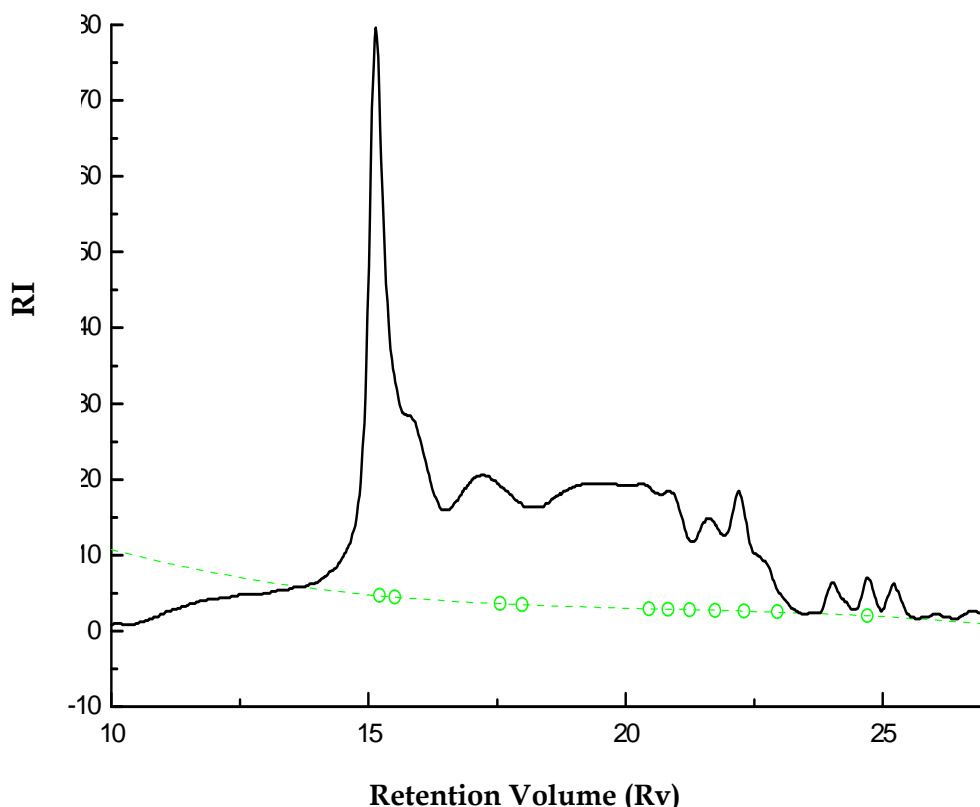


Fig. 62: GPC curves of D/T_H-4

5.4.4 DSC measurements

DSC measurements have been performed in order to study the thermal polymerization process of the samples and the availability of the reactive organic functions on the NBBs.

Matrices were prepared as reported for low trifunctional loaded NBBs (D/T_L) (paragraph 5.2.6), with the following ratio:



A thermal catalyst (BPO) was added in amount equivalent to the 2% molar of the acrylic groups. Ultrasound bath was used for 10 minutes to allow the dispersion of BPO powders in the matrix. The viscous solution was left dry at air in dark conditions for 24 h.

The obtained matrices were analysed without further treatment.

The data of ΔH (J/g), calculated from the polymerization peak in DSC curves are reported in Table 22.

Matrix	Methacrylate precursor	Acid (pK)	ΔH(J/g)
MZrMA	MPTMS	-	8
D/T _H -1ZrMA	D/T _H -1	AcA (4.76)	150
D/T _H -3AZrMA	D/T _H -3A	PA (4.87)	148
D/T _H -3BZrMA	D/T _H -3B	AA (4.10)	58
D/T _H -3CZrMA	D/T _H -3C	FA (3.75)	102
D/T _H -3DZrMA	D/T _H -3D	TGA (3.73)	-
D/T _H -3EZrMA	D/T _H -3E	ASA (3.5)	-
D/T _H -3FZrMA	D/T _H -3F	CA (3.13)	129
D/T _H -3GZrMA	D/T _H -3G	SA (2.97)	151
D/T _H -3HZrMA	D/T _H -3H	Cl-AcA (2.87)	179
MZrMAMon	MPTMS+triacylate monomer		352

Table 22: DSC characteristic data of acid series derived hybrid matrices

Unfortunately two samples were not enough soluble in the solvent used and homogeneous matrices could not be prepared.

Roughly, the polymerisation heat follows a trend of ΔH increase with pK decrease (except for acetic and propionic acid).

5.5 Self-condensation derived NBB

Materials

Glycidoxypropyltrimethoxysilane (Glymo)

Ethanol (EtOH)

Chloroacetic Acid (Cl-AcA) Aldrich

5.5.1 Performed syntheses

The conclusions of the study on the syntheses of DPDO / Glymo NBBs show that in all cases the use of DPDO with Glymo leads to the formation of high Mw species. This result is in perfect agreement with results recently reported in the literature [157]. Thus, the preparation of NBB by the *ISWP* process, starting from the single Glymo precursor, was investigated. The samples discussed in this paragraph are listed in the following table. As for the previous samples (D/T_L and D/T_H) reaction parameters are selected on the basis of previous results (Appendix C).

Label	R-Si(OCH ₃) ₃ (T)	Solvent (S)	S:D	Cat.	Temp
G _S -1	Glymo	EtOH	8:1	Cl-AcA (1%[Si])	70°C
G _S -2	Glymo	EtOH	8:1	Cl-AcA (1%[Si])	RT

Table 23: self condensation derived NBBs (G_S)

5.5.2 Synthesis and procedure

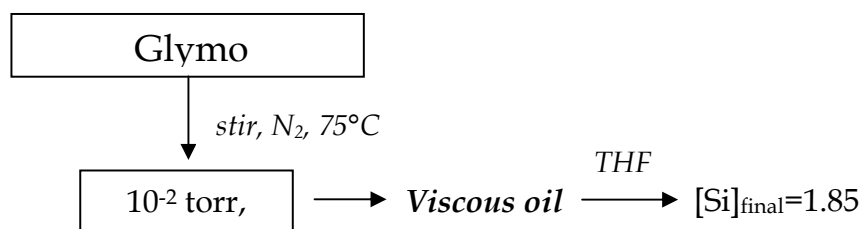


Fig. 63: general reaction scheme for self condensation NBBs - G_S

The complete synthesis procedures are exposed in Appendix A (synthesis 6 and 7).

5.5.3 FT-IR characterisation of the precursors

Since the kinetic of the *ISWP* reaction with acetic acid as condensation promoter was too much slow, chloroacetic acid (Cl-AcA) was used for Gs synthesis, taking into account the results obtained from the study of acid series performed on MPTMS derived NBBs. The influence of temperature on the reaction rate was also studied.

Glymo and ethanol FT-IR spectra and signal assignments can be found respectively at pag. 68 and 100.

Cl-AcA

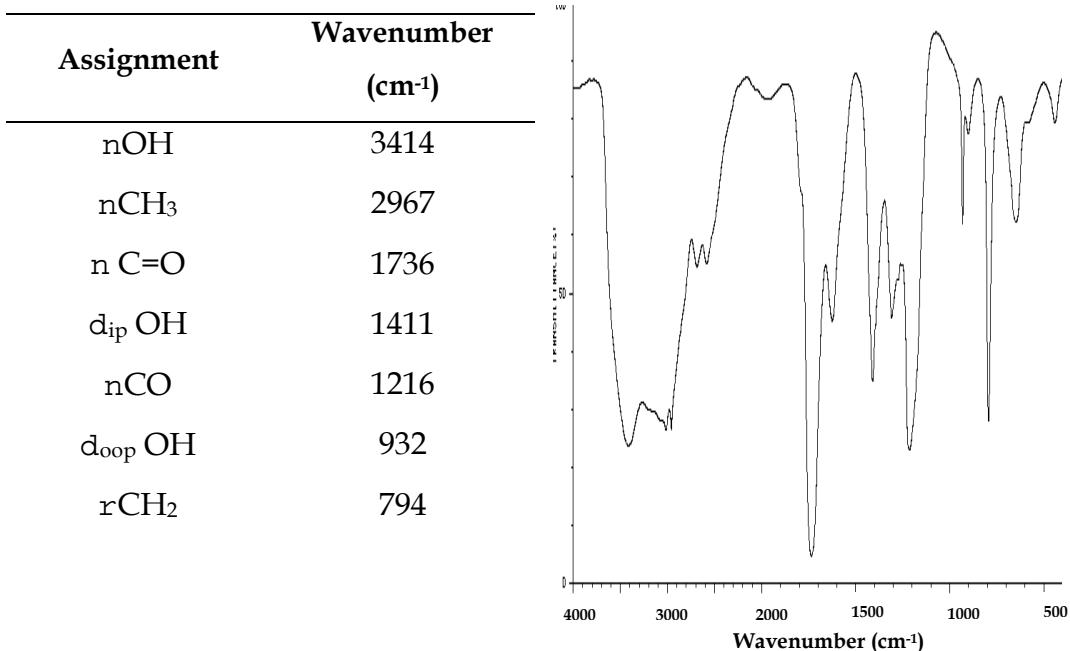


Table 24: FT-IR characteristic vibrations of chloroacetic acid and spectrum [152]

G_S samples characterisation

The evolution of FTIR spectra of the two samples as function of reaction time was studied in the range between 4000 and 400 cm⁻¹.

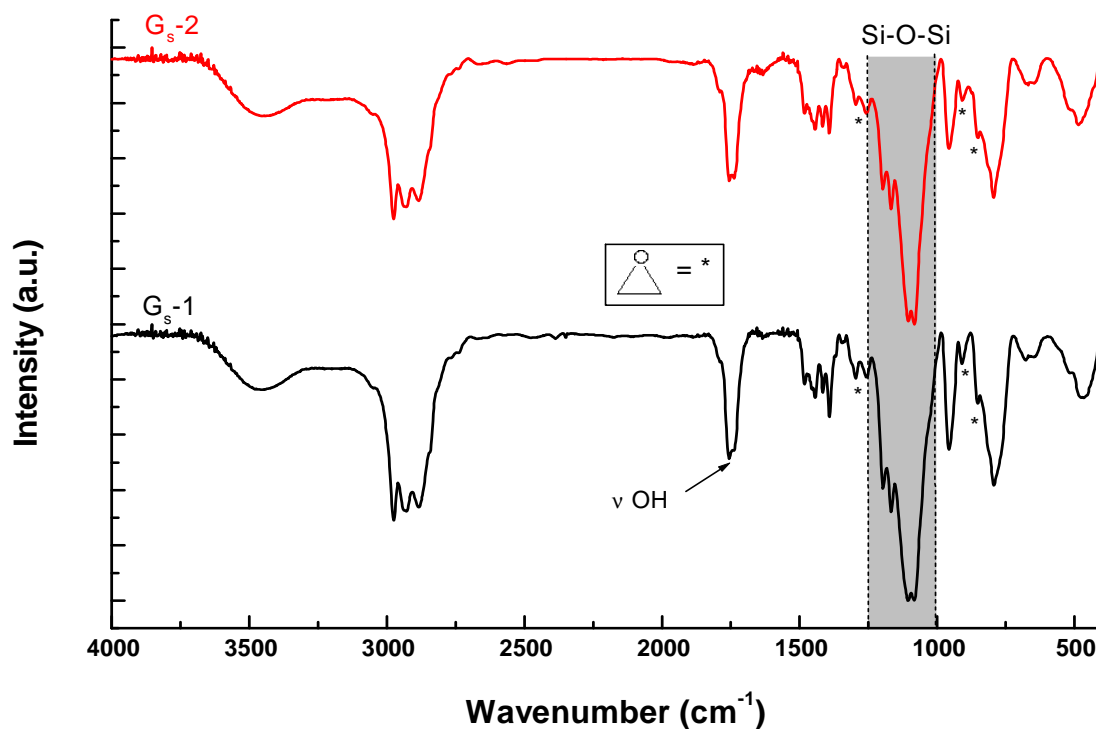


Fig. 64: FT-IR spectrum of G_S-1 and G_S-2

Assignments	Wavenumber (cm ⁻¹)
νOH	3450 (b)
ν _{as} CH ₂ (epoxy ring)	3049 (w)
ν _{as} CH [CH ₃]	2943 (st)
νC=O	1756 (st)
νC=O	1731 (w)
δ _{ip} CH ₂	1467 (w)
ν _s epoxy ring	1253 (w)
ν _{as} epoxy ring	911 (m)
δ epoxy ring	857 (w)
ν Si-C	1166 (w)

Table 25: characteristic vibrations of G_S-1 and assignments

Assignments	Wavenumber (cm ⁻¹)
vOH	3450 (b)
v _{as} CH ₂ (epoxy ring)	3049 (w)
v _{as} CH [CH ₃]	2943 (st)
v _s CH [CH ₃]	2841 (w)
vC=O	1752 (st)
vC=O	1732 (w)
δ _{ip} CH ₂	1467 (w)
v _s epoxy ring	1256 (w)
v _{as} epoxy ring	912 (m)
δ epoxy ring	855 (w)
v Si-C	1166 (w)

Table 26: characteristic vibrations of G_S-2 and assignments

The two spectra in Fig. 64, are very similar, but the use of a higher temperature (G_S-2) lead to the reaction completion in 1 h instead of 3 days (G_S-1).

The disappearance of the signal attributed to the stretching vibration of MeO- groups suggests that the hydrolysis has occurred in a good extent. The sharp peaks, in the 1200–1000 cm⁻¹ range due to the siloxane bridges (SiOSi), are attributable to mainly cyclic products (1103 and 1082 cm⁻¹). The presence of a medium intensity peak at 1165 cm⁻¹ is probably attributable to the presence of EtO groups linked to the silicon centre as a consequence of transesterification reactions occurred between methoxy groups of the precursor and ethoxy functions derived from the alcohol, but the signal could be overlapped with the band due to the stretching vibrations of siloxanes in branched or ladder like polymers [143], as there is also a small shoulder at 1024 cm⁻¹ (G_S-1, Fig. 64). This hypothesis is confirmed by the peak present only at 575 cm⁻¹ in the sample prepared at

70°C (G_S-1) which, according to Yoshino et al. [144] is related to the presence of cyclic species typical of ladder like products as 4-fold siloxane rings.

5.5.4 NMR characterisation

5.5.4.1 ²⁹Si NMR

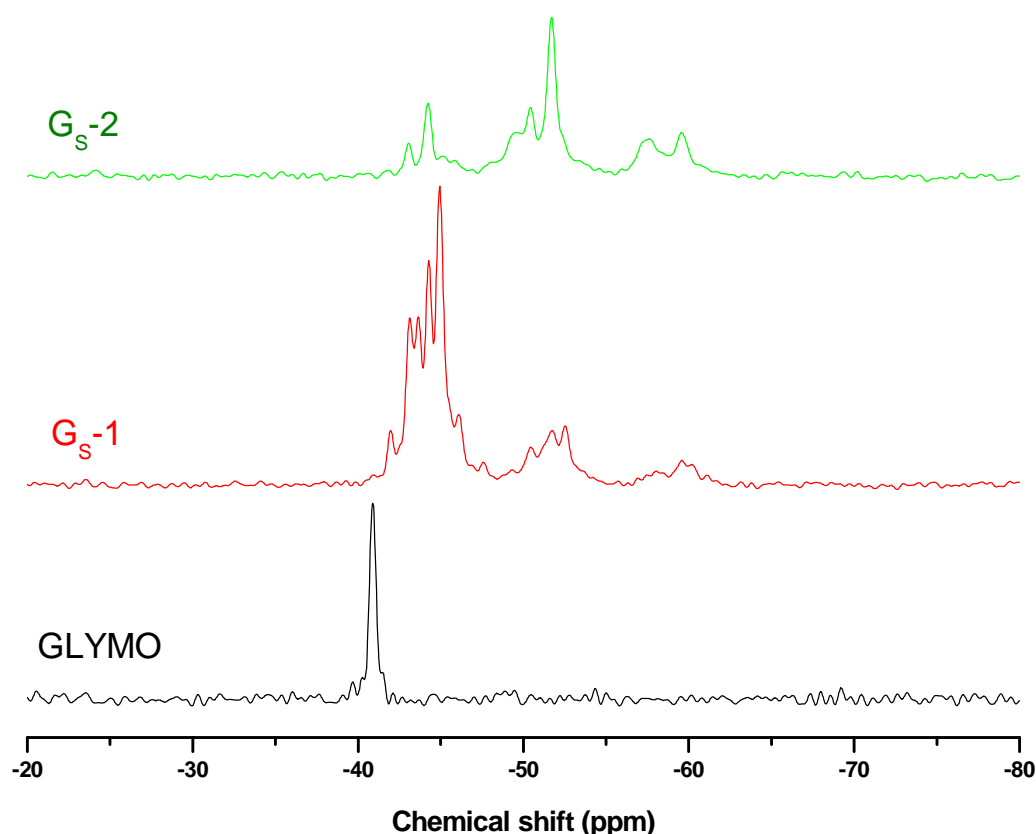


Fig. 65: ²⁹Si spectra of G_S-1, G_S-2 and precursor (Glymo)

The spectra indicate a small presence of T³ units only in high temperature synthesised sample (Fig. 65 and Table 27), which means poor condensation. MeO groups are replaced by EtO groups due to exchange reaction with the solvent as already noticed by FT-IR; this is further proved by the ¹³C spectra discussed in the following paragraph [158]. The final product is a mixture of monomers with different substituents and

without the unreacted precursor. T¹ and T² units and some highly constrained cyclic species, as presented in Table 27 [159, 160].

$\delta(\text{ppm})$	assignment	G _S -1	G _S -2
-43.26	T ⁰ (2Me,1Et)	3.8	nd
-44.36	T ⁰ (1Me,2Et)	15.1	4.1
-44.90	T ⁰ (0Me,3Et)	10.6	nd
-45.50		14.7	11.6
-46.16		18.1	1.7
-47.31	T ² cyclo hydroproduct	9.8	1.6
-48.84	T ² cyclo (7)	3.7	0
-50.56	T ² cyclo	0	15.3
-51.68	T ¹ (2Me,0Et)	5.5	14.5
-52.99	T ¹ (1Me,1Et)	7.8	26.1
-53.75	T ¹ (0Me,2Et)	5.3	nd
-58.88	T ² (1Me,0Et)	1.9	13.7
-61.06	T ² (1Me,0Et)	3.9	11.6
-70.77	T ³	0.95	nd

Table 27: ²⁹Si NMR assignments of G_S samples

The resonances from -45.50 to -48.84 can be attributed to T² cyclic structures with less than 8 members, as the high strained bond angles induce relevant downfield shifts as proposed by Myers et al. [160]

The reaction temperature influences the final products: in NBB G_S-1 (heated) the formation of cyclic species is more favoured than in sample G_S-2 (RT), which is characterised by a higher amount of T¹ units and T² linear species.

5.5.4.2 ^{13}C NMR

The carbon quotation for Glymo and chloroacetic acid is shown in Fig. 66



Fig. 66: carbon quotation for Glymo and chloroacetic acid

Both samples present residual MeO groups, but the hydrolysis extent is higher in G_S-2 respect to G_S-1 sample (Fig. 67).

The epoxy ring is almost stable and only about the 15% of the epoxy function undergoes to ring opening, leading to the formation of alkoxyalcohol and polyether products. The formation of diols is unfavourable since the water is present in the reaction medium in small amount. Indeed, diols are not detected in the spectra (Fig. 67).

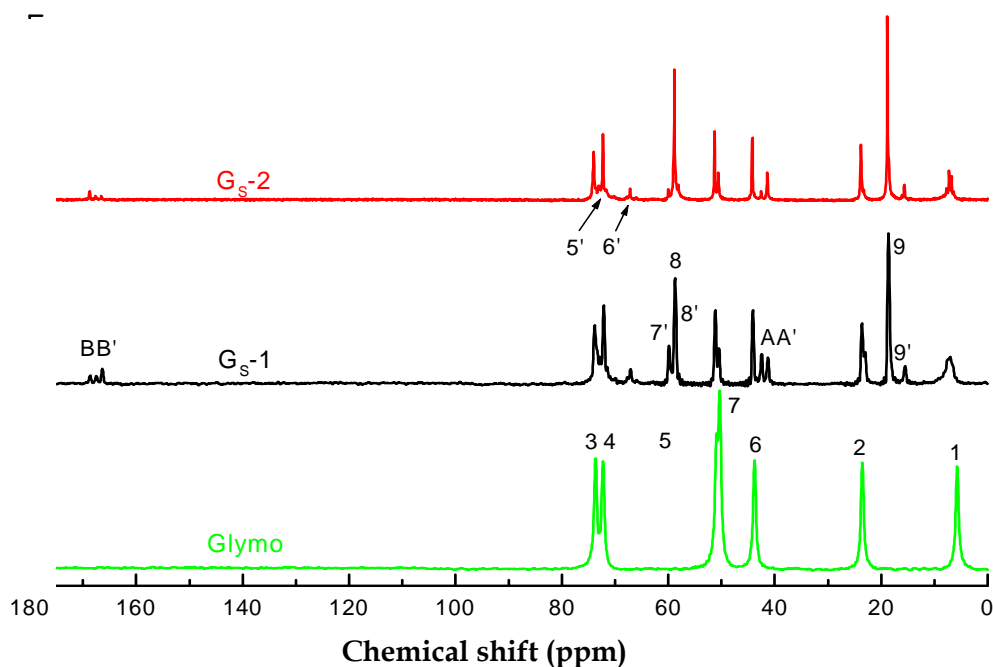


Fig. 67: ^{13}C Spectra of G_S-1 G_S-2 NBB and Glymo

The ring opening is proved by the formation of the peaks at 72.6 and 71 ppm, moreover the resonance at 59.87 ppm can be attributed to methylether carbon ($\delta = \text{C-OCH}_3$) and to the ethyl ether carbons at 15.52 ($\delta' = \text{C-OCH}_2\text{CH}_3$) and 58.74 ppm ($\delta' = \text{C-OCH}_2\text{CH}_3$).

In G_S-1 few residual chloroacetic acid is present in the final sample, the most of the acid reacted with ethanol to form the ester, visible from the splitting of the signal of the carbonyl group (also present in the FT-IR spectra) and the new peaks at 42.6 ppm ($\underline{\text{C}}\text{H}_2$) and 167 ppm ($\underline{\text{C}}\text{OO}$) respectively. On the other hand NBB G_S-2 does not show the peaks due to carbons labelled A and B in Fig. 66 and belonging to chloroacetic acid.

A control of the assignments was made by checking the DEPT ¹³C spectrum (CH and CH₃ are positive, CH₂ are negative, quaternary C are zeroed, see Fig. 68).

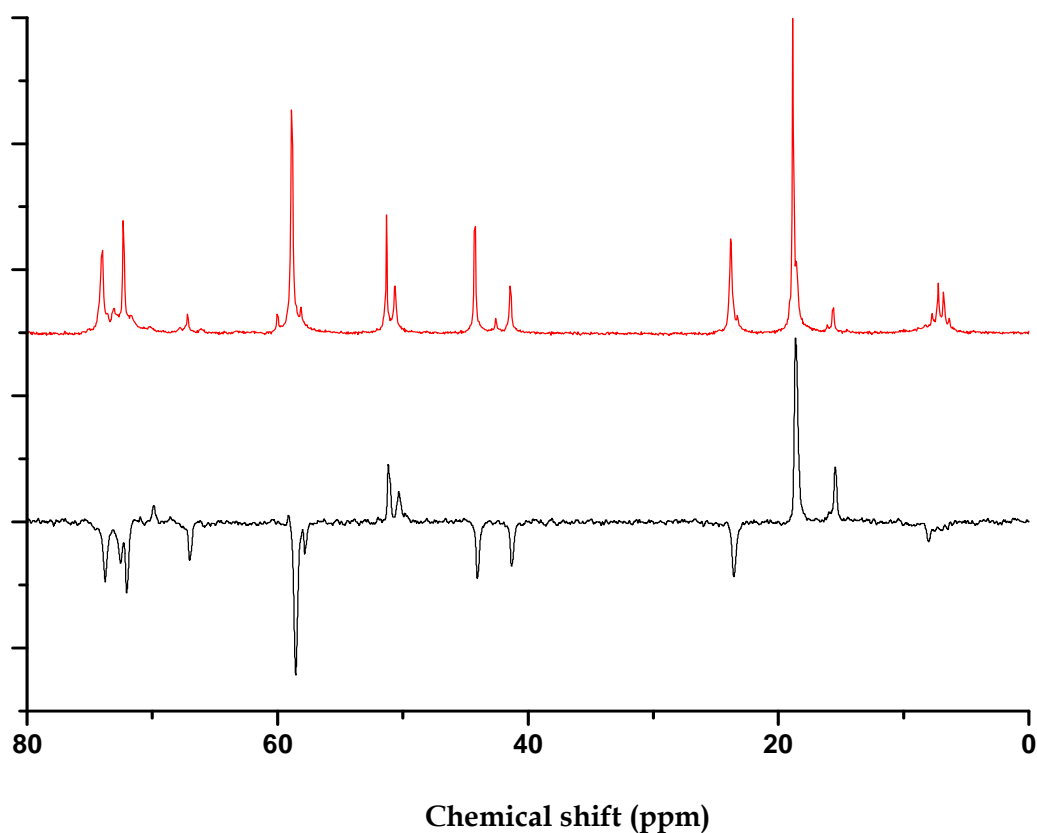
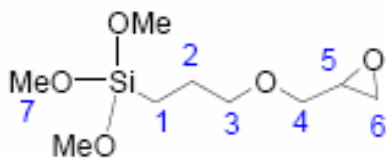


Fig. 68: DEPT ¹³C of sample G_S-1

5.5.5 ^1H NMR

Precursor



proton	1	2	3	4	5	6	7	8	9
ppm	0.3	0.8	3.10	3.8	2.70	2.55	3.80	3.75	1.1

(8')

3.65

Fig. 69: proton assignments for Glymo

Proton spectra confirm the results obtained from ^{13}C experiments. Both samples show (Fig. 70) the presence of silanols (4.5 ppm), together with the reduction of the signal due to the methoxy protons (7 in Fig. 66) ($-\text{OCH}_3$). The reduction in the signal is due both to hydrolysis and transesterification with ethanol. The exchange product is proved by the appearance of new peaks at 3.5 and 1.21 ppm, [161]. The ethoxy groups, which substitute the methoxides linked to the silicon, can react in minor extent with the opened ring.

There is a small shift of the resonances attributed to the partial ring opening (as already stated in ^{13}C spectra) in the region around 3.5 ppm, attributed to the protons quoted 4', 5', 6' in the spectra.

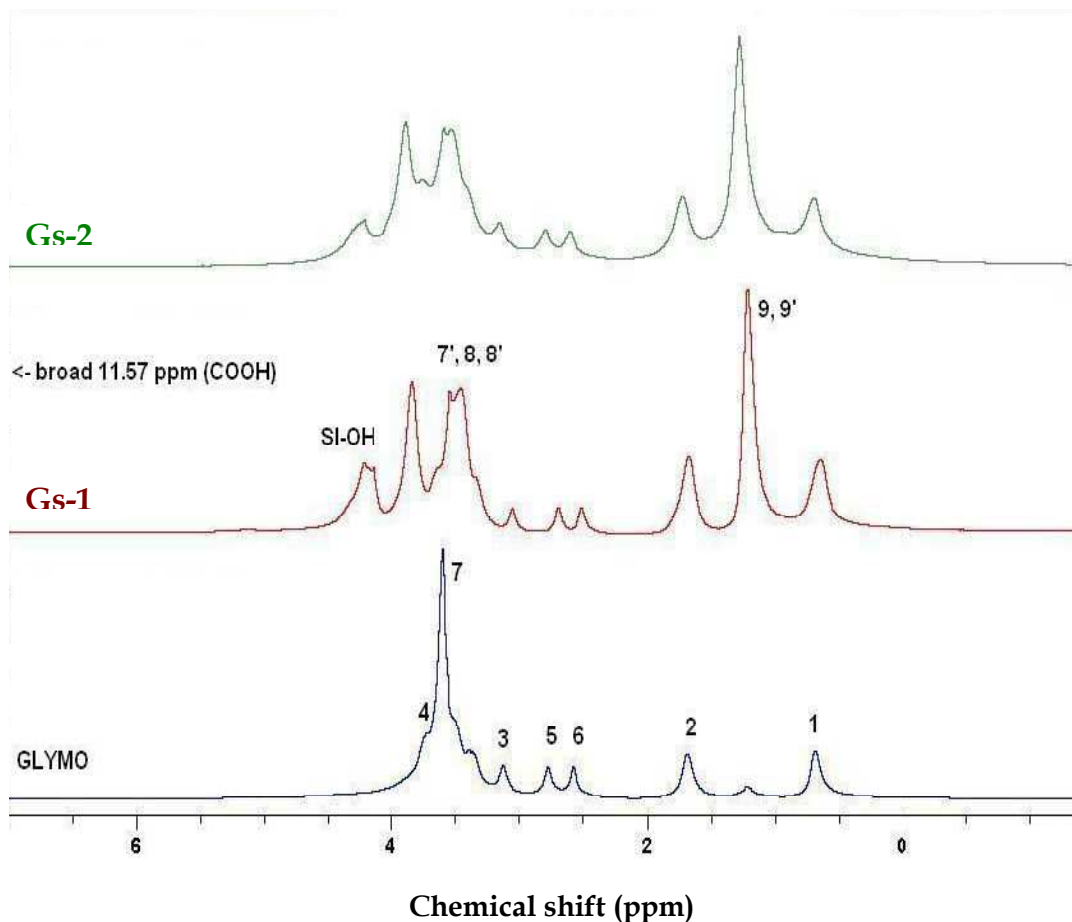


Fig. 70: ^1H NMR spectra of self-condensation derived NBB (G_S) and precursor (Glymo)

5.5.6 GPC measurements

The samples prepared at different temperatures show similar chromatograms.

However, the differences are visible looking at the tables in which R_v are listed (Table 28). Sample G_{S-2} prepared at RT leads to a large number of products with respect to the one synthesised at high temperature (G_{S-1}). Probably this is caused by the tendency of oligomers to aggregate in bigger structures when reaction is carried out at high temperature.

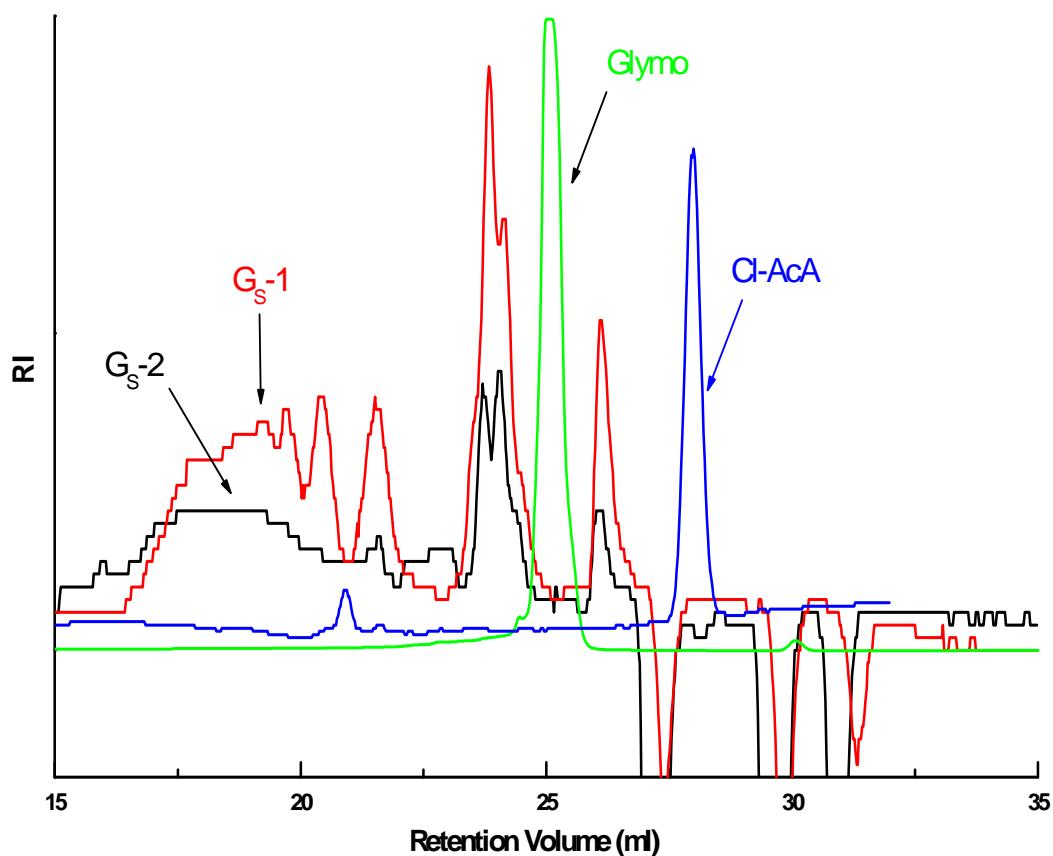


Fig. 71: GPC curves of GS-NBBs , Glymo and AcA

G _S -1			G _S -2		
Rv	Mw	%	Rv	Mw	%
16.01	15,787	5.6	17.78	3,979	15.6
17.57	4,879	37.6	19.22	1,624	14.2
21.65	583	2.9	19.69	1,120	7.5
23.70	228	47.0	20.39	879	9.9
23.92	182	5.9	21.49	561	12.7
25.18	74	1.0	23.81	225	15.5
			24.15	145	13.0
			26.08	32	11.7

Table 28: GPC Rv and associated Mw for GS-NBB

There is still the presence of small cyclic structures, confirming FT-IR and ^{29}Si NMR results, and probably some open cages (i.e. $\text{T}_7(\text{OH})_3$) due to the interaction of open chain trisiloxanes with $\text{T}_4(\text{OH})_4$ units.

The presence of small molecules, as oligomers, is confirmed by the presence of low Mw products. High Mw species are due to the aggregation of the small species in long polymer like structures forming a complex network.

STRUCTURAL CHARACTERIZATION of D/T_H NBB

ISWP was found to be an efficient route to produce nanostructured units starting from DPDO and MPTMS or Glymo.

For MPTMS derived samples, the water production kinetic is strictly dependent on the choice of the alcohol/carboxylic acid mixture. Substitution of ethanol with long or bulky carbon chain bearing alcohols (alcohol series) leads to a minor extent of hydrolysis, with the presence of residual methoxides confirmed by the intense signal at 2839 cm^{-1} in the FT-IR spectra.

On the other hand, water production appears more efficient using low pK carboxylic acids and in particular heteroatom-substituted acids.

GPC analyses show that acids with high pK lead to products with smaller Mw compared to the products obtained with low pK acids. However the GPC traces present a wide distribution of well defined products, which makes the product prepared with acetic acid (D/T_H-1) more suitable for the preparation of hybrid films as it will be reported in the following chapter.

The *ISWP* approach was demonstrated to be also useful in the preparation of Glymo/DPDO-based samples, leading to an efficient Si-O-Si condensation and the preservation of the reactive functional group.

D/T_H-4 presents structures that range from tetramers (Mw 934) to more complex cage-like structures (Mw 1,736). Complex architecture as cages linked with linear species are also present (Mw 5,383). Unfortunately the presence of the difunctional precursor was proved to favour the aggregation into polymeric structures with high molecular weight (Mw 45,340).

Therefore self-condensation of Glymo precursor was performed with ISWP route and chloroacetic acid was used in order to increase the reaction rate, leading to products with the conservation of the epoxy ring (G_S).

From ²⁹Si NMR analyses the condensation degree was quite low, suggesting the presence of small cycles connected together and linked with linear structures in agreement with FT-IR results.

Temperature was found to have a strong influence on the structure of the reaction products. When reaction was carried out at RT a larger number of products with lower Mw was obtained, on the other hand when reaction was run at high temperature the Mw of the products increased but the number of different products decreased, as revealed by GPC measurements.

G_S-NBB were found suitable for the preparation of patternable matrices

6 APPLICATIONS

The synthesized nanobuilding blocks D/T_H-1 and G_S have been used to prepare patternable hybrid O/I coatings.

O/I hybrid are promising materials for optoelectronic, since the final products can be produced with low cost and using large area printing-like manufacturing techniques. The goals are obtaining both active and passive pattern components (see paragraph 2.2, Introduction) with low manufacturing cost, and improving the imprinting capabilities. Currently, the most common patterning techniques follow the top-down approach, and photolithography [162, 163] and inkjet printing (that will not be discussed in this paragraph) [164] are the most exploited techniques in industry.

Photolithography is very versatile, but the major problem to deal with, is the decreasing feature size (smaller than 50 nm) and geometries required for semiconducting materials. In this case the process results very difficult and expensive. Thus, alternative methods for patterning are required, as the bottom-up approach (exploiting the chemical properties of the components or other directing means to lead the components to self-organise in the desired conformation) or the two photon polymerization technique (TPP).

Patternable coatings were prepared in collaboration with Dr. Giovanna Brusatin and co-workers (Dept. of Mechanical Engineering- Materials Section of the University of Padua) for UV photolithography and with Dr. Roberta Signorini and co-workers (Dept. of Chemical Sciences of the University of Padua) for TPP patterning.

6.1 Lithography

In photolithography, light is used to transfer a pattern from a photomask (mask) to a light-sensitive chemical layer (photo-resist) on a substrate, exploiting the selective exposure to different light sources (UV, X-rays, Ion beam. Only UV light will be discussed in this chapter). Subsequently chemical treatments engrave the exposed pattern into the material underneath the photo-resist.

The main steps in the lithographic process can be resumed in the following points:

1. **Resist deposition** - the precursors solution of a sensitive material (resist) is deposited as a thin uniform layer on a clean substrate (i.e. silicon wafer) by spin coating;
2. **Soft bake** - the layer is baked at low temperature in order to allow the evaporation of residual solvent;
3. **Alignment and exposure** - the exposure to the light source (i.e. UV light) through the mask (composed of transparent and opaque regions) forms a "latent image" in the resist. In the case of the use of an electron beam, no mask is needed since the writing is done directly on the layer;
4. **Post-exposure bake**
5. **Development** - the areas that have (or have not) been exposed are removed by rinsing with an appropriate solvent;
6. **Pattern transfer process** - etching (dry or wet) and lift off
7. **Resist stripping**

Resist or photo-resist in case of optical lithography are generally multicomponent materials based on polymer blends and are divided in two categories depending on the behaviour to exposure:

- **positive** - light exposure leads to chain scission, creating shorter units that can be dissolved and washed away in the development process. The mask, therefore, contains an exact copy of the pattern which is wanted to remain on the wafer;
- **negative** - the light exposure results in cross-linking of polymer chains, allowing the unexposed parts to be washed out. Masks used for negative photoresists, therefore, contain the inverse (or photographic "negative") of the pattern to be transferred

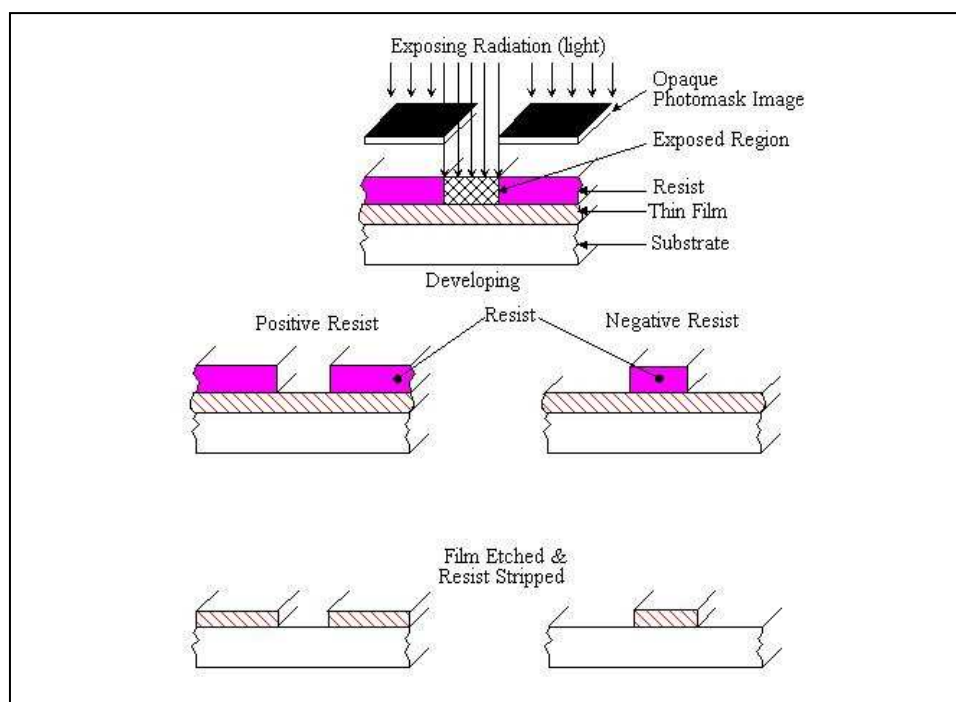


Fig. 72: pattern formation in positive and negative resist [165]

An important parameter influencing pattern quality is the contrast of the resist, which is essential for both resolution and profiles.

The contrast values can be calculated by the contrast curve, which describes the remaining resist fraction of a uniformly illuminated resist versus the logarithm of the applied exposure dose. This is a property of the whole resist process, which means bake time and temperature,

developer normality and time, and determines the performance of the resist.

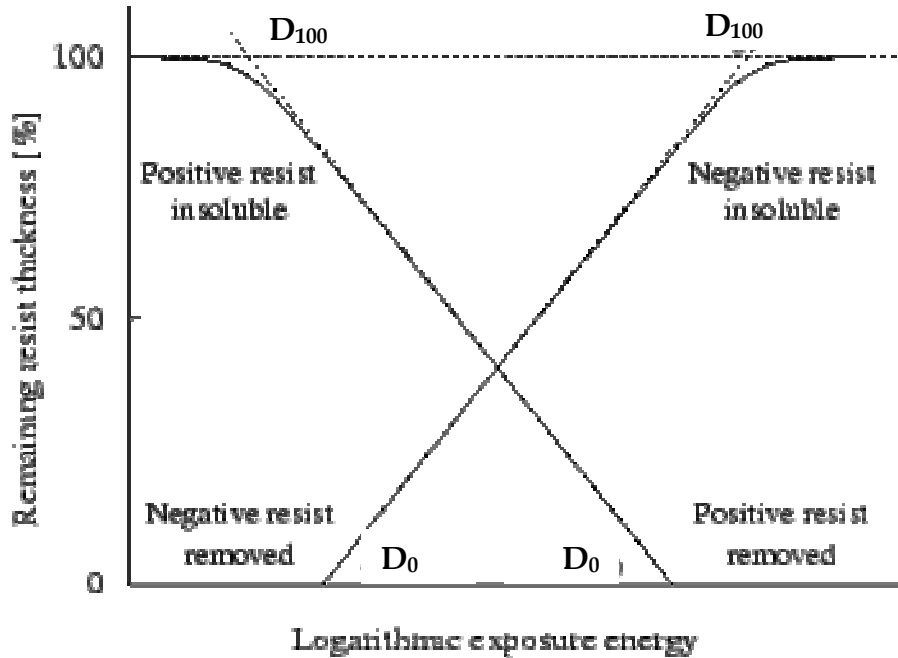


Fig. 73: example of contrast curves (ideal)[166]

Contrast is calculated using expression 1; d_0 is the dose to clear all the resist, whereas d_{100} dose is the extrapolated one at which the film thickness remains unaltered .

$$\gamma = \left[\log\left(\frac{d_0}{d_{100}}\right) \right]^{-1}$$

6.1.1 Optical lithography

Photolithography represents an adaptation of much older photo-based methods in fashion in the late XIX century in the graphic arts. It is the dominant technique among lithographic technologies for patterning integrated circuit (IC). In order to improve production throughputs and to avoid contact-induced damage of the expensive optical mask, projection

mode tools were introduced. At the same time, the improvements in the process resolution enable the manufacture of smaller devices with higher operating speed and the creation of denser circuits in the same chip size.

Traditional “binary intensity” masks (BIMs) consist of opaque chromium lines, which are photo-absorbing, on transparent glass substrates; in these masks the incident light is either blocked or transmitted.

One of the most important steps in the photolithography process is mask alignment. The mask is aligned with the wafer, so that the pattern can be transferred onto the wafer surface. Each mask after the first one must be aligned to the previous pattern.

Once the mask has been accurately aligned with the previous pattern on the wafer’s surface, the photoresist is exposed to a light source (often UV). There are three primary exposure methods: contact, proximity, and projection as illustrates in Fig. 74.

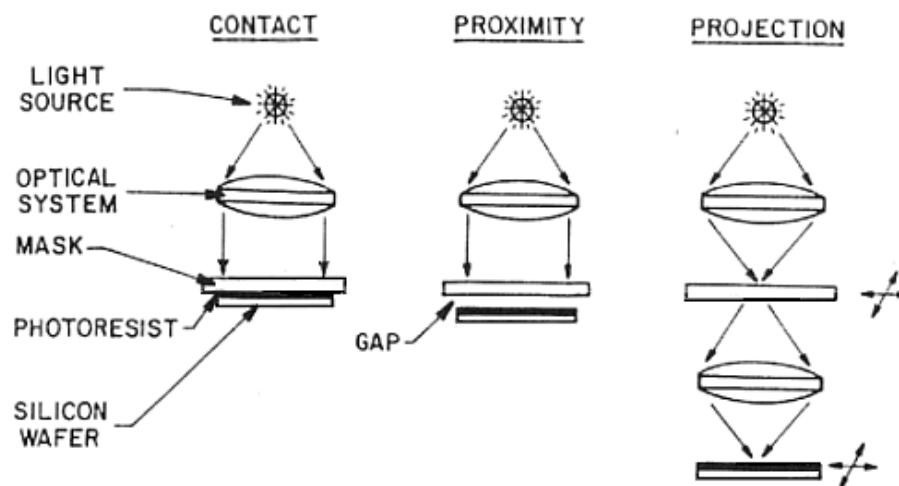


Fig. 74: optical lithography - exposure methods: contact, proximity and projection [167]

➤ CONTACT

This is the simplest technique, wafer coated with the resist and photomask are brought into physical contact. The photoresist is exposed to UV light while the wafer is in contact position with the mask. Because of the contact between the resist and mask, a very high resolution is achievable (i.e. 1 μm features in 0.5 μm of positive resist). The problem with contact printing is that debris, trapped between the resist and the mask, can damage the mask and cause defects in the pattern.

➤ PROXIMITY

This technique was developed in order to reduce the wear of the chromium mask after repeated contact. The wafer is put in close proximity (3 to 50 μm gap) to the mask. Approximately 2 to 4 μm resolution is possible with proximity printing; the resolution estimation can be done using the Fresnel diffraction formula.

In both techniques the image obtained is the same size as the original on the mask. An evolution occurred with the projection mode.

➤ PROJECTION

In this case mask and resist are centimetres away and contact-damage is avoided. An image of the patterns on the mask is projected onto the resist-coated wafer. An optical system (reduction optics) is introduced, which provides an image of the mask on the substrate. Reduction optics reduces (dividing) of a determined number the original image (i.e. x4 means to pass from 1 μm to 0.25 μm). In order to achieve high resolution, only a small portion of the mask is imaged. This small image field is scanned or stepped over the surface of the wafer. Projection printers, which step the mask image over the wafer surface, are called step-and-repeat systems. Masks for step-and-repeat projection printers are called reticles. The

manufacturing of the etched chromium mask exploits this technique in order to reduce the errors.

6.1.2 Resolution

The resolution is the ability to print two close lines, and determines the device density. A line plus space is called half pitch.

It is very difficult to obtain perfectly 90° walls, resists generally have a slight slope (85°-89°), which is the consequence of the light exposure through the mask.

In the case of the projection technique, the ability to project a clear image of a small feature onto the wafer is limited by the wavelength of the light used and the ability of the reduction lens system to capture enough diffraction orders from the illuminated mask.

The minimum resolution is approximated by Rayleigh relations, and is also called minimum feature size or CD (critical dimension):

$$CD = k_1 \frac{\lambda}{NA}$$

where k_1 is a coefficient (k-factor) comprehending process related factors (nowadays is equal to 0.4 in commercial lithography), λ is the wavelength used and NA is the numerical aperture of the imaging system.

According to this equation, half pitch can be decreased by decreasing the wavelength, and increasing the numerical aperture (to achieve a tighter focused beam and a smaller spot size).

6.1.3 Light sources

Until the end of the 1980s, photolithography used UV light from gas-discharge lamps using mercury, sometimes combined with noble gases. These lamps produce a broad spectrum that is filtered to select a single spectral line. First the "g-line" (436 nm) was used, then the "i-line" (365 nm) and finally the radiation at 254 nm.

More recently, lithography has moved to "deep ultraviolet", produced by excimer lasers as krypton fluoride, which produces a 248-nm spectral line, and the more recent argon fluoride excimer laser with the 193-nm line.

Moving to sub 193-nm wavelengths requires to decrease the pressure (vacuum) since the room atmosphere absorbs too much light. These requirements need the consequently rearrangement or new development of resists and reflective optics.

Even though the minimum feature size (CD) is still high with respect to the current technological demand, photolithography is very used in the industrial process for the production of integrated circuits (IC), MEMS devices (Micro-electro-mechanical Systems) [169], sensors, micro-analytical systems.

On the other hand it is not the best technique for non-planar surfaces, it provides almost no control over the surface chemistry and therefore is not suitable to create patterns with specific chemical functionalities (i.e. combinatorial chemistry). Moreover it generally leads to only 2-D microstructures and can exploit only a limited number of photosensitive materials.

6.2 Two Photon Polymerization

Truly 3-D microstructures and devices are attracting the market interest as potential applications in photonic, microelectro-mechanical systems, tissue engineering and other fields [170, 171].

Until nowadays, complex IC with 65-nm features, as the one used in the production of commercial micro-processors, are done by lithographic processes that are restricted to 2D patterning in an exposure step. Some progresses have been made with the bottom-up approach exploiting nanotubes and nanoparticles self-assembly, but this approach is limited to the formation of periodic structures and not complex shapes.

Currently 3D structures with various shapes are achievable by either photon or electron beam lithography, but it is not trivial. Other approaches to obtain 3D patterning comprehend sequential layer-by-layer lithographic processes, stereolithography, direct writing with inks, etc...All these techniques have the major problem of restricted spatial resolution.

An emerging technology is the two-photon lithography (TPL), which offers the possibility to create arbitrary 3D structures in a single "coat-expose-develop" process cycle.

6.2.1 Two-photon absorption (TPA)

The TPA provides a means of activating physical or chemical processes with high spatial resolution in 3D with CD smaller than 100 nm. With a sufficiently intense light, such as the one of a pulsed laser beam, it is possible for a molecule to simultaneously absorb two photons. Each photon will have approximately half the energy normally required to reach the excited state. The probability of a molecule to absorb simultaneously two photons is proportional to the square of the intensity

of the excitation beam. The TPA non-linear intensity dependence gives rise to very interesting and useful effects.

Molecules with a very high degree of spatial confinement in three dimensions are enabled by TPA to excite, leading to feature widths of about 100 nm and excited volumes of about 0.003 μl (3aL). The 3D control of the excitation arises from focusing the intense laser beam into a material and from the fact that the intensity of the beam decreases almost by the square with the distance of the focal plane.

As reported above, the probability of TPA is proportional to the square of the laser beam intensity, thus the probability of TPA will depend approximately to the fourth power of the distance from the focal plane. At appreciable distances (about 2.5 times the beam radius at the focus) from the focal plane, TPA becomes negligible with respect to that at the focal plane leading to a high confinement of the excitation along the propagation direction. Furthermore, with TPA it is possible to excite molecules at deeper level than with one-photon absorption, because the photon energy lies below the energy the medium absorbs via one-photon. Thanks to these features, TPA enabled the production of 3D optical data storage as well as lithographic microfabrication [172a-b].

To exploit these advantages it is of extreme importance the use of engineered photoactive materials, as O/I hybrids, in order to localise and confine the photochemical reactions within a defined excitation volume.

6.2.2 General applications in photonics

Micro-optical components can be fabricated from materials with particular optical properties. The further miniaturization of optical elements to the sub-wavelength size requires special techniques. The use of surface plasmon polaritons on metal surfaces as information carriers in a kind of “optical circuit” is one of these methods [173].

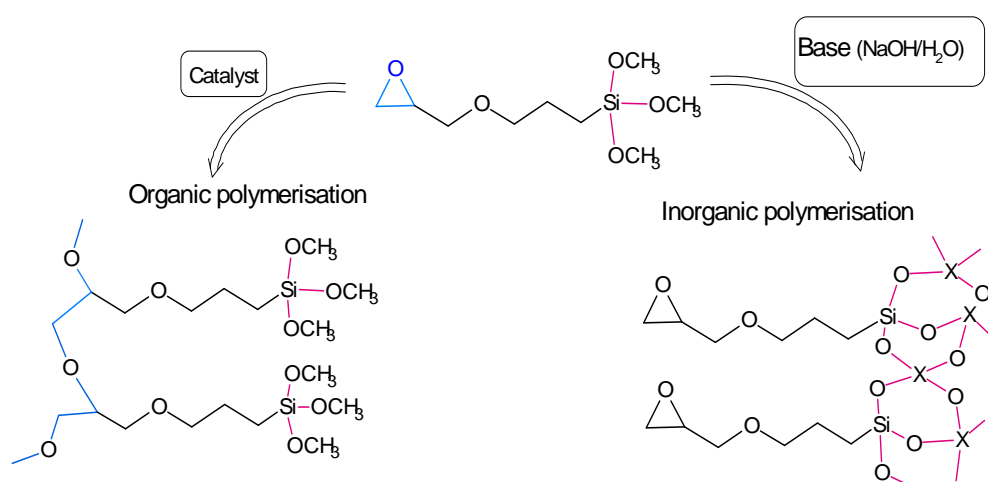
Surface plasmon polaritons are electromagnetic excitations propagating along a bound to an interface between a dielectric and a metal. They can carry information along metallic waveguides on a dielectric substrate or along dielectric structures on metal surfaces. They can be used as high sensitivity sensors for detecting different molecules and biomolecules [174a, b].

6.3 Characterisation

6.3.1 UV photolithography

Sol-gel derived O/I hybrid materials have become attractive patternable materials, because they can behave also as resist in the polymerisation process.

A precursor frequently used in the preparation of optical applications is 3-glycidoxypropyltrimethoxysilane (Glymo, since it presents a reactive function (epoxy ring), which is not sensitive to hydrolysis (mainly) and that can polymerise under UV irradiation adding a suitable photocatalyst as illustrated.



6.3.2 Matrix preparation

The preparation of NBBs-Ge matrices (reactive ratio) and was performed at the Dep. Of Mechanical Engineering – Materials section by the group of Dr. G. Brusatin.

G_S-samples

Germanium ethoxide (Ge(OEt)₄) was dissolved in methoxyethanol by stirring at RT in air, then distilled water was added in 2:1 ratio to the precursor. The final Ge concentration was 2.26 mol/L.

NBB G_S-1 (or G_S-2) was added to the hydrolysed Ge solution to achieve a final Ge load of 15 molar %. The photocatalyst, (4-phenylthiophenyl)-diphenylsulfonetriflate (DPSF) was finally added under stirring, the molar ratio between G_S-1 (or G_S-2) and DPST was equal to 1:115. The final solution was filtered and centrifuged.

The solution was deposited by spin coating (600 rpm) on silicon wafers previously cleaned with distilled water and functionalised with Piranha solution (sulphuric acid and hydrogen peroxide in a 3:1 ratio), and the coatings were dried under reduced pressure at RT.

6.3.3 G_S-1 characterisation

The photopolymerisation experiments were run using a Hamamatsu Hg(Xe) lamp LC5 series to irradiate the films with UV power density estimated at 365 nm equal to 490 W/cm². FT-IR spectroscopy (Perkin - Helmer 2000 with resolution of 1 cm⁻¹) was used to follow the evolution of the polymerisation process, observing the variation in the epoxy ring signal (both intensity and presence). Typical epoxy ring signal absorption

in the IR region can be found at 3060 and at 1256 cm^{-1} . The decrease in peaks intensity is due to ring opening.

6.3.4 FT-IR characterisation

Film characterisation

From the FT-IR spectra of NBB/Ge matrix it is possible to appreciate the change of peaks in the range 3100-2800 cm^{-1} . The peak at 3060 cm^{-1} due to the epoxy ring disappears as the one at 1256 cm^{-1} , showing the almost complete ring opening according to the plot of signal intensity as a function of the UV irradiation.

6.3.5 Film patterning

After UV irradiation, the films were developed in a bath solution obtained from tetraethylammoniumhydroxyde (TEAH) (5 μl) and distilled water (10 ml), for 10 seconds.

The feasibility of the patterning process has been demonstrated recording some patterns by conventional contact photolithographic process using a UV-mercury lamp.

The technique used in this work is called *direct lithography*, since no commercial resists are used as the O/I material used to produce the matrix already acts as the resist.

The approach is similar to the conventional photolithography, but avoiding the step of resists deposition. UV irradiation step is followed by development of the film in a solution bath in order to dissolve the soluble areas.

Pictures of the achieved patterned structures are illustrated in . The mask was in direct contact with the film and the surface images are obtained with an optical microscope.

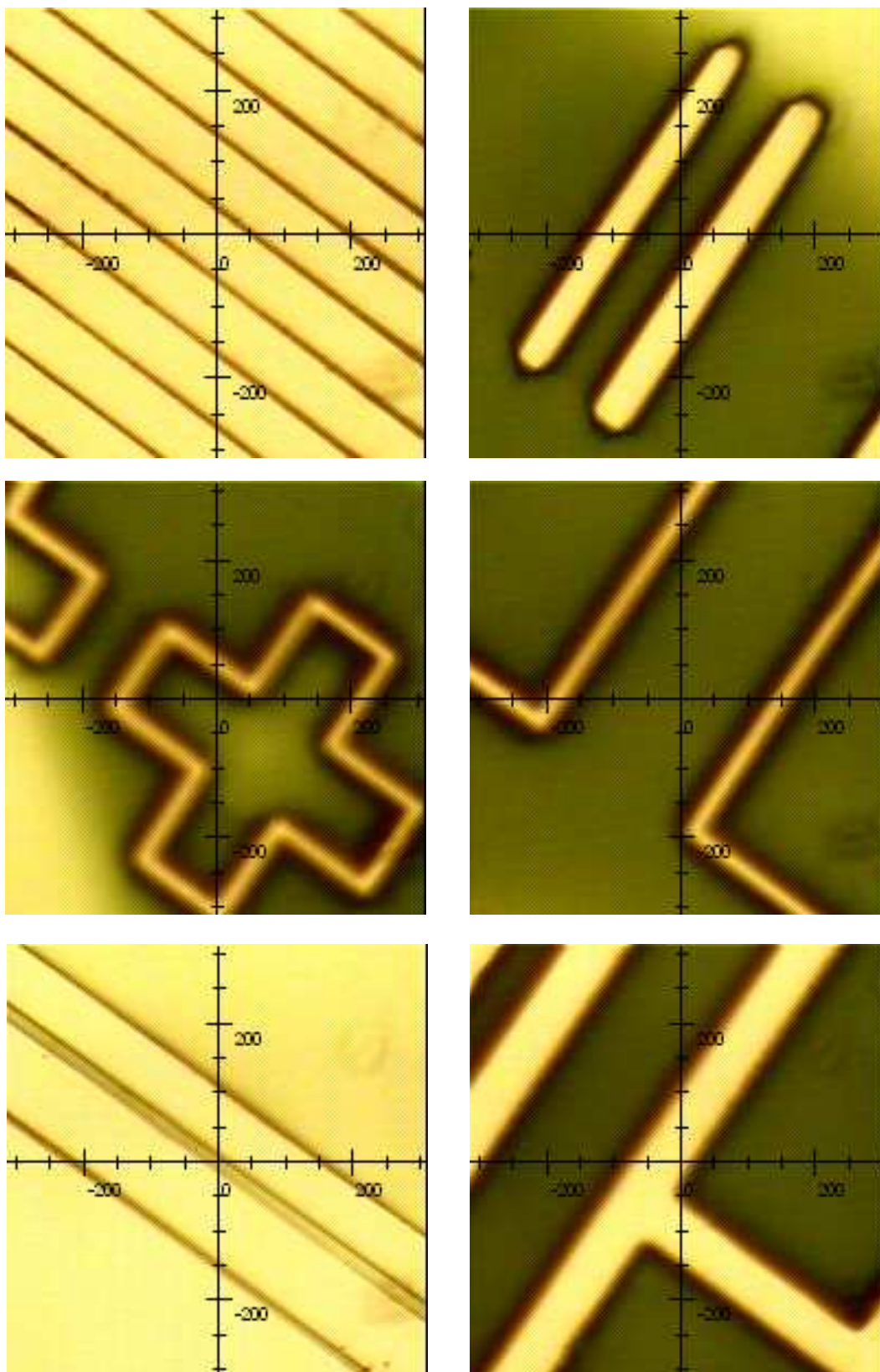


Fig. 75: UV recorded pattern of Gs-1/GE matrix film each division corresponds to 50 μm
(courtesy of Dr. G. Brusatin)

6.3.6 G_S-2 characterisation

➤ G_S-2

In this case matrices with different composition ratios were prepared, as reported in the following table.

	G _S -2/Ge (0.7/0.3)	G _S -2/Ge (0.85/0.15)	G _S -2/Ge (0.9/0.1)
G _S -2	77.2 μl	187.7 μl	298.1 μl
Ge(OEt) ₄	33 μl	33 μl	33 μl

Table 29: compositions of G_S-2/Ge matrices

After UV irradiation, different developing bath were used and compared. Only preliminary studies were completed, but a particularly interesting result was obtained. The load of the NBB in the matrix influences the developing ability. The G_S-2/Ge(0.85/0.15) is able to develop after washing in H₂O/tetraethylammonium hydroxide (20 ml/3 μl) bath and baking at 150°C for 20 min, instead the sample with ratio 0.7/0.3 develops only when not baked.

These preliminary results are still under investigation to better comprehend the NBB behaviour in the germanium oxide matrix as positive and negative resist materials.

6.3.7 Two Photon Polymerisation (TPP)

TPP or Two Photon Induced Polymerisation (TPIP) is based on TPA, (paragraph 6.2). The TPIP has been performed on spin-coated films prepared with the matrices listed in Table 30.

The TPIP was performed by Dr. R. Signorini and co-workers at the Dept. of Chemical Sciences of the University of Padua.

The photopolymerisation has been obtained using a Ti:Sapphire femtosecond laser, operating at 850 (near the maximum of the TPA spectrum of *TPI*) nm at different incident energies. The laser beam was focused on the sample by using a microscope objective 50x with NA= 0.55 or 0.8. Different solvents have been used in order to develop the patterned structures after irradiation [175]. The optical set-up for TPP experiments is shown in Fig. 76.

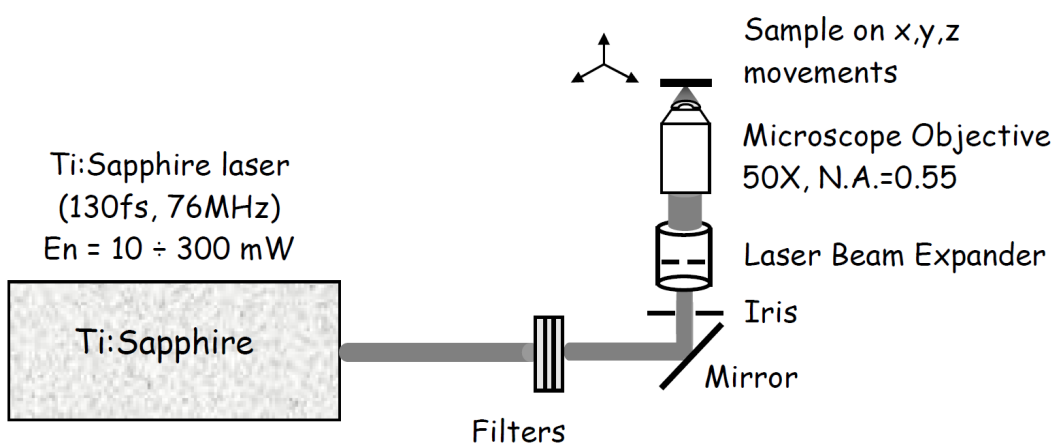


Fig. 76: optical set-up for two photon polymerisation experiments

MATRICES

Matrix	Precursor
MZrMA	MPTMS
MZrMAMon	MPTMS + triacrylate monomer
D/T _L -1ZrMA	D/T _L -1
D/T _L -2ZrMA	D/T _L -2
D/T _H -1ZrMA	D/T _H -1

Table 30: matrices used for TPIP patterning

PROCEDURE

The synthesis and the labelling of matrices are reported in paragraph .

The only difference in TPP process is the addition of a suitable photoinitiator ((E,E,E,E,E,E)-1,13-bis-[4-(diethylamino)phenyl]-tri-deca-1,3,5,6,8,10,12-hexaen-7-one) (*TPI*), in an amount equal to 0.2% respect to the total numbers of acrylic groups.

The obtained solution (concentration of (Si+Zr): 0.093g/L) was kept in ultrasonic bath for 15 minutes in order to allow a good dispersion of *TPI*. The final solution was used to prepare films, which were deposited by spin coating at 2000 rpm for 10 seconds.

Different samples with similar film thickness ($\sim 1 \mu\text{m}$) were prepared and photopolymerised. After the polymerisation process the unreacted units were developed in acetone bath for ten seconds.

6.3.8 Matrices characterisation

PRELIMINARY WORK

The emission line of an Ar ion laser at 488 nm was chosen to pump the photosensitive films.

In order to obtain an efficient photopolymerisation process the initiator must be able to produce radicals after excitation that react with the double bonds in the matrix leading to the propagation of polymerisation.

A first study was done on MZrMA and MZrMAMon films. For both matrices two samples were prepared: one was irradiated in air at 488 nm while the other was irradiated in a box under N_2 flux, in order to study the effect of atmospheric oxygen on the polymerisation.

The samples were irradiated at an excitation power energy varying from 25 to 300 mW and for a time ranging from 1 to 60 seconds.

Matrix containing only MPTMS, as methacrylate precursor, gave no efficient polymerization and the formed structures were etched during the

development step, resulting in poor resolution. MZrMAMon matrix showed a more efficient polymerisation process due to the larger number of acrylic function available. The designed structures (lines) are resistant to the development step for both air and N₂ prepared film. Thin film samples prepared in air atmosphere need higher incident energies (300 mW) and long exposure time with respect to the ones prepared in inert atmosphere (N₂) (50 mW). Increasing the thickness of the film and using low energies (10 mW), better polymerisation and resolution are achieved when the process is done in air (Fig. 77 , (a) air (b) nitrogen).

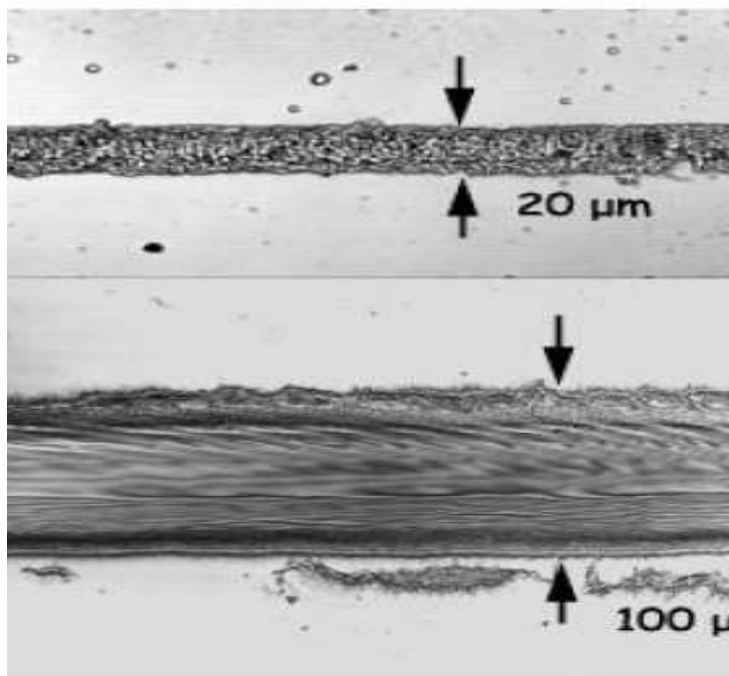


Fig. 77: confocal images of lines after development. Irradiation at 488 nm and 10 mW in (a) air and (b) nitrogen

TPIP – MZrMA and D/T_L-1ZrMA matrices

Incident energies were changed in the 10 to 450 mW range and exposure times varied from 1 to 60 seconds. Both air and nitrogen atmosphere were used. Control of the atmosphere is not so important in this case, as TPIP

promotes the polymerisation strictly in the focal volume. The laser beam is focused into the sample closer to the film-substrate interface leaving not much space in contact with the external atmosphere.

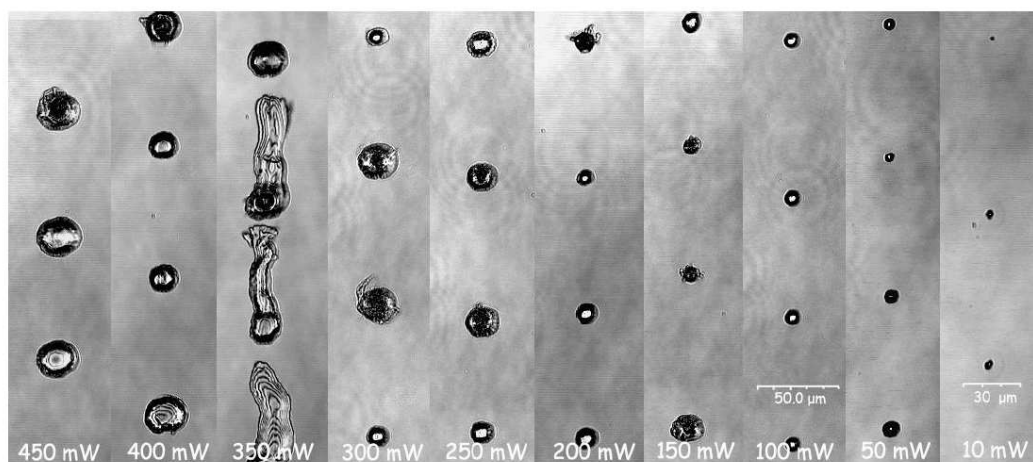


Fig. 78: confocal images of the spots after development of MZaMA matrix irradiated at 850 nm at different incident energies

The effect of input energy and exposure time on final structures was investigated. It was possible to assert that lower energies led to better spot resolutions (Fig. 78). The matrices containing silicon-based NBB with low content of MPTMS (D/T_L) did not allow good polymerisation and patterning after irradiation at both 488 and 850 nm.

Different solvents as developers were used but the dissolution of exposed and unexposed areas was always observed.

6.3.9 TPIP- D/T_H -1 matrices

The negative results obtained with D/T_L based matrices proved that, in order to obtain good patternable films, the amount of available polymerisable function has to be increased. Therefore a matrix (in the same conditions) with NBB D/T_H -1 was synthesised.

The FT-IR spectrum of the hybrid film, deposited by spin coating on a silicon substrate (Fig. 79), shows the almost complete absence of OH groups (vibrations in the 3500-3100 cm^{-1} range). This confirms the high condensation degree of the matrix. The signals at 1719 cm^{-1} attributable to the stretching vibrations of C=O and at 1638 cm^{-1} , due to C=C stretching assure the keeping of the methacrylate function in the hybrid coating.

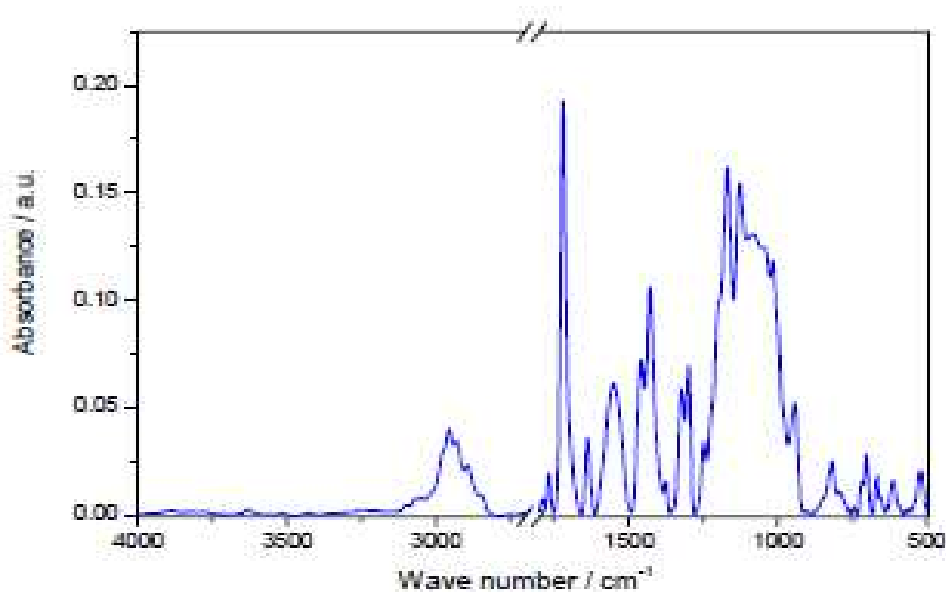


Fig. 79: FT-IR spectrum of the hybrid film deposited on silicon substrate

TPIP EXPERIMENTS

For D/T_H-1 matrix, TPIP experiments were recorded with incident energies from 5 to 50 mW and exposure time less than 1 second on the basis of the previous results obtained [176].

The effect on the input energy has been investigated, observing the confocal images of the pattern after the development step.

In each line of Fig. 80, the single spots obtained after polymerisation with different energies can be observed.

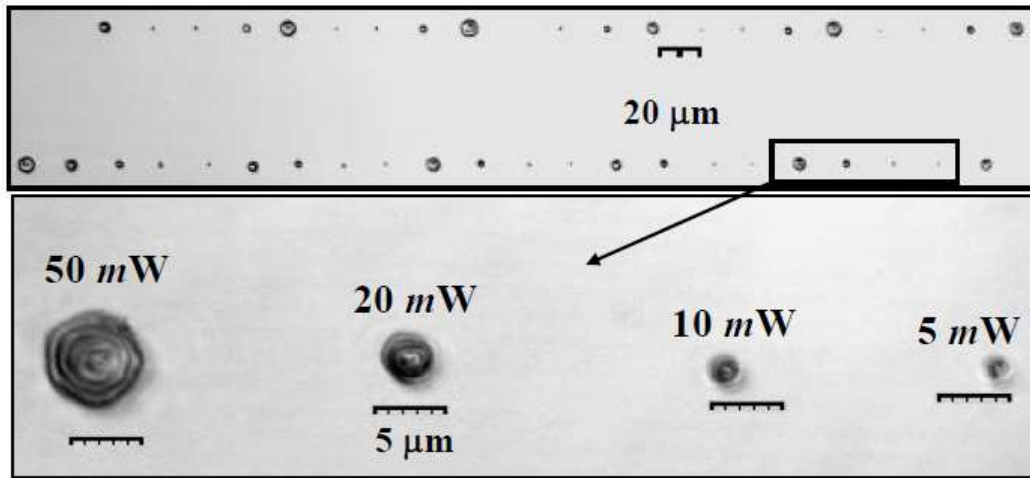


Fig. 80: confocal images of the spots on silicon substrate after development.

The resolution of the final structures improves with the decreasing of the energy input. Polymerisation reactions are more controlled when the energy dose is low enough to prevent the radical diffusion over an area larger than the laser spot.

The estimated spot diameter values are reported in Table 31. Spot sizes obtained with low energy are comparable to the laser beam dimension.

Incident Energies (mW)	Spot diameter $D/T_{H-1ZrMA}$ (μm)
50	5
20	3
10	1.8
5	1.2

Table 31: estimated diametre values of spots in $D/T_{H-1ZrMA}$ film irradiated at 850 nm

AFM measurements were also made and are reported in Fig. 81 and Fig. 82 .

Fig. 81 shows the 2D and 3D AFM images and corresponding profile of developed spot obtained after irradiation at 50 mW, whereas Fig. 82 displays the spot after developing step and irradiation at 5mW. [176]

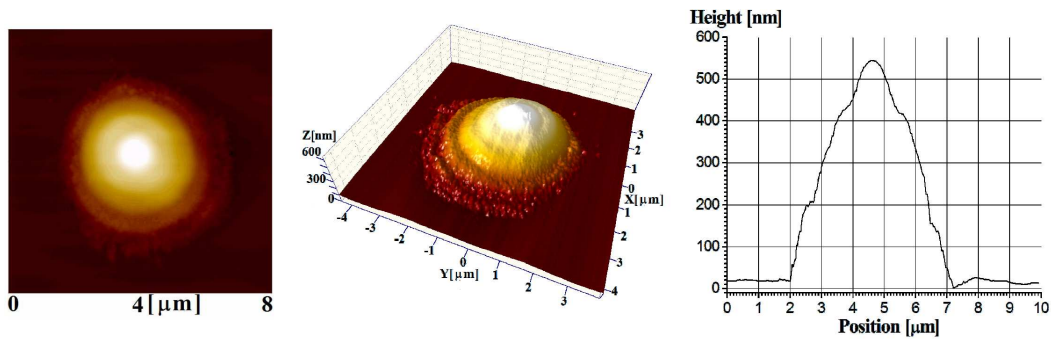


Fig. 81: AFM images and section of spot polymerised with incident energy of 50 mW

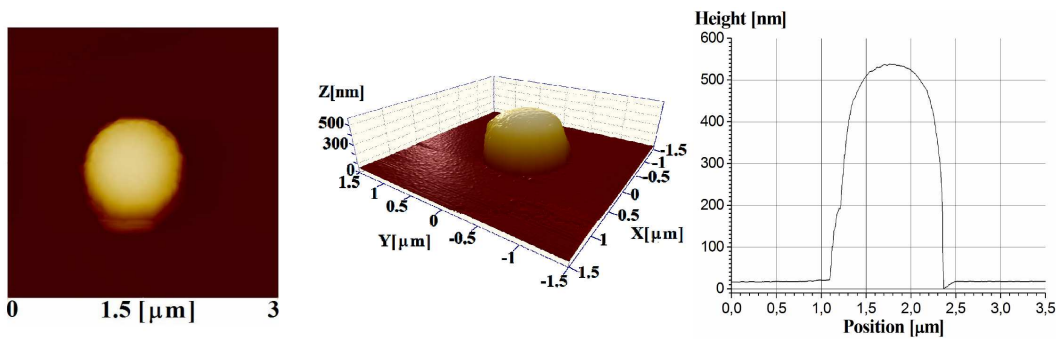


Fig. 82: AFM images and section of spot polymerised with incident energy of 5 Mw

Looking at the profile section, it is noticeable that the spots have the same height despite the different diameter. This suggests that the thickness of the patterned structure depends only on the film depth and not on the irradiation energy, whereas it is worth of note the control in spots diameter achievable through low incident energy.

Using the same NBB, another sample was realised using a 100x objective and NA = 0.8. The structure has been analysed using FE-SEM (Fig. 83).

Micrograph (A) shows a large area of the hybrid film with patterned spots, photopolymerised at different input energies (from 5 to 60 mW), images (B and C) the magnification of two structures are presented.

Also in this case, the best results have been obtained with the lowest radiation energies (5 mW).

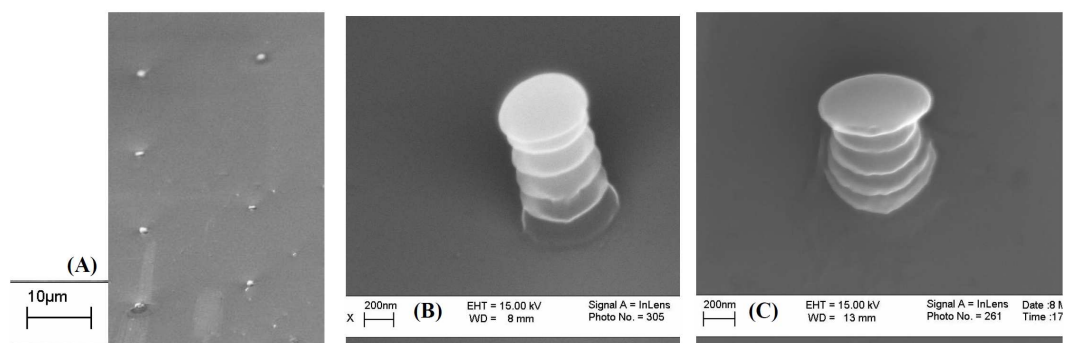


Fig. 83: FE-SEM images of photopolymerised hybrid film (A). (B) and (C) are magnifications of two different structures [176]

6.4 Conclusions

The condensation reactions between difunctional and trifunctional silicon alkoxides for the preparation of Si-based Nano Building Blocks were studied using both basic and acid catalysts.

Using a low amount of trifunctional precursor (D/T_L), a good condensation degree of the obtained products was achieved by the non-hydrolytic approach, whereas good results have been obtained with the in situ water production approach (ISWP) for high MPTMS content (D/T_H).

In the case of Glymo, NBBs with the maintenance of the reactive epoxy function have been obtained using an acid condensation promoter as DBLT, since stronger acids as trifluoroacetic acid or TiCl₄ lead to the epoxy ring opening (syntheses in Appendix C).

A NBB with high content of methacrylate functions (D/T_H-1) was successfully synthesised with the ISWP approach. GPC measurements were undertaken in order to estimate the products sizes and their distribution. One main product was detected (heptamer) plus small quantities of very low Mw products as dimers and tetramers. Two hypothetical structures of the heptamer were proposed, taking in account NMR, FT-IR and GPC characterisation results and are illustrated in Fig. 84.

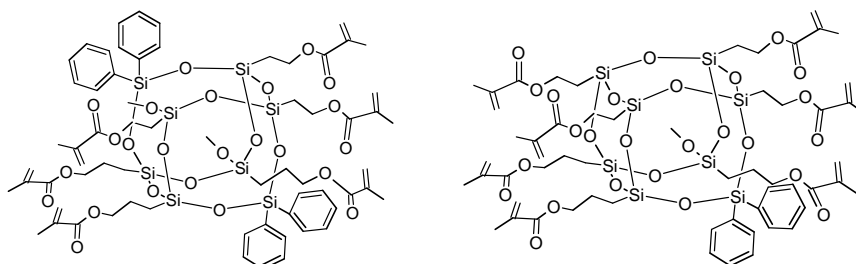


Fig. 84: proposed structures for the heptameric species in NBB D/T_H-1 (left: Mw 1419; right: Mw 1476)

On the basis of this result, a wide study on the influence of steric hindrance and chain length of the alcohol (alcohol series) and pK of the carboxylic acid (acid series) was faced. Si-oligomers condensation decreases with the increase in chain length and steric hindrance of the alcohol, and water production in this case is less effective as residual MeO- groups can be found.

The condensation degree depends also on the pK of the acid employed; a low pK value leads to a higher condensation degree of the sample. Moreover the presence of a heteroatom in the acid molecule like sulphur or chlorine enhances the reaction speed.

High loaded Glymo-based NBB have been synthesised, as Glymo can exploit polymerization reactions thanks to the epoxirane ring. With DPDO and Glymo mixtures, the GPC curve shows a great variety of different

products with Mw ranging from dimeric species to network type ones with very high Mw (>45,000). For this reason the addition of DPDO was avoided for the preparation of controlled sizes NBBs.

Glymo self-condensation syntheses with EtOH and AcA lead to good condensation degree of the Si-O-Si network especially when the reaction was carried out heating. In order to decrease the reaction time, an acid with low pK was chosen (Cl-AcA) on the basis of the previous results obtained. The reaction temperature has an influence also on the structural features of the obtained samples (Gs-1 Gs-2), according to GPC results.

Matrices with addition of the synthesised NBBs were prepared and O/I hybrid films were obtained by spin coating, in collaboration with the University of Padua.

Epoxy-based films were patterned by direct lithography and a good resolution of the patterned structure was obtained.

Methacrylate-based films were patterned exploiting the TPIP technique; sub-micrometric structures were obtained for the first time with a matrix of this composition, with good resolution.

PART 2:

Organic Modified NP

Introduction

The second part of this work is devoted to the synthesis of Si-based nanoparticles (NP). A short introduction on NP will be presented, concerning the general considerations on the synthesis procedures. The main disadvantage of incorporating SiO₂ particles into polymer-based matrices, particularly in the case of polyolefins, resides in particle aggregation owing to the low chemical affinity between filler and matrix. The aim in this work was to synthesise different substituted NP, derived from the corresponding organoalkoxisilane precursors, hence exploiting the affinity between the two moieties. Thus, the non-hydrolysable function in the precursors was chosen between groups with carbon chains of different lengths and reactivity. The obtained particles have also been doped with a fluorescent dye, rhodamine 6G (R6G), and methacryl-functionalised nanoparticles have been tested as fillers in acrylic-based matrices employed as anticorrosion coatings. A preliminary study was conducted on the behaviour of organic modified NP after thermal treatment, in order to observe their morphological and textural modifications.

7 NANO PARTICLES (NP)

The word *particle* derives from the Latin *particula*, diminutive of part. It is generally referred to a minute quantity or fragment portion of something. In science the word defines a small object, generally any basic unit of matter that behaves as a whole unit in terms of properties.

Particles can be further classified according to size or diameter in: micrometre-size particles (fine particles), which are bigger than 1 μm and nanometre-size particles, which range from 1 to 2-300 nm or in any case present sizes below 1 μm . Nanoparticles may exhibit size-related

properties that differ significantly from those observed in fine particles or bulk materials.

Nanoparticle research is currently an area of intense scientific interest due to a wide variety of potential applications in biomedical, optical, electronic fields and for the preparation of protective coatings (anti corrosive, anti-scratch) [177a-e].

Although nanoparticles are generally considered a discovery of contemporary science, they actually have a very long history. As far back as the 3rd century, glass craftsmen in Rome used nanoparticles to generate dichroic glasses, as the marvellous Lycurgus Cup in the British Museum in London (Fig. 85). The glass of this piece of master art is able to change colour depending on light conditions; the green glass becomes purple-red when light is transmitted from inside the vessel instead of being reflected. The origin of this particular optical property (dichroism) was definitively explained about ten years ago by a German-Italian research [179] and is given by a small load (about 0.01-0.1 atomic percent) of gold and silver nanoparticles.



Fig. 85: Lycurgus Cup (III a.C.), reflected (left) and transmitted light (right)

Nowadays, nanoparticles are of great scientific interest as they are effectively a bridge between bulk materials and atomic structures. Bulk materials have constant physical properties regardless the size, whereas size-dependent properties are often observed at the nano-scale. The interesting properties of nanoparticles are largely due to the large surface area, which dominates the contributions made by the small bulk of the material. An excellent example is the bending of bulk copper (i.e. copper wire); it occurs with movement of copper atoms/clusters at about the 50 nm scale. On the other hand copper nanoparticles smaller than 50 nm are considered super hard materials, since they do not exhibit the same ductility and malleability as bulk copper. Other size-dependent property changes include: surface plasmon resonance in some metal particles, quantum confinement in semiconductor particles and superparamagnetism in magnetic materials. Unfortunately in some cases the property changes are undesired, as for ferroelectric materials, which can switch their magnetisation direction exploiting thermal energy at room temperature, thus making them unsuitable for memory storage, if their size is smaller than 10 nm.

The preparation and characterisation of silicon dioxide particles with specific size and morphology is becoming of primary importance for the development of advanced functional materials. As functional-filling material nanosized silica is widely used in different fields [180a-c].

The incorporation of silica nanobeads with an extremely large surface area into polymers is of paramount interest in the fabrication of polymer nanocomposites, since silica addition improves significantly the polymer mechanical performance [181].

However it is not trivial to physically blend hydrophobic polymers (i.e. polystyrene or polypropylene) with hydrophilic inorganic particles (i.e. silica particles); this may lead to phase separation or agglomeration of particles, resulting in poor mechanical, optical, and electrical properties

[178]. Moreover, particles with high surface energy are easily inclined to agglomerate as the size of the particles decreases [182,183]. Nowadays, in order to avoid agglomeration, the most used approaches are physical coating of the particles by surfactants [184] or chemical coating exploiting coupling agents [185a-b]. Chemical surface reactions can be further divided in surface grafting or esterification [186a-b,187a-b].

In the polymer field, clay or ceramic oxide nanoparticles can be incorporated into polymer matrices in order to increase reinforcement, leading to stronger plastics, provable by a higher glass transition temperature and other mechanical property tests.

Yang and Nelson successfully prepared PMMA/silica nanocomposites by solution polymerization, founding that the nanoparticle-doped materials exhibited better mechanical properties when the nanoparticles size decreased or the nanoparticles surface was modified. Kim and Lee [188] modified silica nanoparticles with stearic acid and dispersed them afterwards into polyethylene naphthalate (PEN) using solution blending. The obtained reinforced PEN exhibited higher tensile modulus compared to the one containing unmodified SiO₂ particles. Karayannidis and co-workers [189] prepared isotactic polypropylene (iPP)/silica nanocomposites (NC) by melt blending. The silica nanoparticles were previously treated with dimethyldichlorosilane to enhance the compatibility. For the same matrix another approach was used, activating the NP with sodium hydroxide solution first and then using two coupling agents, 3-aminopropyltriethoxysilane (APTES) and neopentyl (diallyl)oxy tri(dioctyl) phosphate titanate, for surface treatment. The activation process shows its effectiveness in the amino silane coupling system as it increases the tensile strength and Young's modulus of the modified-iPP [190].

Another very interesting application of organic-modified NP is for the preparation of protective coatings.

The use of alternative coatings for aluminium alloys has been pushed by the advent of chromate replacements, in the late 1970s, due to its high toxicity and consequent environmental hazards. It has been shown that coating based on silica, ceria, vanadia can be tailored to produce a functionally gradient coating that will provide covalent bonding for adhesion and act as a barrier coating to limit the transport of water to the surface of the alloy [16–20] and therefore limit the corrosion. The interest for waterborne coatings is increasing, due to the more severe environmental and health laws. At the same time another environmental friendly process related to this field is the use of UV radiation as curing process in substitution of traditional thermal curing. The UV technique is efficient and does not need solvents since it is based on bulk polymerisation [192].

Literature reports a huge amount of syntheses where functionalization of the particles is ensured by post-modification. Little was written about one-pot or direct synthesis, and even in this case co-condensation between an organosilane and TEOS is used in majority [193-197,198]. Therefore an almost new and complete work was accomplished to produce one-pot synthesised organic-modified NP from the alkoxy silanes.

7.1.1 Syntheses approaches

NP synthesis can be divided into two main areas: gas phase synthesis and sol-gel processing. The initial development of new crystalline materials was based on nanoparticles generated by evaporation and condensation (nucleation and growth) in a subatmospheric inert-gas environment [199a-b, 200], subsequently many aerosol processing techniques have been reported to improve the production yield of nanoparticles (201a-b). These techniques include synthesis by combustion flame [202a-c], chemical vapour condensation (CVC) [203a-d], spray

pyrolysis [204], electrospray [205a-d], laser ablation [206], plasma and plasma spray [207].

Sol-gel processing can be resumed as the wet chemical synthesis approach used to generate nanoparticles by gelation, precipitation, and hydrothermal treatment [208].

Additional synthesis techniques include sonochemical processing, cavitation processing, microemulsion processing, and high-energy ball milling. In sonochemistry, an acoustic cavitation process can generate a transient localized hot zone with extremely high temperature gradient and pressure [209]. Such sudden changes in temperature and pressure assist the destruction of the sonochemical precursor (i.e. organometallic solution) and the formation of nanoparticles. This technique can be used to produce a large volume of material for industrial applications. In hydrodynamic cavitation, nanoparticles are generated through creation and release of gas bubbles inside the sol-gel solution [210]. The sol-gel solution is mixed by rapidly pressurizing in a supercritical drying chamber and subsequently exposing to cavitation disturbance and high temperature heating. The erupted hydrodynamic bubbles are responsible for nucleation, growth, and quenching of the nanoparticles. Adjusting the pressure and the solution retention time in the cavitation chamber, it is possible to control particle size.

Microemulsions have been used in order to synthesise nanoparticles of different nature as metallic [211], semiconductor [212a-b], silica [213], magnetic and superconductor ones [214b]. By controlling the very low interfacial tension through the addition of a co-surfactant, these microemulsions are produced spontaneously without the need for significant mechanical agitation.

All the above-mentioned methods are bottom-up strategies; the only top-down approach is high-energy ball milling. This approach has been used for generating magnetic [215], catalytic [216], and structural [217]

nanoparticles. It is a commercial technology, which has been considered “dirty” because of the frequent contamination problems. However, the availability of tungsten carbide components and the use of inert atmosphere and/or high vacuum processes have reduced impurities to acceptable levels for many industrial applications. Common drawbacks include the low surface area, the high size polydispersity and the partially amorphous state of the as-prepared powders.

7.2 The Sol-Gel method for silicon-based NP

This technique is gaining increasing interest in nanoscience, since it is possible to obtain nanostructures from soft chemical approaches (low pressure and temperature). Such a method is primarily used for the fabrication of materials, generally metal oxides, starting from a chemical solution (sol), which acts as the precursor for an integrated network (gel) [4]. The resulting silica-NP and their further processing permits their use in many different fields including chromatography, catalysis, medicine, polishing. Additionally silicon-based NP have been used in coatings, glazes, emulsifiers, strengtheners and binders.

The precursors used in the preparation of NP are the typical sol-gel precursors: metal alkoxides and metal chlorides, which undergo hydrolysis and polycondensation reactions to form a colloidal suspension. As reported in Chapter 1 (Introduction), the formation of a metal oxide involves connecting the metal centres with oxo (M-O-M) or hydroxo (M-OH-M) bridges, therefore generating metal-oxo or metal-hydroxo polymers in solution. The sol evolves then towards the formation of a gel-like system containing both a liquid phase and solid phase of discrete particles [218]. The volume fraction of particles may be so low that a significant amount of fluid must be removed in order to collect the product. Usually colloidal suspensions are allowed to settle by gravitation

or by centrifugation in order to speed up the process. This step is generally followed by a drying step.

The obtained products are mostly named after their final shape as, nanospheres, nanorods, nanoboxes, nanoneedles and shapes can be obtained spontaneously or as an effect of a templating or directing agent present in the synthesis.

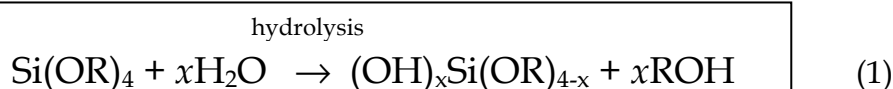
Generally amorphous particles will adopt a spherical shape, due to their microstructural isotropy, whereas anisotropic microcrystalline whiskers will adopt the geometrical form of their particular crystal habit.

7.3 Stöber method

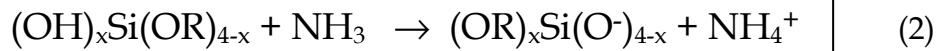
As mentioned in the previous paragraph, the industrial use of silica is widespread. Moreover, the need for well-defined nano-sized structures has increased due to the high demand from the high-tech industries (i.e. biotechnology/ pharmaceuticals and computers).

The Stöber method [219] allows the preparation of sub-micrometric dense silica particles with a homogeneous size distribution and was proposed in 1968 by Stöber, Fink and Bohn. It is an advantageous method since it is a one-pot synthesis and uses mainly cheap precursors. The produced nanoparticles are characterized by simple preparation and surface modification.

The Stöber method is based on the ammonia-catalysed reaction of tetraethylorthosilicate (TEOS) with water in low molecular weight alcohols (according to the following reaction scheme), which produces monodisperse, spherical SiO₂ NP in the range 0.05-2 μm.



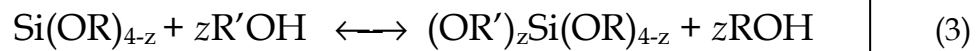
Ionization of hydrolysed monomers



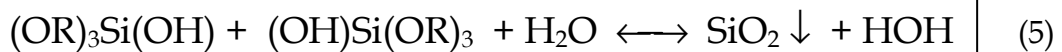
The TEOS hydrolysis rate depends upon the concentration of water and ammonia. Increasing the ammonia concentration, more OH⁻ ions are produced (from water dissociation), which attack the silicon atom and speed up the hydrolysis step [220, 221]. In this first steps single-hydrolysed monomers [(OH)Si(OR)₃] are produced.

Transesterification (eq.3) occurs when an -OR is exchanged with the solvent (alcohol) to produce another alcohol and substituted ligand [222].

transesterification



The condensation involves the polymerisation of hydrolysed and esterified silica species [4]. Later, these intermediates condense to form silica via alcohol (eq. 4) and water condensation (eq. 5).



The Stöber method or Stöber, Fink and Bohn method (SFB) was primarily concerned with empirical predicting the final particles size from a range of initial reactants concentrations.

7.3.1.1 Mechanism

At present time two different models have been proposed to elucidate the growth mechanism of nanospheres by the SFB method: monomer addition and controlled aggregation.

In both cases the formation of silica is divided in two events: nucleation and growth; the difference between the models is the approach used to describe the particle growth.

Monomeric addition supports a LaMer-like mechanism: after an initial nucleation, growth occurs through the addition of hydrolysed monomers onto the particle surface [134].

In the controlled aggregation model it is claimed that nucleation occurs continuously through the reaction. The primary particles (nuclei) aggregate one to the other to give larger aggregates and narrow size distribution [223a-b].

Some authors believe that both mechanisms are responsible for the growth, suggesting a first step by controlled aggregation, in which the formation of the particles occurs followed by monomer addition that leads to smoothing of the colloid surface. This theory is mostly supported by Dynamic Light Scattering (DLS), ²⁹Si NMR and Small Angle x-ray Scattering (SAXS) measurements [221a-b,224].

7.3.2 Modifications to the original SFB method

The SFB approach was originally developed to produce silica spheres from TEOS and has been subjected to extensive investigations because of the remarkable opportunities it offers, since it is possible to control the silica nanoparticles properties as size, size distribution and morphology [225a-f].

For the synthesis of O/I hybrid particles, the most common approach involves the production of Stöber silica particles and the subsequent

grafting of organic groups by chemical reactions with coupling agents [226,227]. Unfortunately this approach is restricted to a limited number of reactive functions on the surface of the particle (OH groups of the residual silanols) that are mostly hindered and difficult to access. Another used approach is mixing organotrialkoxysilane precursors with TEOS [226-197]. Until nowadays, only few syntheses starting from the solely organic-modified precursor, without the use of surfactants or nucleating agents have been presented [228-230a,b]. In other cases the starting solution of organic-modified silane was added with sodium silicate solution that acts as seed for the further growth of unmodified silica particles [231,232]. In our case it was possible, following a two-step synthesis, to form organic-modified silica particles starting from the corresponding trifunctional silanes without the need of surfactants or seeds. The particle sizes range from 100 to 500 nm depending on reaction parameters.

7.3.3 Nanoparticles dye doping

Dye-doped silica nanoparticles provide highly luminescent signals due to the large quantity of dye molecules into the particles and to the high quantum yield of the dye molecules.

Doped-NP can be used not only in bioanalytical assays, or sensing applications but also as optical cavity for laser emission [233].

Dyes can be incorporated employing two methods: the Stöber method to prepare primarily organic dye-doped nanoparticles and the reverse microemulsion method for inorganic and organic dye-doped nanoparticles [234].

The reverse or water-in-oil microemulsion (W/O) are isotropic and thermodynamically stable single-phase systems consisting of three primary components: water, oil, and surfactant. Water nanodroplets are formed in the bulk oil phase and act as nanoreactors, in which the

formation of the nanoparticles occurs. NP size is tuned by varying the water to surfactant molar ratio [235].

In the Stöber method [SFB] suspensions of submicron, silica-based spheres can be obtained, with the particle diameter being controlled through the parameters involved in the process, namely temperature and reactants concentration.

Inorganic dyes as Ru (II) [236] or Eu (III) complexes [237] have been embedded exploiting the microemulsion approach obtaining high photostable doped-nanoparticles with high luminescence. $[\text{Ru}(\text{phen})_3]\text{Cl}_2$ was also successfully embedded in silica-nanoparticles obtained via Stöber synthesis, and high photostability, negligible leakage and longer fluorescence lifetime compared to free $\text{Ru}(\text{phen})_3$ solutions were found. These NP could be further modified in order to obtain bioassay-tools [239].

Organic dye doping in both methods is generally difficult, due to the hydrophobic properties of most organic dyes and the lack of attraction forces between organic molecules and silica matrix. The solubility of these dyes is higher in organic reagents; therefore these molecules prefer to stay in the organic phase of the W/O emulsion system and usually precipitate or form aggregates when the Stöber method is used. Thus, Stöber-based approach has been used here to reduce the hydrophilicity of the silica matrix and allow hydrophobic R6G molecules to be trapped inside the nanoparticle matrix. Organomodified trialkoxysilanes with various functionalities ranging from methyl to octyl were used to prepare modified silica-R6G doped nanospheres with homogeneous size dispersion [240].

7.3.3.1 Rhodamine dyes

The rhodamine dyes family is based on the xanthenes structure (Fig. 86),

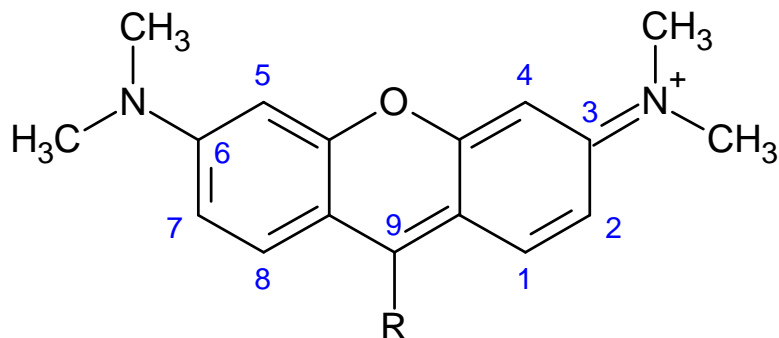


Fig. 86: general structure for xanthenes chromophore

and is created by varying the substituents in position 9 (R) and the amino groups in position 3 and 6. Rhodamine 6G (R6G), also called rhodamine 590, shown in Fig. 87

Fig. 87, is one of the most common dye of this family.

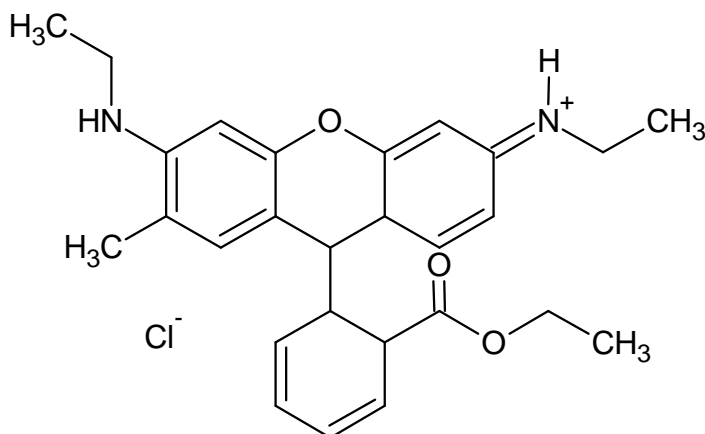


Fig. 87: Rhodamine 6G structure

It has been found that R6G is an efficient but not very stable dye; in aqueous (polar) media it forms aggregates of dimers, trimers and tetramers [241a-d] that can quench the fluorescence.

Rhodamine 6G is also as a laser dye and can be found in Nd:YAG laser or nitrogen laser, in which is pumped by the 2nd harmonic (532 nm) or in ultrashort pulsed lasers as Ti:Sapphire, to change the laser radiation to the

540-600 nm range. The dye presents high photostability, high quantum yield (0.94-0.95)[242a-b], low cost and its lasing range is in close proximity to its absorption maximum (approximately 530 nm). The lasing range of the dye is 555 to 585 nm with a maximum at 566 nm [244].

8 SYNTHESIS OF MODIFIED Si-NP

General considerations about the synthesis requirements will be briefly exposed in this chapter followed by the discussion on the obtained results on NP. Finally some preliminary results on a possible application will be exposed.

The NP are prepared using a modified SFB method consisting in a two steps acid-base hydrolysis-condensation process in hydro-alcoholic medium. The starting solution was prepared either from a single precursor or with a mixture of two different alkoxysilanes in order to obtain organic-modified NP (ONP).

8.1 Precursors

Commercially available reagents with general formula $R-Si-(OR')_3$ (R' = methyl (CH_3), ethyl (C_2H_5 -) and $R = CH_3$ (MTES), C_2H_5 - (ETES), $CH_2=CH$ - (VTES), C_5H_{11} - (ATES), C_8H_{17} - (OTES), C_6H_5 - (PhTES), $-(CH_2)_3NH_2$ (ApTES), $-(CH_2)_3CO_2C(CH_3)=CH_2$ methacryloxypropyl (MPTMS)) were used as precursors (Fig 48 and Fig. 88, Appendix B).

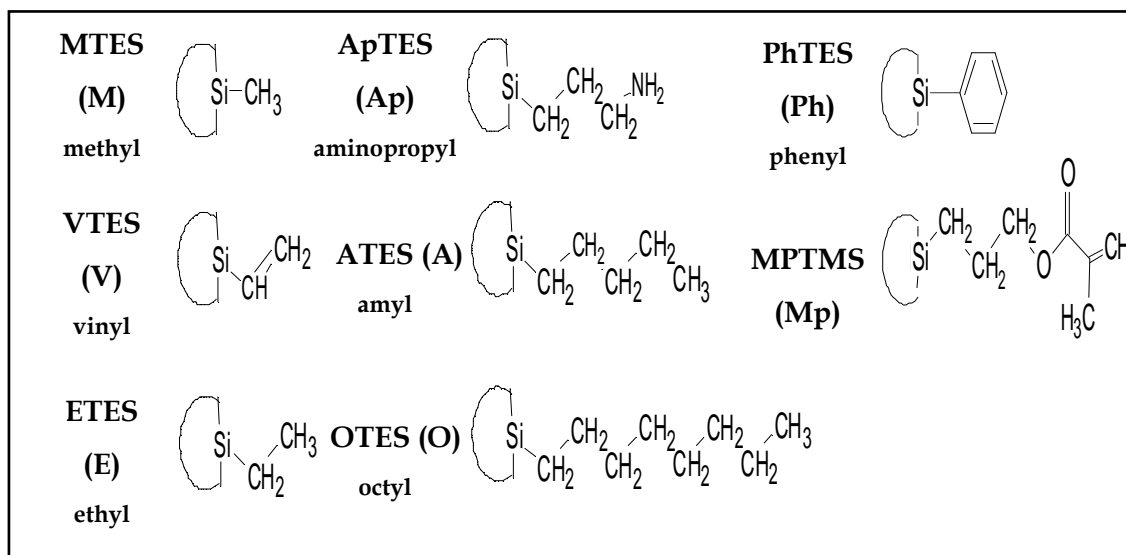


Fig. 88: different functionalities used to obtain ONS

The increase in the carbon chain should increase the lipophilicity of the silica-NP, thus increasing the compatibility between fillers and polymer-matrix reducing the formation of aggregates and therefore allowing a better dispersion.

Furthermore, the presence of reactive groups such as vinyl and methacryl can assure the formation of strong interfaces between fillers and matrix, acting as coupling agents.

8.2 Experimental

Reagents

Methyltriethoxysilane (MTES or M) 99%

Ethyltriethoxysilane (ETES) 97%,

Vinyltriethoxysilane (VTES or V) 98%,

Phenyltriethoxysilane (PhTES) 97%,

Amyltriethoxysilane (ATES) >97%,

Octyltriethoxysilane (OTES) 96%,

Aminopropyltriethoxysilane (ApTES or Ap),

Double distilled water

Ethanol

Hydrochloric acid

Ammonia solution 29%

All reagents were used without further purification unless otherwise stated.

8.2.1 Characterization Techniques

➤ *Fourier transformed infrared spectroscopy (FT-IR)*

FT-IR was used to control the reaction evolution. FT-IR spectra of the solutions were recorded with a Thermo Optics Avatar 550 instrument in transmission mode, using KRS5 platelets, in the 4000–400 cm⁻¹ range (64 scans, 4 cm⁻¹ resolution).

➤ *Multinuclear magnetic resonance spectroscopy (NMR)*

²⁹Si and ¹³C NMR spectra were recorded with a Bruker 400 WB spectrometer with carrier frequency of 400.13 MHz (¹H) equipped with a double band probe. Samples were packed in 4 mm zirconia rotors and spun at 6 kHz (except VTES ¹³C at 13 kHz). ²⁹Si single pulse (SP) pulse length 4.3 μs power level -2 dB delay 5s, scans 4K; CP-MAS ct 5ms, ct pulse 3 μs, power level -4.2dB, decoupling pulse 5.3 μs. Q8M8 was used as external secondary reference (12,6 and -108 ppm). ¹³C proton decoupling spectra were acquired with 90° pulse length 3.36 μs, power level -1.7 dB, decoupling power -4.2 dB decoupling pulse length 4.90 μs, delay 7.5 s, 256 scans. Adamantane was used as external secondary reference (38.56 and 29.6 ppm).

Si units are labelled according to classical T_mⁿ notation, with T representing the three functional silicon unit, n the number of oxo bridges and m the number of silicon atoms in the cyclic species (Chapter 5, pag.62).

➤ *Thermal analyses (TG-DTA)*

Thermal analysis (TG-DTA) were performed on a Netzsch Thermobalance STA 409, the samples were heated in air (100 cc/min) or in N₂ (100 cc/min), from 20° to 1000°C with a heating rate of 10K/min (reference alumina).

➤ *Differential Scanning Calorimetry (DSC)*

DSC curves were recorded on a DSC 2010 TA instrument, with a heating rate of 10°C/min in the range 30-200°C in N₂ flow (100 cc/min).

➤ *Nitrogen physisorption*

Specific surface area and porosity were characterized by N₂ adsorption-desorption using a Micromeritics ASAP 2010 instrument. Specific Surface Area (SSA) values are calculated using the BET equation and pore size distribution is obtained applying the BJH model.

➤ *Scanning Electron Microscopy (SEM)*

Particle morphology and size were studied using a SEM JEOL JSM-5500 instrument, operating from 5 to 20 kV.

Field emission SEM (FE-SEM) was recorded on a SEM Supra40 Zeiss, in high vacuum mode operating at 5 and 7 kV.

➤ *Contact angle measurements*

Contact angle measurements were performed using water drops of 3 µl and measuring both sessile (static) and equilibrium angle.

Sessile angles are given by a sitting drop (i.e.: a drop of water resting on a flat support); equilibrium angles are taken after letting the drop vibrate for 15 seconds at 20 Hz.

8.3 Synthesis and procedure standardization

At first, some general synthetic parameters were studied and applied to the different syntheses. Different parameters were changed: dilution, water/silane ratio, concentration of the condensation promoters, and reaction time of the two steps.

The research of the best conditions to obtain spherical, homogeneous in size distribution and small particles, was accomplished using MTES as precursor.

The synthesis of MTES-NP is schematically presented in

Fig. 89. Reactions were carried out at room temperature (RT) and in air.

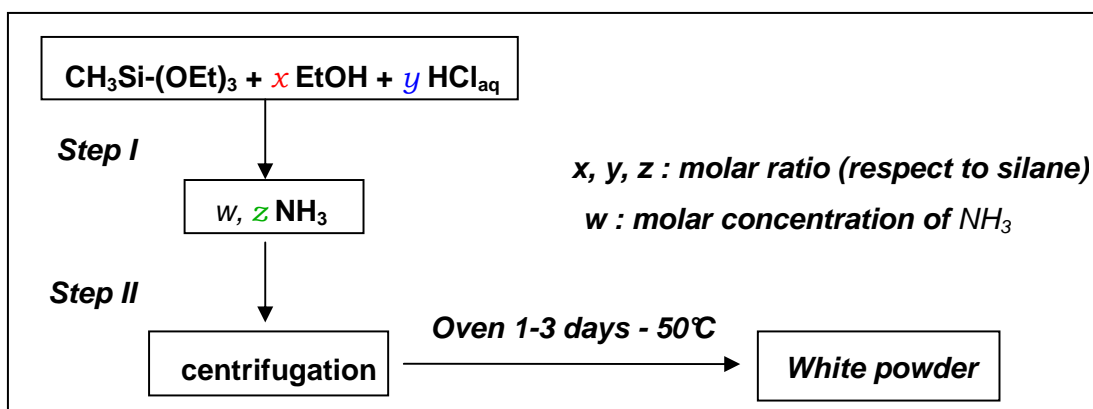


Fig. 89: general reaction scheme for MTES nanoparticles preparation

8.3.1 MTES-NP

MTES (10 mmol, 1.992 ml) was dissolved in EtOH and allowed to homogenize for 1 minute under stirring. Then, a diluted hydrochloric acid solution (water 3.6 ml and HCl in various content, see Table 32) was added. The final solution (solution A) was let stirring at RT in air for 4h (step I).

An ammonia solution (solution B) was prepared with different concentrations. In step II, solution A was added to 50 ml of solution B under vigorous stirring at RT and air. The mixture was let stirring for several hours until a white suspension was formed.

The suspension was centrifuged at about 5000 rpm for 15 min and the precipitate washed twice with water. The samples were allowed to dry at 50°C for 24 h and a white powder was obtained.

Table 32 reports the different syntheses parameters used.

Label	<i>x</i>	<i>y</i>	<i>w</i>	<i>z</i>	<i>step I</i>	<i>step II</i>
MTES-1 NP	20	20	180	2.3 M	4 h	20 h
MTES-2 NP	100	20	180	2.3 M	4 h	20 h
MTES-3 NP	20	20	180	Conc	4 h	20 h
MTES-4 NP	20	40	180	2.3 M	4 h	20 h
MTES-5 NP	10	20	180	2.3M	4 h	20 h
MTES-6 NP	20	20	180	2.3 M	4 h	7 h

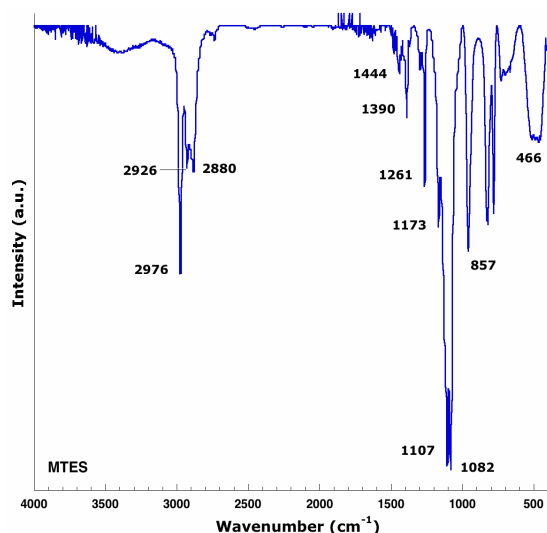
Table 32: syntheses parameters for MTES-NP

Conc. means that ammonium hydroxide (~ 29% NH₃) was used pure, without dilution (~ 15.5 M).

MTES-NP characterisation

FT-IR characterisation of the precursor

MTES



Assignment	Wavenumber (cm ⁻¹)
ν CH ₃	2976 (st)
ν CH [CH ₂]	2926 (w)
ν CH [OCH ₂ CH ₃]	2880 (w)
δ_{as} CH [CH ₃]	1444 (w)
ω -OCH ₂	1390 (m)
ν Si-CH ₃	1261(st)
Si-OCH ₂ -	1173 (m),
ν_{as} Si-OC [-OEt]	1107, 1082 (st)
ν_s Si-OC	957 (m)
δ_{as} Si-OC [-OEt]	466 (m, br)

Fig. 90: FT-IR spectrum of pure MTES precursor and relative group vibrations assignments (table)
[adapted from 238]

8.3.2 FT-IR characterisation of MTES-1 NP sample

The IR spectroscopy evidences the maintenance of the methyl group linked to Si (1261 cm⁻¹, see Fig. 90).

The IR spectrum of MTES-NP sample in Fig. 97 is in agreement with the one of pure MTES precursor, the assignments of which are given in the table in Fig. 90.

Peaks at 2971 and 2909 cm⁻¹ are attributed to ν CH₃ (anti- and symmetric respectively at 1407 cm⁻¹ the antisymmetric bending deformation of the methyl group (δ_{as} CH₃), is observable, whereas the rocking vibration (ρ CH₃) is present at 769 cm⁻¹. The siloxane bonds generate two bands in the range 1200-1000 cm⁻¹.

8.3.3 SEM characterisation of the sample

The SEM microscopy was used to characterize dimension and shape of the particles.

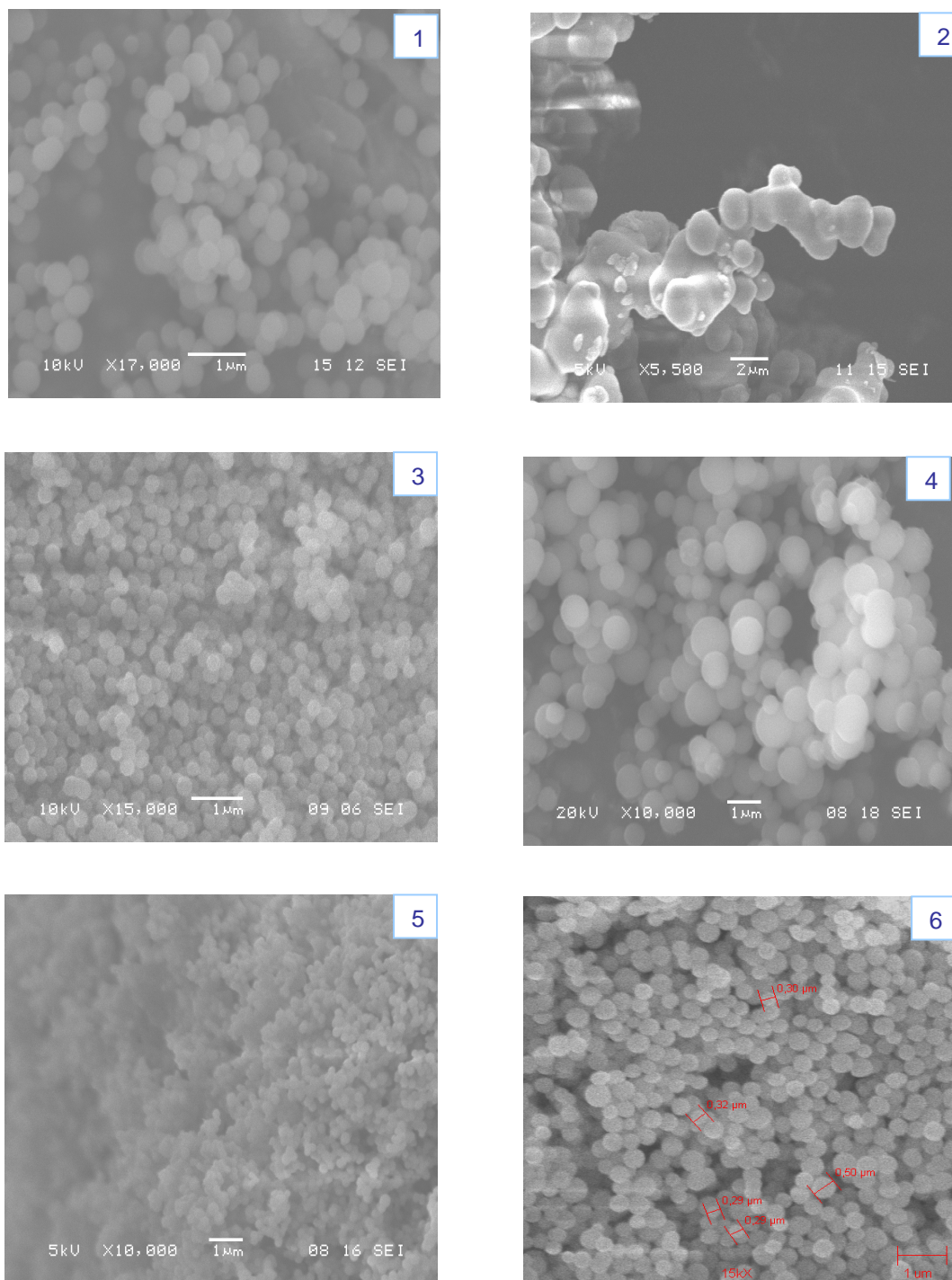


**Fig. 91: SEM micrographs of MTES-NP samples (the synthesis label is reported on the image)
(unit bar 1μm)**

Sample	Average particle size
MTES-1 NP	170 nm
MTES-2 NP	-
MTES-3 NP	243 nm
MTES-4 NP	1.034 μm
MTES-5 NP	341 nm
MTES-6 NP	197 nm

Table 33: average particle size of MTES samples prepared in different conitions

The SEM study revealed that the best results were obtained with synthesis MTES-1 NP.

A higher alcohol ratio leads to a marked Oswald ripening effect (Fig. 91-2): a coral-like structure of fused spheres is observable instead of separate spheres. On the other hand lower dilutions lead to bigger size spherical particles, as in the case of a higher molar concentration of ammonia catalyst (see Table 33). A higher acid catalyst concentration produces particles with big sizes and large size distribution (0.6-1.6 μm). Decreasing the 2nd step duration (MTES-6 NP) does not affect significantly the particles dimension respect to the standard conditions.

8.3.4 N₂ physisorption characterisation

Nitrogen sorption analyses are used for the determination of the surface area and pore size distribution. The Brunauer-Emmett-Teller (BET) method was used for the determination of specific surface area (SSA). Conventionally the quantity of gas adsorbed is expressed as its volume at standard conditions of temperature and pressure (0°C and 760 torr, STP), while the pressure is expressed as a relative pressure, P/P_0 , where P is the actual gas pressure and P_0 is the vapour pressure of the adsorbing gas at

the test temperature. To calculate the pore size the Barrett, Joyner, Halenda, hence called BJH method is used.

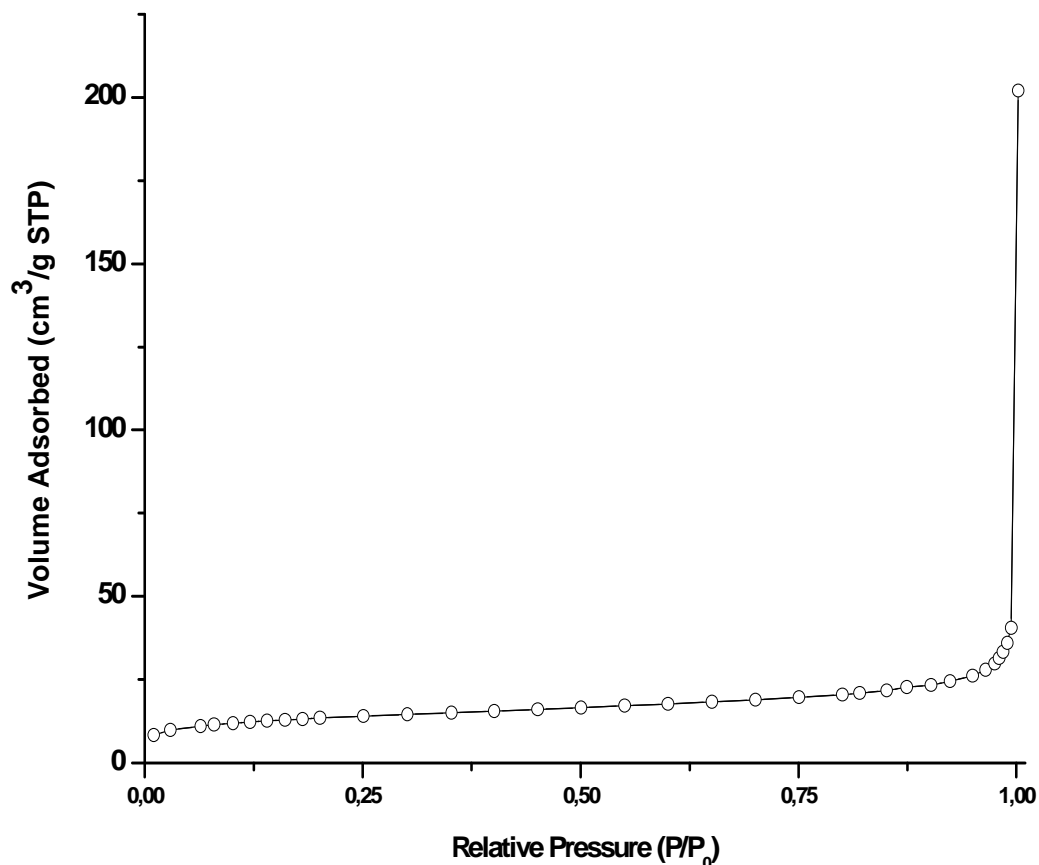


Fig. 92: nitrogen sorption isotherms: adsorption (circle), desorption (cross)

Porosity calculations were done on the absorption isotherm branch. The absorption volume and the total porosity result low. The sample presents a type II isotherm (Fig. 92) and porosity is mainly due to few micropores. The desorption branch does not overlap to the adsorption one, probably due to the need of longer equilibration time. The powder produced starting from MTES is mainly microporous (67% of total porosity), however there is also the presence of higher diameter pores (at 25, 30, 125 and 175 Å). BET SSA values, pore volumes and (BJH)-calculated pore diameters are given in Table 34.

Sample Label	BET SSA (m ² /g)	Total Pore Volume (cm ³ /g)	BJH Absorption Average Pore diam (Å)
MTES-1-NP	47.7	0.0626	88
MTES-2-NP	8.4	0.0240	148
MTES-3-NP	98.0	0.1339	103
MTES-4-NP	31.9	0.0506	99
MTES-5-NP	85.9	0.1873	125
MTES-6-NP	28.4	0.0582	118

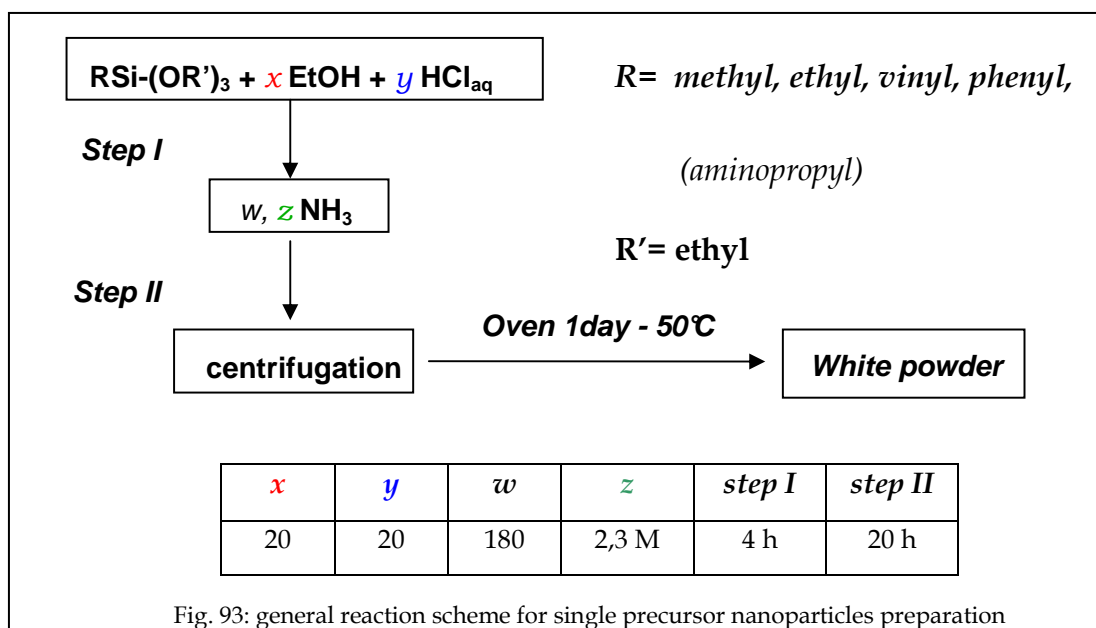
Table 34: N₂ physisorption data for MTES samples

From nitrogen physisorption data we can state that the SSA is influenced by the nature of the catalyst. Increasing the concentration of acid catalyst the SSA decreases (MTES-4-NP). With increasing the concentration of ammonia, both SSA and total pore volume increase (MTES-3-NP, Table 34).

8.4 NP prepared from a single precursor

8.4.1 Syntheses and procedure

The synthesis procedure and parameters were derived from the results presented in the previous paragraph (Fig. 93). The addition of a second organosilane bearing a NH₂ group (ApTES), in 1 mol.%, was performed in order to verify the possible improvement of the condensation reactions by the amino group acting as catalyst. The sample is labelled MApTES1%.



8.4.1.1 Single precursor RTES-NP

Step I) NP were prepared starting from a single alkoxy silane as reported in table 1a. The precursor (RTES) was dissolved in ethanol (0.2 mol, 11.68 ml) at RT by stirring; acidified water (HCl $4.7 \cdot 10^{-4}$ mol, 0.017 g and distilled water 0.2 mol, 3.6 ml) was subsequently added. The solution was kept stirring at RT for 4 hours.

Step II) The hydrolyzed organosilane solution was added to an aqueous ammonia solution 2.3 M (1.8 mol, 50 ml) and was kept stirring for 20 h at RT.

A white suspension was obtained, which was centrifuged at 5000 rpm for 15 min to separate the sample from the solution. The sample was collected, washed twice with distilled water and dried in oven at 50°C for 24 h.

Sample	RTES	R (mmol)
MTES-NP	MTES	10 (1.992 ml)
ETES-NP	ETES	10 (2.147 ml)
VTES-NP	VTES	10 (2.115 ml)
PhTES-NP	PhTES	10 (2.413 ml)
ATES-NP	ATES	10 (2.649 ml)
OTES-NP	OTES	10 (3.146 ml)

Table 35: quantity of RTES precursor used for NP production

8.4.2 FT-IR characterisation of the precursors

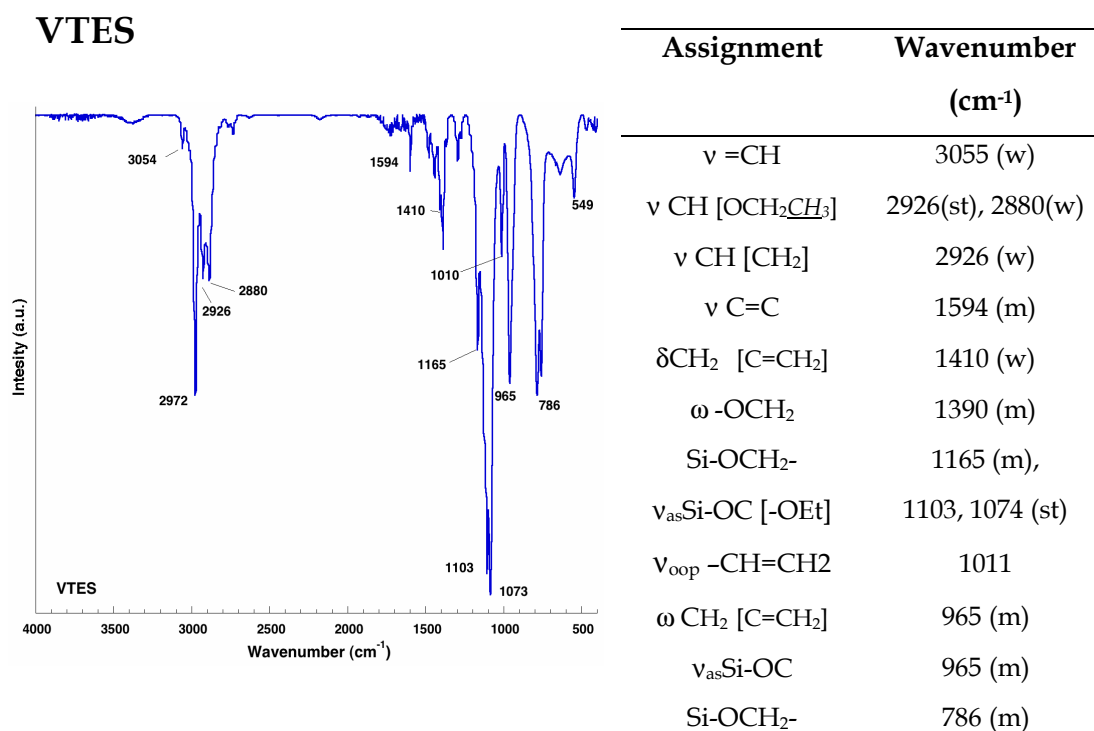
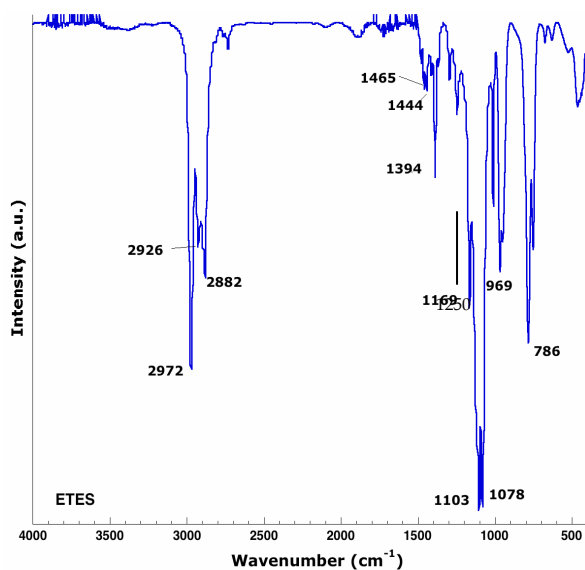


Fig. 94: FT-IR spectra of VTES precursor and relative vibration assignments (table)

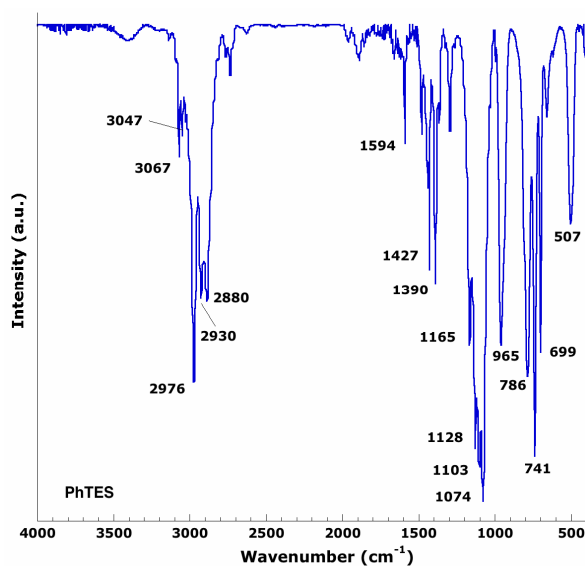
ETES



Assignment	Wavenumber (cm ⁻¹)
ν CH ₃	2972 (st)
ν CH [CH ₂]	2926 (w)
ν CH [OCH ₂ CH ₃]	2882 (w)
σ_i -CH ₂ -	1465 (w)
δ_{as} CH	1444 (w)
ω -OCH ₂	1394 (m)
ω CH ₂ - [Si-Et]	1250 (w)
Si-OCH ₂ -	1169 (m),
ν_{as} Si-OC [-OEt]	1103, 1078 (st)
ν_s Si-OC	969 (m)
Si-OC	786 (m)
Si-OC [-OEt]	466 (m, br)

Fig. 95: FT-IR spectra of ETES precursor and relative vibration assignments (table)

PhTES



Assignment	Wavenumber (cm ⁻¹)
ν CH [ring]	3067, 3047 (m-w)
ν CH ₃	2980 (st)
ν CH [CH ₂]	2930 (w)
ν CH [OCH ₂ CH ₃]	2880 (w)
ν C=C	1594 (m)
δ CH ₂ + ring vibr	1427 (m)
ω -OCH ₂	1390 (m)
Si-OCH ₂ -	1165 (m),
X sensitive band	1128 (st)
ν [Si-Ph]	1103, 1074 (st)
ν_{as} Si-OC [-OEt]	1103, 1074 (st)
ν_s Si-OC	965 (m)
δ_{oop} CH [ring]	741 (s), 699 (s)
δ_{oop} Si-C-C [ring]	507 (m)

Fig. 96: FT-IR spectra of PhTES precursor and relative vibration assignments (table)

8.4.3 FT-IR characterisation of the samples

Fig. 97 reports the spectra of the RTES-NP particles analyzed. The spectra have been normalized with respect to the intensity of the main peak.

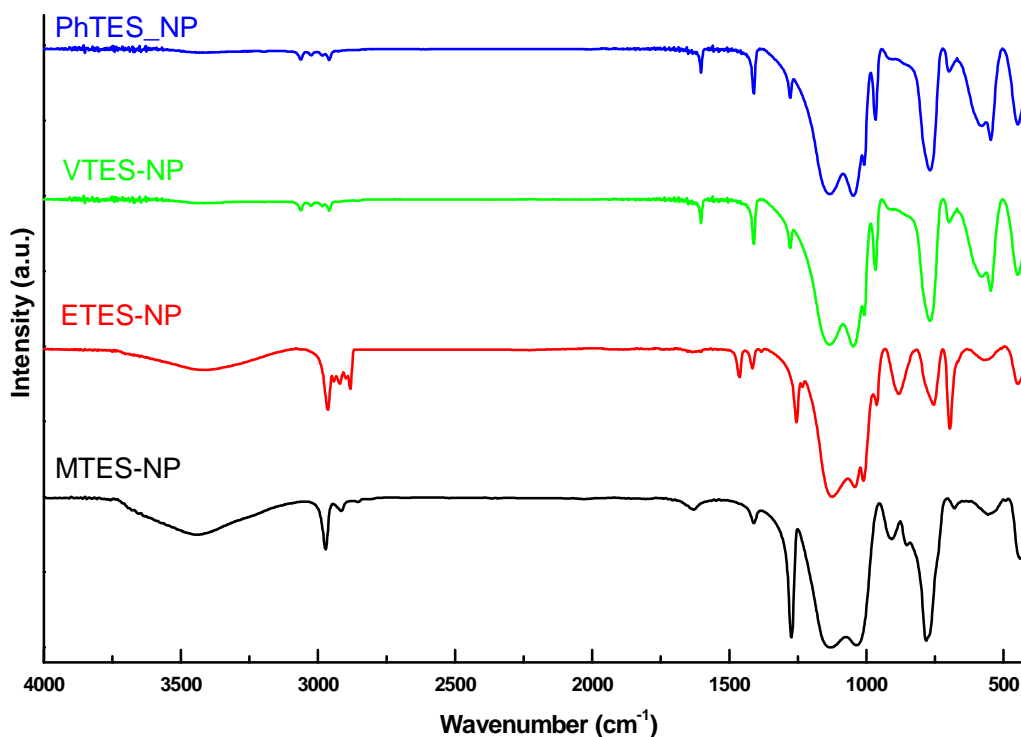


Fig. 97: FT-IR spectra of RTES- NP

The functional R group is maintained in all samples. For the MTES-NP sample it is possible to observe the peaks due to the methyl group at 2972 and 2912 cm^{-1} (νCH_3 , antisymmetric and symmetric respectively), 1407 ($\delta_s\text{CH}_3$) and at 1273 cm^{-1} ($\delta_s\text{CH}_3$ of Si- CH_3) and at 768 cm^{-1} (ρCH_3). The ETES-NP spectrum shows the same peaks of methyl (in the case of the CH_3 group), plus the peaks at 2922 and 2850 cm^{-1} attributable to the antisymmetric and symmetric stretching vibrations of CH_2 , respectively. The methylene group wagging vibration can be found at 1258 and 962 cm^{-1} . In the case of VTES the peaks at 3063 ($\nu_{\text{as}}\text{CH}_2$), 3020 (νCH), 1602 ($\nu\text{C}=\text{C}$) 1411 ($\delta_{\text{ip}}\text{CH}_2$) and 963 cm^{-1} ($\omega\text{-CH}_2$) confirm the presence of the

vinyl group; finally the presence of the phenyl group in PhTES is confirmed by the bands at 3067 and 3042 cm^{-1} ($\nu\text{CH}_{\text{aryl}}$), and the characteristic triplet due to the in phase out of plane vibrations of the 5 H in the monosubstituted aromatic ring (at 741 cm^{-1}) and the out of plane bending of the CH of the ring at 731 and 695 cm^{-1} (table Fig. 96).

The hydrolysis of the ethoxy groups can be followed by the disappearance of the typical signals at 2925 (νCH_2), 2880 (νCH_3), 1170-1165 cm^{-1} (Si-OCH_2 -) (Fig.96). For all the samples, in the region 1200-1000 cm^{-1} it is observable a broad band typical of the $\nu_{\text{asSi-O-Si}}$ stretching bands of condensation products, which is generally split in two peaks. In the case of methyl-derived particles we can observe the main absorption at 1135 cm^{-1} indicating the formation of cyclic products and a second intense signal at 1033 cm^{-1} due to the presence of cyclic T^3 products [153]. For the ethyl-derived particles the main absorption at 1124 cm^{-1} indicates the presence of cyclic products (T_8 cube-like) [245] and the band at 1040 cm^{-1} is related to ladder-like oligomeric species and open-chain oligomers [153]. There is no much difference between the vinyl-derived particles and the ethyl ones, we can observe a main peak at 1137 cm^{-1} attributable to cyclic species and a second absorption at 1049 cm^{-1} due to ladder like oligomers, in this case there is no presence of open-chain oligomers. In Fig. 97 the IR spectrum of the phenyl-derived sample is shown; a very intense absorption peak at 1132 cm^{-1} is observable accompanied by two shoulders at about and at 1028 cm^{-1} . The first band is typical for cyclic species (and is associated with the vibrations at 1028 cm^{-1}). The shoulder band at 1110 cm^{-1} is also attributed to cycles but of smaller dimensions. However the presence at 1044 cm^{-1} of a small band evidences also the presence of a ladder like structures.

8.4.4 NMR characterization

8.4.4.1 ^{29}Si CP-MAS NMR

Table 36 reports chemical shifts, assignments and integral value of the signals of different silicon units in RTES-NP samples. In most cases the network is constituted by T^3 and T^2 units (Fig 98). The only exception is presented by ETES-NP sample that show also a small amount of T^1 units.

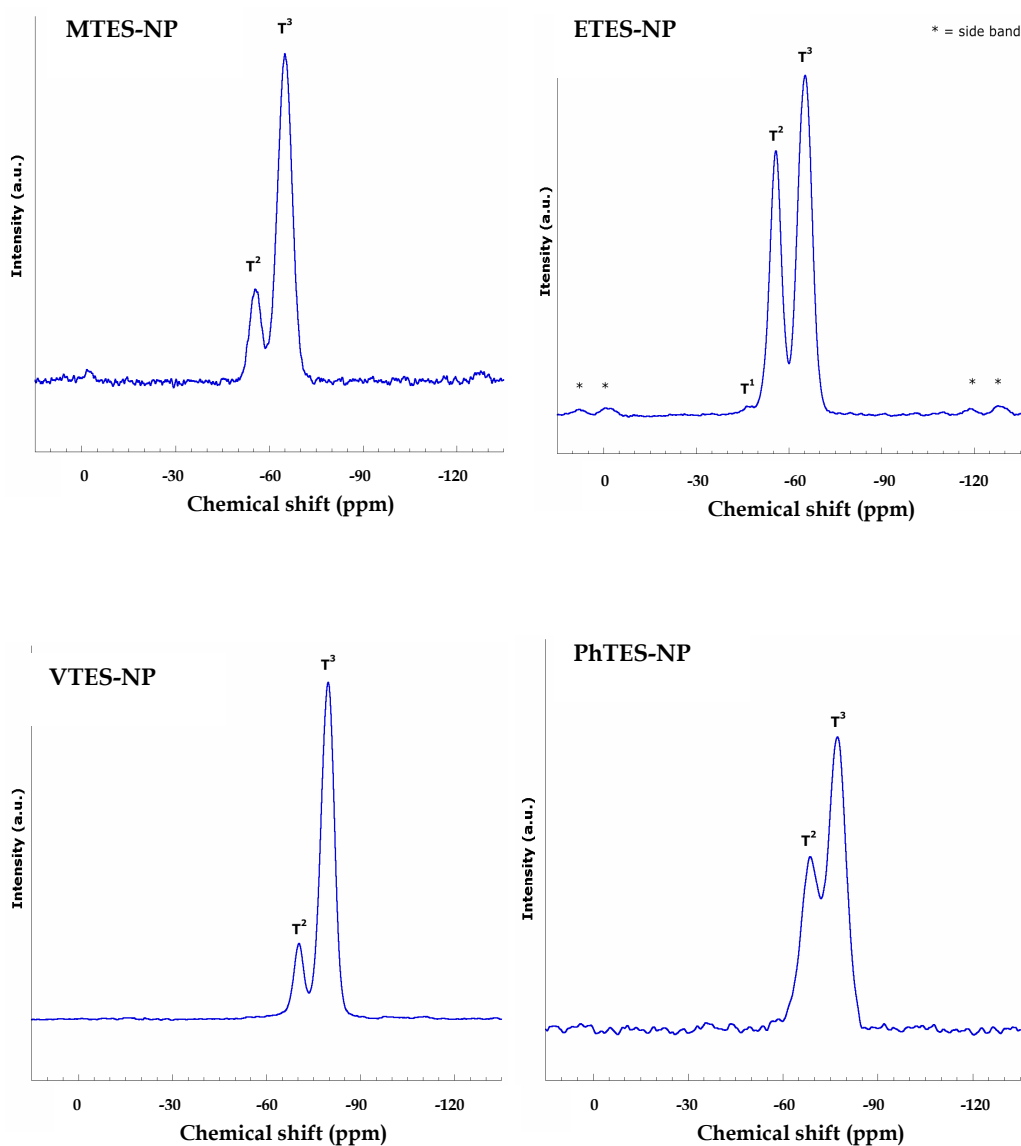


Fig. 98: ^{29}Si CP-MAS Spectra of single precursors derived nanoparticles

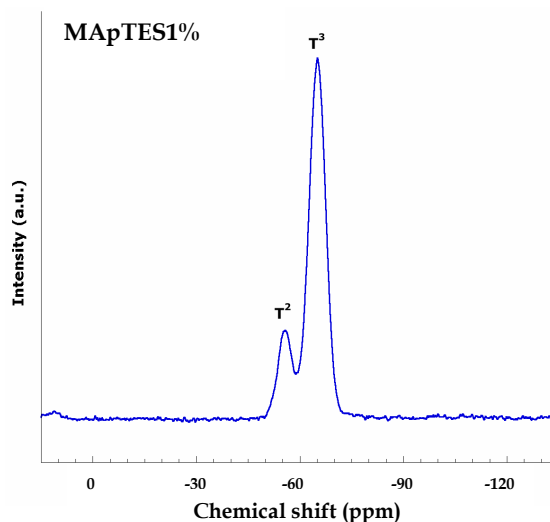


Fig. 99: ^{29}Si CP-MAS Spectra of MApTES1% nanoparticles

Fig. 98 and Fig. 99 show the spectra obtained for MTES-NP, ETES-NP, VTES-NP, PhTES-NP and MApTES1% respectively. In the spectral region characteristic of T-type signals, the resonance around -55.5 is due to T^2 units, while the signal around -65.0 ppm is associated to T^3 units, there is a shift to higher field in the case of phenyl and vinyl-derived particles. In the case of ETES-NP, a small presence of T^1 units is found at -46.5 ppm. The T^2/T^3 ratio is 1:2.4 for MTES-NP, 1:1.5 for ETES-NP whereas for PhTES-NP it is 1:3 and changes to 1:3.9 in MApTES1%; VTES-NP (1:4.7) presents the highest degree of condensation.

Table 36 summarizes the chemical shift and the ratio, estimated from the ^{29}Si NMR spectra between the different T unit types.

The ^{29}Si NMR reveals that the degree of condensation of the silsesquioxane network is higher when the chain length of the organic constituent is shorter. There is also an influence of the nature of the carbon atom in the R group, since the presence of an sp^2 C seems to favour the condensation. The presence of a small amount of ApTES (MApTES1%) favours the condensation process of MTES (from 70.8 to 79.8%), probably thanks to the basic NH_2 group, which acts as a catalyst for the condensation reaction [246].

Sample	T ³ (%)	T ² (%)	T ¹ (%)	T ² /T ³	T ³ (ppm)	T ² (ppm)	T ¹ (ppm)
MTES-NP	70.8	29.2		1: 2.4	-65.0	-55.5	
MApTES1%	79.8	20.2		1: 3.9 1: 22: 32.5*	-65.1	-55.7	
ETES-NP	58.5	39.7	1.8	1: 1.5	-65.0	-55.3	-46.2
PhTES-NP	75	25		1: 3	-76.9	-68.8	
VTES-NP	82.4	17.6		1: 4.7	-79.7	-70.5	

Table 36: ²⁹Si NMR data - chemical shifts and estimated ratio between the T units [247]- * ratio T¹/T²/T³

8.4.4.2 ¹³C MAS NMR

¹³C NMR experiments were run on NP in order to check the stability of the functional group of PhTES and VTES, and in the case of MApTES1% NP in order to confirm the ability of ApTES to further promote the condensation of MTES.

The stability of aromatic ring was assessed and confirmed for the PhTES-NP; the VTES-NP spectrum shows the typical signals of the vinyl group and only the small peak at 22.81 ppm, which represents the 0.1% of the main species, suggests a negligible polymerization of the vinyl group.

Carbon numbering follows Fig. 100 and the assignments are summarized in Table 37 .

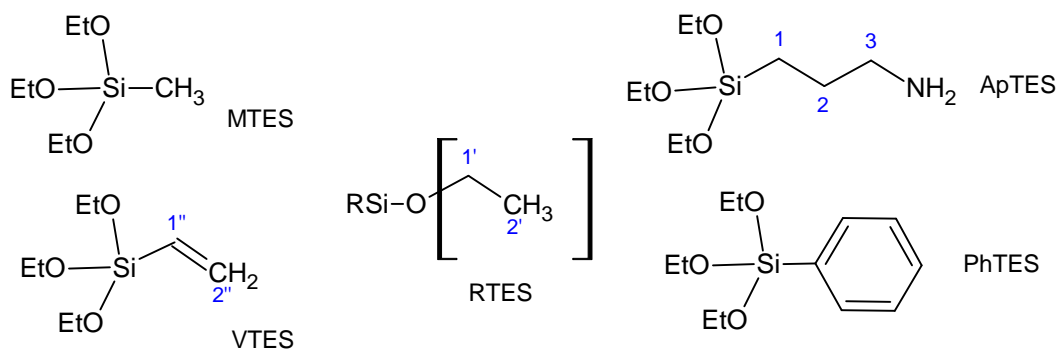


Fig. 100: carbon numbering in the used silane precursors

M-APTES 1%		VTES-NP		PhTES-NP	
Si-CH ₃	2.82				
2'	18.81	2'	18.64	2'	18.9
			22.81		
1'	58.75	1'	58.97	1'	58.6
1	11.07	1''	131.09	ortho	128
2	26.70	2''	136.74	para	130.7
3	45.08			meta	134.3

Table 37: ¹³C chemical shifts and related carbons of R-TES samples [248a-d].

The characteristic peaks for the ethoxy group are identified at 18.5 (CH₃) and at 58.7 ppm (CH₂) and are detectable in percentage lower than 2.5% in most of the samples. In the case of MApTES1% the sample is fully hydrolysed and shows the highest condensation degree (Fig. 101) despite the low amount of ApTES.

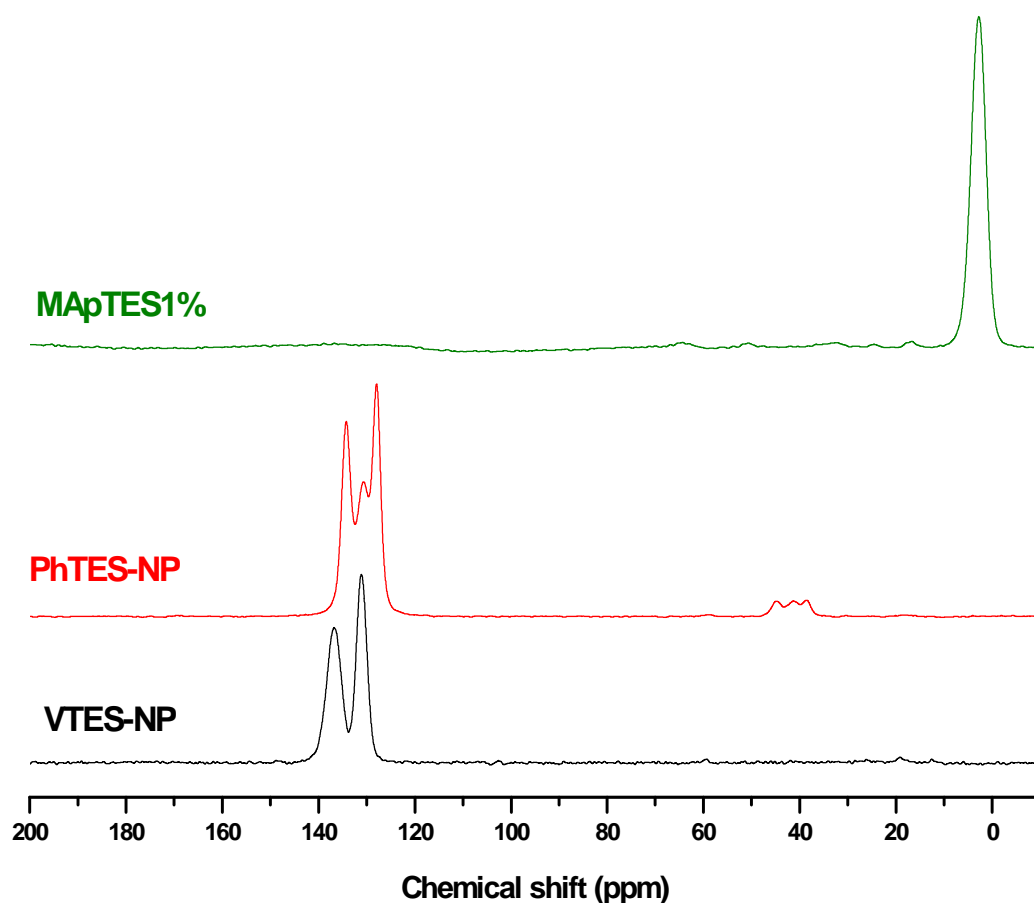


Fig. 101: ^{13}C spectra of MApTES1%, VTES-NP and PhTES-NP samples

8.4.5 SEM characterisation

The SEM micrographs show that all the precursors₇ gave regularly shaped particles, as shown in

Fig. 102 and 21.

The particles present a distribution of the dimension (Table 38) depending on the R function of the precursor.

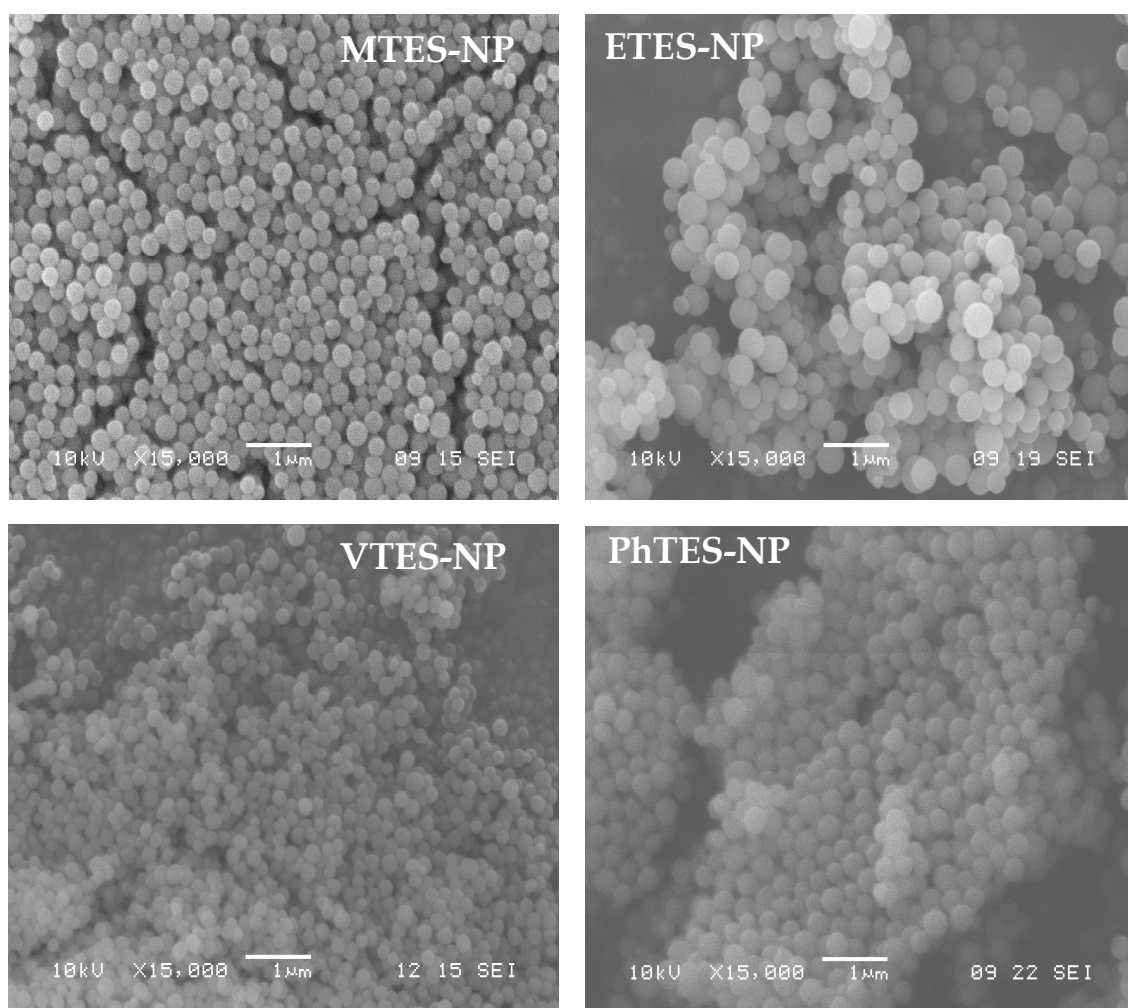


Fig. 102: SEM micrographs of modified NP (unit bar 1 μm)

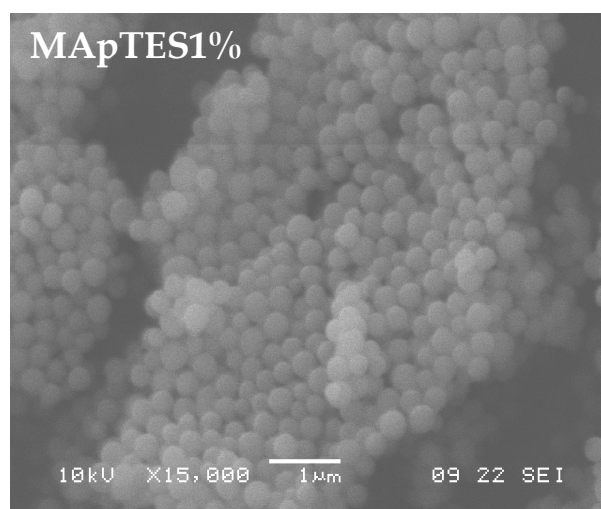


Fig. 103: SEM micrographs of modified NP (unit bar 1 μm)

Sample	Average particle size	range
MTES-NP	169 nm	54-296 nm
VTES-NP	197 nm	121-280 nm
PhTES-NP	255 nm	105-436 nm
ETES-NP	427 nm	224-535 nm
MApTES1%	312 nm	187-417 nm

Table 38: average particle size of the NP produced

ApTES has a strong influence on the particles size, leading to a strong increase of size (Table 38). This is again connected with the ability of the amino group to catalyse the condensation reaction.

8.4.6 N₂ physisorption characterisation

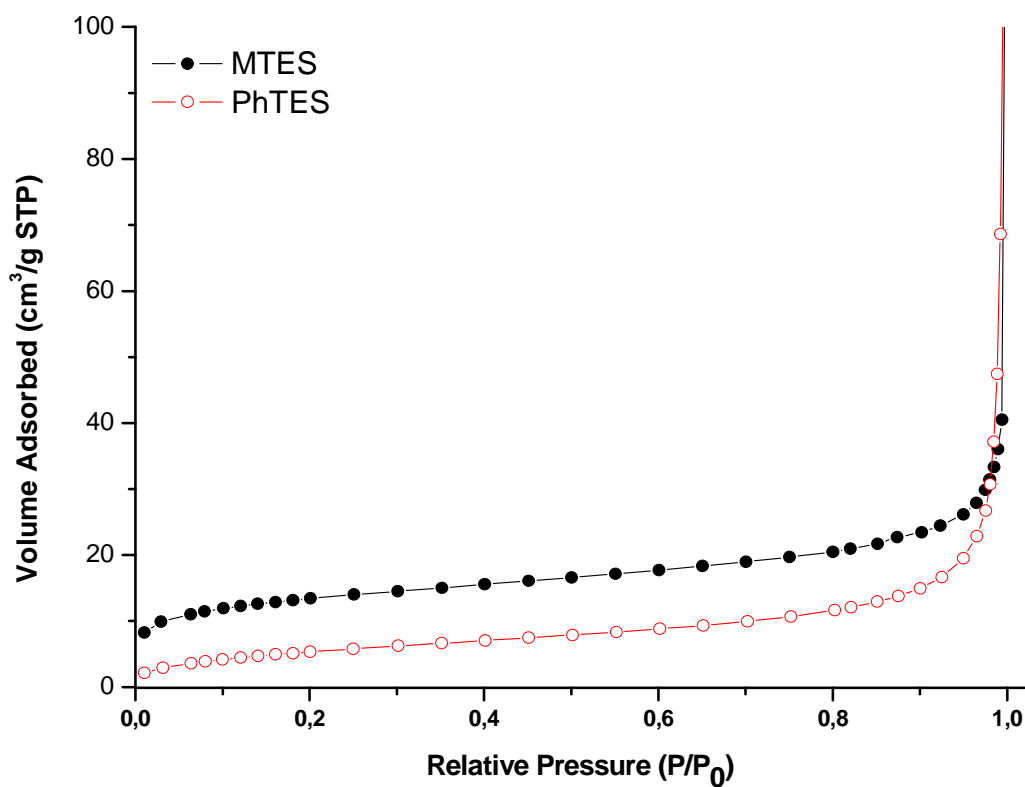


Fig. 104: Adsorption isotherms for organically-modified particles

The analyzed samples show a low porosity (Table 39), with type II isotherm. As the chain's size of the organic substituent increases, we observe a shift towards the mesopores region and also the macropore range.

The use of a cumbersome functional group as the phenyl ring generates larges pores, and a significant presence of "open throated" macropores is detected [243].

Sample	BET SSA (m ² /g)	Total Pore Volume (cm ³ /g)*	BJH Absorption Average Pore diameter (Å)	BJH Desorption Average Pore diameter (Å)
MTES-NP	46.8	0.063	88	129
VTES-NP	22.5	0.044	83	96
PhTES-NP	20.3	0.106	226	603
ETES-NP	7.9	0.032	159	105

Table 39: N₂ physisorption data of the samples (* P/P₀=0.99)

8.4.7 Thermal analyses (TG-DTA)

Figure 105 shows the TG traces recorded in air on RTES-NP.

The total weight loss increases with the increase in size of the organic group of the alkoxide precursor following the trend: methyl > vinyl > ethyl > phenyl (Table 40).

The weight increase noticeable in the vinyl derived sample is always observed when vinyl is used as precursor for the NP, and is due to the oxidation of the vinyl group.

In general the thermal stability follows the trend: Phenyl > Vinyl > Methyl > Ethyl, according to T_{onset} values in Table 40.

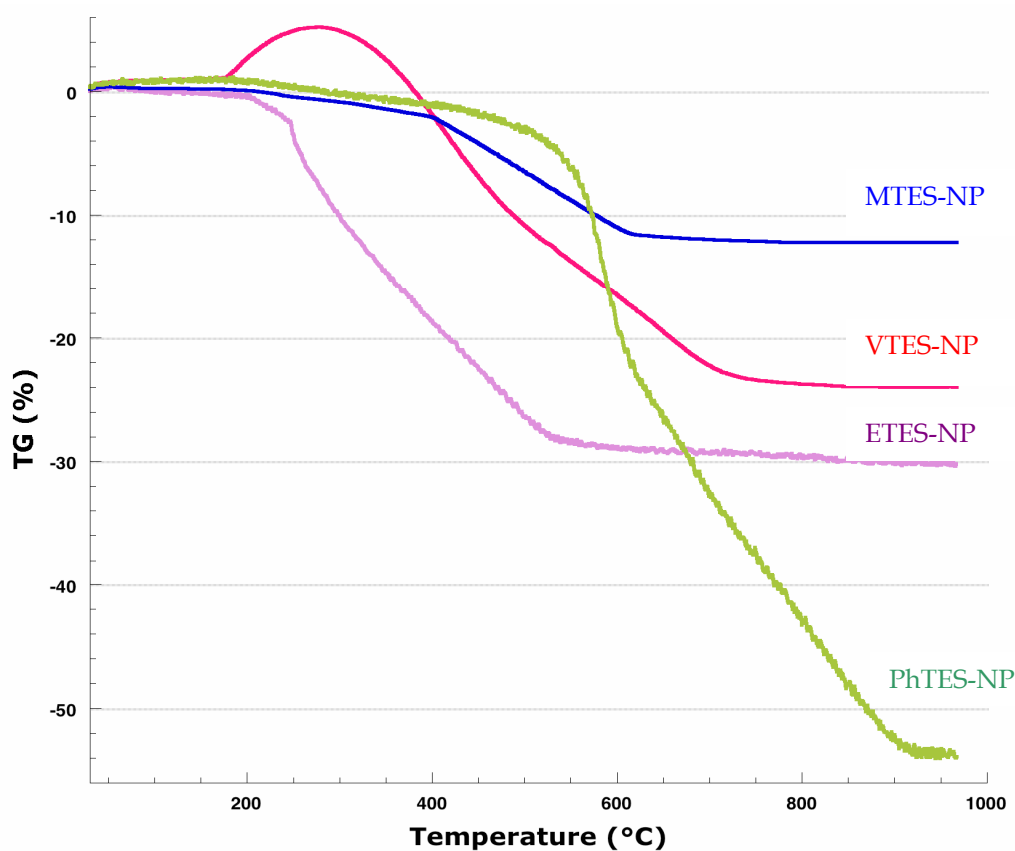


Fig. 105: TG curves of organically-derived nanoparticles

Sample	Total weight loss	Weight Loss steps (temperature range)	Exothermal peaks	T_{onset}
MTES-NP	13.5%	13.5% (25-850°C)	450.6; 535.5; 629.8°C	220°C
VTES-NP	28,3%	28.3% (280-900°C)	218.2; 606.5; 655.5°C	279°C
ETES-NP	30%	30% (100-900°C)	238.8; 518.3; 613.8°C	212°C
PhTES-NP	78,8%	24.7% (200-30°C), 54.1% (630-980°C)	638.9; 736.9; 856.3°C	400°C

Table 40: TG-DTA data of RTES-NP

8.5 NP prepared from two precursors - Binary systems (RR'-NP)

The reagents used for the syntheses of the binary systems are listed in Appendix B.

8.5.1 Syntheses and procedure

The synthesis procedure is schematised in Fig. 106; the reaction parameters were reported in Fig. 93.

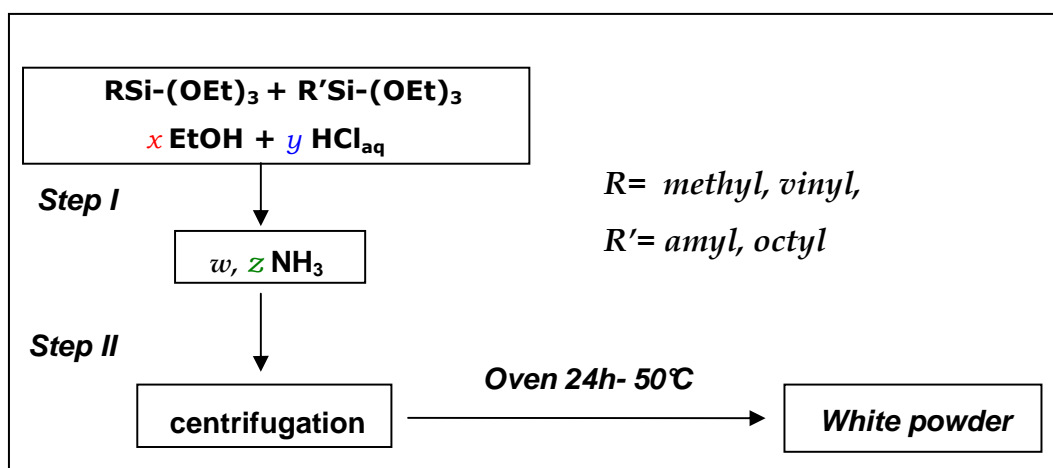


Fig. 106: general reaction scheme for RR'-NP preparation

8.5.1.1 RR'NP- synthesis

Exploiting the approach used for the other organosilane precursors, ATEs and OTEs were not able to give nanoparticles alone. Binary systems with MTES and VTES were then prepared, to increase the chain length of the organic modifier group on the particles surface.

Binary System

Step I) Silica particles were prepared starting from a mixture of alkoxy silanes. The trialkoxy silane precursors ($\text{RSi}(\text{OEt})_3$, $\text{R}' \text{RSi}(\text{OEt})_3$) were dissolved in ethanol (0.2 mol, 11.68 ml) at RT by stirring and

acidified water (0.2mol - distilled water 3.6 ml and HCl 0.017 g) was added. The solution was kept stirring at RT for 4 hours.

Step II) The hydrolyzed organosilane solution was added to an aqueous ammonia solution 2.3M (1.8 mol, 50 ml) and was kept stirring at RT for 20 h. After 20 h of stirring a white suspension was formed, which is centrifuged at 5000 rpm for 15 min to separate the sample from the solution. The sample was collected and washed twice with distilled water and dried in oven at 50°C for 24h.

Two binary systems were prepared based on MTES and VTES with the addition of ATES and OTES in various molar ratios to the first alkoxide. The sample are labelled MATES and MOTES .

The maximum load of the precursor with a long alkyl chain was 75% molar for ATES and in the case of OTES was added in the ratio of 25% to VTES and MTES.

8.5.2 FT-IR characterisation of the precursor

ATES

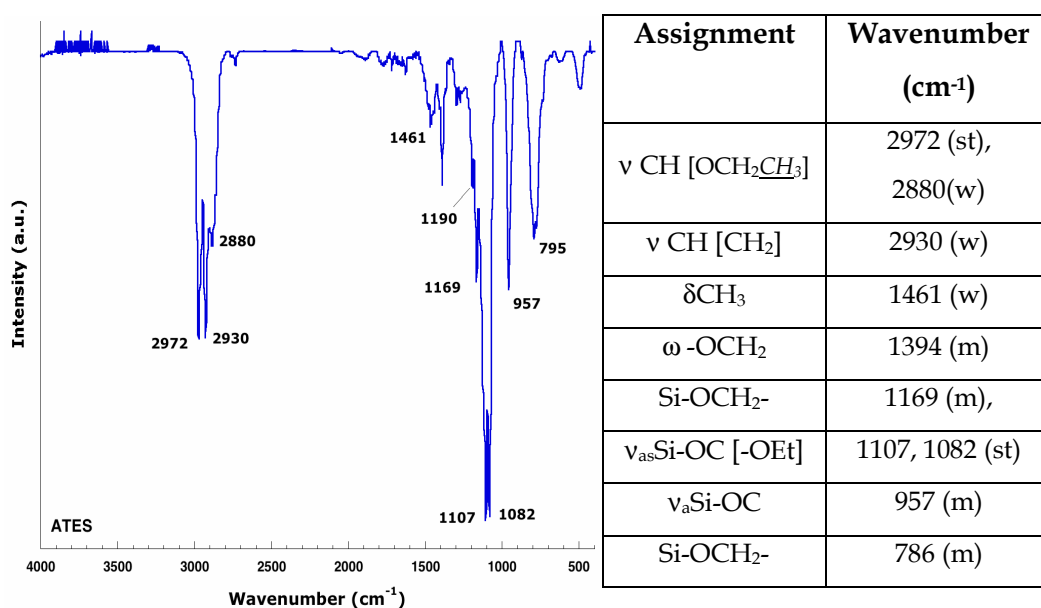


Fig. 107: FT-IR spectrum and typical group vibration assignments (table) for ATES precursor

OTES

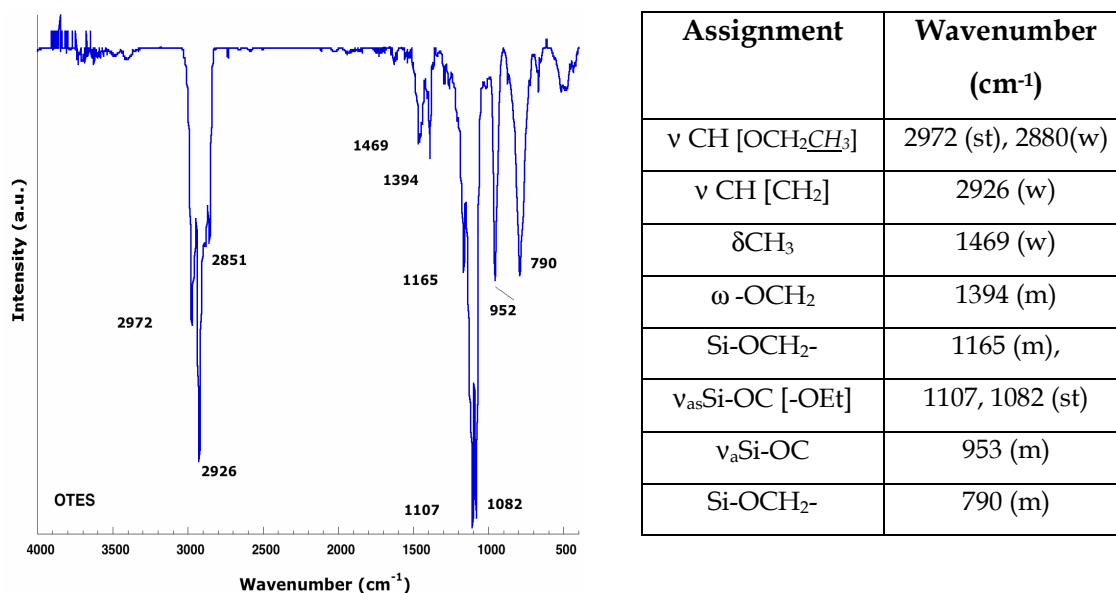


Fig. 108: FT-IR spectrum and typical group vibration assignments (table) for OTES precursor

8.5.3 FT-IR characterisation of the samples

In Fig. 109 the spectra of MTES and VTES-NP (already discussed in the previous paragraph) and of two binary systems-samples (MOTES 25 and VOTES25) are shown.

In the case of ATES the spectra are similar to those reported in Fig. 109.

Unfortunately, most of the peaks due to OTES are overlapped to those of MTES, as in both cases the functional group is an alkyl chain. Thus the only observable peaks are CH₂ antisymmetric stretching vibrations related to OTES (-[CH₂]₇CH₃) and Si-CH₃ vibration, which is present in MTES (see Fig. 90 and 108)

In MOTES25, it is possible to observe both ν_{as} CH₂ (2832 cm⁻¹) and the sharp band assigned to Si-CH₃ at 1275 cm⁻¹. In both cases, the signals present a shift to higher wavenumbers, which is probably due to the presence of the second precursor in the mixture.

In the case of VTES systems, the presence of the vinyl group is easy to detect since it does not overlap to the signals due to OTES. The peaks attributable to the vinyl group can be found at 3061 ($\nu_{\text{as}}\text{CH}_2$ vinyl), 1605 ($\nu\text{C}=\text{C}$) and 1404 cm^{-1} (δCH_2 vinyl) and 963 cm^{-1} (ωCH_2 [$\text{C}=\text{CH}_2$]), whereas the stretching modes for CH_3 and CH_2 of the alkyl chain are found at 2972 and 2928 cm^{-1} respectively.

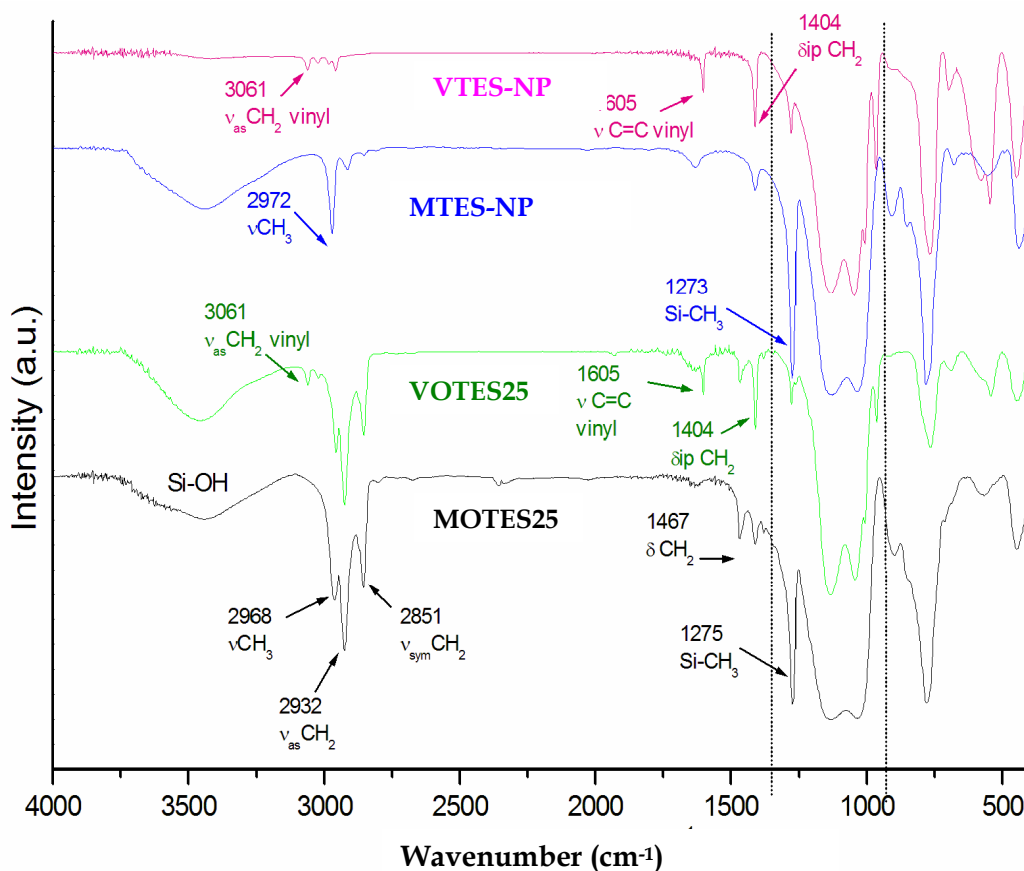


Fig. 109: FT-IR spectra of MTES-NP and VTES-NP and of binary systems with OTES (25 mol. %)

Two main bands due to the Si-O-Si bonds stretching vibrations are present in the range 1200-1000 cm^{-1} . For MTES based-NP, the peaks are found at 1136-1132 cm^{-1} and at 1036-1032 cm^{-1} respectively; in the case of VTES-based NP, the signals are detected at 1136 cm^{-1} and 1044 cm^{-1} . The two peaks are attributable to T_n cube-like silsesquioxanes with $n > 8$. However, the fact that a second peak at 1040-1030 cm^{-1} accompanies the

band at 1136 cm^{-1} suggests the presence of double chain, ladder like oligomeric species. The presence of T_n cube-like products (cages), variously substituted ($R = \text{methyl, vinyl...}$) is also supported by the presence of bands in the range $550\text{-}585\text{ cm}^{-1}$, typical of $R\text{-SiO}_{1.5}$ networks.

Orel et al. proposed to assess the proportion between similar but different condensation products on the basis of the relative height ratio (R) between the peaks of the doublet in the Si-O-Si bonds range [153]. R values are indicative of the condensation state of the gel; if $R > 1$ a "beads on a string" - like structure is present (see figure pag. 45), in which more T-cube like species are connected together by open chain polymeric siloxane and few ladder-like structures are present. $R < 1$ values corresponds to a small amount of T cube-like species and a predominance of open chain polymeric siloxane species, whereas in the case of $R \sim 1$ the products are mainly irregular T_n ($n = 8, 10$ and 12) cages connected with short ladder like bridging 4-member rings.

In the case of methyl, the calculated R value is almost 1 for low ATEs contents (10 and 25%) and becomes > 1 when the ATEs load increases. The samples with the octyl chain show the opposite behaviour, $R > 1$ for the 10% of OTES and $R \sim 1$ when increasing OTES load. In the case of vinyl, the addition of the precursor with the octyl alkyl chain changes the intensity ratio of the peaks respect to pure VTES derived NP ($R < 1$) resulting in a $R \gg 1$ ratio. However, these results should be carefully considered since the validity of the model is not well verified for siloxane networks obtained from different alkoxy silane precursors.

8.5.4 Multinuclear NMR chracterization

8.5.4.1 ^{29}Si MAS NMR

Table 41 reports the ^{29}Si NMR chemical shifts, the assignments and the integral value of the detected species. The table reports the results for selected samples in comparison with MTES-NP data.

Sample	T ³ (%)	T ² (%)	T ³ (ppm)	T ² (ppm)
MTES-NP	70.8	29.2	-65.0	-55.5
MATES 10	70.8	29.2	-65.1	-55.6
MATES 75	71.9	28.1	-66.9	-56.7
MOTES 10	72.2	27.8	-65.2	-56.7
MOTES 25	71.7	28.3	-65.4	-55.7

Table 41: ^{29}Si NMR data - chemical shifts and estimated ratio between the T units [247]- in MTES derived samples.

All the samples give rise to a network constituted by T² {RSi(OSi)₂OR'} and T³ {RSi(OSi)₃} units. The R-doped MTES particles appear as an homogenous family, showing the same chemical shift and a similar T²/T³ ratio, suggesting that the length of the alkyl chain has no significant influence on the condensation; unfortunately, it is not possible to distinguishing the condensation degree of the species derived from the two silane precursors.

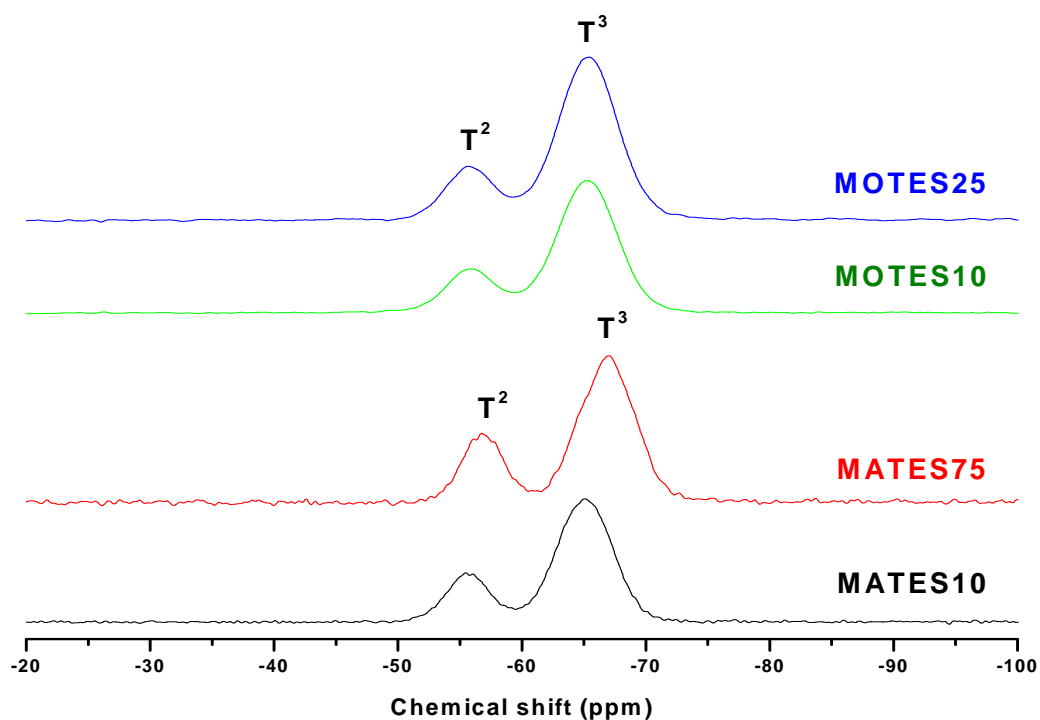


Fig. 110: ^{29}Si CP MAS NMR spectra of binary systems MOTES and MATES

Replacing MTES with VTES leads to the possibility of distinguishing both contributions (**Fig. 111**). Thus, the assignment and the evaluation of the condensation degree is possible via peak deconvolution (Table 42).

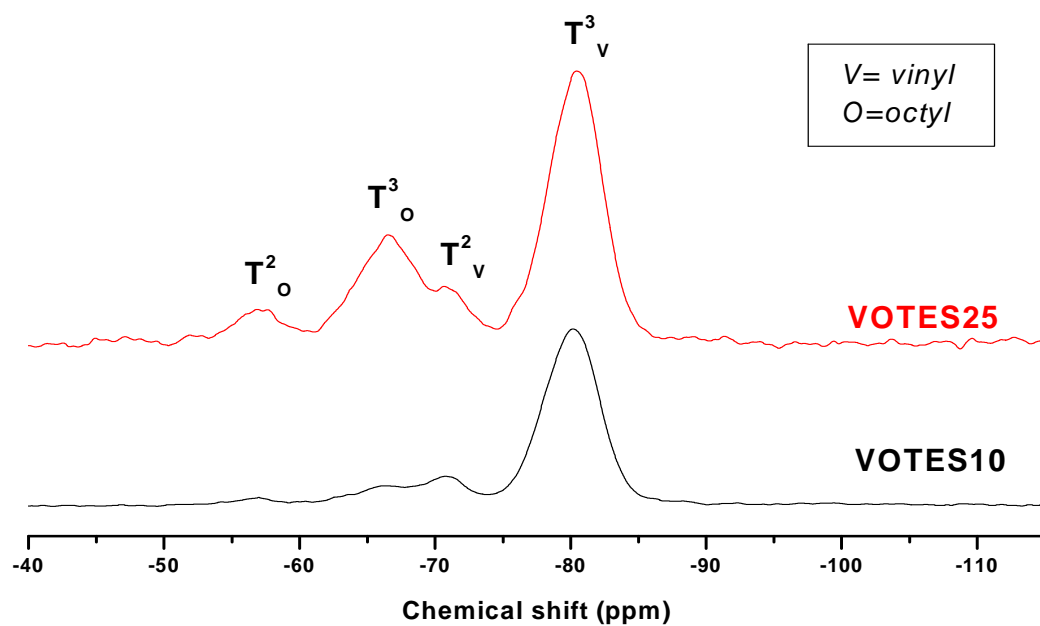


Fig. 111: ^{29}Si CP MAS NMR spectra of binary systems VOTES

Sample	T ³ (%)	T ² (%)	T ³ (ppm)	T ² (ppm)	
VTES-NP	82.4	17.6	-79.7	-70.5	
VOTES 10	85.0	15.0	-80.2	-70.8	vinyl
	83.5	16.5	-66.5	-56.9	octyl
VOTES 25	88.0	12.0	-80.4	-70.9	vinyl
	87.4	12.6	-65.9	-56.9	octyl

Table 42: ²⁹Si NMR data - chemical shifts and estimated ratio between the T units [52]

The ²⁹Si NMR results of Table 42 indicate an increase in crosslinking degree of VTES-derived units with the addition of OTES and an overall high condensation of the Si atoms in the resulting networks.

8.5.4.2 ¹³C MAS NMR

From ¹³C NMR spectra of the selected samples, small quantities of unreacted ethoxy group are present (CH₂ (labelled 1') and CH₃ (labelled 2') at 18.15 and 58.07 ppm respectively for VOTES10 and 18.12 and 57.63 ppm respectively for VOTES 25). The carbon numbering follows Fig. 112 and the assignments were compared with literature data [247] and are listed in Table 43.

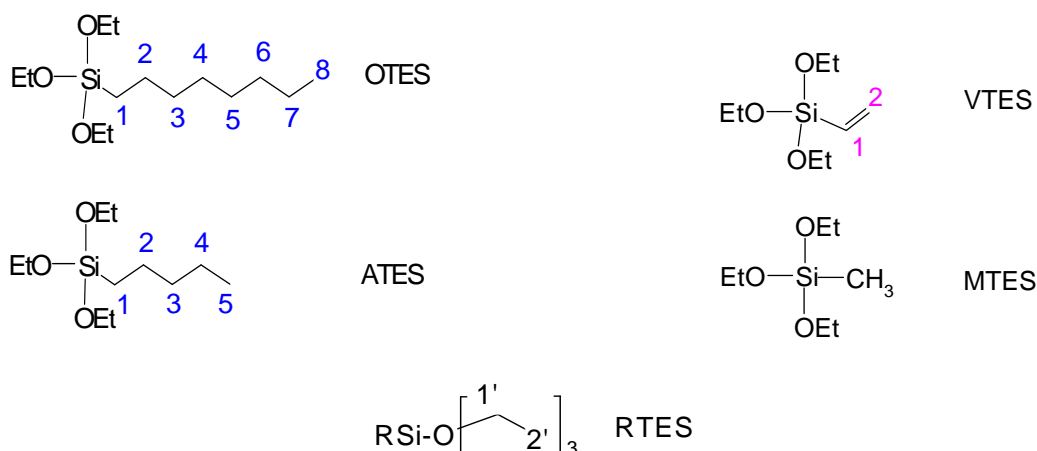
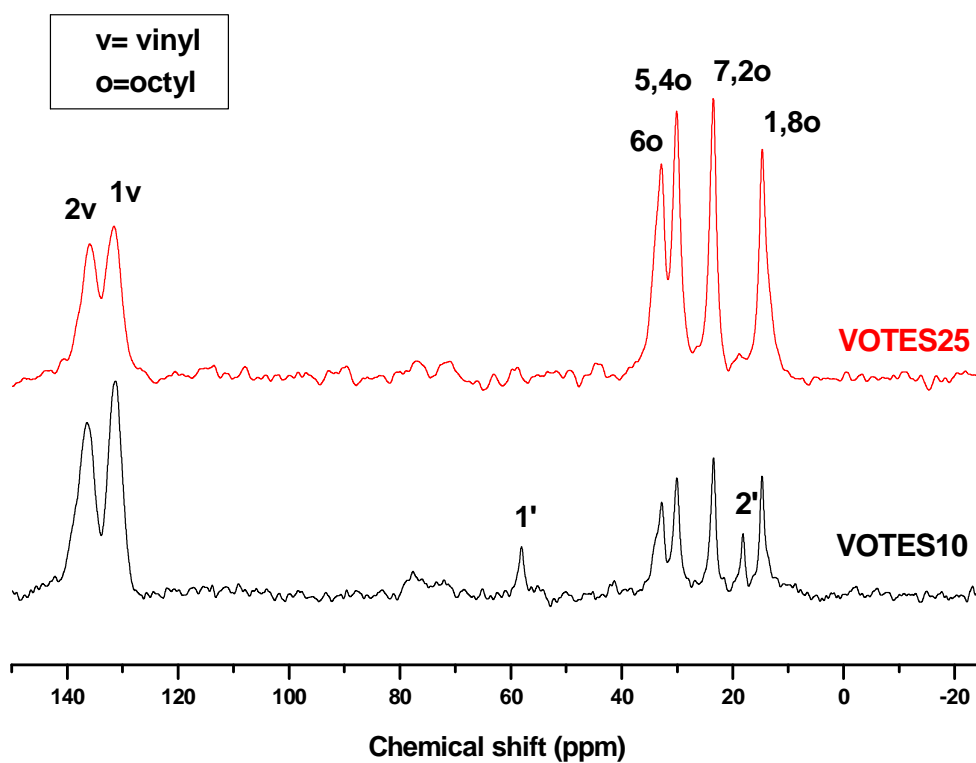


Fig. 112: carbon numbering of OTES, ATES, MTES, VTES and general R-TES

Fig. 113: ^{13}C spectra of VOTES 10 and VOTES 25 samples

	MATES10	MATES75	MOTES10	MOTES25	VOTES 10	VOTES25
Si-CH ₃	-2.84	-2.84	-2.8	-2.8		
2'		18.85			18.15	18.12
1'	58.82	58.82	58.66	58.5	58.07	57.63
			78.46			
1	12.29	12.29	1.58	1.58		
	13.84	13.84	13.08	13.08		
1, 5	14.53	14.53	1, 8	14.72	14.72	
2, 4	23.17	23.17	7, 2	23.56	23.56	
3	31.18	31.18		37.02	37.02	
		33.02	5, 4	30.2	30.2	
	36.11	36.11	6	32.87	32.87	

Table 43: ^{13}C chemical shifts and related carbons for selected binary systems

VOTES 25 and PhTES-NP show negligible residual ethoxy groups.

In the case of VOTES-NP the experiments have been run also in order to assess the conservation of the functional vinyl group.

8.5.5 SEM characterisation

Dimension and shape of the particles were characterized by SEM microscopy. The micrographs show that all the binary systems gave regularly shaped particles, as shown in Fig. 113a-b, except for MOTES 50 where the particles tend to aggregate, probably by Ostwald ripening.

The particles are regularly shaped and with a distribution of the dimension depending on the precursors reactive organic function. The average size of the particle is in the range 150-450 nm (Table 44).

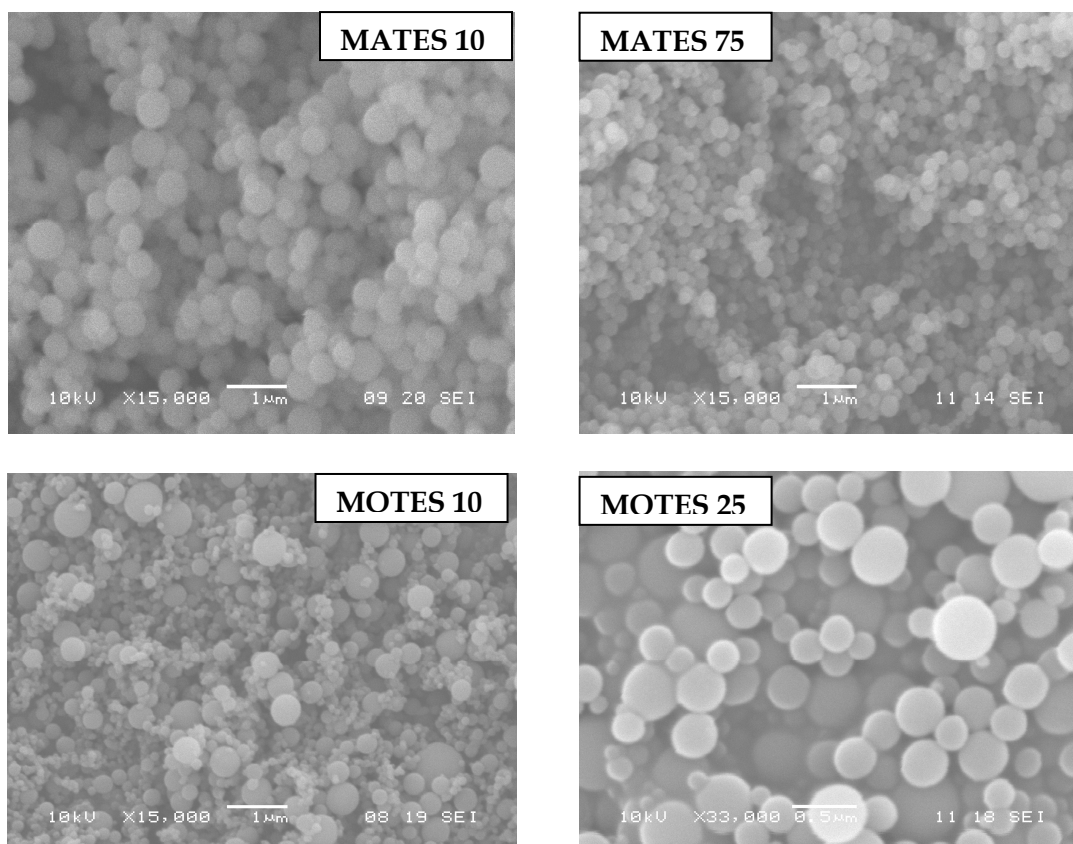


Fig. 114a: SEM micrograph of MATES and MOTES samples

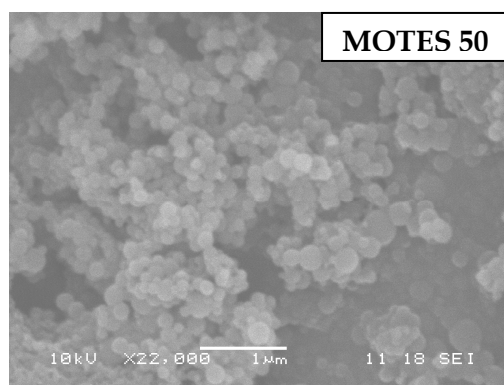


Fig. 114b: SEM micrograph of MOTES 50 sample

Sample	Average particle size
MATES10	423 nm
MATES25	380 nm
MATES35	251 nm
MATES50	191 nm
MATES75	149 nm
MOTES10	196 nm
MOTES25	295 nm

Table 44: average particle size of MTES-based system with alkyl chain (C5 and C8)

The increase in ATES load respect to MTES leads to the formation of smaller particles, as shown from the data listed in Table 44. The introduction of OTES increases the particles size; the same trend is observed for VTES-based binary systems (Table 45).

Sample	Average particle size
VOTES10	149 nm
VOTES25	222 nm

Table 45: particle size of system with VTES and OTES

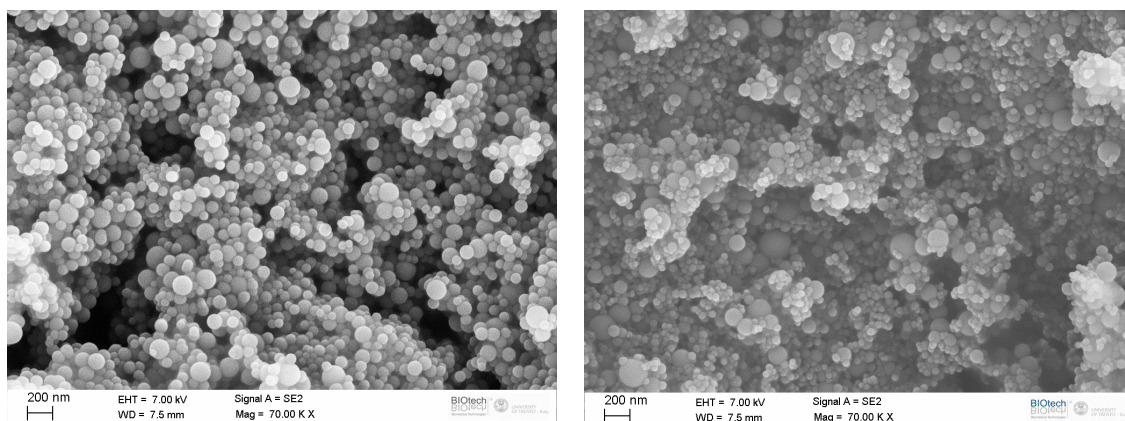


Fig. 115: FE-SEM micrograph of VOTES 10 and VOTES 25

8.5.6 N₂ physisorption characterisation

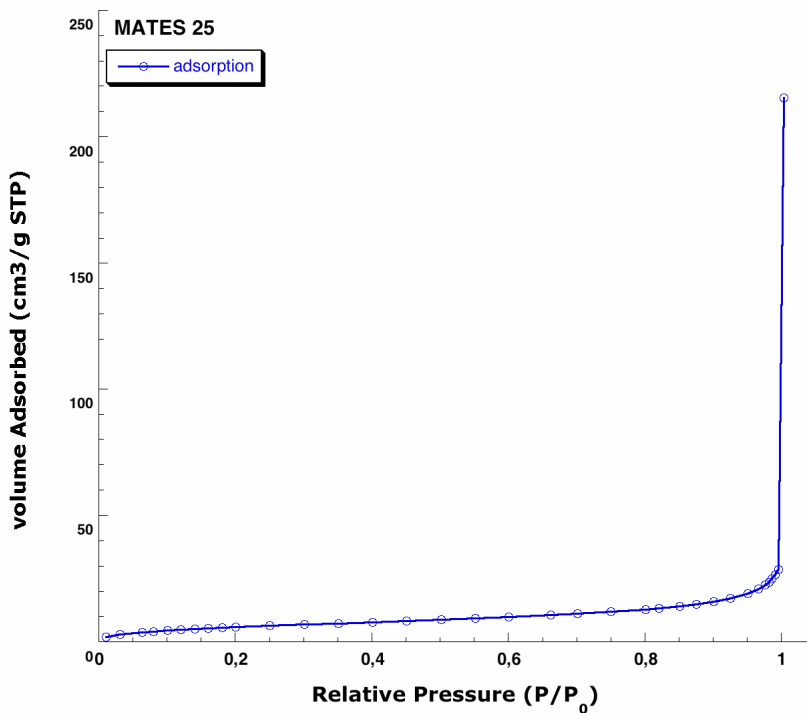


Fig. 116: N₂ adsorption isotherm for sample MATES 25

Fig. 116 presents a typical N₂ adsorption isotherm recorded on samples prepared from binary systems. For samples prepared with ATEs, isotherms of type II are found. The powders produced with low amount of ATEs were highly microporous, with some mesopores in the range 25-100 Å.

The specific surface area values, calculated by BET equation, are summarized in Table 46.

The introduction of ATEs up to 1:1 ratio to MTES (MATES 50) leads to increase in SSA and Total Pore Volume (TPV) whereas a further addition of ATEs conducts to a drop in both SSA and TPV (Table 46).

On the other hand the introduction of OTES produces the decrease of SSA and TPV.

The bulky functional group, especially in high ratio leads to large open throated pores.

Sample	BET SSA (m ² /g)	Total Pore Volume (cm ³ /g)*
MATES10	25	0.055
MATES25	27	0.057
MATES35	29	0.234
MATES50	30	0.307
MATES75	2	0.003
MOTES10	55	0.129
MOTES25	36	0.072

Table 46: N₂ physisorption data of the samples MATES and MOTES (* calculated at P/P₀=0.99)

With VTES, an increase in BET SSA and TPV is found but the quantity of micropores decreases with increasing the OTES ratio in the system.

Indeed, these results appear contradictory, since the NMR study showed an increase in crosslinking degree with increasing OTES amount.

This point requires further investigation; however, one possible explanation could be that the presence of bulky octyl groups could inhibit the condensation on the surface in a larger extent than in the case of ATES.

Sample	BET SSA (m ² /g)	Total Pore Volume (cm ³ /g)*
VOTES10	45	0.486
VOTES25	65	0.760

Table 47: N₂ physisorption data of the samples VOTES (* P/P₀=0.99)

8.5.7 Thermal analyses (TG-DTA)

Thermal analyses were performed on the binary systems with amyl and octyl. Fig. 117 shows two typical traces recorded for VOTES 25 and MOTES 25 nanoparticles

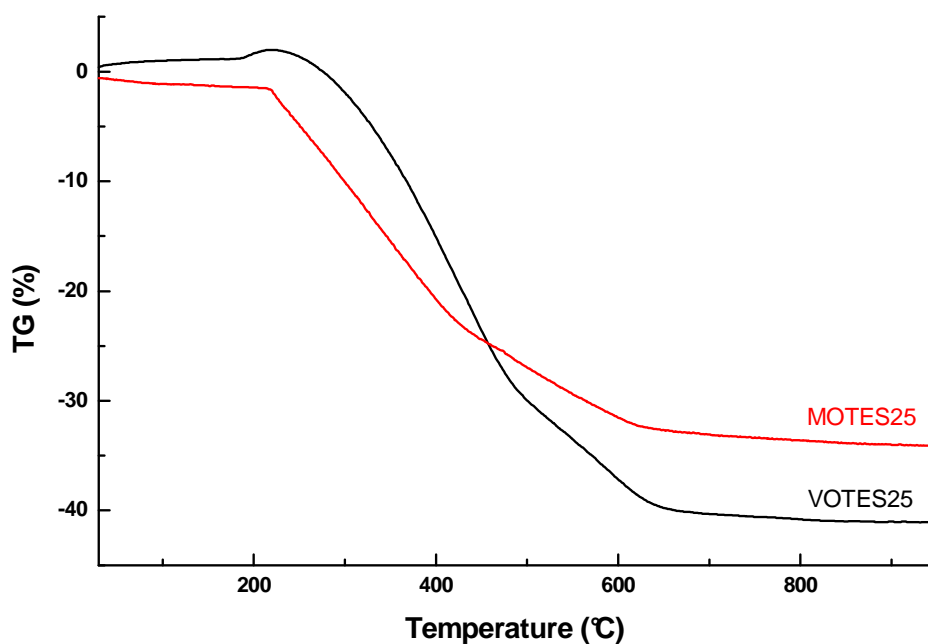


Fig. 117: TG curves of VOTES 25 and MOTES 25

As for the the VTES-NP sample shown in Fig.105, the VOTES25 sample in Fig. 117 shows an increase in weight due to the oxidation in air of the -CH=CH₂ group.

The weight loss onset temperature (T_{onset}) depends on the presence of MTES or VTES and decreases with increasing the amount of the second precursor bearing the long alkyl chain

TG traces are characterized by two weight loss steps, and the second step is always around 10% (Fig. 118). The total weight loss has the following trend: MATES75 > VOTES25 > VOTES10 > MOTES25 > MOTES10 > MATES10. This suggests that the mass loss depends on two parameters: nature of the alkyl chain (octyl > amyl) and amount of long chain precursor (75% > 10%).

Sample	Total weight loss	Loss steps	T_{onset}
MATES 10	22.9%	14.8% (25-850°C)	209°C
		8.1% (25-850°C)	
MATES 25	25.7%	18.6% (280-900°C)	231°C
		8.1% (25-850°C)	
MATES 35	33.7%	28.5% (100-900°C)	212°C
		5.2% (100-900°C)	
MATES 50	43.3%	39.4% (100-900°C)	202°C
		3.9% (100-900°C)	
MATES 75	56.0%	56% (100-900°C)	212°C
MOTES 10	22.5%		218°C
MOTES 25	32.3%		212°C
VOTES 10	34.7%	19.2% (100-900°C)	258°C
		15.5% (100-900°C)	
VOTES 25	43.3%	30.9% (100-900°C)	225°C
		12.4% (100-900°C)	

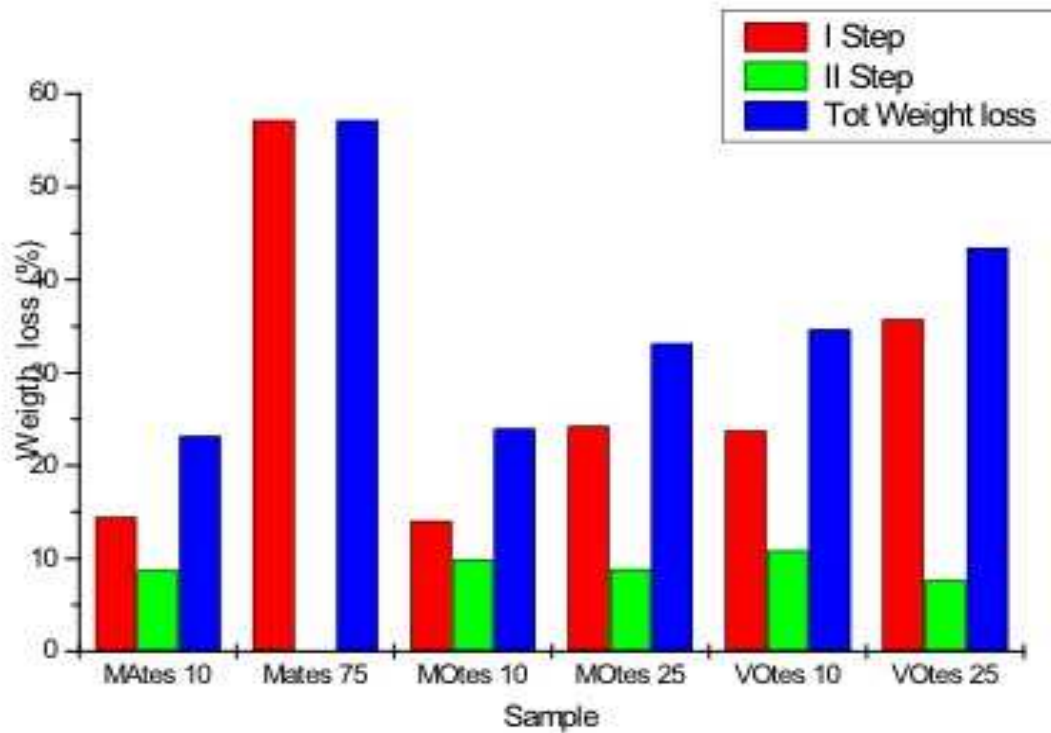


Fig. 118: W_{loss} and loss steps for binary systems

8.5.8 Contact angle measurements

Contact angle measurements were performed on films obtained by deposition of NP suspensions on clean soda-lime sheets by spin coating.

Different suspensions and different spin-coating rates were tested. The parameters are listed in the following table.

Suspension	RSiO _{1.5}	EG	H ₂ O	EtOH	solvent	[Si] _{final}
A	400 mg				-	
B	0.228 mg	100 μ l	25 μ l		-	10% v/v
B2	100 mg	100 μ l	50 μ l	454 μ l	-	10% v/v
C	100 mg	100 μ l	50 μ l	362.2 μ l	H ₂ O (90.8)	5% v/v
D	100 mg	43.8 μ l	10.9 μ l	454 μ l	-	10% v/v

... Continues from previous page

Suspension	RSiO _{1.5}	EG	H ₂ O	EtOH	solvent	[Si] _{final}
D2	100 mg	43.8 µl	10.9 µl	439.1 µl	H ₂ O (15.4)	10% v/v
E	100 mg	43.8 µl	10.9 µl	-	Acetone 454 µl	10% v/v
F	100 mg	43.8 µl	10.9 µl	227.25 µl	Acetone 227.25 µl	10% v/v
G1	100 mg	43.8 µl	10.9 µl	666.7 µl	Acetone 333.3 µl	5% w/v
G2	100 mg	43.8 µl	10.9 µl	333.3 µl	Acetone 166.7 µl	10% w/v
G3	50 mg	43.8 µl	10.9 µl	333.3 µl	Acetone 166.7 µl	20% w/v

EG = ethylene glycol

Spin-coater rates

Spin coater						
Label	I step speed	I step time	II step speed	II step time	III step speed	III step time
1	150 rpm	900"	-	-	-	-
2	200 rpm	800"	-	-	-	-
2a	200 rpm	800"	250 rpm	60"	-	-
3	250 rpm	60"	500 rpm	600"	-	-
4	250 rpm	60"	500 rpm	500"	1000 rpm	400"
4a	250 rpm	30"	500 rpm	180"	1000 rpm	180"
5	250 rpm	5"	500 rpm	5"	1000 rpm	400"
6	100 rpm	120'	125 rpm	240"	250 rpm	400"

Samples prepared where dried either at RT or in oven for 24 h at 50 °C.

Film morphology was observed by means of SEM. Thick and relative homogeneous films were obtained, in agreements with the following SEM micrographs.

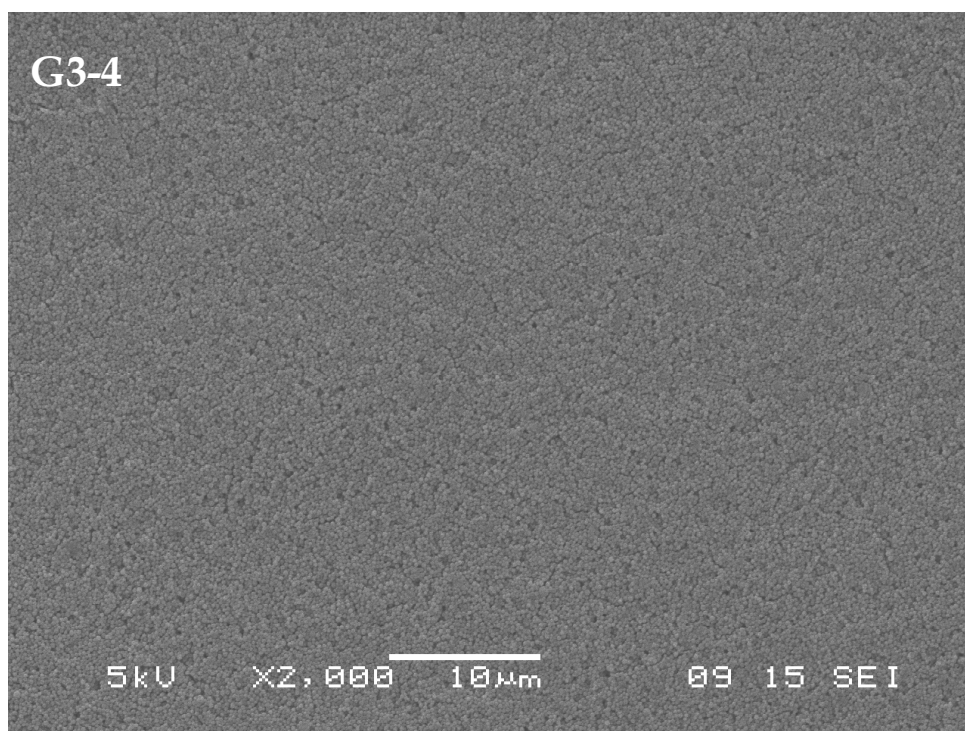
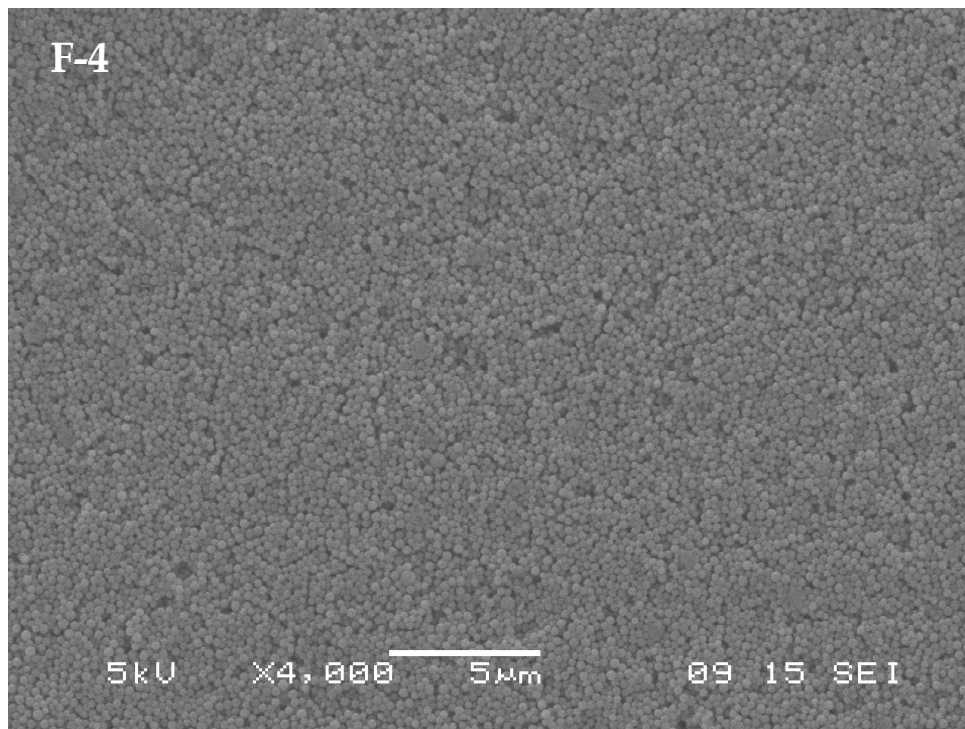


Fig. 119 SEM micrograph of film F-4 and G3-4

Good films were prepared with suspension 3G and F and spin program 4 (sample G3-4 and F-4 respectively).

Exploiting the same parameters, films with other organic-modified NP were prepared.

Both sessile and equilibrium angle were measured and are listed in the following table

Sample	Static angle	Equilibrium angle
MTES-NP	$119.8 \pm 4.0^\circ$	$80.7 \pm 6.2^\circ$
ETES-NP	$134.4 \pm 2.1^\circ$	$91.0 \pm 4.3^\circ$
VTES-NP	$115.8 \pm 3.9^\circ$	$62.4 \pm 6.6^\circ$
PhTES-NP	$140.5 \pm 3.6^\circ$	$128.9 \pm 3.9^\circ$
MATES 25	$108,4 \pm 4.3^\circ$	$67.5 \pm 5.8^\circ$
MOTES 25	$113.7 \pm 1.4^\circ$	$71.0 \pm 8.6^\circ$
MATES 75	$145.7 \pm 4.0^\circ$	$145.6 \pm 3.6^\circ$

Fig. 120: data obtained by means of contact angle measurements

All the samples have a high contact angle when a drop of water is placed on their surface, indicating the hydrophilicity of the layer. After vibration only two samples show again high contact angles: PhTES-NP and MATES 75. Especially the last one exhibited a roll over effect (the drop tend to slip on the surface) when the drop of water was poured on to the film. From the data collected and the behaviour of the water drop, it is possible to suggest a super-hydrophobic behaviour of these two surfaces.

In the case of the other samples the vibration could have let to rearrangement of the film or creation of cracks. More analyses have to be accomplished to elucidate this point.

8.6 Dye doping

NP prepared both from a single precursor and two organosilanes were doped with Rhodamine 6G in a molar ratio Si : R6G = 1: $1 \cdot 10^{-4}$.

Particles were prepared following the syntheses parameters reported in Fig. 93 for single precursor-NP. Rhodamine was added to the ethanol solution in step I.

Fig. 121 shows the morphology of dye-doped ETES-NP. Particles almost preserve shape and size distribution.

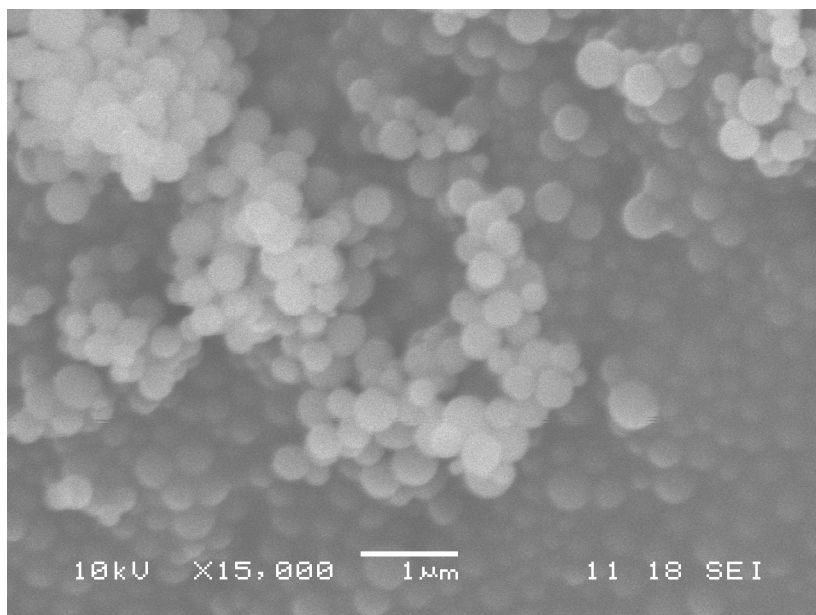


Fig. 121: SEM micrograph of ETES-R6G NP

A preliminary study on the optical properties of the doped NP was undertaken, with the aim to observe possible emission changes vs. NP composition.

The dye absorption spectra (Fig. 122a), recorded on a spectrofluorometer JASCO-FP 770 instrument in the 400-600 nm range, present the main absorption peak at 535 nm and two shoulders at 500 and 470 nm respectively, attributed to monomer, dimer and trimers [249].

The dye emission spectra were recorded spectrofluorometer JASCO-FP 770 instrument in the 500-800 nm range with an excitation wavelength of 480 nm. The normalized spectra are reported in Fig. 123.

Absorption

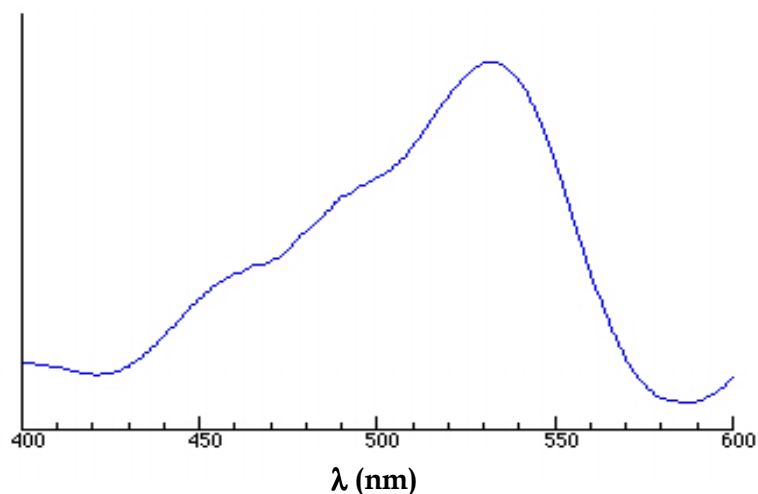


Fig.122a: absorption spectrum for MTES-1-R6G NP

Emission spectra λ_{ex} 480 nm

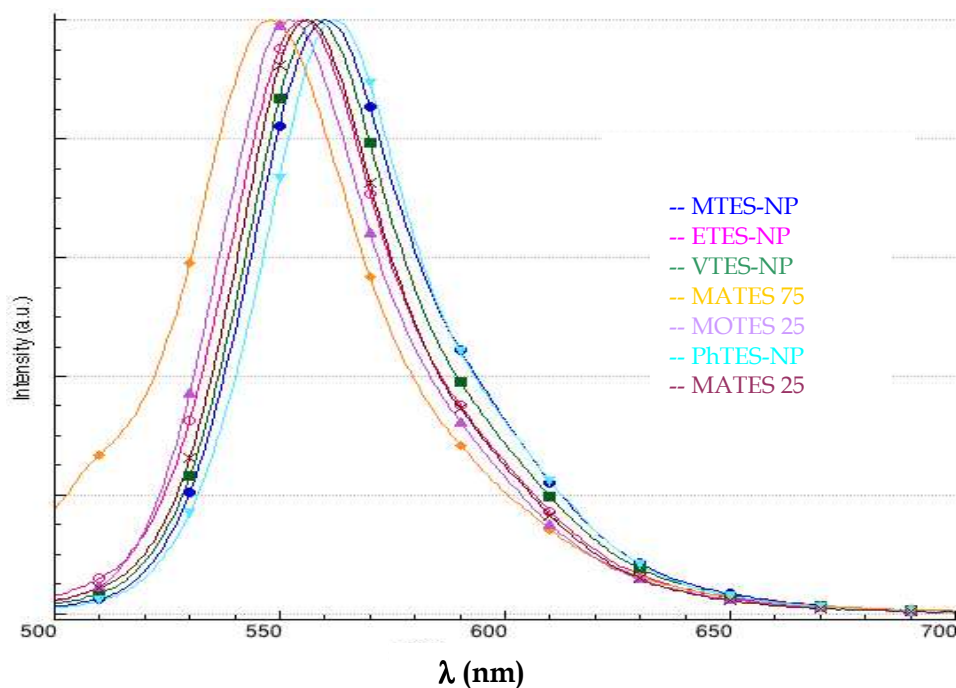


Fig. 122b: emission spectra of R6G doped NP (λ_{ex} 480 nm)

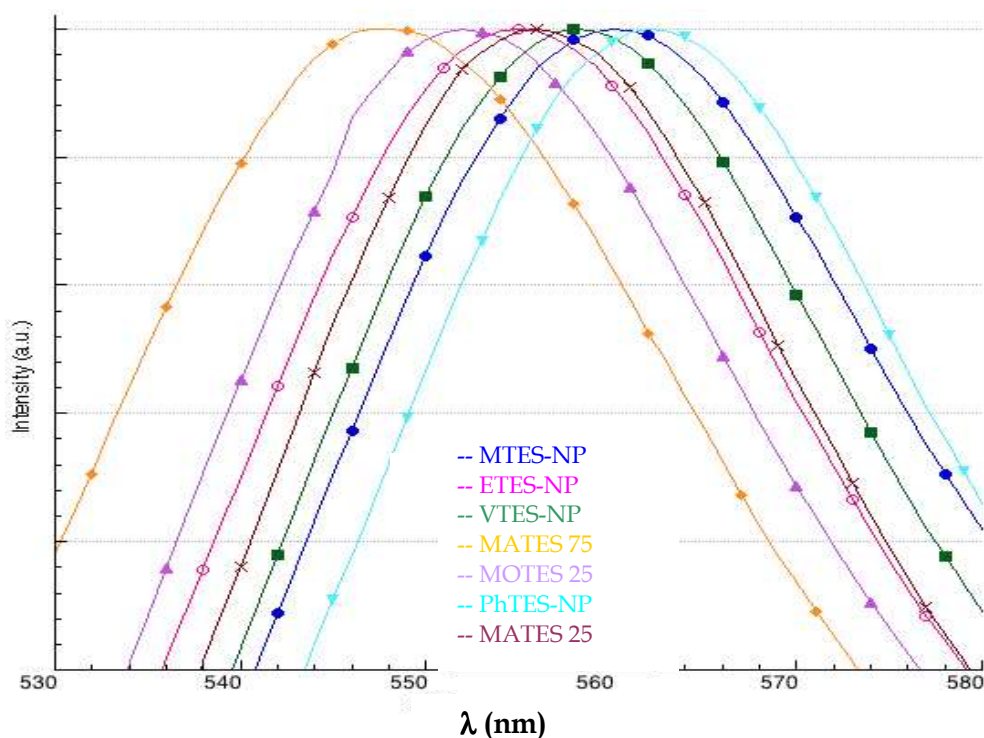


Fig. 123: emission spectra of R6G doped NP (λ_{ex} 480 nm) enhancement

Spectra are characterized by a single asymmetric peak whose position changes with changing the composition of the nanoparticles according to the following trend: MATES75 < MOTES25 < MATES25 = ETES-NP < VTES-NP < MTES-NP < PhTES-NP

Rhodamine 6G emission is affected by the nature of the organic group linked to the siloxane network suggesting that dye molecules, entrapped inside the cavities of the network, experience different local environments. In NP prepared from MTES and ATEs or OTEs, the quantity and the nature of the long chain bearing precursor also influences the dye emission leading to a blue shift respect to the case of pure MTES derived NP.

8.7 High temperature behaviour of organic-modified NP

With the purpose to ascertain the ability of prepared nanoparticles to conserve a regular morphology after a high temperature treatment, a preliminary study has been undertaken on NP samples listed in the following table, in collaboration with Prof. G.D. Sorarù of Dept. of Materials Engineering and Industrials Technologies of the University of Trento.

Sample
MTES-NP
PhTES-NP
MATES 25
MATES 50
MATES 75

NP samples were heated in argon flow (100 ml/min) from 30 to 1000 °C with a heating rate of 10°C/min. The morphology characterization was conducted on a FE-SEM Supra40 Zeiss in high vacuum modality. Measurements were taken in the laboratories of the BIOTech Research Centre in Mattarello (TN).

Measurements of particles size were accomplished on FE-SEM micrographs of pristine NP and heat-treated samples.

FE-SEM images of different samples are reported on Figures 124-133.

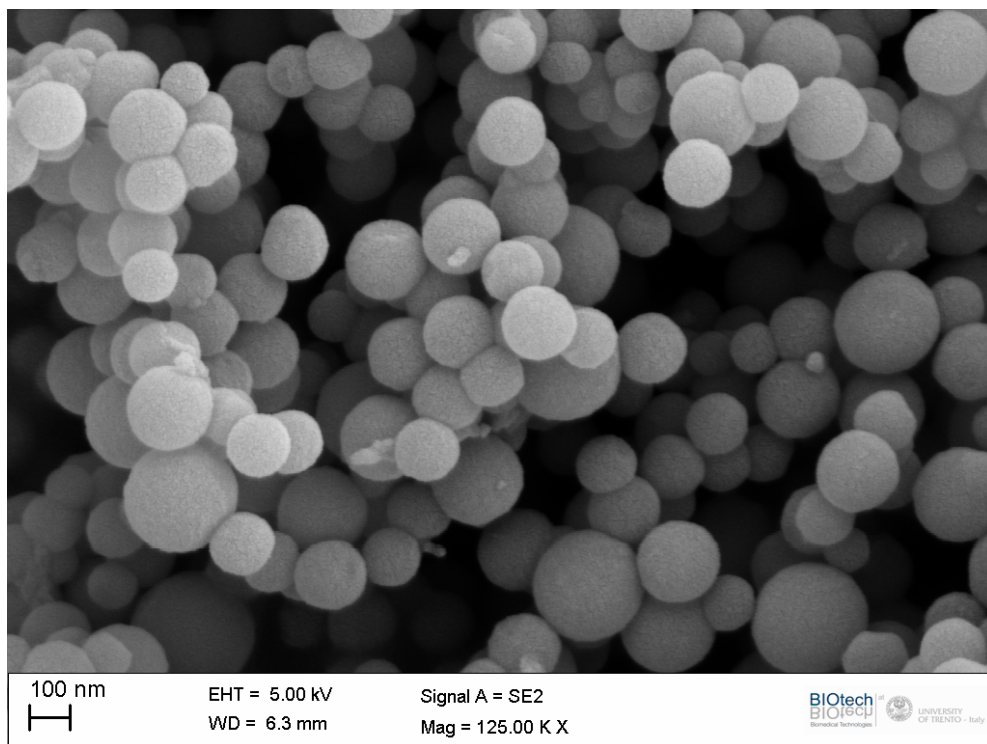


Fig. 124: MTES-NP

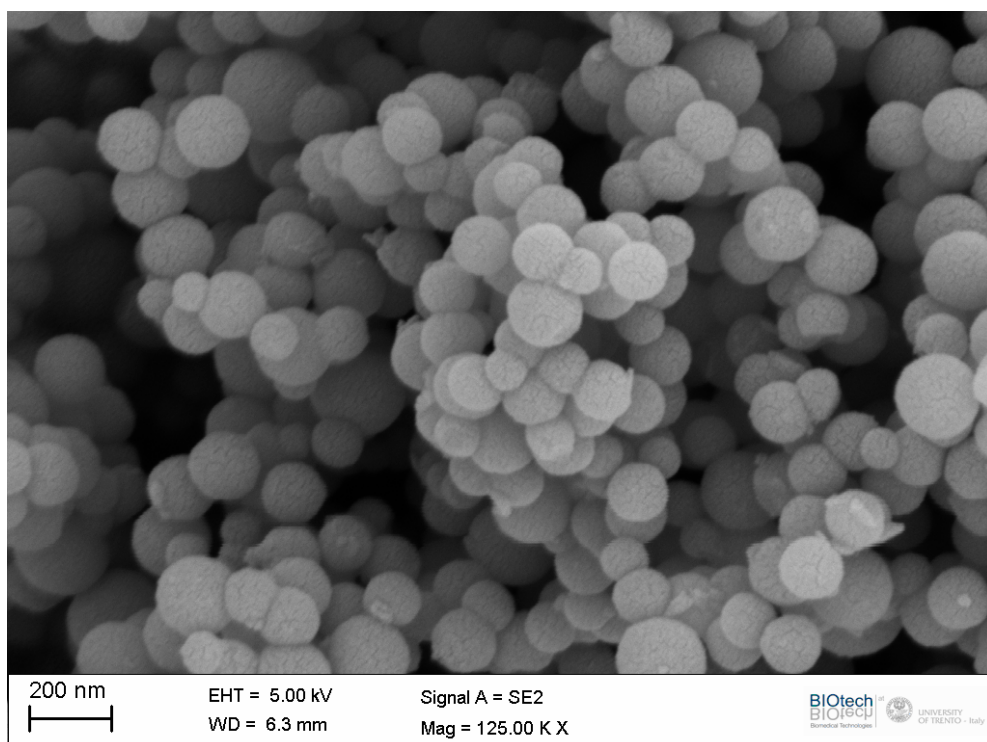


Fig. 125: MTES-NP heated at 1000°

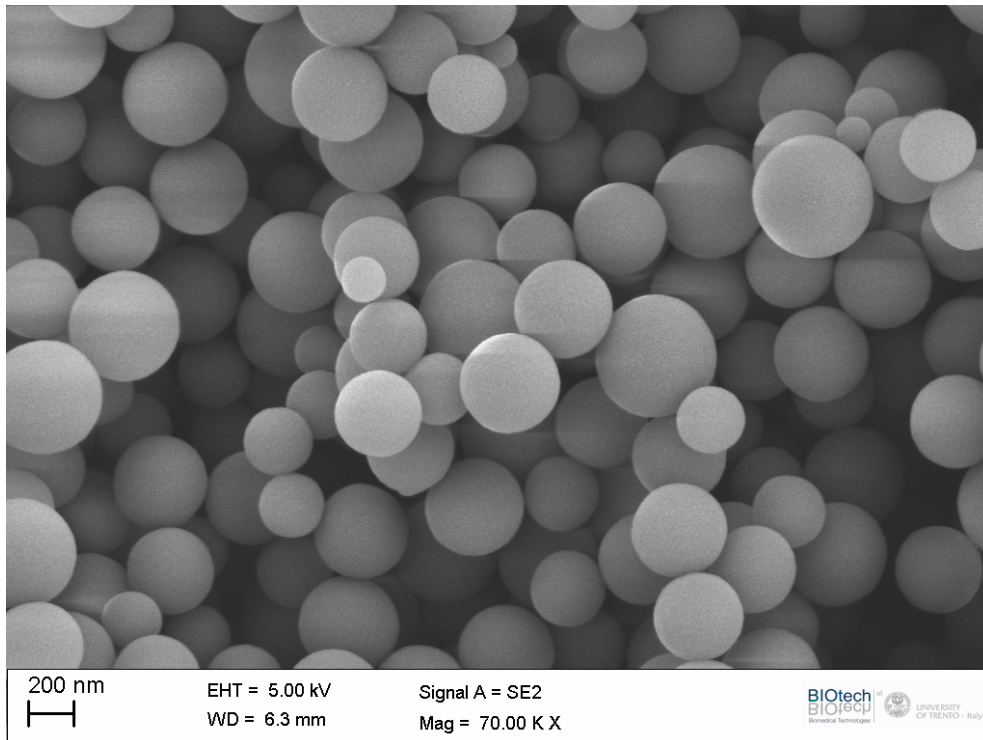


Fig. 126: MATES 25 particles

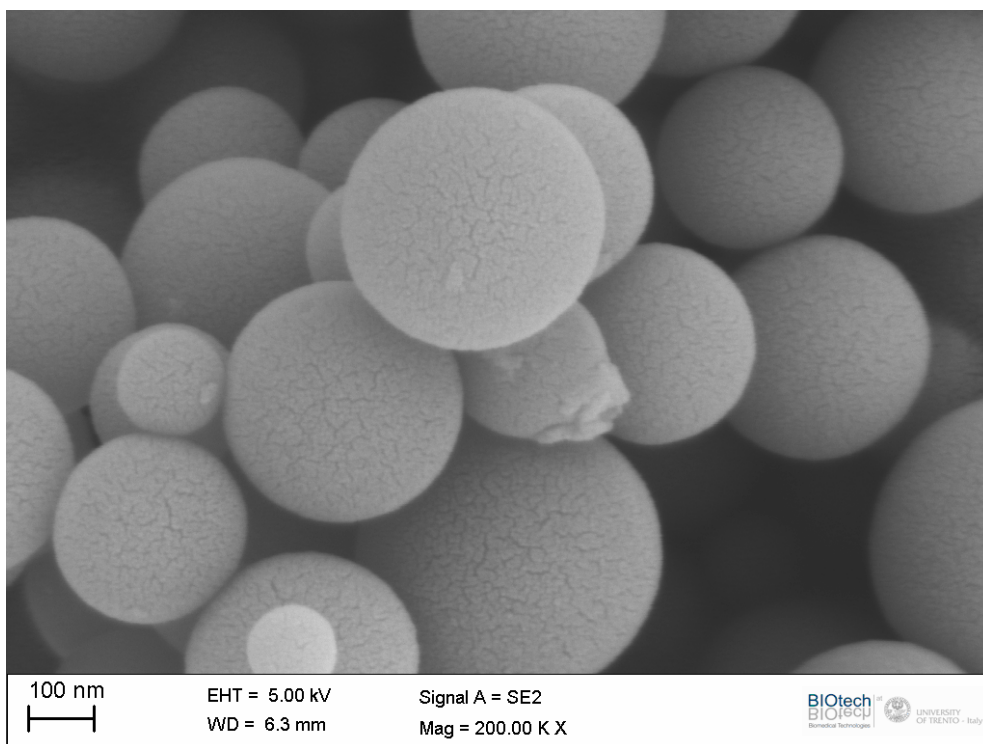


Fig. 127: MATES 25 particles heated at 1000°

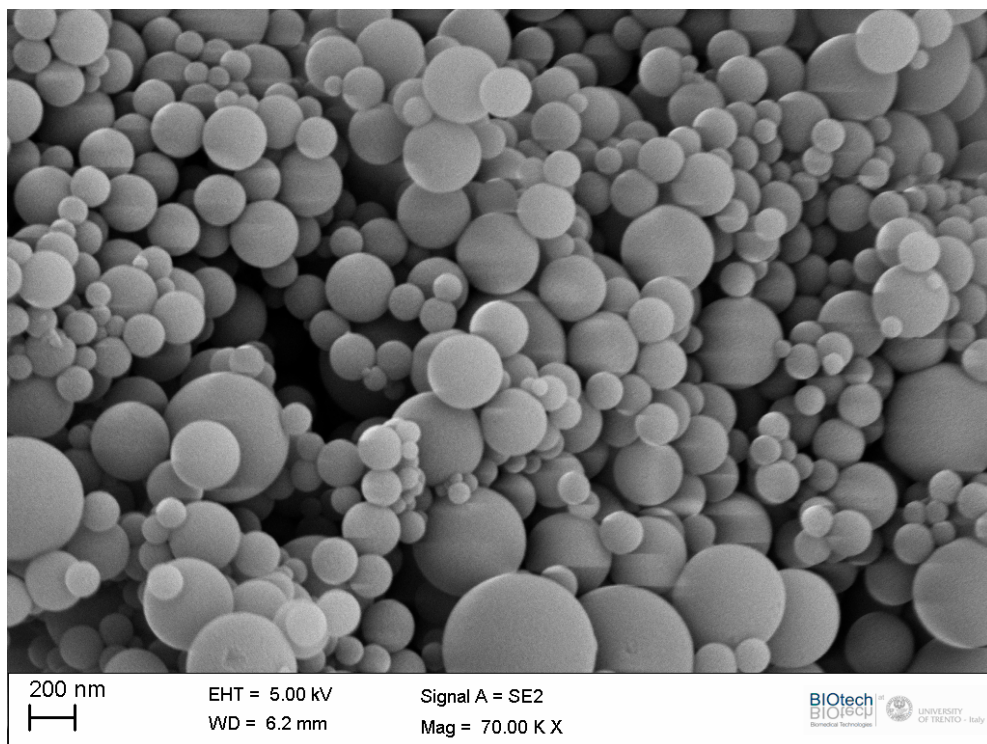


Fig. 128: MATES 50 particles

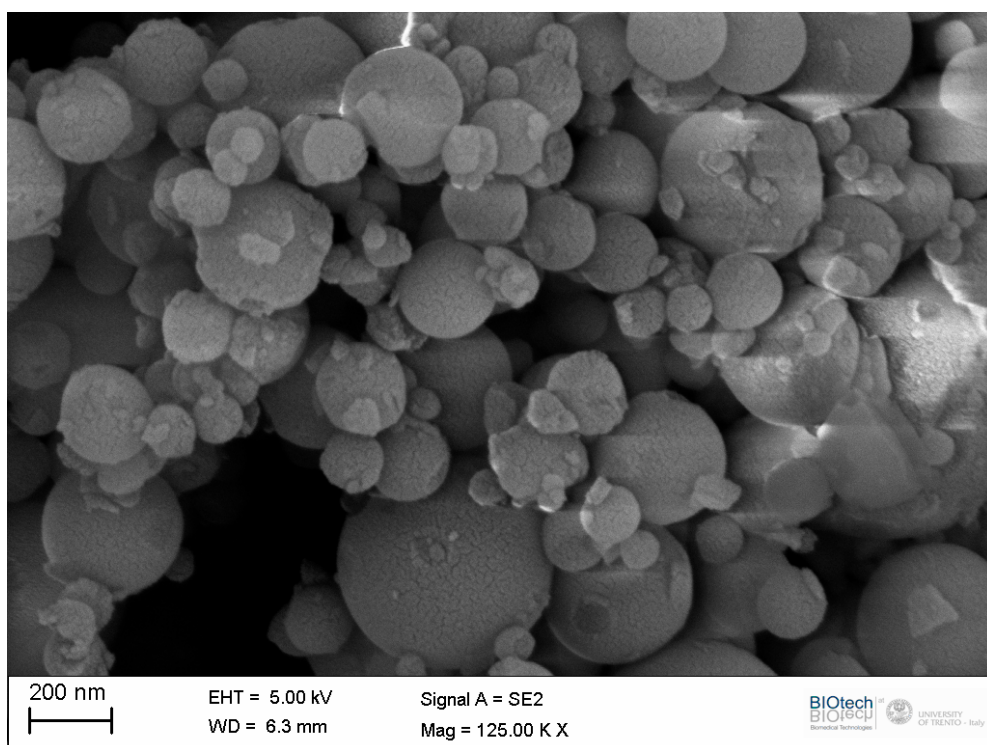


Fig. 129: MATES 50 particles heated at 1000°

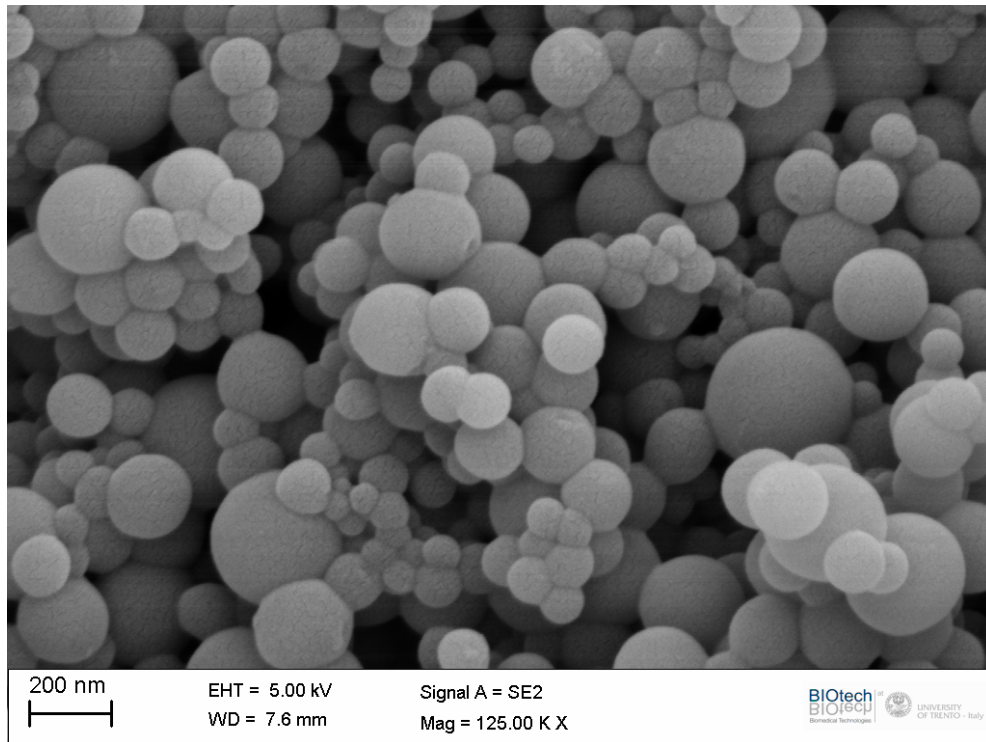


Fig. 130: MATES 75 particles

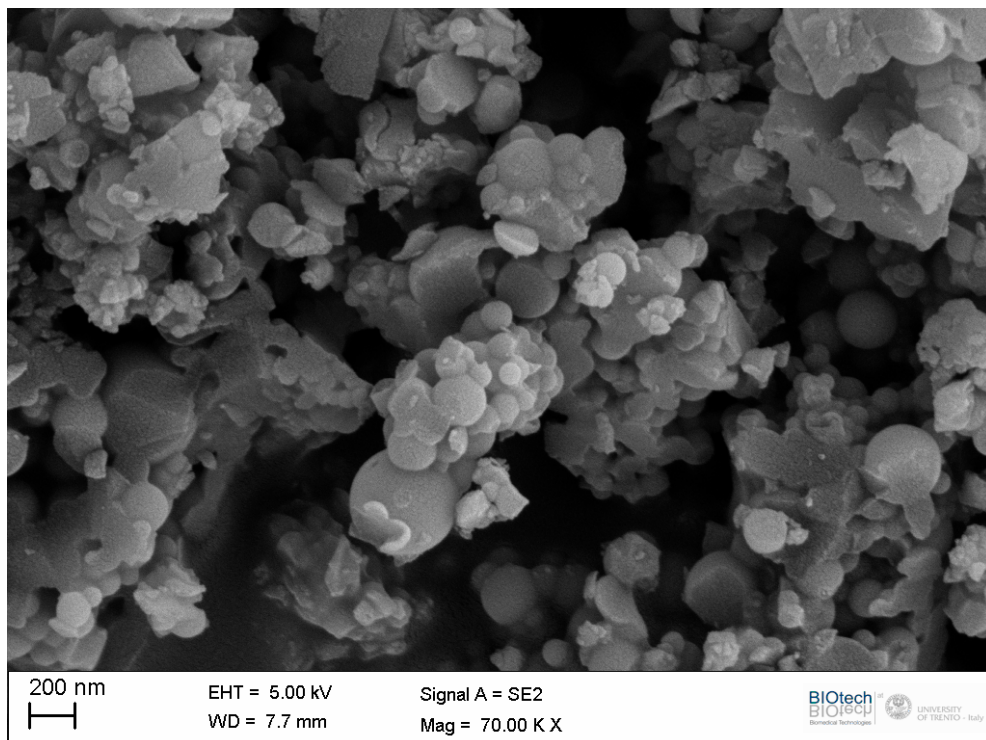


Fig. 131: MATES 75 particles heated at 1000°

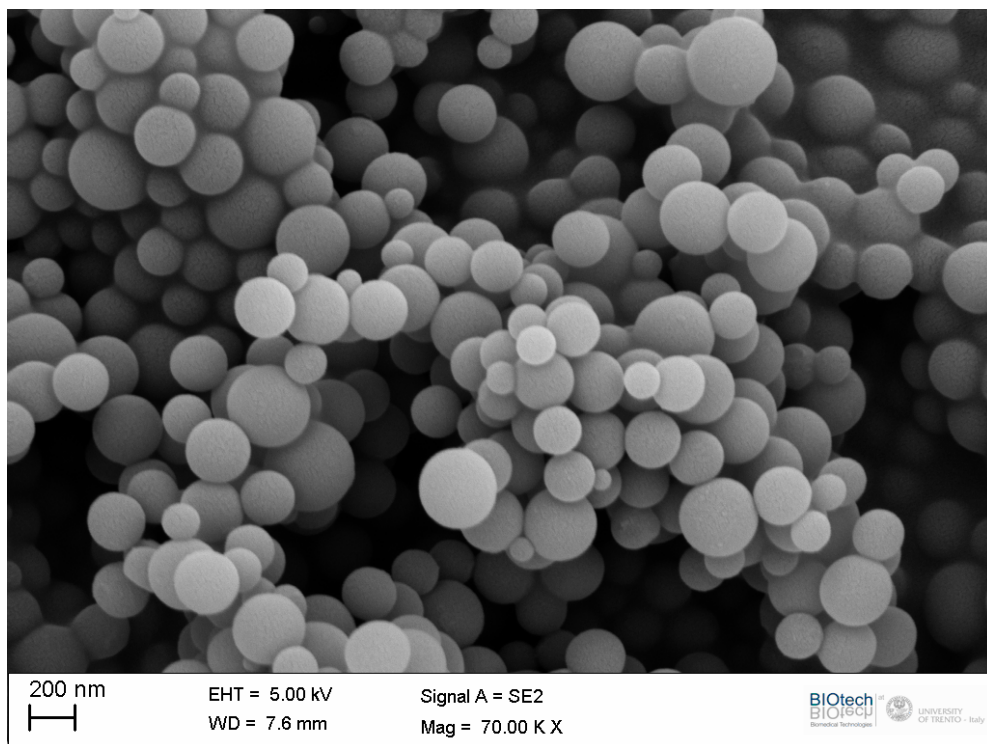


Fig. 132: PhTES-NP

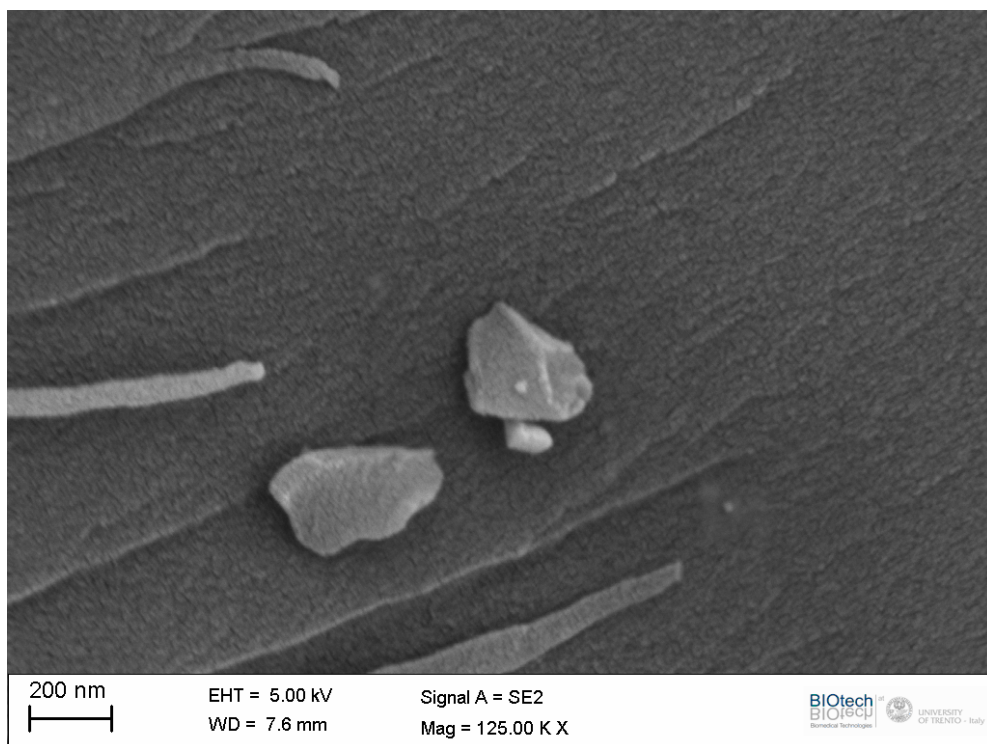


Fig. 133: PhTES-NP heated at 1000°

The NP composition affects the microstructural features of samples after heating at 1000°C.

FE-SEM micrographs (Fig. 124-Fig. 131) highlight that MTES-NP and MATES-derived NP with ATEs load up to 50 molar % retain the spherical shape after the thermal treatment at high temperature. Increasing ATEs content, a progressive aggregation of pristine NP is observed (MATES 75-Fig. 131).

In the case of phenyl-modified NP (Fig. 132 and Fig. 133) an almost flat surface sample is obtained after thermal heating at 1000°C. Indeed, the thermoplastic behaviour of particles prepared from phenyltriethoxysilane was recently reported in the literature [250] and exploited to produce dense films. It is noteworthy that a beginning of aggregation due to the thermoplastic behaviour was detected also on untreated PhTES-NP under the electron beam of the FE-SEM instrument.

8.7.1 Evolution of NP sizes

The average size of the particles before and after the heat-treatment, size distribution ranges and diameter decrease after thermal treatment are reported in the following table.

Sample	Before treatment		After treatment		Decrease (%)
	Average diameter	range	Average diameter	range	
MTES-NP	169 nm	54-296 nm	150 nm	95-257 nm	11.2
MATES 25	380 nm	156-543 nm	263 nm	68-468 nm	30.8
MATES 50	191 nm	51-514 nm	214 nm	58-491 nm	-
MATES 75	149 nm	47-360 nm	-	-	-
PhTES-NP	255 nm	105-436 nm	-	-	-

Table 48: NP sizes before and after treatment

The average particle diameter shrinks after thermal treatment in different extent, depending on the ATEs ratio (Table 48). In general the size distribution broadens, probably as a result of the growth of bigger particles at the expense of smaller spheres, as in the case of MMp 50-NP that presents a higher average size after heating with respect to that of pristine NP.

The results obtained from the preliminary study on NP morphology are noteworthy. It is known that hybrid sol-gel materials are suitable preceramic polymers, able to produce silicon oxycarbide glasses and silicon carbide-based ceramics [251-255]. Thus, the possibility to exploit hybrid NP for the preparation of SiOC-based spherical particles is exciting. Work is in progress on selected samples (MTES-NP and MATES25) in order to characterize the particle morphology behaviour at temperature higher than 1000°C and phase composition and porosity features of heated samples.

9 EXPERIMENTAL

9.1 Methacrylate-based NP (MMp-NP)

Reagents

Methacryloxypropyltrimethoxysilane (MPTMS) 98%,

Methyltriethoxysilane 99% (MTES)

Ethanol (EtOH) >99.8%

Hydrochloric acid 37%

Ammonia solution 29%

double distilled water

All reagents were used without further purification unless otherwise stated.

9.1.1 MMp-NP syntheses

The prepared samples discussed in detail in this work are listed in Table 49. The reaction parameters are the consequence of the preliminary study on MTES, exposed in Chapter 8.

The synthesis of MMp-NP is schematized in Fig. 106. Reactions were carried out in air and at RT.

Sample	MTES	MPTMS
MMp 10	90	10
MMp 25	75	25
MMp50	50	50
MMp75	25	75

Table 49: precursors molar ratio of MMp-NP samples

9.2 MMp-NP characterization

FT-IR characterization of the precursors

MPTMS and MTES FT-IR spectra and assignments can be found at pages 77 and 190 respectively.

9.2.1 FT-IR characterization of the samples

From the FT-IR spectra it is possible to observe the maintenance of the reactive methacrylate function ($\nu\text{C}=\text{O}$ at 1722 and $\nu\text{C}=\text{C}$ at 1639 cm^{-1}) and the decrease in the intensity of the peak attributed to the Si-CH₃ bond at 1273 cm^{-1} (Fig), with the decrease of MTES content.

The condensation reaction can be followed, as for the other NP systems studied in the previous paragraphs, is proved by the intensity decrease of the peaks due to the MeO- groups (2838 cm^{-1}) and by the simultaneous formation of the siloxane network (1200 - 1000 cm^{-1} range).

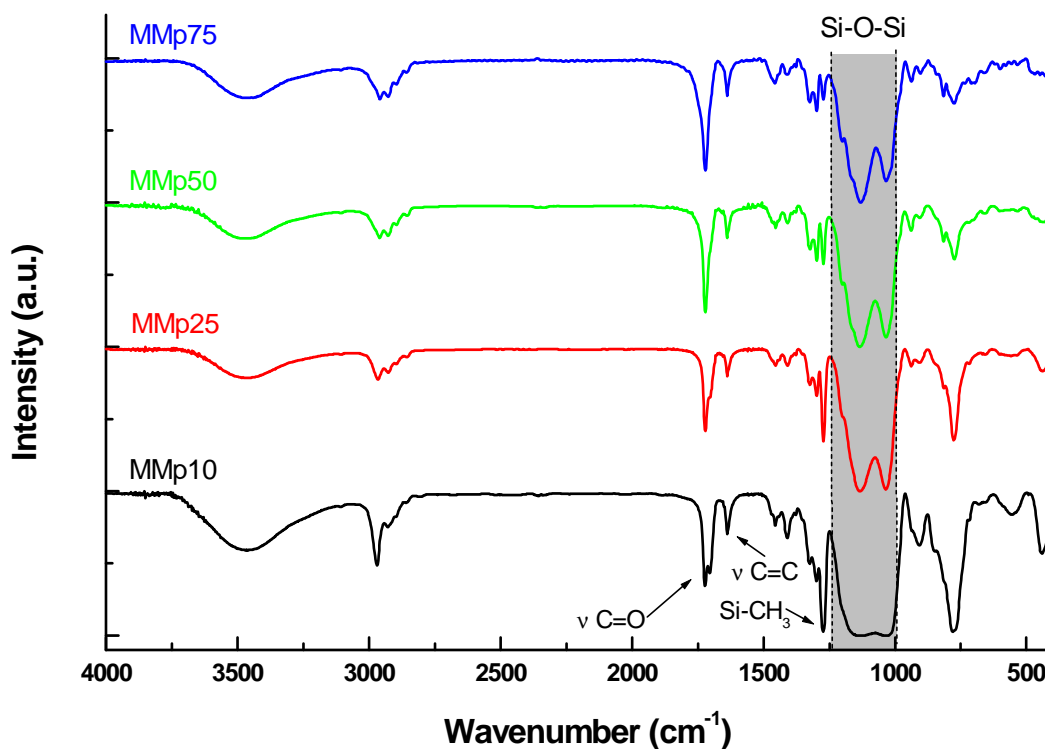


Fig. 134: FT-IR spectra of MMp-NP

All the samples present a doublet of peaks in the Si-O-Si range, the first at 1135 and the second at 1035 cm^{-1} . These bands can be attributed to the vibrations of cage like and cyclic ladder-like structures, as referred in literature.

As reported in paragraph ..., the ratio (R) between the intensity (height) of the peaks of the doublet express the proportion between cage-like structures and ladder-like or polymers in the products [153].

Increasing the amount of MPTMS in the system R passes from 1 (in MMp10) to $R > 1$ and the peaks are less broad and more defined, thus suggesting This means that there is a structure rearrangement from irregular T_n cages that are connected through short ladder like bridging 4-member oligomers to a network in which cage structures are predominant.

9.2.2 SEM characterization of MMp-NP

From the micrographs shape of the particles was observed and dimensions extracted.

Particles dimensions (Table 50) tend to decrease in average size with increasing MPTMS content, but the size distribution becomes broader with MPTMS addition.

Sample	Average particle size	range
MMp10	275 nm	164-372 nm
MMp25	250 nm	127-362 nm
MMp50	234 nm	92-366 nm
MMp75	190 nm*	116-284 nm*

Table 50: average NP size from SEM micrographs (* MMp 75 are aggregated)

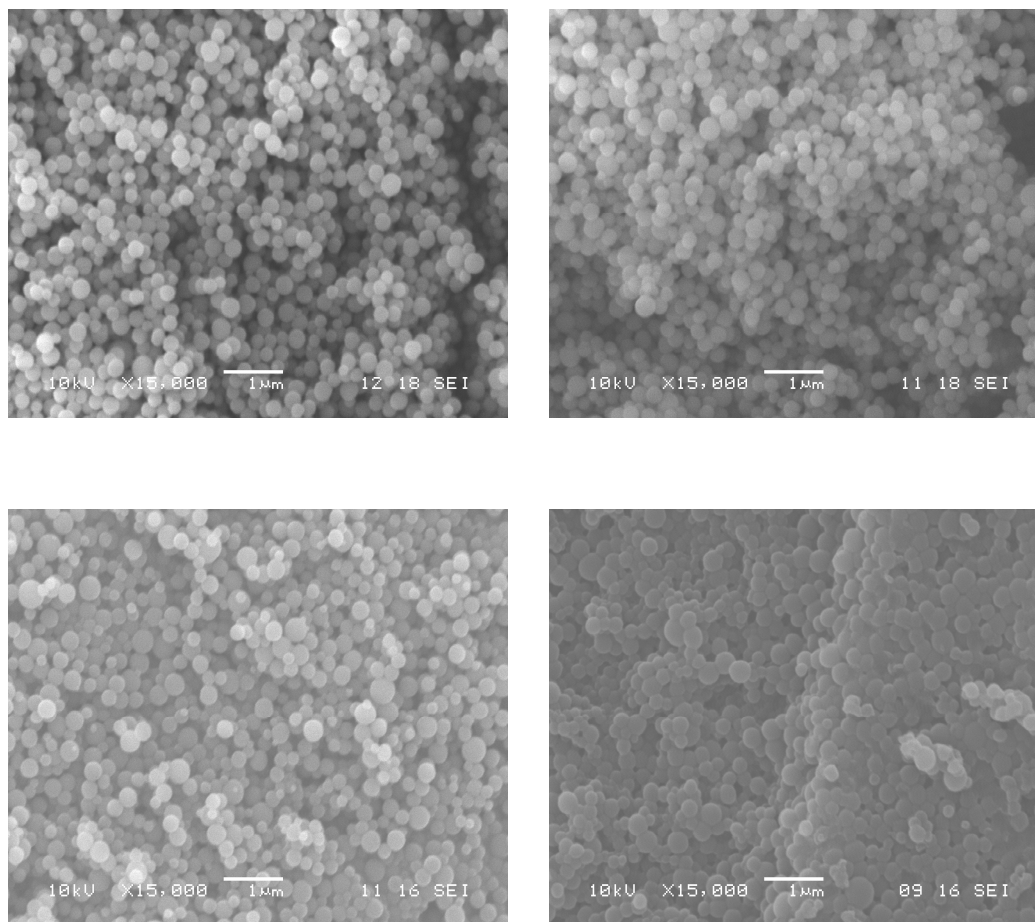


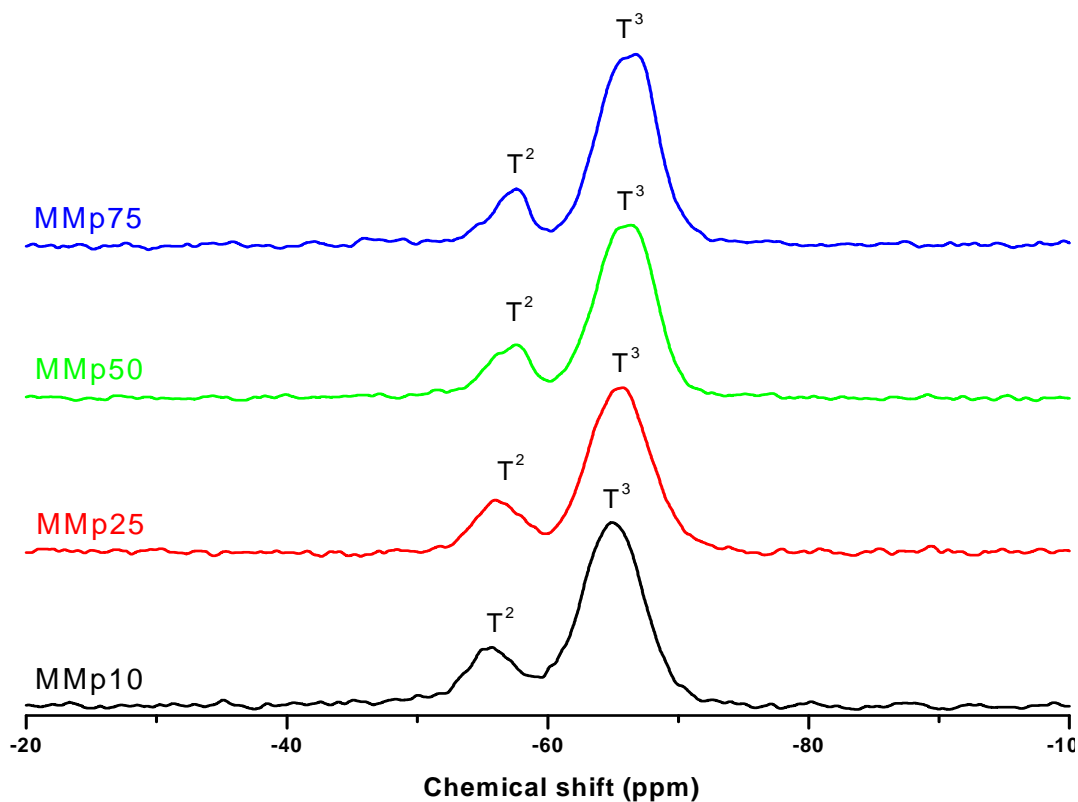
Fig. 135: SEM micrograph for MMp-NP

In the case of MMp 75 it is possible to observe a strong Ostwald ripening effect. Consequently, particles sizes were measured on single particles in selected areas where aggregation was negligible.

9.2.3 Multinuclear NMR characterisation

9.2.3.1 ^{29}Si NMR characterisation

Fig. 136 shows the ^{29}Si NMR spectra for MMp samples in various ratios. The samples are characterized by a high degree of condensation, confirmed by the calculation of the T^3/T^2 ratio (4:1).

Fig. 136: ^{29}Si NMR spectra of MMp-NP

9.2.3.2 ^{13}C NMR characterisation

^{13}C NMR experiments were run in order to check the accordance between final and nominal composition of the particles. The calculated results as listed in Table 51. The carbon numbering is shown in figure X, which reports the ^{13}C MAS NMR spectra of MMp-NP.

Sample	Si-CH _s (MPTMS)	Si-CH ₃ (MTES)
MMp10	12.7	82.3
MMp25	25.9	74.1
MMp50	46.9	53.1
MMp75	70.7	29.3

Table 51: calculated percentages of MPTMS and MTES in MMp-NP

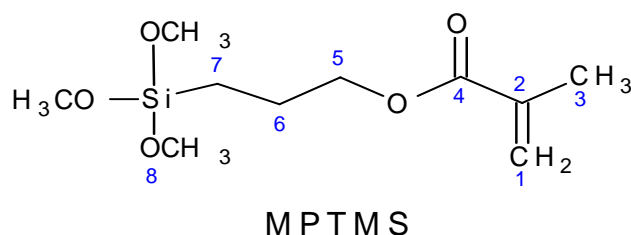
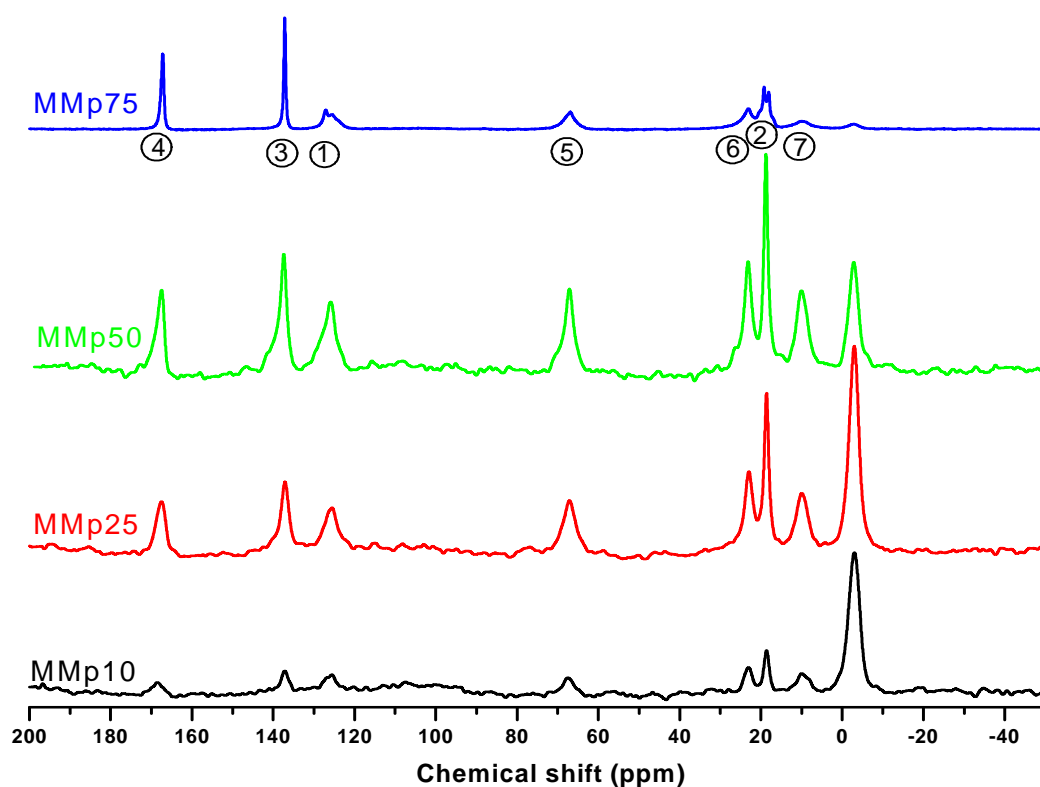


Fig. 137: ¹³C NMR spectra of MMp-NP and relative carbon numbering

From Table 51 it is possible to observe that the nominal ratio between the two precursors is almost kept in the final samples.

The hydrolysis is complete for all the samples as the peaks due to EtO- (58 and 18 ppm) and MeO- (18 ppm) groups are not detected; the peak quoted 7 presents a downfield shift due to condensation.

The polymerisation of the organic function can be excluded as peaks 1 and 3 appear unmodified. Only in the case of MMp75, the peaks of carbons quoted 1 and 3 are subject to splitting, indication of small changes in the local environment around CH₃ and the CH₂ bound to the vinyl carbon C2.

A possible interpretation is that the quantity of MPTMS is so high that the reactive groups are packed together as the bristles in a brush, with some chains more compressed than others

9.2.4 DSC analyses

From DSC analyses it is possible to verify the availability of the methacrylate groups for polymerisation. For each sample, a single broad exothermal peak due to polymerisation is observed (Fig. 138).

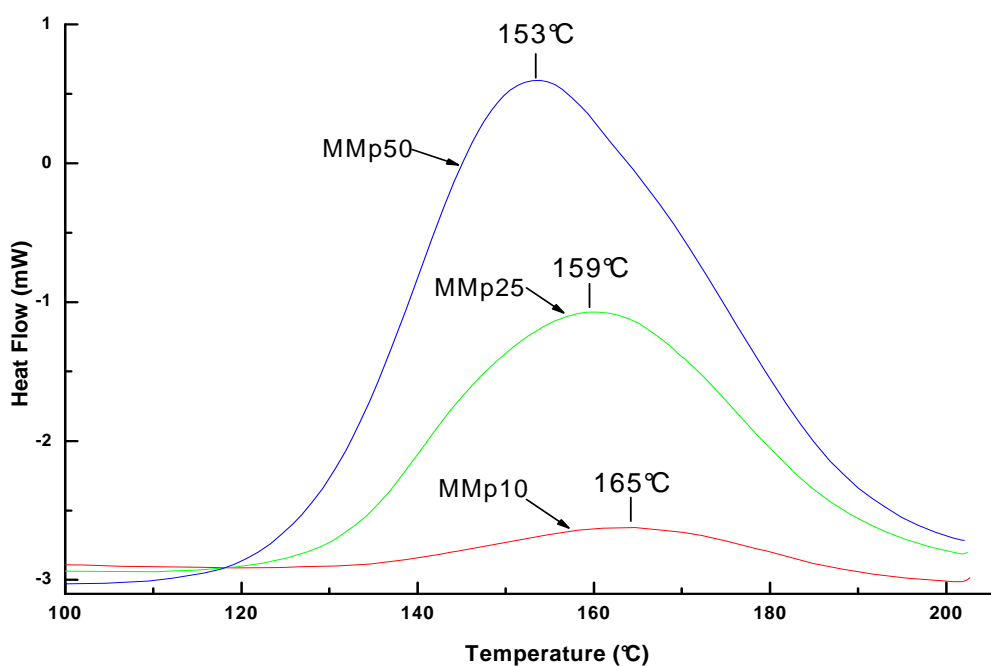


Fig. 138: DSC curves of MMp-NP

The characteristic DSC data are shown in the following table.

Sample	ΔH (J/g)	Peak max (°C)
MMp 10	7.36	165
MMp 25	40.86	159
MMp 50	80.16	153
MMp 75	88.3	155

Table 52: DSC data: polymerisation heat and peak maximum position

The samples are prone to polymerisation, since DSC traces were recorded without the addition of a thermal initiator.

The polymerization peak intensity is almost linearly dependent on MPTMS content, with the exception of MMp75 that presents a small increase in polymerization heat respect to MMp50. This could be due to some methacrylate groups not easy available for polymerization or present in a different local environment as suggested by the splitting of carbons 1 and 3 signals in the ^{13}C NMR spectrum of MMp75.

9.2.5 Thermal analyses (TG)

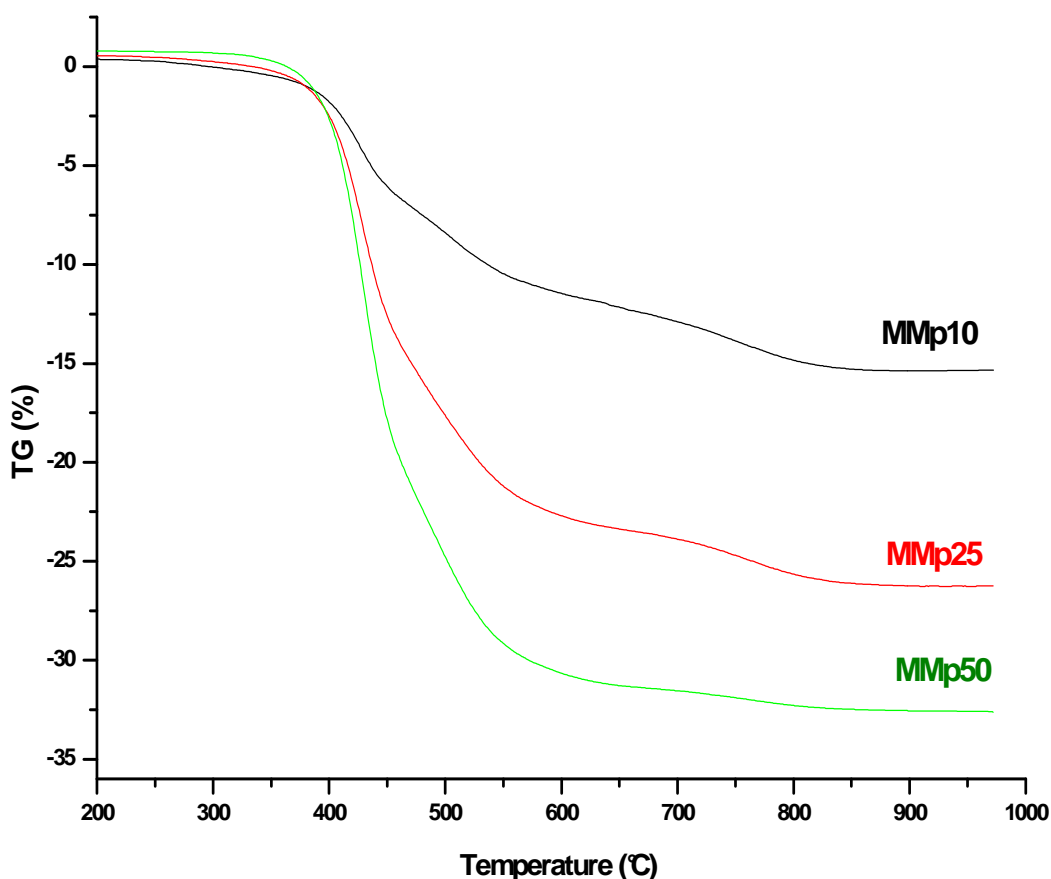


Fig. 139: TG curves (nitrogen) of MMp-NP

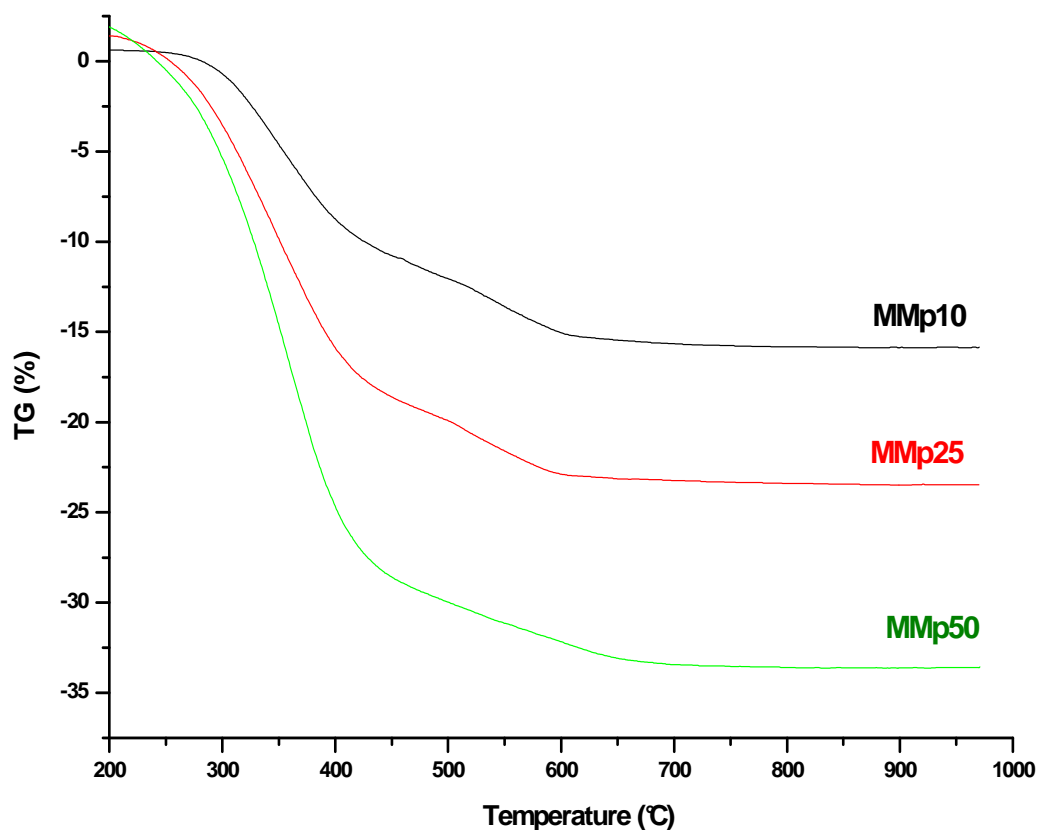


Fig. 140: TG curves (air) of MMp-NP

Sample	air			nitrogen			
	I step (250-500°C)	II step (500-900°C)	Wtot (%)	I step (250-480°C)	II step (480-620°C)	III step (650-900°C)	Wtot (%)
MMp 10	17.7	7.9	25.6	11.6	6.7	5.3	23.6
MMp 25	32.0	7.8	39.8	20.2	9.4	3.8	33.4
MMp 50	50.6	8.3	58.9	32.9	9.2	5.7	47.8
MMp 75	46.5	13.2	59.7	35.9	9.4	5.7	51.0

Table 53: data from DSC curves in air and nitrogen flow

The TG curves recorded in air (Table 53) present two loss steps. The weight loss in the first step increases with the increase of MPTMS content, whereas the weight loss of the second step presents a constant value

except for MMp75 (Table 53). Consequently, the first step is probably due to the loss of the methacrylate function.

Under nitrogen, three steps are observable in TG traces. The total weight losses depend again on the MPTMS load, but the thermal stability of samples does not change with composition since the onset temperature is around 400°C for all samples.

9.2.6 N₂ physisorption

Fig. 141 presents MMp-10 sorption isotherm. The samples shows type-II isotherms and are characterised by low porosity.

The specific surface area values, calculated by BET equation, are summarized in Table 54. Increasing the MPTMS amount, SSA values decrease, TPV and average pore size increase. The addition of the methacryloxypropyl chain influences also the micropores present in the sample, whose percentage passes from around 35% (MMp10) to 14% (MMp50).

Sample	BET SSA (m ² /g)	Total Pore Volume (cm ³ /g)*	Adsorption BJH Average Pore diameter (Å)
MMp10	36	0.126	174
MMp25	28	0.130	192
MMp50	16	0.145	360

Table 54: N₂ physisorption data of MMp samples (* P/P0=0.99)

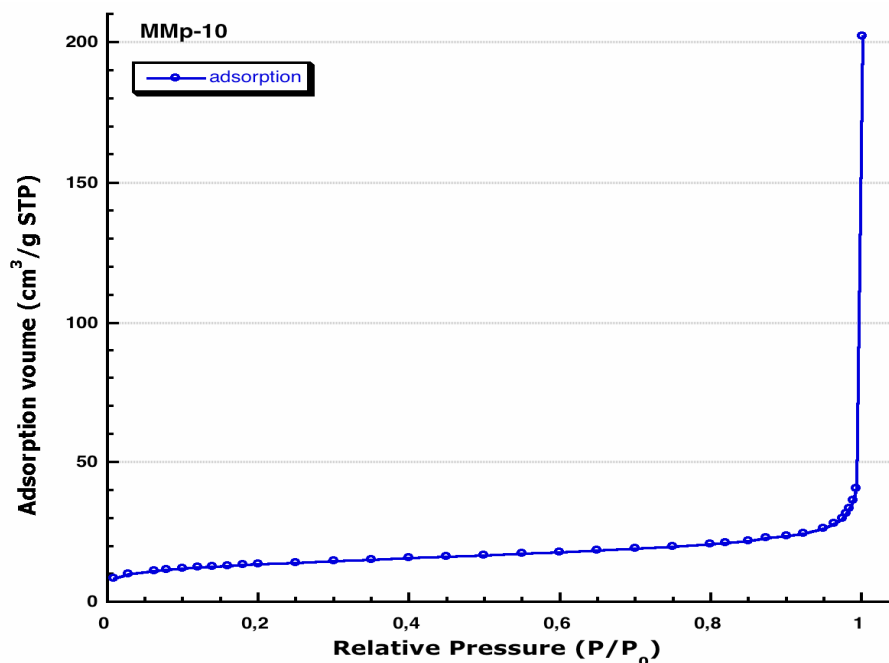


Fig. 141: MMp10 adsorption isotherm

10 APPLICATIONS

10.1.1 Methods and measurements

MMp-NP were used as active fillers for the preparation of nanostructured UV curable acrylic coatings applied on mild steel substrates for corrosion protection purposes. This work was pursued in collaboration with the group of Prof. F. Deflorian of the Dept. of Materials Engineering and Industrial Technologies of the University of Trento (EIS measurements) and the group of Prof. R. Bongiovanni of the Dep. of Materials Science and Chemical Engineering of the Polytechnic of Turin (Urethane-acrylic matrices and substrate coatings preparation).

Coatings were characterised by means of gloss measurements, DSC measurements (glass temperature T_g) and electrochemical behaviour.

Electrochemical behaviour of the coatings was evaluated by means of electrochemical impedance spectroscopy (EIS) and potential vs time.

Samples were tested with a 0.3% w/w Na_2SO_4 testing solution. Impedance spectra were acquired for about 200 hours of continuous immersion in the conductive solution. A convenient equivalent electric circuit was used for data modelling in order to obtain the electrical parameters describing the coatings properties [256].

Different matrices obtained by adding to an acrylic resin (BEDA, Fig. 142) the same amount of NP (6% w/w) were prepared by different approaches: one based on the blending of preformed NP in the matrix and the other, on the in situ production of modified silica fillers; prepared samples are listed in the table below.

Sample	Description
Pure resin	BEDA (acrylic resin)
BEDA:MPTMS (80:20)	In situ production
BEDA:TEOS:MPTMS (80:15:5)	In situ production
BEDA+MTES-NP	Blending of MTES-NP
BEDA+MMp25	Blending of MMp25-NP
BEDA+MMp50	Blending of MMp-50NP

Table 55: composites matrices for protective coatings applications

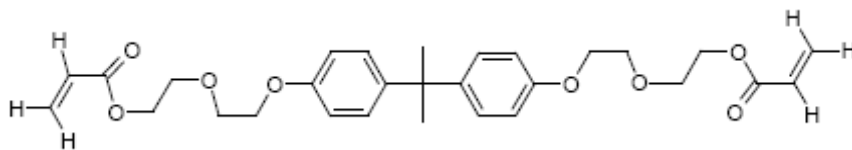


Fig. 142: acrylic resin containing bisphenol A (BEDA)

10.1.2 Coating characterisation

The mixtures were coated onto glass sheets and on mild steel using a blade and UV-cured.

The surface of the coating was first characterised measuring the gloss at 60° (Table 56).

Sample	Gloss
Pure resin	100
BEDA:MPTMS (80:20)	98.9
BEDA:TEOS:MPTMS (80:15:5)	99.3
BEDA+MTES	100
BEDA+MMp25	100
BEDA+MMp50	100

Table 56: prepared matrices and relative gloss measurements

There is a matting effect on the surface of the sample as shown by the decrease of the gloss value. This effect is probably ascribable to a scattering effect of the incident light due to not perfectly specular surfaces.

The formation in situ of the silica-NP affects the surface roughness.

Glass transition temperatures (T_g) were calculated from DSC measurements (Table 57).

Sample	T_g
Pure resin (BEDA)	38
BEDA:MPTMS (80:20)	73
BEDA:TEOS:MPTMS (80:15:5)	71
BEDA+MTES	42
BEDA+MMp25	40
BEDA+MMp50	46

Table 57: glass transition temperature by means of DSC

The glass transition temperature is remarkably higher in matrices with in situ silica NP production, respect to pure resin and blended matrices. Probably, the presence of smaller functionalised silica domains (average diameter of in situ created particles: 100 nm) leads to a thermal stabilisation of the coating.

The electrochemical characterisation was performed on different coatings applied onto mild steels in order to evaluate the corrosion protection performances of the coatings.

All the coatings except BEDA:MPTMS (80:20) show a stable value of free corrosion potential (0.0-0.2 V).

Concerning EIS measurements of total impedance at low frequencies, Fig. 143 reports the impedance spectra (Bode modulus). It is possible to notice that all samples show high impedance values (10^{10} - $10^{11} \Omega^{-1}$) except BEDA-MMp50; this measurements are a rough index of the protective properties of the coating.

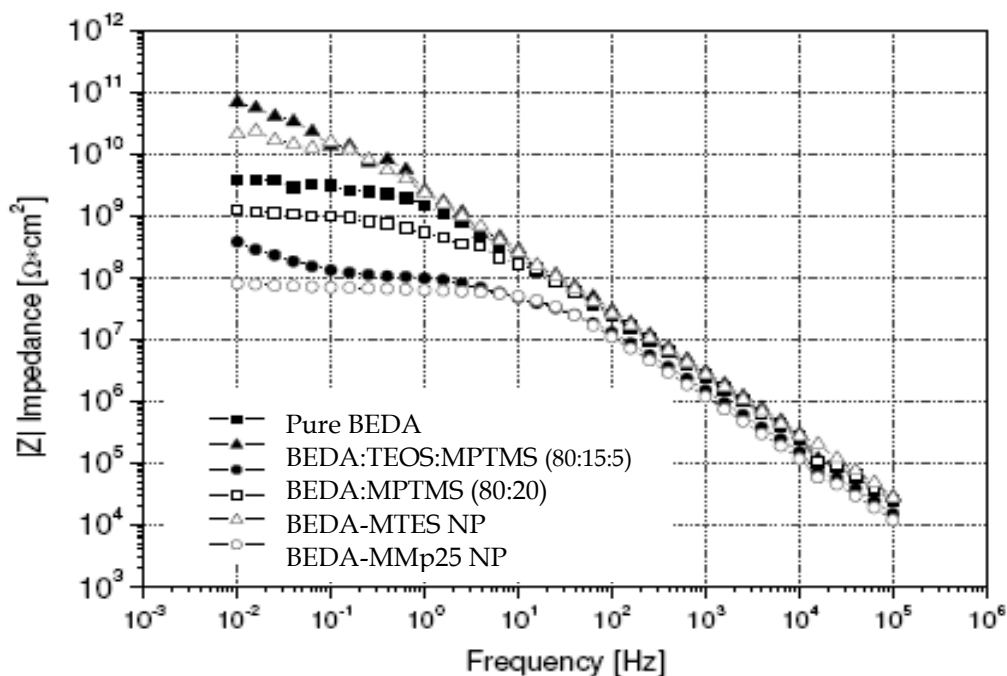


Fig. 143: Bode modulus after 10 days of immersion in Na_2SO_4 solution 0.3% w/w [47]

Impedance measurements are used in order to understand the H₂O barrier properties. In our samples, the best results are obtained with BEDA:TEOS:MPTMS (80:15:5) and BEDA-MMp25 samples, which show higher values of impedance with respect to pure BEDA resin. This means that the introduction of NP in the resin improves the corrosion protection properties, increasing the H₂O barrier ability, probably due to the strong effect of bonding between SiO₂ particles and polymeric matrix.

In order to prove the obtained data EIS data were fitted using convenient electric equivalent circuits [ECT]. The parameter used to analyse the protective properties was coating resistance (R_c) that is the ability as ion diffusion barrier of the layer.

Fig. 144 shows the trend of coatings resistance, evidencing the capability of BEDA:TEOS:MPTMS (80:15:5) and BEDA-MMp25 to act as barrier. Interesting is the value reached at the plateau, which is one order of magnitude higher with respect to the pure resin.

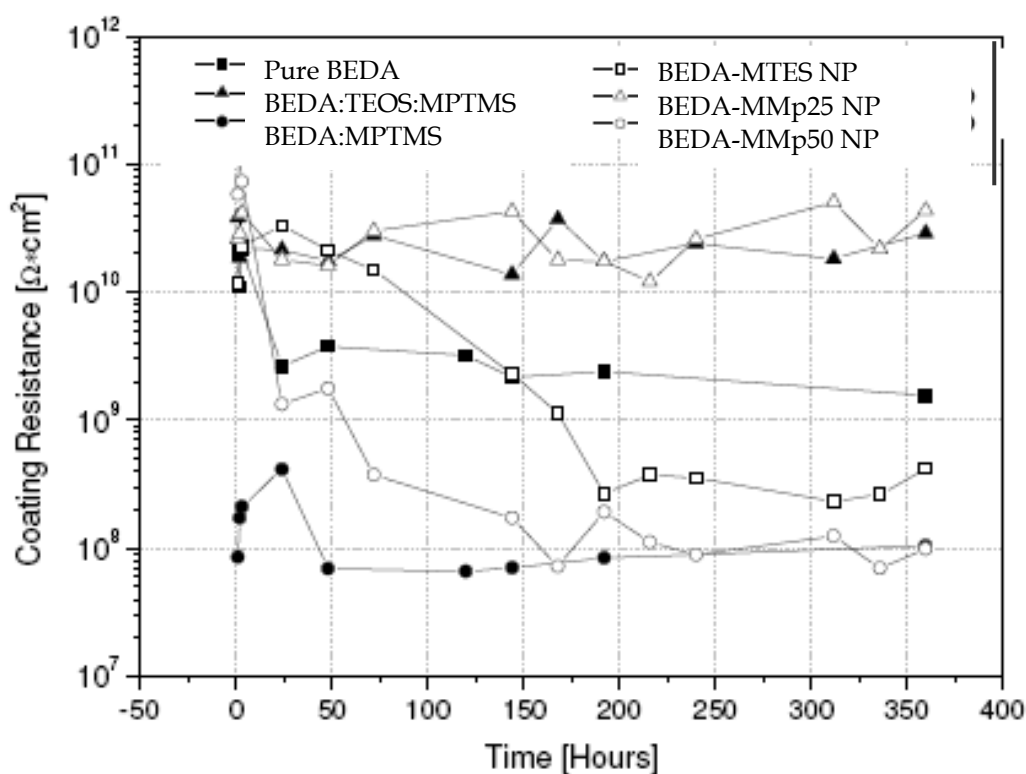


Fig. 144: coatings resistance with immersion time in Na₂SO₄ solution 0.3% w/w [47]

PRELIMINARY CONCLUSIONS ON MMp-NP

In this part of the work, appropriate synthesis parameters were selected in order to obtain spherical-shaped NP of sub-micrometer size. Different organic modified NP were synthesised starting from single precursors (methyl, ethyl, vinyl, phenyl) and from binary systems (methyl and amyl or octyl and vinyl and octyl) in different molar ratios.

NP with reactive methacryl functions were also prepared in a mixture with MTES (MMp) in different ratio. The MMp-NP have been used as fillers in urethane acrylic matrices for protective coatings. BEDA-MMp25 matrices showed interesting properties despite the blending process, which normally leads to a less homogeneous film production. Work is still in progress in order to complete the characterization study of polymer-based coatings.

FINAL REMARKS

The research activity during this PhD thesis was focused on the synthesis, and structure investigation of hybrid organic-inorganic (O/I) materials with different application fields (materials for optical devices and protective coatings), exploiting the sol-gel method on either the non-hydrolytic or the *in situ* water production route.

In the first part of the work we were able to develop synthesis and synthesis parameters in order to obtain NBBs with small dimensions, and controlled architecture and functionality.

The obtained NBB have been exploited to obtain patternable films with good resolution for optical devices, even in the case of Glymo-based NBB, in which the Si-O-Si condensation degree was low.

NP instead have been synthesised with the aim of obtaining fillers and active fillers.

In the second part of the work a new synthesis and new synthetic parameters to obtain organic-modified NP directly from the alkoxy silane without the addition of TEOS or SiO₂ seeds were developed and optimised (Chapter 8).

Both single and binary systems can be obtained through the above mentioned method, with tailored properties as showed by surface and thermal characterisation.

The surface activity of films prepared with single and binary mixture derived NP was studied. These films, which have no reactive function, can be used to obtain, eventually, engineered dielectric films.

The polymerisation ability of active fillers was studied confirming the high reactivity of the NP. MMp-NP were tested in a preliminary study on the dispersion in matrices with anti-corrosion applications, showing good preliminary results in the case of MMp25.

A starting work on the conservation of the particles shape at high temperature, in order to obtain ceramic particles was conducted, revealing the ability of the particles to retain their shape, except in the case of binary systems with high loading of long alkyl chain precursor.

Finally NP were efficiently doped with a fluorescent dye (Rhodamine 6G), analyses on the NP are still in progress, but from the first results a relationship between dye and local environment of the network emerges.

REFERENCES

- 1 R. Corriu and N.T. Anh, *Molecular Chemistry of Sol-Gel Derived Nanomaterials*, 2009, John Wiley & Sons
- 2 J. Livage, M. Henry and C. Sanchez, *Sol-Gel Chemistry of Transition Metal Oxides*, *Progress in Solid State Chemistry*, 1988, 18, 259-342
- 3 L.G. Hubert-Pfalzgraf, *New J. Chem.*, 1995, 19, 727
- 4 C.J. Brinker, and G.W. Scherer, *Sol-Gel Science*, 1990, Academic Press, Dan Diego
- 5 R.T. Morrison and Boyd, *Organic Chemistry*, 1992, Prentice-Hall International Ltd., London (UK)
- 6 A. Vioux, *Non hydrolytic sol-gel routes to oxides*, *Chem. Mater.*, 1997, 9, 2292
- 7 L. Bourget, R.J.P. Corriu, D. Leclercq, P.H. Mutin, A. Vioux, *Non-Hydrolytic sol-gel routes to silica*, *J. Non Cryst. Sol*, 1998, 242, 81-91
- 8 G.P. Shulman, M. Trusty, J.H. Vickers, *Thermal decomposition of aluminium alkoxides*, *J. Org. Chem*, 1963, 28, 907
- 9 S. Acosta, R.J.P. Corriu, D. Leclercq, P. Lefèvre, P.H. Mutin, A. Vioux, *Preparation of alumina gels by a non-hydrolytic sol-gel processing method*, *J. Non-Cryst. Solids*, 1994, 170, 234
- 10 L. Bourget, D. Leclercq, A. Vioux, *Catalyzed nonhydrolytic sol-gel route to organosilsesquioxane gels*, *J. Sol-Gel Sci. Tech.*, 1999, 14, 137
- 11 P. Arnal, R.J.P. Corriu, D. Leclercq, P.H. Mutin, A. Vioux, *A solution chemistry study of nonhydrolytic sol-gel routes to titania*, *Chem. Mater.*, 1997, 9, 694
- 12 S. Dirè, V. Tagliazucca, G. Brusatin, J. Bottazzo, I. Fortunati, R. Signorini, T. Dainese, C. Andraud, M. Trombetta, M.L. Di Vona, S. Licocchia, *Hybrid organic/inorganic materials for photonic application via assembling of nanostructured molecular units*, *J. Sol-Gel Sci. Technol*, 2008, 48, 217-223

References

- 13 C. Sanchez and F. Ribot, *New J. Chem*, 1994, 18, 1007-1047
- 14 D. Levy, D. Avnir, *Effects of the changes in the properties of silica cage along the gel/xerogel transition on the photochromic behavior of trapped spiropyrans*, *J. Phys. Chem.*, 1988, 92, 4734-4738
- 15 L. Borello, B. Onida, C. Barolo, K. J. Edler, C. Otero Areán and E. Garrone, *Accessibility of dye next term molecules previous term embedded next term in surfactant-silica previous term hybrid next term materials in both powder and film forms*, *Sensors and Actuators B: Chemical*, 2004, 100, 107-111
- 16 Q. Wang, R. Choy, Q. Dai, A.E. Ostafina, *Preparation of dye-loaded SiO₂ nanoparticles*, *J. Non Cryst. Solids*, 2007, 353, 354-365
- 17 a) K. A. Mauritz, C. K. Jones, *Novel poly(n-butyl methacrylate)/titanium oxide alloys produced by the sol-gel process for titanium alkoxides*, *J. Appl. Polym. Sci.*, , 40, 1401-1420; b) M. Toki, T.Y. Chow, T. Ohnaka, H. Samura and T. Saegusa, *Structure of poly(vinylpyrrolidone)-silica hybrid*, *Polym.. Bull*, 1992, 29, 653-660
- 18 M.J. Folkes, R.H. Cruz-Estrada, *In-situ production of electrically conductive polyaniline fibres from polymer blends*, 2002, (PhD thesis. Brunel University, UK <http://bura.brunel.ac.uk/handle/2438/2406>)
- 19 A.D. Pomagailo, *Polymer-immobilised nanoscale and cluster metal particles*, *Russ. Chem. Rev.*, 1997, 66, 679-716
- 20 T.W. Smith, D. Wychick, *Colloidal iron dispersions prepared via the polymer-catalyzed decomposition of iron penta-carbonyl*, *J. Phys. Chem.*, 1980, 84, 1621-1629.
- 21 K-H. Haas and K. Rose, *Hybrid Inorganic/Organic polymers with nanoscale building blocks: precursors, processing, properties and applications*, *Rev. Adv. Mater. Sci.*, 2003, 5, 47-52
- 22 P.M. Ajayan, L.S. Schadler, P.V. Braun, *Nanocomposite science and technology*, Wiley VCH, 2003

- 23 B.K.G. Theng, *Formation and Properties of Clay Polymer Complexes*, Elsevier, New York, 1979
- 24 B. Boury and R.J.P. Corriu, *Auto-organisation of hybrid organic-inorganic materials prepared by sol-gel chemistry*, Chem. Commun., 2002, 795-803
- 25 a) O. M. Yaghi, M. O'Keeffe, N. W. Ockwig, H. K. Chae, M. Eddaoudi and J. Kim, *Reticular synthesis and the design of new materials*, Nature, 2003, 423, 705-714; b) H. K. Chae, D. Y. Siberio-Pérez, J. Kim, Y. Go, M. Eddaoudi, A. J. Matzger, M. O'Keeffe and O. M. Yaghi, *A route to high surface area, porosity and inclusion of large molecules in crystals*, Nature, 2004, 427, 523-527
- 26 G. Férey, C. Mellot-Draznieks, C. Serre and F. Millange, *Crystallized Frameworks with Giant Pores: Are There Limits to the Possible?*, Acc. Chem. Res., 2005, 38, 4, 217-225
- 27 A. K. Cheetham and C. N. R. Rao, *Toward the Rational Design of Open-Framework Materials*, MRS Bull., 2005, 30, 2, 93-98
- 28 G. J. de A. A. Soler-Illia, C. Sanchez, B. Lebeau and J. Patarin, *Chemical Strategies To Design Textured Materials: from Microporous and Mesoporous Oxides to Nanonetworks and Hierarchical Structures*, Chem. Rev., 2002, 102, 4093.
- 29 R.J.P. Corriu, A. Mehdi, C. Reye and C. Thieuleux, *Control of coordination chemistry in both the framework and the pore channels of mesoporous hybrid materials*, New J. Chem., 2003, 27, 905-908
- 30 T. Koch, F.R. Kogler, U. Schubert and S. Seidler, *Mechanical Properties of Organic-Inorganic Hybrid Materials Determined by Indentation Techniques*, Monatshefte für Chemie, 2007, 138, 293-299
- 31 E. O. Dare, G. A. Olatunji, D. S. Ogunniyi, *Organic-Inorganic Hybrid Material. I. Synthesis, Characterization, and Thermal Property of a Novel Polyhedral Cubic Silsesquioxanes*, J. Appl. Polym. Sci., 2004, 93, 907-910

References

- 32 Q. Huang, J.D. Mckenzie. *A study on reinforcements of rubber-like ormosils. Ceramic Transactions*, Vol. 55, Sol-Gel Science and Technology, ed. The American Ceramic Society, 1995, 291-298
- 33 T. Iwamoto and J.D. Mackenzie, *Ormosils of high hardness*, Mater. Res. Soc. Symp. Proc., 1994, 346, 397-402
- 34 G. Schottner, K. Rose and U. Posset, *Scratch and Abrasion Resistant Coatings on Plastic Lenses – State of the Art, Current Developments and Perspectives*, J. Sol-Gel Sci. Technol., 2003, 27, 71-79
- 35 K.H Haas, S. Amberg-Schwab, K. Rose, G. Schottner, *Functionalized coatings based on inorganic–organic polymers (ORMOCER®s) and their combination with vapor deposited inorganic thin film*, Surface Coat. Tech., 1999, 111, 72- 79
- 36 J. Wen, K. Jordens, G.L. Wilkes, *Hybrid organic/inorganic coatings fir abrasion resistance on plastic and metal substrates*, *Better Ceramics Through Chemistry VII: Organic /Inorganic Hybrid Materials*, ed. Mater. Res. Soc. Symp. Proc., 1996, 435, 207-213
- 37 a) C. Koos, P. Vorreau, T. Vallaitis, P. Dumon, W. Bogaerts, R. Baets, B. Esembeson, I. Biaggio, T. Michinobu, F. Diederich, W. Freude & J. Leuthold, *All-optical high-speed signal processing with silicon–organic hybrid slot waveguides*, Nature Photonics, 2009, 3, 216 – 219; b) C. Massard, J.L. Taverdet, S. Brouillet and C. Donnet, *Hybrid Sol–gel thin films for magneto-optical applications: Chemical, optical and tribological study*, Surf. Coat. Technol., 2007, 202, 1067-1072; c) J.A. Bootsma, M. Entorf, J. Eder, B.H. Shanks, *Hydrolysis of oligosaccharides from distillers grains using organic–inorganic hybrid mesoporous silica catalysts*, Bioresource Technology, 2008, 99 5226-5231; d) J.J.E. Moreau, M. Wong Chi Man, *The design of selective catalysts from hybrid silica-based materials*, Coordination Chemistry Reviews, 1998, 178-180, Part 2 1073-1084
- 38 W. Geffchen, E. Berger, Deutsches Reichspatent, DE736421 assigned to Jenär Glaswerk Schott&Gen, 1939, Jena (Germany)

- 39 K. Izumi, H. Tanaka, Y. Uchida, N. Tohge, T. Minami, *Hydrolysis of trifunctional alkoxysilanes and corrosion resistance of steel sheets coated with alkoxysilane-derived-films*, J. Mater. Sci. Lett., 1993, 12, 724-727
- 40 M. Menning, C. Schelle, A. Duran, J.J. Damborena, M. Guglielmi and G. Brusatin, *Investigation of Glass-Like Sol-Gel Coatings for Corrosion Protection of Stainless Steel Against Liquid and Gaseous Attack*, J. Sol-Gel Sci. Technol., 1998, 13, 717-722
- 41 P. Galliano, J.J. Damborenea, M.J. Pascual and A. Durán, *Sol-Gel Coatings on 316L Steel for Clinical Applications*, J. Sol-Gel Sci. Technol., 1998, 13, 723-727
- 42 J. Gallardo, A. Durán, J.J. Damborenea, *Electrochemical and in vitro behaviour of sol-gel coated 316L stainless steel*, Corrosion Sci., 2004, 46, 795-806
- 43 T.P. Chou, C. Chandrasekaran, S.J. Limmer, S. Serali, Y. Wu. M.J. Forbess, C. Nguyen, G.Z. Cao, *Organic-inorganic hybrid coatings for corrosion protection*, J. Non-Crist. Solids, 2001, 290, 153-162
- 44 J. Gallardo, A. Duran, I. Garcia, J.P. Celis, M.A. Arenas and A. Conde, *Effect of Sintering Temperature on the Corrosion and Wear Behavior of Protective SiO₂-Based Sol-Gel Coatings*, J. Sol-Gel Sci. Technol., 2003, 27, 175-183
- 45 H. Schmidt, G. Jonschker, S. Goedicke and M. Mennig, *The Sol-Gel Process as a Basic Technology for Nanoparticle-Dispersed Inorganic-Organic Composites*, J. Sol-Gel Sci. Technol, 2000, 19, 39-51
- 46 S.P. Pappas, *Radiation curing, science and technology*, ed. Plenum Press, New York, 1992
- 47 M. Fedel, F. Deflorian, S. Dirè, V. Tagliazucca, R. Bongiovanni, L. Vescovo, *Characterization of Nano-structured UV cured Acrylic Coatings*, ECS Transaction, 2009, accepted
- 48 R. Kasemann, H.K. Schmidt, and E. Wintrich, Mater. Res. Soc. Symp. Proc., 1994, 346, 915-

References

- 49 J. Martínez Urreaga, M.C. Mathias, V. Lorenzo, and M.U. de la Orden, *Mater. Lett.*, 2000, 45, 293-
- 50 H.-J. Streitberger, K.-F. Dössel, *Automotive Paints and Coatings*, 2008, Wiley VCH, 2nd ed.
- 51, M.Groenwolt, *Highly scratch resistant coatings for automotive applications*, *Prog. Org. Coat.*, 2008, 61, 106-109
- 52 G.W. Sherrer, R. Flatt, G. Wheeler, *Materials science esearc for the conconservation of sculpture and monuments*, *MRS Bull.*, 2001, 26, 24-50
- 53 J.D. Mackenzie and E. Bescher, *Some Factors Governing the Coating of Organic Polymers by Sol-Gel Derived Hybrid Materials*, *J.Sol-Gel Sci. Technol.*, 2003, 27, 7-14
- 54 E. Carretti, L. Dei and R.G. Weiss, *Soft matter and art conservation. Rheoreversible gels and beyond*, *Soft Matter*, 2005, 1, 17-22
- 55 E. Smy, *Sol-Gel; Potential Creative Applications for the Artist, Focusing on the Colloidal Alkali Silicate Route*, *J. Sol-Gel Sci. Technol.*, 1998, 13, 233-236
- 56 P. Laurie, *Preservation of Stone*, U.S. Patent 1.607.762, 1926
- 57 C.J. Brinker , C.S. Ashley, A.S. Sellinger, R.T. Cygan, K.L. Nagy, R. assink, T. Alam, S. Rao, S. Prabkar, C.S. Scotto, *Sol-Gel preservation of mankind's cultural heritage in objects constructed of stone*, Sandia Nat. Lab. Geochemical Dep, Technical report, 1998, 1-36
- 58 E.K. Kim, J. Won, J-Y. Do, S.D. Kim, Y.S. Kang, *Effects of silica nanoparticle and GPTMS addition on TEOS-based stone consolidants*, *J. Cult. Heritage*, 2009, 10, 214-221
- 59 F. Tanno, S. Saka, K. Takabe, *Antimicrobial TMSAC-added wood-inorganic composites prepared by the sol-gel process*, *Mater. Sci. Res. Int.*, 1997, 3, 137-142
- 60 B. Dal Bianco, R. Bertocello, *Sol-gel silica coatings for the protection of cultural heritage glass*, *Nucl. Instrum. Methods Phys. Res B*, 2006, 266, 2358-2362

- 61 M. Berger, *Nanotechnology materials to the rescue of stone monuments*, 2008, <http://www.nanowerk.com/spotlight/spotid=4587.php>
- 62 C. Domingo et al., *Possibilities of monitoring the polymerization process of silicon-based water repellents and consolidants in stones through infrared and Raman spectroscopy*, *Progress in Organic Coatings*, 2008, 63, 5–12
- 63 E. Bescher, F. Piqué, D. Stulik, J.D. Mackenzie, *Long-Term Protection of the Last Judgment Mosaic in Prague*, *J. Sol-Gel Sci. Technol.*, 2000, 19, 1-3, 215-218
- 64 S. Voltolina, *Studio e rilievi per la conoscenza e il restauro della Grande Vetrata della Chiesa di San Giovanni e Paolo a Venezia*, 2009, Un. Padua- (PhD thesis), <http://paduaresearch.cab.unipd.it/1736/>
- 65 K. Abe Y. Sanada, T. Morimoto, *Anti-reflection coatings for CRTs by sol-gel process*, *J. Sol-Gel Sci. Technol.*, 2001, 22, 151-166
- 66 J. Mackenzie, *Applications of the sol-gel process*, *J. Non Cryst. Solids*, 1988, 100, 162-168
- 67 S. Sakka, *Sol-gel preparation of coating films containing noble metal coatings*, *J. Sol-Gel Sci. Technol.*, 1998, 13, 701-706
- 68 C.C. Chen, D.J. Lin, T.M. Don, F.H. Huang, L.P. Cheng, *Preparation of organic-inorganic nano-composites for antireflection coatings*, *J. Non-Cryst. Solids*, 2008, 354, 3828–3835
- 69 D. Chen, Y. Yan, E. Westenberg, D. Niebauer, N. Sakaitani, S.R. Chaudhuri, Y. Sato and M. Takamatsu, *Development of Anti-Reflection (AR) Coating on Plastic Panels for Display Applications*, *J. Sol-Gel Sci. Techn.*, 2000, 19, 77-82
- 70 O. Takahashi et al., Japanese Patent 298545, 1994, 29854
- 71 H-J. Jeong, D-K. Kim, S-B. Lee, S-H. Kwon, K. Kadono, *Preparation of Water-Repellent Glass by Sol-Gel Process Using Perfluoroalkylsilane and Tetraethoxysilane*, *J. Colloid Interface Sci.*, 2001, 235, 130-134

References

- 72 Y. Furukawa, T. Yoneda, *Synthesis and properties of fluorosilicone with perfluorooctylundecyl side chain*, J. Polym. Sci. Part A: Polym. Chem., 2003, 41, 2704-2714
- 73 L.D. Carlos et al., *Planar and UV written channel optical waveguides prepared with siloxane-poly(oxyethylene)-zirconia organic-inorganic hybrids. Structure and optical properties*, J. Mater. Chem., 2005, 15, 3937-3945
- 74 U. Streppel, P. Dannberg, C. Wächter, A. Bräuer, L. Fröhlich, R. Houbertz, M. Poppal, *New wafer-scale fabrication method for stacked optical waveguide interconnects and 3D micro-optic structures using photoresponsive (inorganic-organic hybrid) polymers*, Optical Materials, 2000, 21, 475-483
- 75 S. Uhlig, L. Fröhlich, M. Chen, N. Arndt-Staufenbiel, G. Lang, H. Schröder, R. Houbertz, M. Poppal and M. Robertsson, *Polymer Optical Interconnects - A Scalable Large-Area Panel Processing Approach*, IEEE Transactions on Advanced Packaging, 2006, 29, 158-170
- 76 P. Etienne, P. Coudray, Y. Moreau and J. Porque, *Photocurable Sol-Gel Coatings: Channel Waveguides for Use at 1.55 μm* , J. Sol-Gel Sci. Technol., 1998, 13, 523-527
- 77 T.P. Nguyen, C.W. Lee, S. Hassen, H.C. Le, *Hybrid nanocomposites for optical applications*, Solid State Sci., 2009, 11, 1810-1814
- 78 E.J.A. Pope, *Sol-gel optical nanocomposites: Design and applications*, J. Sol-Gel Sci. Technol, 1994, 2, 717-722
- 79 D. Wang, X. Chen, X. Zhang, W. Wang, Y. Liu, L. Hu, *Fabrication of nonlinear optical films based on methacrylate/silica hybrid matrix*, Curr. Appl. Phys., 2009, 9, S170-S173
- 80 C. Sanchez and B. Lebeau, *Hybrid organic - inorganic materials with second-order optical nonlinearities synthesized via sol - gel chemistry*, Pure Appl. Opt., 1996, 5, 689-699
- 81 P. Innocenzi and B. Lebeau, *Organic-inorganic hybrid materials for non-linear optics*, J. Mater. Chem, 2005, 15, 3821-3831

- 82 M. Barboiu, C. Guizard, N. Hovnanian, L. Cot, *New molecular receptors for organics of biological interest for the facilitated transport in liquid and solid membranes*, *Separ. Purif. Technol.*, 2001, 25, 211-218
- 83 G. Tishchenko and M. Bleha, *Diffusion permeability of hybrid chitosan/polyhedral oligomeric silsesquioxanes (POSSTM) membranes to amino acids*, *J. Membr. Sci.*, 2005, 248, 45-51
- 84 R.R. Bhave, *Inorganic membranes, synthesis, characteristics and applications*, 1991, Van Nostrand Reinhold, NY
- 85 O.S. Wolfbeis, *Materials for fluorescence-based optical chemical sensors*, *J. Mater. Chem.*, 2005, 15, 2657-2669
- 86 C. Malins, B.D. MacCraith, *Dye-doped organically modified silica glass for fluorescence based carbon dioxide gas detection*, *Analyst*, 1998, 123, 2373-2376
- 87 C. Von Bulzingslöwen, A.K. McEvoy, C. McDonagh, B.D. MacCraith, I. Klimant, C. Kraus et al., *Sol-gel based optical carbon dioxide sensor employing dual luminophore referencing for application in food packaging technology*, *Analyst*, 2002, 127, 1478-1483
- 88 Clair N. Sawyer, Perry L. McCarty, Gene F. Parkin, *Chemistry for Environmental Engineering and Science*, 5th ed., 2003, McGraw-Hill, New York
- 89 L. Lin, L.L. Xiao, S. Huang, L. Zhao, J.S. Cui, X.H. Wang et al., *Novel BOD optical fiber biosensors based on co-immobilized microorganisms in ormosils matrix*, *Biosens. Bioelectron.*, 2006, 21, 1703
- 90 Y. Jiang, L.L. Xiao, L. Zhao, X. Chen, X. Wang, K.J. Wong, *Optical biosensor for the determination of BOD seawater*, *Talanta*, 2006, 70, 97
- 91 B. König, O. Kohls, G. Holst, R.N. Glud, M. Kühl, *Fabrication and test of sol-gel based planar oxygen optodes for use in aquatic sediments*, *Mar. Chem.*, 2005, 97, 262
- 92 C. Rottman, G.S. Grader, D. Avnir, *Chem Mater.*, 2001, 13, 3631

References

- 93 D. Avnir, S. Braun, O. Lev, M. Ottolenghi, *Enzymes and other proteins entrapped in sol-gel materials*, *Chem. Mater.*, 1994, 6, 1605-1614
- 94 E. Angeletti, C. Canepa, G. Martinetti, P. Venturello, *Tetrahedron Lett.*, 1988, 29, 2261
- 95 A.C. Blanc, D.J. Macquarrie, S. Valle, G. Renard, C.R. Quinn, D. Brunel, *The preparation and use of novel immobilised guanidine catalysts in base-catalysed epoxidation and condensation reactions*, *Green Chem.*, 2000, 2, 283.
- 96 M.A. Harmer, Q. Sun, M.J. Michalczyk, Z. Yang, *Unique silane modified perfluorosulfonic acids as versatile reagents for new solid acid catalysts*, *Chem. Commun.*, 1997, 1803.
- 97 C.T. Kresge, M.E. Leonowicz, W.J. Roth, J.C. Vartuli, J.S. Beck, *Nature* 1992, 359, 710.
- 98 D.J. Macquarrie, R. Maggi, A. Mazzacani, G. Sartori, R. Sartorio, *Understanding the influence of the immobilization procedure on the catalytic activity of aminopropylsilicas in C-C forming reactions*, *Appl. Catal. A*, 2003, 246, 183 – 188
- 99 a) H.H.P. Yiu, P.A. Wright and N.P. Botting, *Enzyme immobilisation using siliceous mesoporous molecular sieves*, *Micro. Meso. Mater.*, 2001, 44-45, 763-768; b) J.M. Gómez, J. Deere, D. Goradia, J. Cooney, E. Magner and B.K. Hodnett, *Transesterification Catalyzed by Trypsin Supported on MCM-41*, *Catal. Lett.*, 2003, 88, 183-186
- 100 J. Yang , G.W. Stevens and A.J. O'Connor, *Adsorption of lysozyme and trypsin by modified MCM-41 with postsynthesis hydrothermal treatment and hydrophobic functionalisation*, *J. Aust. Ceram. Soc.*, 2008, 44, 1-6
- 101 Y. Li, G. Zhou, W. Qiao and Y. Wang, *Immobilization of Porcine pancreas lipase on fiber-like SBA-15 mesoporous material*, *Mater. Sci. Eng: B*, 2009, 162, 120-126

- 102 F. Hoffmann, M. Cornelius, J. Morell, and M. Fröba, *Silica-Based Mesoporous Organic–Inorganic Hybrid Materials*, *Angew. Chem. Int. Ed.* 2006, 45, 3216 – 3251
- 103 A.P. Wight and M.E. Davis, *Design and Preparation of Organic–Inorganic Hybrid Catalysts*, *Chem. Rev.*, 2002, 102, 3589–3614
- 104 T.K. Jain, I. Roy, T.K. De and A. Maitra, *Nanometer Silica Particles Encapsulating Active Compounds: A Novel Ceramic Drug Carrier*, *J. Am. Chem. Soc.*, 1998, 120, 11092-11095
- 105 B. Thierry, L. Zimmer, S. McNiven, K. Finnie, C. Barbé, H.J. Griesser, *Langmuir*, 2008, 24, 8143–
- 106 M.M. van Schooneveld et al., *Nano Lett.*, 2008, 8, 2517-
- 107 Q. He, L. Guo, F. Cui, Y. Chen, P. Jiang, J. Shi, *Facile one-pot synthesis and drug storage/release properties of hollow micro/mesoporous organosilica nanospheres*, *Mater. Lett.*, g, 63, 1943–1945
- 108 X. Yang, L. Chen, B. Huang, F. Bai, X. Yang, *Synthesis of pH-sensitive hollow polymer microspheres and their application as drug carriers*, *Polymer*, 2009, 50, 3556–3563
- 109 R.Y. Cheung, R. Kuba, A.M. Rauth, X. Yu Wu, *A new approach to the in vivo and in vitro investigation of drug release from locoregionally delivered microspheres*, *J. Control. Release*, 2004, 100, 121–133
- 110 Z.Z. Li, L.X. Wen, L. Shao, J.F. Chen, *Fabrication of porous hollow silica nanoparticles and their applications in drug release control*, *J. Control. Release*, 2004, 98, 245– 254
- 111 P. Horcajada, A. Ra'mila, J. Pérez-Pariente, M. Vallet-Regí, *Influence of pore size of MCM-41 matrices on drug delivery rate*, *Microporous Mesoporous Mater.*, 2004, 68, 105–109.
- 112 L. Pasqua, F. Testa, R. Aiello, S. Cundari and J.B. Nagy, *Preparation of bifunctional hybrid next term mesoporous previous termsilicanext term potentially useful for drug targeting*, *Micro. Meso. Mater.*, 2007, 103, 166-173

References

- 113 C. Sanchez, G.J.d. A. A. Soller-Illia, F. Ribot, T. Lalot, C.R. Mayer, V. Cabuil, *Designed Hybrid Organic-Inorganic Nanocomposites from Functional Nanobuilding Blocks*, *Chem. Mater.*, 2001, 13, 3061-3083
- 114 C. Zhang, F. Babonneau, C. Bonhomme, R.M. Laine, C.L. Soles, H.A. Hristo, and A.F. Yee, *J. Am. Chem. Soc.*, 1998, 120, 8380
- 115 P.A. Agaskar, *J. Chem. Soc. Chem. Commun.*, 1992, 1024
- 116 D. Hoebbel, K. Endres, T. Reinert, and I. Pitsch, *J. Non-Cryst Solids*, 1994, 176, 179
- 117 F. Ribot and C. Sanchez, *Organically Functionalized Metallic Oxo-Cluster: Structurally Well-defined Nanobuilding Blocks for the Design of Hybrid Organic-Inorganic Materials*, *Comments Inorg. Chem.*, 1999, 20, 327-371
- 118 G. Trimmel, P. Fratzl and U. Schubert, *Cross-Linking of Poly(methyl methacrylate) by the Methacrylate-Substituted Oxozirconium Cluster $Zr_6(OH)_4O_4(Methacrylate)_{12}$* , *Chem. Mater.*, 2000, 12, 602-604
- 119 E. Bourgeat-Lami, *Organic-Inorganic Nanostructured Colloids*, *J. Nanosci. Nanotech.*, 2002, 2, 1-24
- 120 M.G. Voronkov, V.I. Lavrent'yev, *Top Curr. Chem.*, 1982, 102, 9
- 121 a) A. Sellinger, R.M. Laine, *Chem. Mater.*, 1996, 8, 1592; b) R.M. Laine, *J. Mater. Chem.*, 2005, 15, 3725; c) J.D. Lichtenhan, *Comments Inorg. Chem.*, 1995, 17, 115
- 122 P.A. Agaskar, *New synthetic route to the hydridospherosiloxanes $Oh-H_8Si_8O_{12}$ and $D5h-H_{10}Si_{10}O_{15}$* , *Inorg. Chem.*, 1991, 30, 2707-2708
- 123 P.A. Agaskar, W.G. Klemperer, *The higher hydridospherosiloxanes: synthesis and structures of $H_nSi_nO_{1.5n}$ ($n = 12, 14, 16, 18$)*, *Inorg. Chim. Acta*, 1995, 229, 355-364
- 124 G. Calzaferri, D. Herren, R. Imhof, *Helv. Chim. Acta*, 1991, 74, 1278
- 125 D. Herren, H. Bürgy, G. Calzaferri, *Helv. Chim. Acta*, 1991, 74, 24
- 126 A.R. Bassindale, T. Gentle, *J. Organomet. Chem.*, 1996, 521, 391
- 127 a) A. Sellinger, R.M. Laine, *Silsesquioxanes as Synthetic Platforms. 3. Photocurable, Liquid Epoxides as Inorganic/Organic Hybrid Precursors*,

- Chem. Mater., 1996, 8, 1592-1593; b) P. Judenstein, Chem.Mater, 1992, 4, 4; c) P. Judenstein, J. Sol-Gel Sci. Technol, 1994, 2, 147
- 128 K. Wassermann, M. H. Dickman and M. T. Pope, *Self-Assembly of Supramolecular Polyoxometalates: The Compact, Water-Soluble Heteropolytungstate Anion* $[As_{12}III Ce_{16}III(H_2O)_{36}W_{148}O_{524}]^{76-}$, *Angew. Chem., Int. Ed. Engl.*, 1997, 36, 1445-1448
- 129 a) W.H. Knoth, *J. Am. Chem. Soc.*, 1979, 101, 759; b) P. Judeinstein, C. Deprun, L. Nadjo, *J. Chem. Soc., Dalton Trans.*, 1991, 1991; c) P. Judeinstein, *Chem. Mater.*, 1992, 4, 4 ; d) P. Judeinstein, *J. Sol-Gel Sci. Technol.*, 1994, 2, 147; e) N. Ammari, G.Hervc, R. Thouvenot, *New J. Chem.*, 1991, 15,607 ; f) A. Mazeaud, N. Arnmari. F.Robert, R. Thouvenot, *Angew. Chem. Int. Ed. Eng.*, 1996, 35, 1961
- 130 A.Müller, E. Krickemeyer, H. Bögge, M. Schmidtman and F. Peters, *Organizational Forms of Matter: An Inorganic Super Fullerene and Keplerate Based on Molybdenum Oxide*, *Angew. Chem., Int. Ed.*, 1998, 37, 3359-3363
- 131 P. Gouzerh and M. Che, *Polyoxometalates (POMs) revisited and the "missing link" between the bottom up and top down approaches*, *l'actualité chimique*, 2006, 298, 9-22
- 132 Eychenne-Baron, F. Ribot, N. Steunou, C. Sanchez, F. Fayon, M. Biesemans, J.-C. Martins, R. Willem, *Organometallics*, 2000, 19, 1940.
- 133 L.-F. Cui, X. Huang, L.-M. Wang, D.Y. Zubarev, A.I. Boldyrev, J. Li and L.-S. Wang, *Sn122: Stannaspherene*, *JACS*, 2006, 128, 8390-8391
- 134 V. LaMer, *J. Ind. Eng. Chem.*, 1952, 44
- 135 T.H. Galow, A.K. Boal, V.M. Rotello, *A "Building Block" Approach to Mixed-Colloid Systems Through Electrostatic Self-Organization*, *Adv. Mater.* 2000, 12, 576-579
- 136 B. Lebeau, C. Sanchez, *Sol-gel derived hybrid inorganic-organic nanocomposites for optics*, *Current Opinion in Solid State & Materials Science*, 1999, 4, 11-23

References

- 137 O.S. Rösch, W. Bernhard, R. Müller-Fiedler, P. Dannberg, A. Bräer, R. Buestrich, and M. Popall, SPIE 1999.
- 138 R. Buestrich, F. Kahlenberg, M. Popall, P. Dannberg, R. Müller-Fiedler, O. Rösch, *ORMOCER®s for Optical Interconnection Technology*, J. Sol-Gel Sci. Technol., 2001, 20, 181-186
- 139 R. Houbertz, G. Domann, C. Cronauer, A. Schmitt, H. Martin, J.-U. Park, L. Fröhlich, R. Buestrich, M. Popall, U. Streppel, P. Dannberg, C. Wächter and A. Bräuer, *Inorganic-organic hybrid materials for application in optical devices*, Thin Solid Films, 2003, 442, 194-200
- 140 S. Dirè, P. Egger, M.L. Di Vona, M. Trombetta, S. Licoccia, *Siloxane-Based Nanobuilding Blocks by Reaction between Silanediol and Trifunctional Silicon Alkoxides*, J. Sol-Gel Sci. Technol., 2004, 32, 57-61
- 141 M.L. Di Vona, M. Trombetta, S. Dirè, P. Egger, C. D'Ottavi and S. Licoccia, *Hybrid Siloxane-Based Nano Building Blocks for Optical Applications: Optimization of the Synthetic procedures by Spectroscopic Analysis*, J. Sol-Gel Sci. Technol., 2005, 35, 151-157
- 142 B.S. Furniss, A.J. Hannaford, P.W.G. Smith, A.R. Tatchell, *Textbook of practical organic chemistry Vogel's*, 5th ed., 1989, Longman Scientific & Technical
- 143 J.F. Brown jr, L.H. Vogt jr, *The Polycondensation of Cyclohexylsilanetriol*, J. Am. Chem. Soc., 1965, 87, 4313-4317
- 144 H. Yoshino, K. Kamiya, H. Nasu, *IR study on the structural evolution of sol-gel derived SiO₂ gels in the early stage of conversion to glasses*, J. Non Cryst. Solids, 1990, 126, 68-78
- 145 P. Innocenzi, G. Brusatin, M. Guglielmi and F. Babonneau, *Structural Characterization of Hybrid Organic-Inorganic Materials*, in Sol-Gel Science and Technology- Processing Characterization and Applications vol.II, 2005, Kluwer Academic Publishers, Netherlands
- 146 G. Socrates, *Infrared and Raman Characteristic Group Frequencies: Tables and Charts*, 3rd ed., 2001, Wiley, UK

- 147 Y.-J. Eo, T.H. Lee, J.K. Kang, Y.S. Han, B-S. Bae, *Synthesis and molecular structure analysis of nano-sized methacryl-grafted polysiloxane resin for fabrication of nano hybrid materials*, J. Polym. Sci.:B, 2005, 4, 827-836
- 148 A.D. Chomel, P. Dempsey, J. Latournerie, D. Hourlier-Bahloul and U.A. Jayasooriya, *Gel to Glass Transformation of Methyltriethoxysilane: A Silicon Oxycarbide Glass Precursor Investigated Using Vibrational Spectroscopy*, Chem. Mater., 2005, 17, 4468-4473 and ref therein
- 149 X. Li and A. King, *Spectroscopic studies of sol-gel derived organically modified silicates*, J. Non-Crist. Solids, 1996, 204, 235-242
- 150 M. Gnyba, M. Keranen, M. Kozanecki, R. Bogdanowicz, B.B. Kosmowski, P. Wroczynski, *Opto-Electron Rev.*, 2002, 10, 137
- 151 K. Gigant, U. Posset, G. Schottner, L. Baia, W. Kiefer, J. Popp, *J. Sol-Gel Sci. Technol.*, 2003, 26, 369
- 152 SDBS - Spectral Database for Organic Compounds: http://riodb01.ibase.aist.go.jp/sdbs/cgi-bin/direct_frame_top.cgi
- 153 B. Orel, R. Ješe, a. Vilčnik and U. Lavrenčič Štangar, *Hydrolysis and Solvolysis of methyltriethoxysilane Catalysed with HCl of Trifluoroacetic Acid: IR Spectroscopic and Surface Energy Studies*, J. Sol-Gel Sci. Technol., 2005, 34, 251-265
- 154 P. Innocenzi, A. Sassi, G. Brusatin, M. Guglielmi, D. Favretto, R. Bertani, A. Venzo and F. Babonneau, *Chem. Mater.*, 2001, 13, 3635-3643
- 155 D. Hoebbel, I. Pitsch, D. Heidemann, and Z. Anorg. Allg. Chem., 1991, 592, 207
- 156 a) R.H. Baney, M. Itoh, A. Sakakibara and T. Suzuki, *Chem. Rev.*, 2005, 95, 1409; b) N. Yoshinaga, N. Yamada, and S. Katayama, *J. Sol-Gel Sci. Technol.*, 2003, 28, 65
- 157 R.Lu, T. Honda, T. Ishimura and T. Miyakoshi, *Study of a Naturally Drying Laquer hybridized with Organic Silane*, *Polym. J.*, 2005, 37, 309-315
- 158 D. Hoebbel, M. Nacken, H. Schmidt, *A NMR Study on the hydrolysis, condensation and epoxide ring-opening reaction in sols and gels of the system*

References

- glycidoxypropyltrimethoxysilane - water-titaniumtetraethoxide*, J. Sol-Gel Sci. Technol., 1998, 12, 169-179;
- 159 L. Matějka, O. Dukh, J. Brus, W.J. Simonsick jr., B. Meissner, *Cage-like structure formation during sol-gel polymerization of glycidylxypropyltrimethoxysilane*, J. Non-Cryst. Solids, 2000, 270, 34-47.
- 160 S.A. Myers, R.A. Assink, D.A. Loy, K.J. Shea, *Investigation of the transmission of substituent effects by ²⁹Si NMR*, J. Chem. Soc., Perkin Trans., 2000, 2, 545-549
- 161 Y. Binev, J. Aires-de-Sousa, *Structure-Based Predictions of ¹H NMR Chemical Shifts Using Feed-Forward Neural Networks*, J. Chem. Inf. Comp. Sci., 2004, 44, 940-945
- 162 D. Craven, *Photolithography Challenges for the Micromachining Industry*, BACUS Symposium '96 - www.ultratech.com/pdf/bacus96.pdf
- 163 M. Brøkner Christiansen, M. Schøler and A. Kristensen, *Integration of active and passive polymer optics*, Optics express, 2007, 15, 3931-3939
- 164 Y. Ishida, K. Hakiai, A. Baba and T. Asano, *Electrostatic Inkjet Patterning Using Si Needle Prepared by Anodization*, Jpn. J. Appl. Phys., 2005, 44, 5786-5790
- 165 www.mse.vt.edu/faculty/hendricks/mse4206/GaAsTEK/Lithography/ladv.htm
- 166 <http://www.iue.tuwien.ac.at/phd/kirchauer/node29.html>
- 167 <http://www.ece.gatech.edu/research/labs/vc/theory/photoliyh.html>
- 168 M. Brøkner Christiansen, M. Schøler and A. Kristensen, *Integration of active and passive polymer optics*, Optics express, 2007, 15, 3931-3939
- 169 <http://www.memx.com/>
- 170 A. Ovsianikov, B. Chichkov, P. Mente, N.A. Monteiro-Riviere, A. Doraiswamy, R.J. Narayan, *Two Photon Polymerization of Polymer-Ceramic Hybrid Materials for Transdermal Drug Delivery*, Int. J. Appl. Ceram. Technol., 2007, 4, 22-29

- 171 R.J. Narayan et al., *Laser processing of advanced bioceramics*, *Adv Eng Materials*, 2005, 7, 1083-1098
- 172 a) S. Wada, A. Xia, and H. Tashiro, *3D optical data storage with two-photon induced photon-oxidation in C60-doped polystyrene film*, *RIKEN Review*, 2002, 49, 52-54; b) C. C. Corredor, Z.-L. Huang, K. D. Belfield, *Two-Photon 3D Optical Data Storage via Fluorescence Modulation of an Efficient Fluorene Dye by a Photochromic Diarylethene*, *Adv. Mater.*, 2006, 18, 2910 - 2914
- 173 K. Tanaka, M. Tanaka, T. Sugiyama,, *3D simulations of nanometric integrated optical circuits using surface plasmon polariton gap waveguide*, *Int. Conf. on Mathematical Methods in Electromagnetic Theory*, 2004, Dnieprapetravsk, Ukraine
- 174 a) I.D. Alves, C.K. Park and V.J. Hruby, *Plasmon Resonance Methods in GPCR Signaling and Other Membrane Events*, *Curr Protein Pept Sci.*, 2005, 6, 293-312; b) F. Zenhausern, M. Adrian and P. Descouts, *Solution Structure and Direct Imaging of Fibronectin Adsorption to Solid Surfaces by Scanning Force Microscopy and Cryo-electron Microscopy*, *Journal of Electron Microscopy*, 1993, 42, 378-388
- 175 I. Fortunati, T. Dainese R. Signorini, R. Bozio, V. Tagliazucca, S. Dire' G. Lemercier, G. Brusatin, M. Guglielmi , *Photopolymerization of hybrid organic/inorganic materials based on nanostructured units for photonic applications*, In: *Nanoengineering: Fabrication, Properties, Optics, and Devices IV*, Bellingham (WA), SPIE Digital Library, 2007, Vol. 6645, p. 664520
- 176 I. Fortunati, T. Dainese R. Signorini, R. Bozio, V. Tagliazucca, S. Dire' G. Lemercier, G. Brusatin, M. Guglielmi , *Photonic Devices Based On Patterning By Lithographic And Two Photon Induced Polymerization Techniques*. In: *SPIE*, Bellingham (WA), SPIE Digital library, 2008. Vol. 6988, p. 69881J-1-69881J-9.

References

- 177 a) T. Neuberger, B. Schöpf, H. Hofmann, M. Hofmann, B. von Rechenberg, *Superparamagnetic nanoparticles for biomedical applications: Possibilities and limitations of a new drug delivery system*, J. Magn.Magn. Mater., 2005, 293, 483-496; b) N.G. Khlebtsov, L.A. Dykman, *Optical properties and biomedical applications of plasmonic nanoparticles*, J. Quant. Spectr. Rad. Transf., 2010, 111, 1-35; c) T. Akagi, M. Baba, M. Akashi, *Preparation of nanoparticles by the self-organization of polymers consisting of hydrophobic and hydrophilic segments: Potential applications*, Polymer, 2007, 48, 6729-6747; d) S. Luridiana, S. Mutti, *Tribological properties of a CrN coating containing carbon nanoparticles*, Surf.Coat. Technol. 2005, 200, 704-707 e) N.C. Rosero-Navarro, S.A. Pellice, Y. Castro, M. Aparicio, A. Durán, *Improved corrosion resistance of AA2024 alloys through hybrid organic-inorganic sol-gel coatings produced from sols with controlled polymerisation*, Surf. Coat. Technol, 2009, 203,1897-1903
- 178 K.J. Kim, J.L. White, J. Ind. Eng. Chem., 2007, 7, 50
- 179 F.E.Wagner, S. Haslbeck, L. Stievano, S. Calogero, Q.A. Pankhurst, K.-P. Martinek, *Before striking gold in gold-ruby glass*, Nature, 2000, 407, 691-692
- 180 a) Y. Chen, J.O. Iroh, Chem. Mater.,1999, 11, 1218- ; b) X.Y. Shang, Z.K. Zhu, J. Yin, X.D. Ma, Chem. Mater., 2002, 14, 71-; c) M. Preghenella, A. Pegoretti, C. Migliaresi, Polymer, 2005, 46, 12065;
- 181 S.C. Tjong, *Novel Nanoparticle-Reinforced Metal Matrix Composites with Enhanced Mechanical Properties* (review), Adv. Eng. Mater., 2007, 9, 639-652
- 182 T. von Werne, T.E. Patten, J. Am. Chem. Soc., 2001, 123, 7497
- 183 M.Z. Rong, M.Q. Zhang, W.H. Ruan, Mater. Sci. Technol., 2006, 22, 787
- 184 T. Suhara, H. Fukui, M. Yamagnchi, F. Suzuki, Coll. Surf. A, 1996, 119, 15
- 185 a) P. Espiard, A. Guyot, Polymer, 1995, 23, 4391; b) A. Kryszatkiewicz, B. Rager, J. Adhes. Sci. Technol., 1999, 3, 393

- 186 a) S. Kim, E. Kim, S. Kim, W. Kim, *J. Coll. Interf. Sci.*, 2005, 292, 93; b) Y.P. Wang, X.W. Pei, K. Yuan, *Mater. Lett.*, 2005, 59, 520.
- 187 a) M. Fuji, T. Takei, T. Watanabe, M. Chidazawa, *Coll. Surf. A*, 1999, 154, 13; b) M. Fuji, S. Ueno, T. Takei, T. Watanabe, M. Chikazawa, *Coll. Polym Sci.*, 2000, 278, 30
- 188 S. Hoon Ahn, S. Hun Kim, S. Goo Lee, *Surface-modified silica nanoparticle-reinforced poly(ethylene 2,6-naphthalate)*, *J. App. Polym. Sci.*, 2004, 94, 812 - 818
- 189 D.N. Bikiaris, G.Z. Papageorgiou, E. Pavlidou, N. Vouroutzis, P. Palatzoglou, G.P. Karayannidis, *Preparation by Melt Mixing and Characterization of Isotactic Polypropylene/SiO₂ Nanocomposites Containing Untreated and Surface-Treated Nanoparticles*, *J. Appl. Polym. Sci.*, 2006, 100, 2684-2696
- 190 O.H. Lin, H. Md Akil, Z.A. Mohd Ishak, *Characterization and Properties of Activated Nanosilica/Polypropylene Composites With Coupling Agents*, *Polym. Comp.*, 2009, 30, 1693-1700
- 191 O.H. Lin, H. Md Akil, Z.A. Mohd Ishak, *Characterization and Properties of Activated Nanosilica/Polypropylene Composites With Coupling Agents*, *Polym. Comp.*, 2009, 30, 1693-1700
- 192 G. Malucelli, A. Di Gianni, F. Deflorian, M. Fedel, R. Bongiovanni, *Corrosion Science*, 2009, 51, 1762- 1771
- 193 M.L. Dias, M.S. Santos, F.R. Alves and C. Azuma, *Copolymerization of Alkoxysilanes: An Interesting Route to Core-Shell Silica-Silicone Nanoparticles*, *Mater. Sci.. Forum*, 2008, 570, 24-32
- 194 F. Branda, B. Silvestri, G. Luciani, A. Costantini, *Colloids and Surface A: Physiochem. Eng. Aspects*, 2007, 299, 252-255
- 195 Z. Wu, H. Xiang, T. Kim, M.-S. Chun, K. Lee. *Surface properties of submicrometer silica spheres modified with aminopropyltriethoxysilane and phenyltriethoxysilane*, *J. Colloid Interface Sci.*, 2006, 304, 119-124

References

- 196 M. Nakamura and K. Ishimura, *Synthesis and Characterization of Organosilica Nanoparticles Prepared from 3-Mercaptopropyltrimethoxysilane as the Single Silica Source*, *J. Phys. Chem.*, 2007, 111, 18892-18898
- 197 Y. Xu, R. Liu, D. Wu, Y. Sun, H. Gao, H. Yuan, F. Deng, *Ammonia-catalyzed hydrolysis kinetics of mixture of tetraethoxysilane with methyltriethoxysilane by ^{29}Si NMR*, *J. Non-Cryst. Solids*, 2005, 351, 2403-2413
- 198 I.A. Rahman, M. Jafarzadeh, C.S. Sipaut, *Synthesis of organo-functionalized nanosilica via co-condensation modification using γ aminopropyltriethoxysilane (APTES)*, *Ceram. Int.*, 2008, doi: 10.1016/j.ceramint.2008.10.028
- 199 a) H. Gleiter, *Nanocrystalline materials*, *Progr. Mater. Sci.*, 1989, 33, 223-315; b) K. Wegner, B. Walker, S. Tsantilis and S.E. Pratsinis, *Design of metal nanoparticle synthesis by vapor flow condensation*, *Chem. Eng. Sci.*, 2002, 57, 1753-1762
- 200 R. W. Siegel, *Nanophase Materials: Synthesis, Structure, and Properties*, Springer Series in Material Sciences 27, Springer-Verlag, 1994, Berlin
- 201 a) R. Uyeda, *Studies of ultrafine particles in Japan: crystallography*, *Progr. Mater. Sci.* 1991, 35, 1-96; b) T. Ohno, *Morphology of composite nanoparticles of immiscible binary systems prepared by gas-evaporation technique and subsequent vapor condensation*, *J. Nanoparticle Res.*, 2002, 4, 255-260
- 202 a) H. Liang, J.M. Raitano, L. Zhang, S.-W. Chan, *Controlled Synthesis of Co_3O_4 Nanopolyhedrons and Nanosheets at Low Temperature*, 2009, Supplementary Material (ESI) for Chemical Communications; b) E. Sówka, M. Leonowicz, J.A.D. Pomogailo, G.I. Dzhardimalieva, J. Kazmierczak, A. Slawska-Waniewska, M. Kopcewicz, *Formation of stable magnetic nanoparticles by pyrolysis of metal containing polymers*, *J. Magn. Mater.*, 2007, 316, e749-e752; c) S. Yang, Y.-H. Jang, C.H. Kim, C. Hwang, J. Lee, S. Chae, S. Jung, M. Choi, *A flame metal*

- combustion method for production of nanoparticles*, *Powd. Techn.*, 2010, 197, 170–176
- 203 a) C.J. Choi, X.L. Dong and B.K. Kim, *Characterization of Fe and Co Nanoparticles Synthesized by Chemical Vapor Condensation*, *Scripta Mater.*, 2001, 44, 2225–2229; b) J.C. Kim, B.K. Kim, *Synthesis of nanosized tungsten carbide powder by the chemical vapor condensation process*, *Scripta Mater.*, 2004, 50, 969–972; c) J.-C. Kima, J.-W. Lee, B.-Y. Park, C.-J. Choi, *Characteristics of Fe/SiO₂ nanocomposite powders by the chemical vapor condensation process*, *J. Alloys Comp.*, 2008, 449, 258–260; d) S.R. Haldar, A. Nayak, T.K. Chini, S. Bhunia, *Strong temperature and substrate effect on ZnO nanorod flower structures in modified chemical vapor condensation growth*, *Curr. Appl. Phys.*, 2009, doi: 10.1016/j.cap.2009.11.077
- 204 D. Dosev, M. Nichkova, R.K. Dumas, S.J. Gee, B.D. Hammock, K. Liu and I.M. Kennedy, *Magnetic/luminescent core/shell particles synthesized by spray pyrolysis and their application in immunoassays with internal standard*, *Nanotechnology*, 2007, 18, 05510-1/6
- 205 a) J. Fernandez de la Mora, L. de Juan, M. Gamero, *Electrospray Atomization: Fundamentals and its Applications in Nanoparticle Technology*, *J. Aerosol Sci.*, 1997, 28, Suppl. 1, 63; b) K. Nakaso, B. Han, K.H. Ahn, M. Choi, K. Okuyama, *Synthesis of non-agglomerated nanoparticles by an electrospray assisted chemical vapor deposition (ES-CVD) method*, *Aerosol Sci.*, 2003, 34, 869–881; c) C.J. Hogan Jr and P. Biswas, *Narrow size distribution nanoparticle production by electrospray processing of ferritin*, *Aerosol Sci.*, 2008, 39, 432–440; d) H. Oh, S. Kim, *Synthesis of ceria nanoparticles by flame electrospray pyrolysis*, *Aerosol Sci.*, 2007, 38, 1185–1196
- 206 M. Ullmann, S.K. Friedlander, and A. Schmidt-Ott, *Nanoparticle Formation by Laser Ablation*, *J. Nanopart. Res.*, 2002, 4, 499-509

References

- 207 D. N. McIlroy et al., *Nanoparticle formation in microchannel glass by plasma enhanced chemical vapor deposition*, J. Appl.Phys, 2003, 93, 5643-5649
- 208 H.H. Kung, and E.I. Ko, Chem. Eng. J., 1996, 64, 203.
- 209 K.S. Suslick, T. Hyeon, M. Fang, A.A. Cichowlas, *Sonochemical Preparation of Nanostructured Catalysts*, Adv. Cat. Nanostruct. Mater., 1996, 197-212
- 210 W.R. Moser, J.E. Sunstrom IV, B. Marshik-Guerts, *The Synthesis of Nanostructured Pure-Phase Catalysts by Hydrodynamic Cavitation*, Adv. Cat. Nanostruct. Mater., 1996, 285-306
- 211 Kishida, M., T. Fujita, K. Umakoshi, J. Ishiyama, H. Nagata, and K. Wakabayashi, Chem. Commun., 1995, 763.
- 212 a) A.R. Kortan, R. Hull, R.L. Opila, M.G. Bawendi, M.L. Steigerwald, P.J. Carroll, and L.E. Brus, J. Am. Chem. Soc., 1990, 112, 1327; b) Pileni, M.P., L. Motte and C. Petit, Chem. Mater., 1992, 4, 338.
- 213 F.J. Arriagada and K. Osseo-Asave, J. Colloid Interface Sci., 1995, 170, 8.
- 214 a) A. Sellinger, R.M. Laine, *Silsesquioxanes as Synthetic Platforms. 3. Photocurable, Liquid Epoxides as Inorganic/Organic Hybrid Precursors*, Chem. Mater., 1996, 8, 1592-1593. b) Pillai, V. P. Kumar, M.J. Hou, P. Ayyub, and D.O. Shah, Adv. in Colloid and Interface Sci., 1995, 55, 241.
- 215 D.L Leslie-Pelecky and R.D. Reike, Chem. Mater., 1996, 8, 1770.
- 216 J.Y.Ying and T. Sun, *Research needs assessment on nanostructured catalysts*, J. of Electroceramics, 1997, 1, 219-238.
- 217 C.C. Koch, *Materials synthesis by mechanical alloying*, Annual Review of Mater. Sci., 1989, 19, 121-143
- 218 L.L.Hench, J.K.West, *The Sol-Gel Process*, Chem. Rev., 1990, 90, 33-72.
- 219 W. Stöber, A. Fink and E. Bohn, *Controlled growth of Monodispersed Silica Spheres in the Micron Size range*, J. Colloid Interface Sci., 1968, 26, 62-69

- 220 C.H. Byers, M.T. Harris, D.F. Williams, *Ind.En. Chem. Res.*, 1987, 26, 1916
- 221 a) M.T. Harris, C.H. Byers, R.R. Brunson, *J. Non-Cryst. Solids*, 1990, 121, 397; b) D.L.Green, S. Jayasundara, Y.F. Lam, M.T. Harris, *Chemical reaction kinetics leading to the first Stöber silica nanoparticles- NMR and SAXS investigation*, *J. Non-Cryst. Solids*, 2003, 315, 166-179
- 222 B.W. Peace, K.G. Mayhan, J.F. Montle, *Polymer*, 1973, 14, 420
- 223 a) K. Lee, J. Look, M.T. Harris, A.V. McCormick, *J. Colloid interface Sci.*, 1997, 194, 78; b) K. Lee, A. N. Sathyagal, A.V. McCormick, *Colloids Surf. A Physicochem. Eng. Asp.*, 1998, 144, 115;
- 224 A. van Blaaden, J. van Geest, A. Vrij, *J. Colloid Interface Sci.*, 1992, 154, 481
- 225 a) T. Matsoukas and E. Guilari, *J. Colloid Interface Sci.*, 1988, 124, 252; b) G.H Bogush, M.A. Tracy and C.F. Zukoski, *Preparation of monodisperse silica particles: Control of size and mass fraction*, *J. Non-Cryst. Solids.*, 1988, 104, 95-106; c) R. Vacassy, R.J. Flatt, H. Hoffman, K.S. Choi and R.K. Singh, *J. Colloid Interface Sci.*, 2000, 227, 302; d) J.J. Razink and N.E Schlotter, *Correction to "Preparation of monodisperse silica particles: Control of size and mass fraction" by G.H Bogush, M.A. Tracy and C.F. Zukoski*, *J. Non-Cryst. Solids*, 2007, 353, 2932-2933; e) K.D. Hartlen, A.P.T. Athanasopoulos and V. Kitaev, *Facile preparation of Highly Monodisperse Small Silica Spheres (15 to > 200 nm) Suitable for Colloidal templating and Formation of Ordered Arrays*, *Langmuir*, 2008, 24, 1714-1720; f) D.A. Santamaría Razo, L. Pallavidino, E. Garrone, F. Geobaldo, E. Descrovi, A. Chiodoni, F. Giorgis, *A version of Stöber synthesis enabling the facile prediction of silica nanospheres size for the fabrication of opal photonic crystals*, *J. Nanopart. Res.*, 2008, 10, 1225-1229; g) X.-D. Wang, Z.-X. Shen, T. Sang, X.-B. Cheng, M.-F. li, L.-Y. Chen, Z.-S. Wang, *Preparation of spherical silica particles by Stöber process with high*

References

- concentration of tetra-ethyl-orthosilicate*, J. Colloid Interface Sci., 2009, doi: 10/1016/j.jcis.2009.09.018
- 226 A. van Blaaden, and A. Vrij, J. Colloid Interface Sci., 1993, 156
- 227 I. Suratwala, M.L. Hanna, E.L. Miller, P.K. Whitman, I.M. Thomas, P.R. Ehrmann, R.s. Maxwell and A.K. Burnham, J. Non-Cryst. Solids, 2003, 316, 349
- 228 R. Yin and R.M. Ottenbrite, Polym. Prepr., 1996, 36, 265
- 229 J.Y. Choi, C.H. Kim, D.K. Kim, J. Am. Ceram. Soc., 1998, 81, 1184
- 230 a) K. Katagiri, K. Hasegawa, A. Matsuda, M. Tatsumisago and M. Minami, J. Am. Ceram. Soc., 1998, 81, 2501; b) A. Matsuda, T. Sasaki, T. Tanaka, M. Tatsumisago and M. Minami, J. Sol-Gel Sci. Technol., 2002, 23, 247
- 231 P.A. Buining, L.M. Liz-Marzan and A.P. Philipse, J. Colloid Interface Sci., 1996, 179, 318
- 232 A. Arkhireeva and J.N. Hay, *Synthesis of sub-200 nm silsesquioxane particles using a modified Stöber sol-gel route*, J. Mater. Chem., 2003, 13, 3122-3127
- 233 S. Shibata, T. Taniguchi, T. Yano and M. Yamane, *Formation of Water-Soluble Dye-Doped Silica Particles*, J. Sol-Gel Sci. Technol., 1997, 10, 263-268
- 234 a) X. Gao, J. He, L. Deng, H. Cao, *Synthesis and characterization of functionalized rhodamine B-doped silica nanoparticles*, Opti. Mater., 2009, 31, 1715-1719
- 235 R.P. Bagwe, K. C. Khilar, Langmuir, 1997, 13, 6432-6438
- 236 C. Song, Z. Ye, G. Wang, D. Jin, J. Yuan, Y. Guan, J. Piper, Preparation and time-gated luminescence bioimaging application of ruthenium complex covalently bound silica nanoparticles, Talanta, 2009, 79, 103-108
- 237 Y. Wang, W. Qin, J. Zhang, C. cao, J. Zhang, Y. Jin, X. Ren, Z. Zheng, S. Lü, *Synthesis, photoluminescence and bioconjugation of rare-earth (Eu)*

- complexes-embedded silica nanoparticles*, Solid State Comm., 2007, 142, 689–693
- 238 S. Sakka, Handbook of Sol-Gel Science and Technology - *Processing Characterization and Applications. Vol.II: characterization of sol-gel materials and products*, 2005, Kluwer Academic Publishers, Boston
- 239 L.M. Rossi, S. Lifang, F.H. Quina, Z. Rosenzweig, *Stöber synthesis of monodispersed luminescent silica nanoparticles for bioanalytical assays*, Langmuir, 2005, 21, 4277-4280
- 240 S. Dirè, E. Callone, A. Quaranta, V. Tagliazucca, *Modification of the surface properties of sol-gel particles prepared from organoalkoxysilanes for nanocomposites applications - in preparation*
- 241 a) W. Inaoka, S. Harada, T. Yasunaga, *Kinetic and Spectrophotometric Studies of Rhodamine 6G Dimerization in Aqueous Solutions*, Bull. Chem. Soc. Jpn, 1980, 53, 2120-2122; b) D. Toptygin, B.Z. Packard, L. Brand, *Resolution of absorption spectra of rhodamine 6G aggregates in aqueous solution using the law of mass action*, Chem. Phys. Lett., 1997, 277, 430-435; c) V.I. Gavrilenko and M.A. Noginov, *Ab initio study of optical properties of rhodamine 6G molecular dimers*, J. Chem. Phys., 2006, 124, 044301-1/6; d) A. Anedda, C.M. Carbonaro, R. Corpino, P.C. Ricci, *Formation of fluorescent aggregates in Rhodamine 6G doped silica glasses*, J. Non-Cryst. Solids, 2007, 353, 481–485
- 242 a) R. F. Kubin and A. N. Fletcher, *Fluorescence quantum yields of some rhodamine dyes*, J. Luminescence, 1983, 27, 455-462; b) M. Fischer, J. Georges, *Fluorescence quantum yield of rhodamine 6G in ethanol as a function of concentration using thermal lens spectrometry*, Chem. Phys. Lett., 1996, 260, 115-118
- 243 P.Egger, G.D. Sorarù, R. Ceccato and S. Diré, *YSZ freestanding films from hybrid polymer-oxide composites by the sol-gel process: Influence of polymer features on ceramic microstructure*, Journal of the European Ceramic Society, 2005, 25, 2647-2650

- 244 <http://www.exciton.com/pdfs/RH590.pdf>
- 245 M. Voronkov and V.I. Lavrentyev, *Top. Curr. Chem.*, 1982, 102, 199
- 246 B. Riegel, W. Kiefer, S. Hofacker and G. Schottner, *FT-Raman-Spectroscopic Investigations of the System Glycidoxypropyl-trimethoxysilane/Aminopropyltriethoxysilane*, *J. Sol-Gel Sci. Technol.*, 1998, 13, 385-390.
- 247 Z. Olejniczak, M. Łęczka, K. Cholewa-Kowalska, K. Wojtach, M. Rokita, M. Mozgawa, *²⁹Si MAS NMR and FTIR study of inorganic-organic hybrid gels*, *J. Molec. Struct.*, 2005, 744-747, 465-471 and ref therein
- 248 a) D. Derouet et al, *J. Polymer Sci.: Polymer chem.*, 1998, 36, 437-453; b) H. Juvaste, E.I. Iiskola, T.T. Pakkanen, *Preparation of new modified catalyst carriers*, *J. Mol. Cat. A: Chemical*, 1999, 150, 1-9; c) M. Jaber, *Microporous and Mesoporous Mater.*, 2003, 65, 155-163; d) L. Wei et al., *Microporous & Mesoporous Mater.*, 2004, 67, 175-179
- 249 D. Toptygin, B.Z. Packard, L. Brandmitri, *Resolution of absorption spectra of rhodamine 6g aggregates in aqueous solution using the law of mass action*, *Chem. Phys. Lett.*, 1997, 277, 430-435
- 250 A. Matsuda, T. Sasaki, T. Tanaka, M. Tatsumisago and T. Minami, *Preparation of Copolymerized Phenylsilsesquioxane-Benzylsilsesquioxane Particles*, *J. Sol-Gel Sci. Technol.*, 2002, 23, 247-252
- 251 C.G. Pantano, A. K. Singh and H. Zhang, *Silicon Oxycarbide Glasses*, *J. Sol-Gel Sci. Technol.*, 1999, 14, 7-25
- 252 G.M. Renlunf, S. Prochazka and R. Doremus, *Silicon Oxycarbide Glasses. 2. Structures and Properties*, *J. Mater. Res.*, 1991, 6, 2723-2734
- 253 G.D. Sorarù, S. Modena, E. Guadagnino, P. Colombo, J. Egan and C. Pantano, *Chemical durability of silicon oxycarbide glasses*, *J. Am. Ceram. Soc.*, 2002, 85, 1529-1536
- 254 S. Dirè, R. Ceccato, F. Babonneau, *Structural and microstructural evolution During Pysolysis of Hybrid Polydimethylsiloxane-Titania Nanocomposites*, *J. Sol-Gel Sci. Technol.*, 2005, 34, 53-62

- 255 G.D. Sorarù, E. Dallapiccola, G. D'Andrea, *Mechanical Characterization of sol-gel derived Silicon Oxycarbide Glasses*, *J. Am. Ceram. Soc.*, 2005, 79, 2074-2080
- 256 M. Fedel, F. Deflorian, S. Dirè, V. Tagliazucca, R. Bongiovanni, L.Vescovo, *Electrochemical characterization of nanostructured UV-cured urethane-acrylic coatings*, *Advances in corrosion protection 2009*, Cambridge (UK)

APPENDIX A

NBB- SYNTHESSES PROCEDURES

Syntheses procedure for MPTMS and GLYMO based D/T_L samples

1. DPDO/MPTMS/TEA/THF - (D/T_L-1)

DPDO (2.5 mmol, 0.5408 g) was dissolved with THF (50 mmol, 4.06 mL) at RT in a two-neck flask equipped with reflux, and the condensation promoter TEA (5 mmol, 0.697 mL) was added to the solution, stirring at 75 °C for 20 min before addition of MPTMS (1.67 mmol, 0.397 mL). Molar ratios between precursors are: DPDO:MPTMS=1.5:1, DPDO:THF:TEA=1:20:2. The solution was kept stirring at 75 °C for 2 h under N₂ and aged at RT for 7 days. After ageing, the solution appeared clear and was evaporated to dryness, removing volatile compounds at 10⁻² mmHg and 50°C for 2 h. A viscous oil was obtained, which was dissolved with dry THF to give a final [Si] = 1.85 M.

2. DPDO/MPTMS/TIPO/THF - (D/T_L-2)

The mixture of DPDO (2.5 mmol, 0.5408 g), THF (50 mmol, 4.06 mL), MPTMS (3.75 mmol, 0.552 mL) and Ti(OPri)₄ (0.01472 g, 15.3 µL) was kept stirring for 24 h under N₂. Molar ratios DPDO:MPTMS:THF = 1:1.5:20, TIPO = 1 wt.% calculated with respect to total silanes. After aging for 7 days at RT, the clear solution was evaporated to dryness removing volatile compounds at 10⁻² mmHg and 50°C for 2 h. A viscous oil was obtained and diluted with THF to give a final [Si] = 1.85 M.

3. DPDO/Glymo/DBDLT/THF - (D/T_L-3)

DPDO (2.5 mmol, 0.5408 g), was dissolved Glymo (2.5 mmol, 0.891 mL) at RT in a two-neck flask equipped with reflux, DBDLT (0.01132 g, 10.6 μ L) was added at the suspension, which was dissolved with THF (50 mmol, 4.06 mL). The solution was kept stirring for 24 h under N₂ at 75°C. Molar ratios DPDO: Glymo: THF = 1:1:20, DBDLT = 1 wt.% calculated with respect to total silanes. After aging for 7 days at RT, the clear solution was evaporated to dryness removing volatile compounds at 10⁻² mmHg and 50°C for 2 h. A viscous oil was obtained and diluted with THF to give a final [Si] = 1.85 M.

Syntheses procedure for MPTMS based D/T_H samples

4. DPDO/MPTMS /AcA/EtOH - (D/T_H-1)

A mixture of DPDO (2.5 mmol, 0.5408 g), MPTMS (12.5 mmol, 2.971 mL) and AcA (5 mmol, 0.286 mL) in two-neck flask equipped with reflux, was allowed to homogenize under stirring for 10 min at 75°C in air. The solution was dissolved in EtOH (10 mmol, 0.584 mL) and kept stirring for 7 days. Molar ratios DPDO:MPTMS=1:5, DPDO:EtOH:AcA=1:4:2. The final solution was kept stirring for further 7 days leading to a clear yellowish solution. The solution was evaporated to dryness at 10⁻² mmHg and 60°C for 2 h. A viscous oil was obtained and diluted with THF to give a final [Si] = 1.85 M.

5. DPDO/Glymo /AcA/EtOH - (D/T_H-4)

A mixture of DPDO (2.5 mmol, 0.5408 g), Glymo (12.5 mmol, 2.761 mL) and AcA (5 mmol, 0.286 mL) in two-neck flask equipped with reflux, was allowed to homogenize under stirring for 10 min at 65°C in air.

The solution was dissolved in EtOH (10 mmol, 0.584 mL) and kept stirring for 7 days. Molar ratios DPDO:Glymo=1:5, DPDO:EtOH:AcA = 1:4:2. The final solution was kept stirring for further 7 days leading to a clear colourless solution. The solution was evaporated to dryness at 10^{-2} mmHg and 60°C for 2 h. A viscous oil was obtained and diluted with THF to give a final $[\text{Si}] = 1.85 \text{ M}$.

Syntheses procedure for Glymo self-condensation G_s samples

6. Glymo/AcA/EtOH - (G_s-1)

Glymo (1 mmol, 0.221 ml) and Cl-AcA (1 mmol, 94.5 mg), in two-neck flask equipped with reflux, were allowed to homogenize under stirring for 5 min in air. The solution was dissolved in EtOH (8 mmol, 0.467 mL) and kept stirring for 1h at 70°C . Molar ratios Glymo:EtOH:Cl-AcA=1:8:1. The final solution was kept stirring for further 23h leading to a clear colourless solution. The solution was evaporated to dryness at 10^{-2} mmHg and 60°C for 2 h. A viscous oil was obtained and diluted with THF to give a final $[\text{Si}] = 1.85 \text{ M}$.

7. Glymo/AcA/EtOH - (G_s-2)

Glymo (1 mmol, 0.221 ml) and Cl-AcA (1 mmol, 94.5 mg), in two-neck flask equipped with reflux, were allowed to homogenize under stirring for 5 min in air. The solution was dissolved in EtOH (8 mmol, 0.467 mL) and kept stirring at RT for 3 days leading to a clear colourless solution. Molar ratios Glymo:EtOH:Cl-AcA = 1:8:1. The solution was evaporated to dryness at 10^{-2} mmHg and 60°C for 2 h. A viscous oil was obtained and diluted with THF to give a final $[\text{Si}] = 1.85 \text{ M}$

APPENDIX B

Reagents

1. NBB

Precursors

Diphenylsilanediol (DPDO) 95%, 99%, M_w 178.30 d 0.89, ABCR

Methacryloxypropyltrimethoxysilane (MPTMS) 98%, M_w 248.35 d 1.045 Aldrich

Glycidoxypropyltri-methoxysilane (Glymo) 98%, M_w 236.34 d 1.07 ABCR

Solvents

Tetrahydrofuran anhydrous (THF) 99.9%, M_w 72.10 d 0.889, (Sigma-Aldrich)

Acetone >99.9% , M_w 58.08 d 0.79, (Sigma-Aldrich)

Toluene 99.5%+, M_w 92.14 d 0.866 JT Backer

Acetonitrile ACS, M_w 41.05 d 0.79, Aldrich

Alcohols

Ethanol (EtOH) >99.8%, M_w 46.07 d 0.79 Aldrich

1-propanol (*n*PrOH) 99%, M_w 60.10 d 0.8 Aldrich

2-Propanol (*i*PrOH) 99.7%, M_w 60.10 d 0.785 JT Backer

n-Butanol (*n*BuOH), M_w 74.12 d 0.808 Riedel de Haen

sec- Butanol (*s*BuOH), M_w 74.12 d 0.808 Carlo Erba Reagents

tert- Butanol (*t*BuOH)>99.7%, M_w 74.12 d 0.79 Fluka

Condensation promoters

Basic

Triethylamine (NEt₃ - TEA) 99%, M_w 101.19 d 0.728 Aldrich

Acid

Titanium isopropoxide (TIPO) 97%, M_w 284.23 d 0.95 Aldrich

Dibutyl dilauryl Tin (DBDLT) 95%, M_w 631.55 d 1.05 ABCR

Trifluoroacetic acid (TFA) 99%, Mw 114.02 d 1.535 Carlo Erba Reagents

TiCl₄ 99.9%, Mw 189.69 d 0.964 Aldrich

Carboxylic acid

Acetic Acid (AcA) glacial, >99.5%, Mw 60.05 d 1.048 Carlo Erba Reagents

Formic acid (FA) ACS grade, Mw 46.03 d 1.22 Aldrich

Propionic acid (PA) >99%, Mw 74.08 d 0.99 Aldrich

Acetylsalicylic acid (ASA) >97%, Mw 180.16 d 1.35 Aldrich

Thioglycolic acid (TGA) 99%, Mw 32.11 d 1.503 Aldrich

Salicylic acid (SA) 99.5%, Mw 138.12 mp: 158-161 °C

Chloroacetic acid (Cl-AcA) 99%, Mw 94.50 d 1.58

Citric acid (CA) 99.8%, Mw 210.14 d 1.54

Ascorbic acid (AA), Mw 176.13 mp: 190-192°C

2. Nanoparticles (NP)

Precursors

Methyltriethoxysilane (MTES or M) 99%, Mw 178.30 d 0.89, ABCR

Ethyltriethoxysilane (ETES) 97%, Mw 192.33 d 0.896, ABCR

Vinyltriethoxysilane (VTES or V) 98%, Mw 190.31 d 0.90, ABCR

Phenyltriethoxysilane (PhTES) 97%, Mw 240.37 d 0.996, ABCR

Amyltriethoxysilane (ATES) >97%, Mw 234.41 d 0.895, Aldrich

Octyltriethoxysilane (OTES) 96%, Mw 276.49 d 0.879, Aldich

Aminopropyltriethoxysilane (ApTES or Ap), Mw 221.37 d 0.942, ABCR

Solvents, acids and bases

Double distilled water

Ethanol (EtOH) >99.8%, Mw 46.07 d 0.79 Aldrich

Ammonium hydroxide 29%, Mw 35.05 d 0.9, Aldrich

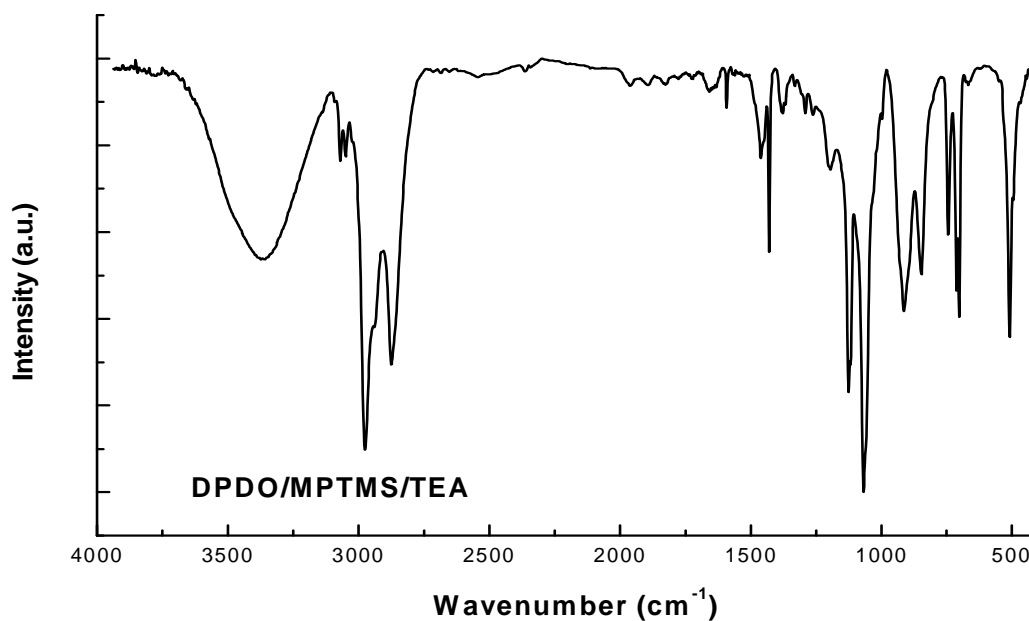
Hydrochloric acid fuming 37%, Mw 36.46 d 1.2, Sigma-Aldrich

APPENDIX C

REACTION CONDITIONS

Non-Hydrolytic

a) DPDO/TEA/THF



1. MPTMS- D/T_L-NBB

DPDO/ NET/THF (D/T_L-1)

* ratio respect to DPDO

Sample	DPDO/MPTMS	TEA*	Temp.
D/T _L -1a	1: 1.5	1	RT
D/T _L -1b	1.5: 1	1	RT
D/T _L -1c	1: 1.5	0.1	RT
D/T _L -1d	1.5: 1	0.1	RT
D/T _L -1e	1: 1.5	0.1	70°C
D/T _L -1f	1: 1.5	1	70°C
D/T _L -1g	1: 1.5	2	70°C
D/T _L -1h	1.5: 1	2	70°C
D/T _L -1i	1.5: 1	1	70°C

Different ratio between the precursor, amount of condensation promoter (TEA) and reaction temperature were used.

Reaction progress was monitored by means of FT-IR and the best reaction conditions were chosen step by step. First, the DPDO/MPTMS ratio 1.5:1 (0.67) resulted the best, as the Si-O-Si condensation was higher, with both amount of condensation promoter (0.1 and 1); the next attempt was to carry out the reactions at high temperature (70°C). Moreover, to improve the condensation rate the amount of TEA was increased.

The best reaction parameters were used to synthesise sample D/T_L-1h, which has been described in Part 1 as D/T_L-1.

DPDO/ TIPO/THF (D/T_L-2)

Sample	DPDO/MPTMS	TIPO*	Temp.
D/T _L -2a	1: 1.5	1%	RT
D/T _L -2b	1.5: 1	1%	RT
D/T _L -2c	1: 1.5	5%	RT
* D/T _L -2d	1: 1.5	10%	RT

ratio respect to [Si]

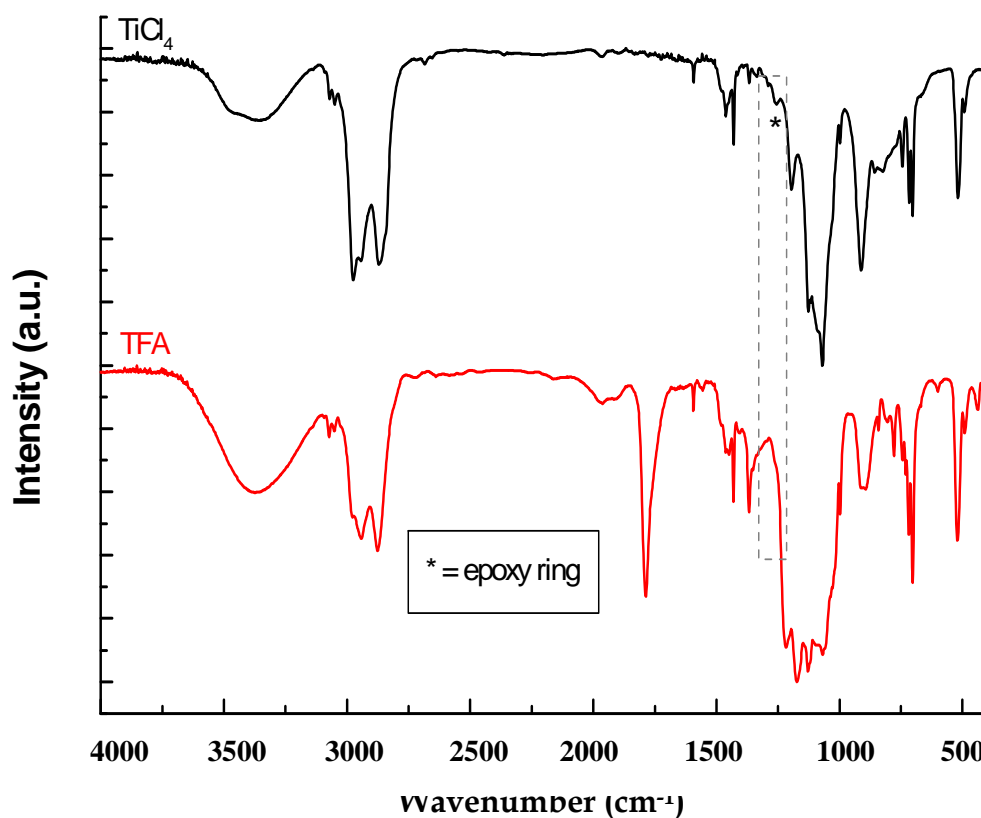
The ratio 1:1.5 (DPDO/MPTMS) resulted the best option, since the condensation reaction rate was higher respect to the 1.5:1 (0.67) ratio.

In this case, only syntheses at RT were performed, as the reaction proceeded even without the use of high temperature. Different amounts of condensation promoter were tested. Reactions with 5 and 10% on the [Si] content, did not differ from 1% in their catalytic activity.

The best reaction parameters were use to synthesise sample D/T_L-2a, which in the experimental discussion of Part 1 is labelled D/T_L-2.

2. Glymo D/T_L-NBB

In order to enhance the hydrolysis-condensation rate, strong acids, such as TiCl_4 and trifluoroacetic acid (TFA) were used as condensation promoters. FT-IR spectra are shown below.

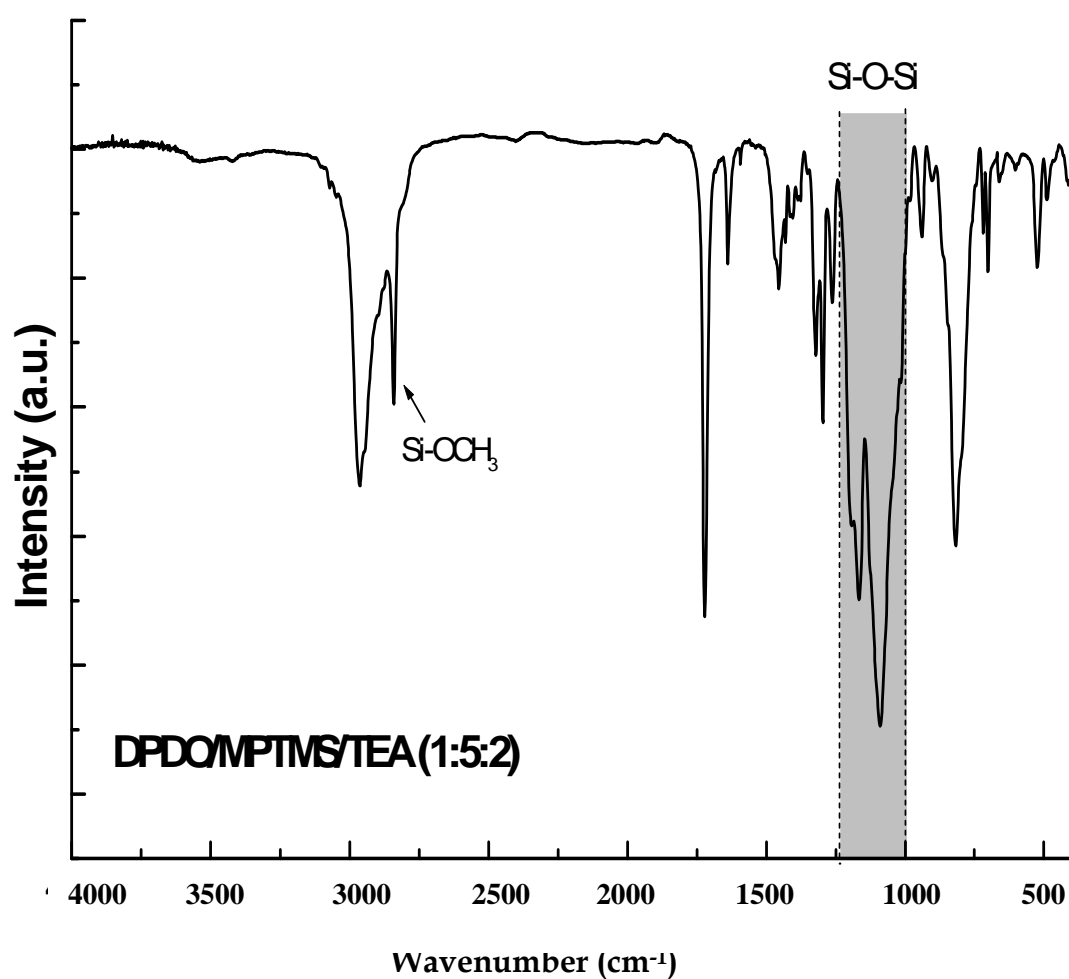


The use of strong acids leads to the loss of the epoxirane ring. The spectra show in both cases the disappearance of the typical peaks due to the epoxy ring vibrations (1256, 910, 856 cm^{-1}).

In order to maintain the reactive organic function, a weak acid as dibutyl dilauryl Tin (DBDLT) was chosen. In this case the epoxy function was preserved (Experimental section Part 1, sample D/T_L-3)

3. MPTMS- D/T_H-NBB

The non-hydrolytic approach was not efficient enough with high MPTMS loaded samples; both reactions rate and Si-O-Si condensation were low as it is noticeable from both, the very intense peak at 2838 cm⁻¹ due to vibration of the residual methoxy groups (Si-OCH₃) and the low presence of peaks in the 1200-900 cm⁻¹ range, typical of the Si-O-Si bonds vibrations. Spectrum for DPDO/MPTMS with TEA as catalyst is presented below.

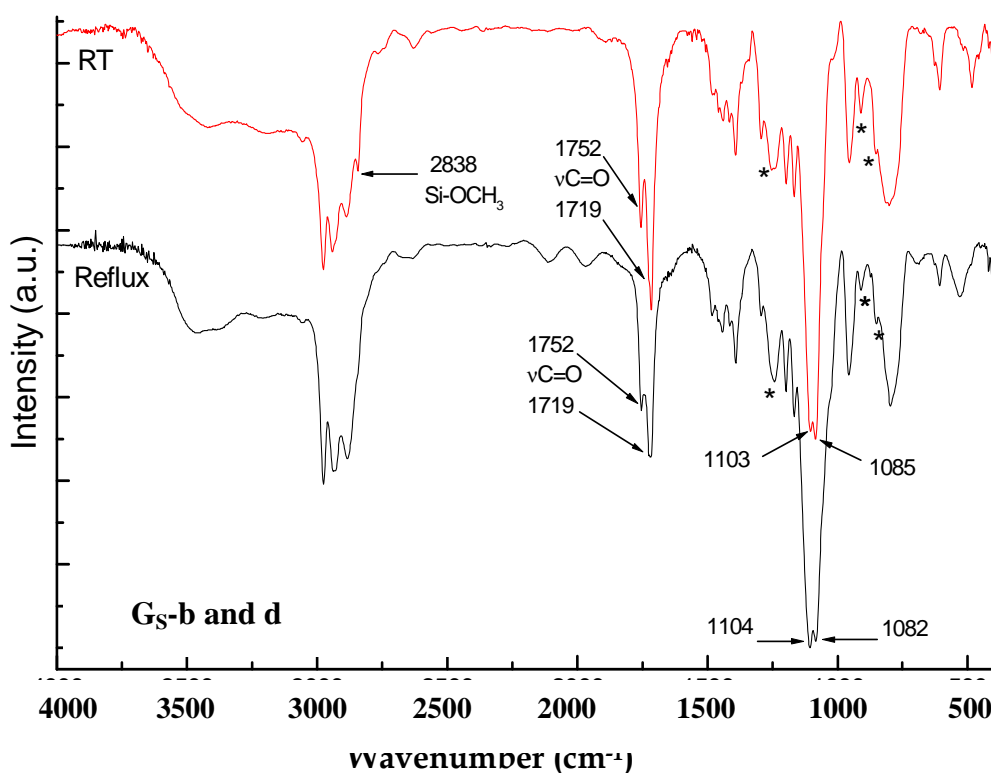


4. Glymo- G_S-NBB

ISWP was exploited also for the first attempt of glymo self-condensation reactions.

Sample	Ethanol*	Acetic Acid*	Temp.
G _S -a	4	2	RT
G _S -b	8	2	RT
G _S -c	4	2	70°C
G _S -d	8	2	70°C

*ratio respect to Glymo



Good condensation degree of the Si-O-Si network and the maintenance of the reactive function were obtained (see spectra above), but still the reaction rate was slow, especially when the reaction was carried out at RT (7 to 14 days). Thus, chloroacetic acid (Cl-AcA) was used in order to increase the reaction rate. Samples were presented in the experimental part as G_S -1 and G_S -2.

Other Syntheses performed

D/T_L-syntheses

DPDO/MPTMS

*ratio respect to DPDO

DPDO / MPTMS	solvent	solvent*	Cond. Prom. (*)	Temp.
1: 1	-	-	TEA (1)	75°C
1: 1	-	-	TIPO 1% [Si]	75°C
1.5: 1	acetone	20	TIPO 1% [Si]	75°C
1.5: 1	acetone	20	TEA (2)	50°C
1.5: 1	acetone	20	TIPO (1% [Si])	50°C
1: 1	THF	20	TiCl ₄	RT
1:1	THF	5	DBDLT	75°C
1:1.5	THF	5	DBDLT	75°C
1:1.5	THF	5	DBDLT	75°C

DPDO/Glymo

DPDO / Glymo	solvent	solvent*	Cond. Prom. (*)	Temp.
1: 1	THF	20	TFA (3)	RT
1: 1	THF	5	TFA (3)	RT
1: 1	THF	5	TIPO 1% [Si]	RT
1: 1	THF	5	TIPO 1% [Si]	75°C
1: 1	THF	20	TIPO 1% [Si]	75°C
1: 1	THF	5	DBDLT 1% [Si]	75°C
1: 1	THF	20	TiCl ₄ 1% [Si]	RT
1: 1.5	THF	5	DBDLT 1% [Si]	75°C
1.5: 1	THF	5	DBDLT 1% [Si]	75°C

DPDCI/MPTMS

*ratio respect to DPDO

DPDCL = diphenyl dichosilane

DPDCI/ MPTMS	solvent	solvent*	Cond. Prom. (*)	Temp.
1.5: 1	THF	20	TEA (2)	75°C
1.5: 1	THF	20	TIPO 1% [Si]	75°C
1.5: 1	toluene	20	TIPO 1% [Si]	75°C
1.5: 1	Acetone	20	TIPO 1% [Si]	50°C
1. 1.5	Acetone	20	TIPO 1% [Si]	50°C
1: 1	-	-	TIPO 1% [Si]	75°C
1.5: 1	CH ₃ CN	20	TIPO 1% [Si]	75°C
1: 1	THF	5	DBDLT 1% [Si]	75°C
1.5: 1	THF	20	TIPO 1% [Si]	75°C

DPDCI/Glymo

DPDCI/ Glymo	solvent	solvent*	Cond. Prom. (*)	Temp.
1: 1	-	-	TFA (3)	RT
1: 1	-	-	TIPO 1% [Si]	RT
1: 1	THF	5	DBDLT 1% [Si]	75°C
1: 1	-	-	DBDLT 1% [Si]	75°C

D/T_H-syntheses**DPDO/MPTMS**

*ratio respect to DPDO

DPDO/ MPTMS	solvent	solvent*	Cond. Prom. (*)	Temp.
1:5	-	-	TEA (2)	75°C
1:5	THF	5	AcA (2)	75°C
1:5	EtOH	4	TEA (2)	75°C
1:5	MeOEtOH	4	TEA (2)	75°C

MeOEtOH= methoxyethanol

DPDO/Glymo

DPDO/ Glymo	solvent	solvent*	Cond. Prom. (*)	Temp.
1:5	EtOH	2	AcA (2)	RT
1:5	THF	5	AcA (2)	RT
1:5	THF	5	AcA (2)	75°C
1:5	THF	5	AcA (2)	RT
1:5	EtOH	5	DBDLT (1%[Si])	RT
1:5	THF	5	DBDLT (1%[Si])	RT

DPDCl/Glymo

DPDCl/ Glymo	solvent	solvent*	Cond. Prom. (*)	Temp.
1:5	EtOH	5	DBDLT (1%[Si]	RT

Samples in experimental section of this thesis work were chosen for both, good condensation degree of the siloxane network and samples' colour. Some performed syntheses led to good products, but with dark-brown or intense yellow colours. Unfortunately the clearness and transparency are key points for the final applications of these materials.

ACKNOWLEDGMENTS

First of all, I would like to thank my advisor Prof. Sandra Dirè, for giving me the possibility to work in a small but stimulating environment, for the ability of leading me through this work with the strength of a chief and the patient of a mother, and for the possibility to learn from competent professors and researchers.

A special thanks goes to the technicians of the lab, Alexia and Livio, for being always available, also for trivial questions.

I would like also to acknowledge all the researches and Professors I met during my PhD and who helped with measurements and discussions the evolution of my work:

Dr. Emanuela Callone (NMR), Dr. Giovanna Brusatin and co-workers of the Un. of Padua (Raman and UV lithography), Dr. Roberta Signorini and co-workers of the Un. of Padua (TPIP measurements), Prof. Jocelyne Galy (INSA-Lyon) for giving me the possibility to use the GPC instrument, Dr. Mariangela Fedel (FE-SEM), Dr. Claudio Della Volpe (contact angle measurements), Prof. A. Quaranta (spectrofluorometer), Prof. S. Licoccia and Dr. M.L. Di Vona (NMR) Un. of Rome "Tor Vergata", Dr. M. Trombetta (ATR/FT-IR) Centro Interdisciplinare Ricerche Biomediche (C.I.R.) Rome, Dr. E. Callone (NMR) Un. of Trento and all the people I surely forgot in these short acknowledgments.

Thank you all.

RINGRAZIAMENTI

Un doveroso ringraziamento va al mio capo, Prof. Sandra Dirè, per la capacità di promuovere con passione e rigore aspetti della chimica che non avevo affrontato in precedenza, e per aver saputo lottare senza sosta, al fine di rendermi migliore sotto tanti aspetti.

Un ringraziamento particolare va al Prof. Riccardo Ceccato, che con la sua profonda conoscenza e l'infinita pazienza mi hanno guidato lungo il cammino, a volte tortuoso, di questi anni di dottorato. Un grazie va anche al Prof. Quaranta, che ha rallegrato i laboratori con l'umorismo e la goliardia tipica della mia università d'origine: Padova.

Tanti sono stati, come precedentemente detto, i professori e/o i ricercatori con cui ho avuto l'occasione e la fortuna di confrontarmi, a tutti loro va un ringraziamento.

Un doppio grazie va ad Alexia e Livio, i tecnici del laboratorio, per avermi aiutato quando ero nel bisogno: GRAZIE!

Molte sono le persone che hanno attraversato la mia vita in questo lungo periodo, e ognuna di loro ha in un modo o nell'altro influenzato il mio percorso. Dei compagni di dottorato vorrei ringraziare in special modo Anna Rita e Giusy e naturalmente Dario, senza il quale il primo anno in special modo, non sarebbe trascorso in modo così divertente.

Tra le persone che voglio ringraziare ci sono sicuramente Lung Hao Hu, per le lunghe chiacchierate a pranzo, Lorenzo per la grande amicizia e le serate a teatro (ti auguro ogni bene), Francesca De Genua per l'immensa disponibilità, anche umana, Icio per i voli mentali sul Giappone, che tanto mi tenevano compagnia durante le ore passate a fare misure, Emanuela che mi ha "sopportato" negli ultimi tempi.

Certo non ci si può dimenticare di chi tenta di tenermi in forma, facendomi correre dietro ad una pallina da tennis e non solo (Pic), o chi, anche se lontano ha sempre tempo per risolvere un problema o rispondere a una

domanda bizzarra (Marco).

Ai tecnici dei laboratori adiacenti (idraulica e strutture), che con il loro umorismo allietano le giornate!

I miei più vivi ringraziamenti vanno a Daniel che mi ha sorretto in uno dei periodi più bui (te ne sarò grata per sempre!), a Claudia per le chiacchiere, le uscite, le discussioni, e un grazie particolare alla mia stampella vivente, Gabriele, per esserci quando ne ho bisogno, senza tante domande (davvero il mio "angelo custode").

A voi tutti un enorme grazie.

Ultima, ma assolutamente non ultima, la mia famiglia, per il continuo supporto, l'amore e la dedizione, che solo un focolare domestico sanno dare.

Ai miei genitori, che incredibilmente, dopo tutti questi anni di studio ancora non si sono stufati; a mia sorella, che per quanto possiamo discutere, non cambierei per nulla al mondo, a nonna, che ancora sorride orgogliosa quando vado a trovarla, a mia zia, zii e cuginetti, che mi supportano sempre.

Ai miei nipoti, specialmente Asia, che con il suo incondizionato affetto, mi fa pensare che di buono al mondo ce ne è tanto, bisogna solo cercarlo.

Un ultimo pensiero va alle persone che mi hanno amata e non ci sono più, spero siate orgogliosi di me.

Sicuramente avrò dimenticato molte persone, non me ne vogliono...

Grazie mille ancora.